

AD-A013 167

INTERNAL STRUCTURE AND PHYSICAL PROPERTIES OF CERAMICS  
AT HIGH TEMPERATURES

W. C. Tripp, et al

Systems Research Laboratories, Incorporated

Prepared for:

Aerospace Research Laboratories

June 1975

DISTRIBUTED BY:

**NTIS**

National Technical Information Service  
U. S. DEPARTMENT OF COMMERCE

Reproduced by  
**NATIONAL TECHNICAL  
INFORMATION SERVICE**  
U.S. Department of Commerce  
Springfield, VA. 22151

UNCLASSIFIED

SECURITY CLASSIFICATION OF THIS PAGE (When Data Entered)

REPORT DOCUMENTATION PAGE		READ INSTRUCTIONS BEFORE COMPLETING FORM															
1. REPORT NUMBER ARL 75-0130	2. GOVT ACCESSION NO.	3. RECIPIENT'S CATALOG NUMBER AD-A013 167															
4. TITLE (and Subtitle)  Internal Structure and Physical Properties of Ceramics at High Temperatures.		5. TYPE OF REPORT & PERIOD COVERED Final Technical Report 30 June 1971 - 30 Nov. 1974															
7. AUTHOR(s) W. C. Tripp, J. W. Hinze, M. G. Mendiratta, R. H. Duff, A. F. Hampton, J. E. Stroud, and E. T. Rodine.		6. PERFORMING ORG. REPORT NUMBER 6731															
9. PERFORMING ORGANIZATION NAME AND ADDRESS Systems Research Laboratories, Inc. (SRL) 2800 Indian Ripple Road Dayton, Ohio 45440		8. CONTRACT OR GRANT NUMBER(s)  F33615-71-C-1841															
11. CONTROLLING OFFICE NAME AND ADDRESS Metallurgy & Ceramics Research Laboratory (LL) Aerospace Research Laboratories (AFSC) Wright-Patterson AF Base, Ohio 45433		10. PROGRAM ELEMENT, PROJECT, TASK AREA & WORK UNIT NUMBERS 61102F 70210337 (70210264)															
14. MONITORING AGENCY NAME & ADDRESS (if different from Controlling Office)		12. REPORT DATE JUNE 1975															
		13. NUMBER OF PAGES 277															
		15. SECURITY CLASS. (of this report)  Unclassified															
16. DISTRIBUTION STATEMENT (of this Report)  Approved for public release; distribution unlimited.		15a. DECLASSIFICATION/DOWNGRADING SCHEDULE															
17. DISTRIBUTION STATEMENT (of the abstract entered in Block 20, if different from Report)																	
18. SUPPLEMENTARY NOTES																	
PRICES SUBJECT TO CHANGE																	
19. KEY WORDS (Continue on reverse side if necessary and identify by block number): <table border="0"> <tr> <td>oxidation</td> <td>microstructure</td> <td>silicon nitride</td> </tr> <tr> <td>corrosion</td> <td>electron-microprobe analysis</td> <td>silicon</td> </tr> <tr> <td>alloys</td> <td>silicon carbide</td> <td>silicon carbide plus</td> </tr> <tr> <td>transport properties</td> <td>hafnium diboride plus silicon</td> <td>mullite composite</td> </tr> <tr> <td>mechanical properties</td> <td>carbide composite</td> <td></td> </tr> </table>			oxidation	microstructure	silicon nitride	corrosion	electron-microprobe analysis	silicon	alloys	silicon carbide	silicon carbide plus	transport properties	hafnium diboride plus silicon	mullite composite	mechanical properties	carbide composite	
oxidation	microstructure	silicon nitride															
corrosion	electron-microprobe analysis	silicon															
alloys	silicon carbide	silicon carbide plus															
transport properties	hafnium diboride plus silicon	mullite composite															
mechanical properties	carbide composite																
20. ABSTRACT (Continue on reverse side if necessary and identify by block number) <p>This final technical report summarizes investigations which have been conducted in order to gain an understanding of materials behavior at high temperatures. Investigations were conducted in five principle areas: 1) oxidation of silicon-base materials, 2) corrosion of experimental nickel-chromium-aluminum alloys, 3) transport properties of high-temperature oxides, 4) mechanical properties and microstructure of titanium alloys, and 5) electron-microprobe analysis of high-temperature materials. The oxidation behavior of silicon carbide, silicon</p>																	

DD FORM 1473 EDITION OF 1 NOV 65 IS OBSOLETE 1

UNCLASSIFIED

SECURITY CLASSIFICATION OF THIS PAGE (When Data Entered)

UNCLASSIFIED

SECURITY CLASSIFICATION OF THIS PAGE(When Data Entered)

Block 19 - Key Words (Continued) -

silicon plus silicon carbide composite	cobalt oxide
silicon nitride plus black glass composite	aluminum oxide
high-temperature materials	hafnium dioxide
Ni-Cr-Al	Ti-6Al-2Sn-4Zr-2Mo
silicon dioxide	Ti-6Al-2Sn-4Zr-6Mo
tantalum pentoxide	embrittlement
magnesium oxide	

Block 20 - Abstract (Continued) -

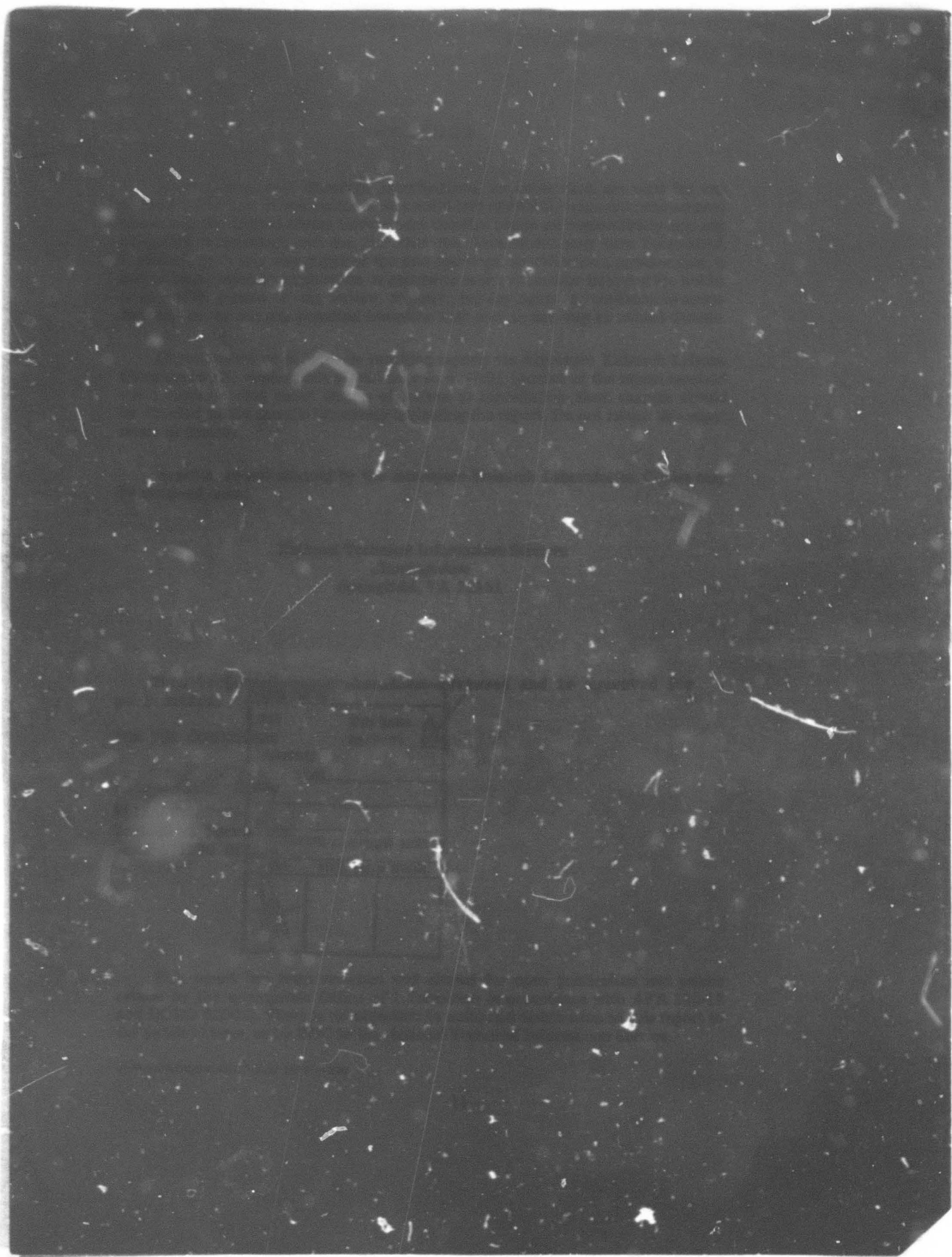
nitride, and silicon as well as composites such as hafnium diboride plus silicon carbide, silicon plus silicon carbide, silicon carbide plus mullite, and silicon nitride plus black glass was investigated in the temperature range (excepting silicon) 1200-1550°C. Oxidation kinetics and resulting oxide microstructures were found to be extremely sensitive to impurities in the matrix. Activation energies for oxidation ranged from 28 kcal/mole for silicon to 122 kcal/mole for Norton HS-110 silicon nitride. The high-temperature corrosion of nickel-chromium-aluminum alloys was investigated in severe environments including sodium sulfate/oxygen, sodium carbonate/oxygen, hydrogen/hydrogen sulfide, and carbon monoxide/carbon dioxide. Rapid rates of alloy attack were observed, especially in hydrogen/hydrogen sulfide environments. Transport properties of the high-temperature oxides silicon dioxide, tantalum pentoxide, magnesium oxide, cobalt oxide, aluminum oxide, and hafnium dioxide were investigated. The specific properties studied were ionic and electronic conductivity, ionic transference number, Seebeck coefficient, thermionic emission, and interdiffusivity. Microstructures and mechanical properties of two commercial high-temperature titanium alloys were investigated--Ti-6Al-2Sn-4Zr-2Mo and Ti-6Al-2Sn-4Zr-6Mo. The embrittlement of the Ti-6242 alloy after long exposures at elevated temperatures was correlated with the precipitation of coherent, ordered alpha sub 2 phase particles in the alpha-phase matrix. The tempering of the orthorhombic martensite in the Ti-6246 alloy imparts appreciable strength at elevated temperature while causing severe embrittlement at room temperature. Electron microprobe techniques were used to examine x-ray emission energy changes upon chemical combination of third-period metals such as magnesium, aluminum, and silicon with second-period nonmetals such as oxygen, nitrogen, and carbon. The energy change was related to the bond type and can be used for determination of chemical species present.

1a

UNCLASSIFIED

SECURITY CLASSIFICATION OF THIS PAGE(When Data Entered)





## PREFACE

This report was prepared by the Research Applications Division, Systems Research Laboratories, Inc., Dayton, Ohio, under Air Force Contract No. F33615-71-C-1841, Project 7021. Dr. H. C. Graham of the Metallurgy and Ceramics Research Laboratory (LL), Aerospace Research Laboratories, (AFSC), Wright-Patterson Air Force Base, Ohio, 45433, was the government project scientist.

# TABLE OF CONTENTS

SECTION	PAGE
I INTRODUCTION	1
II HIGH-TEMPERATURE OXIDATION OF SILICON-BASE MATERIALS	4
Oxidation of Hot-Pressed SiC	4
Experimental	5
Results	6
Discussion	13
Oxidation of $\text{HfB}_2 + 20 \text{ v/o SiC}$	14
Experimental	15
Results	16
Discussion	23
Oxidation of $\text{Si}_3\text{N}_4$	33
Reaction-Sintered $\text{Si}_3\text{N}_4$	33
Norton HS-110 $\text{Si}_3\text{N}_4$	33
Norton HS-130 $\text{Si}_3\text{N}_4$	37
Summary and Conclusions	71
Oxidation Behavior of a Si-SiC Composite	72
Experimental	72
Materials Characterization	73
Results and Discussion	77
Summary and Conclusions	88
Oxidation of SiC-Mullite Composites	94
Experimental	94
Results and Discussion	96
Summary and Conclusions	104
Oxidation of a $\text{Si}_3\text{N}_4 + \text{"Black Glass"}$ Composite	104
Experimental	104
Results and Discussion	106
Summary and Conclusions	113
Oxidation of Si at High Temperatures	116
Experimental	117
Results and Discussion	118
Summary and Conclusion	125

Preceding page blank

# TABLE OF CONTENTS (continued)

SECTION	PAGE
III	HIGH-TEMPERATURE CORROSION OF EXPERIMENTAL Ni-Cr-Al ALLOYS 126
	Investigation of the Mechanism of Sodium Salt Induced Accelerated Oxidation of Ni-Base Alloys 126
	Experimental 128
	Results and Discussion 128
	Summary and Conclusions 139
	Degradation of Ni8Cr6Al at 1000°C in Gaseous Environments Containing Carbon or Sulfur 139
	Experimental 140
	Results and Discussion 140
	Summary and Conclusions 150
IV	TRANSPORT PROPERTIES OF HIGH-TEMPERATURE OXIDES 151
	High-Temperature Electrical Properties of SiO <sub>2</sub> 151
	Results 152
	Discussion 157
	Defect Structure of Ta <sub>2</sub> O <sub>5</sub> 163
	Experimental Procedure 163
	Results and Discussion 164
	Electrical Property Measurements on Refractory Oxides Above 1600°C 176
	Summary of Applicable Literature 177
	Experimental Procedures 180
	Results 184
	Conclusions 192
	Interdiffusion Studies on the CoO-MgO System 194
	Experimental 194
	Analysis Techniques 196
	Results and Discussion 198

SECTION		PAGE
V	MECHANICAL PROPERTIES AND MICROSTRUCTURES OF HIGH-TEMPERATURE Ti-BASE ALLOYS	211
	Tensile Properties to 550°C and Microstructures in Quenched and Aged Ti-6Al-2Sn-4Zr-6Mo Alloy	211
	Tensile Properties at Room Temperature and at 550°C Microstructure Correlations	212 215
	Embrittlement of Ti-6Al-2Sn-4Zr-2Mo Alloy by $\alpha_2$ -Phase Precipitation	222
VI	ELECTRON-MICROPROBE ANALYSIS OF HIGH-TEMPERATURE MATERIALS	227
	Quantitative Analysis	227
	Procedures	227
	Standards	229
	Chemical-Combination Analysis by X-Ray Emission Energy Shifts	239
	Experimental	240
	Results	241
	Discussion	241
	Conclusion	249
	REFERENCES	251

# LIST OF ILLUSTRATIONS

FIGURE		PAGE
1	Temperature Dependence of the Weight Gain of SiC in 150 torr O <sub>2</sub> .	7
2	Arrhenius Plot of the Parabolic Rate Constants for the Oxidation of SiC in 150 torr O <sub>2</sub> .	8
3	SEM Micrographs of the Fractured Cross Sections of SiC Specimens Oxidized in 150 torr O <sub>2</sub> .	10
4	Oxygen Partial Pressure Dependence of the Weight Gain of SiC in O <sub>2</sub> and O <sub>2</sub> /Ar Gas Mixtures at 1400°C (Total Pressure = 150 torr).	11
5	Oxygen Partial Pressure Dependence of the Parabolic Rate Constant for SiC In O <sub>2</sub> and O <sub>2</sub> /Ar Gas Mixtures (Total Pressure = 150 torr).	12
6	Typical Parabolic Plot of Kinetic Data for HfB <sub>2</sub> + SiC Oxidation at 1500°C in 250 torr O <sub>2</sub> .	17
7	Arrhenius Plot of Parabolic Rate Constants for Total Oxygen Consumption of HfB <sub>2</sub> + SiC in 250 torr O <sub>2</sub> .	18
8	Optical Micrograph of a HfB <sub>2</sub> + SiC Specimen Oxidized at 1400°C in 250 torr O <sub>2</sub> for 24 hr.	20
9	Electron-Beam Microprobe Scan of a HfB <sub>2</sub> + SiC Specimen Oxidized at 1400°C in 250 torr O <sub>2</sub> for 24 hr.	21
10	Total Oxygen Consumption of HfB <sub>2</sub> + SiC as a Function of Oxygen Partial Pressure at 1400°C.	22
11	Light Micrograph of a HfB <sub>2</sub> + SiC Specimen Oxidized at 1400°C in 975 ppm O <sub>2</sub> /Ar (P <sub>O<sub>2</sub></sub> = 3.2 x 10 <sup>-4</sup> atm) for 24 hr.	24
12	SEM Micrographs Showing the Effect of Oxygen Partial Pressure on Oxide-Scale Morphologies. Specimens Were Oxidized at 1400°C for 24 hr.	25
13	Light Micrographs of Two HfB <sub>2</sub> + SiC Samples Oxidized at 1400°C in CO/CO <sub>2</sub> Gas Mixtures for 24 hr.	26
14	Comparison of the Rates of HfO <sub>2</sub> Formation during Oxidation of HfB <sub>2</sub> + 20 v/o SiC, Hf, and HfB <sub>2</sub> in 250 torr O <sub>2</sub> .	28
15	Comparison of the Rates of SiO <sub>2</sub> Formation during Oxidation of HfB <sub>2</sub> + 20 v/o SiC and Hot Pressed SiC in 250 torr O <sub>2</sub> .	29

# LISI OF ILLUSTRATIONS (continued)

FIGURE		PAGE
16	Comparison of the Rates of Total Oxygen Consumption for $\text{HfB}_2 + 20 \text{ v/o SiC}$ and $\text{ZrB}_2 + 20 \text{ v/o SiC}$ at $1400^\circ\text{C}$ in 250 torr $\text{O}_2$ .	32
17	Oxidation Behavior of Reaction Bonded $\text{Si}_3\text{N}_4$ in 150 torr $\text{O}_2$ at $1400^\circ\text{C}$ .	34
18	Oxidation of Reaction Sintered $\text{Si}_3\text{N}_4$ at $1300^\circ\text{C}$ in 150 torr $\text{O}_2$ .	35
19	Weight Change Data for Norton HS-110 $\text{Si}_3\text{N}_4$ in 150 torr $\text{O}_2$ .	36
20	Hot-Pressed Norton HS-110 $\text{Si}_3\text{N}_4$ Oxidized at $1400^\circ\text{C}$ in Undried (●) and in Dried $\text{O}_2$ (○).	38
21	Parabolic Plot of Oxidation of Norton HS-110 $\text{Si}_3\text{N}_4$ in 150 torr Dried $\text{O}_2$ .	39
22	Arrhenius Plot of Parabolic Rate Constants for Norton HS-110 Hot Pressed $\text{Si}_3\text{N}_4$ in 150 torr Dried $\text{O}_2$ .	40
23	Comparison of the Oxidation Rate of Norton HS-110 and HS-130 $\text{Si}_3\text{N}_4$ at $1400^\circ\text{C}$ in 150 torr Dried $\text{O}_2$ .	41
24	Weight-Change Data for Norton HS-130 $\text{Si}_3\text{N}_4$ in 150 torr $\text{O}_2$ .	42
25	Parabolic Plot of Weight Change Data for Norton HS-130 $\text{Si}_3\text{N}_4$ in 150 torr $\text{O}_2$ .	43
26	Parabolic Plot of Weight Change Data for Norton HS-130 $\text{Si}_3\text{N}_4$ at $1500^\circ\text{C}$ in 150 torr $\text{O}_2$ .	44
27	Arrhenius Plot of the Parabolic Rate Constants for Norton HS-130 $\text{Si}_3\text{N}_4$ in 150 torr $\text{O}_2$ .	45
28	Long Time Weight Change Data of Norton HS-130 $\text{Si}_3\text{N}_4$ in 150 torr $\text{O}_2$ .	47
29	Parabolic Plot of Long Time Weight Change Data of Norton HS-130 $\text{Si}_3\text{N}_4$ in 150 torr $\text{O}_2$ .	48
30	Comparison of Oxidation Rate of Norton HS-130 $\text{Si}_3\text{N}_4$ in $\text{H}_2\text{O} + \text{O}_2$ and Dry $\text{O}_2$ at $1400^\circ\text{C}$ (Total Pressure = 150 torr).	49
31	Weight-Change Data of Norton HS-130 $\text{Si}_3\text{N}_4$ in the Range 75 to 600 torr $\text{O}_2$ at $1400^\circ\text{C}$ .	50
32	Weight Change Data of Norton HS-130 $\text{Si}_3\text{N}_4$ in the Range 75 to 600 torr Using $\text{O}_2/\text{N}_2$ Mixtures at $1400^\circ\text{C}$ (Total Pressure = 600 torr).	51



# LIST OF ILLUSTRATIONS (continued)

FIGURE		PAGE
33	Weight Change Data of Norton HS-130 $\text{Si}_3\text{N}_4$ in $10^{-6}$ to $10^{-9}$ atm $\text{O}_2$ Using $\text{CO}/\text{CO}_2$ Mixtures at $1400^\circ\text{C}$ .	53
34	Parabolic Plot of Weight Change Data for $\text{Si}_3\text{N}_4$ Oxidized at $1400^\circ\text{C}$ in $\text{O}_2$ , $\text{O}_2/\text{N}_2$ , $\text{O}_2/\text{Ar}$ , and $\text{CO}/\text{CO}_2$ Mixtures.	54
35	Microprobe Analysis of Scale Composition for Specimens Oxidized in 150 torr $\text{O}_2$ for 24 hr.	55
36	Optical Micrographs of the Scales Formed on $\text{Si}_3\text{N}_4$ Oxidized in 150 torr $\text{O}_2$ for 24 hr.	57
37	Scanning Electron Micrographs of the Scales Formed on $\text{Si}_3\text{N}_4$ after 24 hr of Reaction in 150 torr $\text{O}_2$ at $1400^\circ\text{C}$ .	59
38	Scanning Electron Micrographs of the Scales Formed on $\text{Si}_3\text{N}_4$ after 24 hr of Reaction in 150 torr $\text{O}_2$ at $1475^\circ\text{C}$ .	60
39	Optical Micrographs of Scales Formed on $\text{Si}_3\text{N}_4$ after 24 hr of Reaction in 75, 150, 300, and 600 $\text{O}_2$ at $1400^\circ\text{C}$ .	61
40	Scanning Electron Micrographs of the Scales Formed on $\text{Si}_3\text{N}_4$ in $\text{O}_2$ and in $\text{O}_2/\text{N}_2$ Gas Mixtures after Reaction for 24 hr at $1400^\circ\text{C}$ .	62
41	Scanning Electron Micrograph of the Scale Formed on $\text{Si}_3\text{N}_4$ after 24 hr of Reaction in 150 torr $\text{O}_2$ and 450 torr $\text{N}_2$ at $1400^\circ\text{C}$ .	63
42	Scanning Electron Micrographs of the Scale Formed on $\text{Si}_3\text{N}_4$ after 24 hr of Reaction in 300 torr $\text{O}_2$ and 300 torr $\text{N}_2$ at $1400^\circ\text{C}$ .	64
43	Parabolic Plot of Weight Change Data for $\text{Si}_3\text{N}_4$ Oxidized at $1400^\circ\text{C}$ in $\text{CO}/\text{CO}_2$ and $\text{CO}/\text{CO}_2/\text{N}_2$ Mixtures.	65
44	Scanning Electron Micrographs of the Scale Formed on $\text{Si}_3\text{N}_4$ after 24 hr of Reaction in $\text{CO}/\text{CO}_2 + \text{N}_2$ at $1400^\circ\text{C}$ ( $\text{CO}/\text{CO}_2 = 150$ torr, $\text{N}_2 = 450$ torr; $P_{\text{O}_2} = 10^{-6}$ atm).	
45	Macroscopic Appearance of Composite Coupons Used in Oxidation Studies.	74
46	Optical Micrographs of a Cross Section of Composite Coupon Showing Si Matrix (Light Region on the Right) and SiC Fiber Region.	75

# LIST OF ILLUSTRATIONS (continued)

FIGURE		PAGE
47	Fracture Surface of As-Received Composite in SiC Fiber Region.	76
48	Fractured Composite Sample in Region of Si/SiC Interface (Si is Smooth Region on the Left).	78
49	Microprobe X-Ray Scans of Cross Section of As-Received Composite Material.	79
50	Observed Sample Weight Gain and Oxygen Consumption (OC) as a Function of Exposure Time during Oxidation of Si/SiC Composite at Various Temperatures in Pure Flowing O <sub>2</sub> at an Ambient Pressure of 150 torr.	80
51	Parabolic Plot of Sample Weight Change and Oxygen Consumption (OC) as a Function of Exposure Time during Oxidation of Si/SiC Composite at Various Temperatures in Pure Flowing O <sub>2</sub> at an Ambient Pressure of 150 torr.	81
52	Arrhenius Plot of the Scaling-Rate Constant for the Si + SiC Composite Compared with Si and SiC.	82
53	Microstructure of Cross Section of Composite after 100 hr Exposure at 1200°C. (a) Oxide Scale over SiC Braid Region. (b) Oxide Scale in Region of Si/SiC Interface (Si is Smooth Region on Left).	84
54	Microstructure of Cross Section of Composite Oxidized at 1400°C for 100 hr. (a) and (b) Optical Micrographs of Oxide Scale over Si/SiC Regions. (c) Fracture Surface of Oxide Scale over SiC Region.	85
55	Cross Section of Composite Oxidized at 1200°C for 100 hr.	86
56	Macrographs of Surface Topography of Composite Coupons Oxidized at 1400°C and 1500°C.	87
57	Surface Topography of Composite Oxidized at 1500°C for 20 hr.	89
58	Fracture Surface of Composite after Oxidation at 1500°C for 20 hr Showing Fiber Pullout and Apparent "Sealing" of Fiber Tip.	90
59	Cross Section of Composite Oxidized at 1500°C for 20 hr.	91
60	Cross Section of Composite Oxidized at 1500°C for 20 hr.	92

# LIST OF ILLUSTRATIONS (continued)

FIGURE		PAGE
61	Optical Micrograph of Cross Section of Composite Coupon Oxidized at 1500°C for 20 hr, Showing Evidence of Oxidation Penetration above SiC Fiber Channels.	93
62	Optical Micrograph (a) and SEM Micrograph (b) of "As-Received" Composite Material, SiC-20 w/o Mullite.	95
63	Observed Weight Change as a Function of Exposure Time During Oxidation of SiC-Mullite Composites at Various Temperatures in Pure Flowing O <sub>2</sub> (Total Pressure = 150 torr).	97
64	Parabolic Plot of Sample Weight Change Data as a Function of Exposure Time during Oxidation of SiC-Mullite Composites at Various Temperatures in Pure Flowing O <sub>2</sub> (Total Pressure = 150 torr).	98
65	Arrhenius Plot of the Parabolic Rate Constants for SiC-Mullite Composites.	99
66	Plot of the Normalized Recession Rates for SiC-Mullite Composites Compared with Those Obtained for Si, SiC, and Norton HS-130 Si <sub>3</sub> N <sub>4</sub> Described Elsewhere in this Report.	101
67	Optical and SEM Micrographs of Cross Sections of Oxidized Composite Samples.	102
68	Cross Section of Scale Formed on SiC-20 w/o Mullite after 100 hr in 150 torr O <sub>2</sub> .	103
69	Microstructure of the As-Received Si <sub>3</sub> N <sub>4</sub> + Black Glass Composites Revealing Black-Glass Agglomerations.	105
70	Parabolic Plot of Weight Change as a Function of Time for 20BG Material.	107
71	Parabolic Plot of Sample Weight Change and Oxygen Consumption (OC) as a Function of Time for 30BG Material.	108
72	Arrhenius Plot of the Scaling-Rate Constant for 20BG and 30BG Material Compared with Norton HS-130 Si <sub>3</sub> N <sub>4</sub> .	109
73	Macrophotographs of 20BG and 30BG Specimens Oxidized at 1500°C for 100 hr.	110
74	Light Micrographs of 20BG Specimen Oxidized at 1570°C for 100 hr.	111

# LIST OF ILLUSTRATIONS (continued)

FIGURE		PAGE
75	Microprobe Analysis of 20BG Specimen Oxidized at 1500°C for 100 hr.	117
76	Macrophotographs of Oxidized Specimens Revealing the Effect of Porosity on Scale Morphologies.	114
77	Macrophotographs Comparing Scale Morphologies on Specimens Oxidized at 1500°C.	115
78	Arrhenius Plot of Parabolic Rate Constants for the Oxidation of Si in 600 torr O <sub>2</sub> .	119
79	Light Micrographs of Sample Surfaces Revealing Two Types of Scales Formed on Si during Oxidation in 600 torr O <sub>2</sub> .	120
80	Oxygen Pressure Dependence of the Scaling Rate Constant for Si Oxidation at 1300°C.	122
81	Comparison of the Oxidation Kinetics Obtained in This Investigation with Those in Previous Studies at Lower Temperatures in 1 atm O <sub>2</sub> .	123
82	Comparison of the Oxidation Kinetics Obtained in This Investigation with Those of Other Si-Base Materials Presented in This Report.	124
83	Representative Microstructures of Ni8Cr6Al and Ni8Cr6Al0.2Y. Magnification X55.	129
84	Observed Weight Gain as a Function of Exposure Time During the Oxidation of Na <sub>2</sub> SO <sub>4</sub> Coated Ni8Cr6Al and Ni8Cr6Al0.2Y Alloys at 1000°C in 150 torr O <sub>2</sub> .	130
85	Microstructure of Cross Section of Na <sub>2</sub> SO <sub>4</sub> Coated Ni8Cr6Al after 100 hr Exposure at 150 torr O <sub>2</sub> at 1000°C. Note Sulfides Precipitated in Matrix.	131
86	Microstructure of Cross Section of Na <sub>2</sub> SO <sub>4</sub> Coated Ni8Cr6Al after 30 min Exposure in 150 torr O <sub>2</sub> at 1000°C. Scale Has Spalled Revealing Sulfide Precipitates in Matrix.	131
87	Cross Section of Scale Formed on Na <sub>2</sub> SO <sub>4</sub> Coated Ni8Cr6Al Oxidized in 150 torr O <sub>2</sub> for 30 min at 1000°C.	133
88	Cross Section of Scale Formed on Na <sub>2</sub> SO <sub>4</sub> Coated Ni8Cr6Al Oxidized in 150 torr O <sub>2</sub> for 100 hr at 1000°C.	134

# LIST OF ILLUSTRATIONS (continued)

FIGURE		PAGE
89	Observed Weight Gain as a Function of Exposure Time During the Oxidation of $\text{Na}_2\text{CO}_3$ Coated Ni8Cr6Al and Ni8Cr6Al0.2Y at 1000°C in 150 torr $\text{O}_2$ .	135
90	Cross Section of Scale Formed on $\text{Na}_2\text{CO}_3$ Coated Ni8Cr6Al after 100 hr in 150 torr $\text{O}_2$ at 1000°C.	136
91	Observed Weight Gain as a Function of Exposure Time during Oxidation of $\text{NaNO}_3$ Coated Ni8Cr6Al and Ni8Cr6Al0.2Y at 1000°C in 150 torr $\text{O}_2$ .	137
92	Cross Section of Scale Formed on $\text{NaNO}_3$ Coated Ni8Cr6Al after 150 hr in 150 torr $\text{O}_2$ at 1000°C.	138
93	Optical Micrographs of Specimen Exposed to a $\text{CO}/\text{CO}_2$ Environment for 100 hr at 1000°C.	141
94	Microprobe Scans of Region 1 in the Preceding Figure Depicting Thick Al Rich $\text{Cr}_2\text{O}_3$ Layer with $\text{Al}_2\text{O}_3$ Internal Oxidation.	143
95	Microprobe Scans of Region 3 in Figure 93 Depicting Multiple Internal $\text{Al}_2\text{O}_3$ Layers.	144
96	Microprobe Scans of Region 2 in Figure 93 Depicting Grain Boundary Penetration of $\text{Al}_2\text{O}_3$ .	145
97	Microprobe Scans of Region 4 in Figure 93 Revealing Grain Boundary and Intragranular Carbides.	146
98	Optical Micrographs Showing the Formation of Sulfides after a 1 hr Exposure to a $\text{H}_2/\text{H}_2\text{S}$ Environment at 1000°C.	147
99	Microprobe Scans of Sulfidized Region after 42 min in $\text{H}_2/\text{H}_2\text{S}$ Followed by a 15 hr Exposure to $\text{O}_2$ at 1000°C. Note the Thick $\text{Al}_2\text{O}_3$ Scale Formed.	148
100	Comparison of Corrosion Rates and Microstructures for Specimens Exposed to $\text{O}_2$ , $\text{Na}_2\text{SO}_4/\text{O}_2$ , $\text{CO}/\text{CO}_2$ , and $\text{H}_2/\text{H}_2\text{S}$ Environments at 1000°C.	149
101	Total ac Conductivity in $\text{SiO}_2$ as Function of Temperature at $P_{\text{O}_2} = 10^{-1}$ atm.	153
102	Plot of $\log \sigma_T$ as a Function of $\log P_{\text{O}_2}$ at 1400 and 1500°C, Revealing Mixed Ionic and Electronic Character of $\text{SiO}_2$ .	154

# LIST OF ILLUSTRATIONS (continued)

FIGURE		PAGE
103	Plot of $t_1$ as a Function of $\log P_{O_2}$ for $SiO_2$ at $1500^\circ C$ . Solid line is $t_1$ predicted from the conductivity data in Figure 102.	156
104	DC Polarization Data: Observed Current (I) as a Function of Applied Voltage ( $\epsilon u$ ).	158
105	Plot of $\log \sigma_n$ and $\log \sigma_T$ as a Function of $1/T$ at $P_{O_2} = 10^{-15}$ atm.	159
106	Plot of $\log \sigma_n \sigma_p$ as a Function of $1/T$ , Giving the $0^\circ K$ Band Gap Energy.	160
107	(a) Electrical Conductivity and (b) Ionic Transference Number of $Ta_2O_5$ as Functions of $P_{O_2}$ .	165
108	Plot of $\log \sigma_T$ as a Function of $\log P_{O_2}$ Derived from Eq (31).	168
109	Determination of $\beta$ as a Function of Temperature Obtained from Eq (31) and from Conductivity Data of Fig. 107(a).	170
110	Oxygen Vacancy Concentration in $Ta_2O_5$ at $P_{O_2} = 10^{-16}$ (atm) Determined from Weight Change Measurements.	172
111	Seebeck Coefficient of $Ta_2O_5$ as a Function of $P_{O_2}$ .	173
112	Comparison of Electrical Conductivity Data for $Al_2O_3$ Single Crystals (Two Data Points from Present Study). Figure and References Taken from Brook et al. (75)	181
113	Schematic Diagram of Sample Region of Conductivity Measurement Apparatus.	183
114	Conductance Between Electrodes without a Sample, Measured in Air.	185
115	Conductance of Air Gap as a Function of Air Gap Distance (1 1/2 Turns = 1/16 in.).	187
116	Log Log Plot of Air Gap Conductance as a Function of Air Gap Distance (1 1/2 Turns = 1/16 in.).	188
117	Richardson-Dushman Plot of Air Gap Data.	189
118	Effect of Bias Voltage on Air Gap Conductance.	191
119	Comparison of Air Gap Conductance with Conductivity of Sapphire.	192

# LIST OF ILLUSTRATIONS (continued)

FIGURE		PAGE
120	Plot of Cation Concentration as a Function of Distance for CoO-MgO Interdiffusion Couple No. 8.	199
121	Plot of Calculated Diffusion Coefficient as a Function of Composition for CoO-MgO Couple No. 8.	201
122	Plot of Calculated Interdiffusion Coefficient as a Function of $1000/T$ ( $^{\circ}\text{K}$ ) for Couples Annealed in $P_{\text{O}_2} = 1 \text{ atm.}$	205
123	Plot of Calculated Interdiffusion Coefficient as a Function of $1000/T$ ( $^{\circ}\text{K}$ ) for Couples Annealed in $P_{\text{O}_2} = 8 \times 10^{-6} \text{ atm.}$	207
124	Tensile Properties of Ti-6246 at $550^{\circ}\text{C}$ as Function of Annealing Temperature. Specimens Water Quenched from Annealing Temperatures and Then Aged at $550^{\circ}\text{C}$ for 48 hr.	213
125	Tensile Properties of Ti-6246 at $550^{\circ}\text{C}$ as Function of Aging Temperature. Specimens Annealed at $950^{\circ}\text{C}$ and Water Quenched Prior to 48 hr Aging Treatments.	214
126	Bright-Field Electron Micrograph Showing High Volume Fraction of Primary- $\alpha$ Plates. Heat Treatment: $800^{\circ}\text{C}/1 \text{ hr} \rightarrow \text{w.q.}; 550^{\circ}\text{C}/48 \text{ hr} \rightarrow \text{air cool (a.c.).}$	216
127	Light Micrograph Showing General Microstructure of Tempered Martensite. Light Particles, as Shown by Arrow, Belong to Primary- $\alpha$ Phase. Heat Treatment: $950^{\circ}\text{C}/1 \text{ hr} \rightarrow \text{w.q.}; 550^{\circ}\text{C}/48 \text{ hr} \rightarrow \text{a.c.}$	217
128	Diamond-Pyramid Hardness Values of Ti-6246 as Function of Aging Time at $550^{\circ}\text{C}$ . Specimens Annealed at $950^{\circ}\text{C}/1 \text{ hr} \rightarrow \text{w.q.}$ Prior to Aging Treatments.	218
129	(a) Bright Field Electron Micrograph Showing Precipitate Contrast in the Tempered Martensite. Heat Treatment: $950^{\circ}\text{C}/1 \text{ hr} \rightarrow \text{w.q.}; 550^{\circ}\text{C}/8 \text{ hr} \rightarrow \text{a.c.}$ (b) Corresponding Electron Diffraction Pattern Showing $[\bar{1}\bar{1}20]_{\alpha}$ Hexagonal Zone Axis Coinciding with $[001]_{\beta}$ Zone Axis.	220
130	Different Area of the Thin Foil of Figure 129 Showing Region of Retained $\beta$ in Which $\alpha$ Particles Have Precipitated. (a) Electron Diffraction Pattern. (b) Dark-Field Micrograph.	221



# LIST OF ILLUSTRATIONS (continued)

FIGURE		PAGE
131	Bright-Field Electron Micrograph Showing $\alpha$ - $\beta$ Structure in Ti-6242 Alloy. 1650°F Processed $\rightarrow$ Air Cooled; 1100°F/8 hr Stress Relieved.	224
132	Selected Area Diffraction Pattern Taken from a Primary- $\alpha$ Grain of Figure 131. $[2\bar{1}\bar{1}0]_{\alpha}$ Zone Axis. Arrow Shows Position of Faint $(01\bar{1}1)_{\alpha_2}$ Reflection.	224
133	(a) $[2\bar{1}\bar{1}0]_{\alpha}$ -Zone-Axis Diffraction Pattern Showing Intense $(01\bar{1}1)_{\alpha_2}$ Super-Lattice Reflections. (b) Dark Field Taken from the $\alpha_2$ Reflection Showing Uniform Distribution of $\alpha_2$ Needles. 1650°F Processed $\rightarrow$ Air Cooled; 1100°F/8 hr Stress Relieved, Followed by 1000°F/1000 hr Aging Treatment.	
134	Calculated and Experimental Curves of the Intensity Ratios of the Metal Radiation in the Metal/Metal Oxide System as a Function of Accelerating Voltage.	231
135	Intensity Ratios for Hafnium in Hafnium Dioxide as Function of Accelerating Potential.	235
136	Intensity of Strontium X-Radiation as Function of Weight Fraction of Strontium in Lanthanum Chromite.	237
137	Strontium X-Ray Intensities from Strontium in Lanthanum Chromite.	238
138	Silicon $K_{\beta}$ X-Ray Emission Spectra for the Element, Carbide, Nitride, and Oxide.	242
139	Percent Ionic Character Calculated from Pauling's Electronegativities and Formula vs Percent Change in Energy or $K_{\beta}$ X-Ray Emission Spectra of the Metals from a Number of Compounds.	248

# LIST OF TABLES

TABLE		PAGE
I	Published Activation Energies for Powdered SiC Oxidation	5
II	Scale Etching Experiments for Calculation of Percent N <sub>2</sub> Retained in Scales	70
III	Weight Gain per Unit Surface Area for SiC + 3 w/o Mullite and SiC + 20 w/o Mullite Compared to Si and Norton HS-130 Si <sub>3</sub> N <sub>4</sub>	96
IV	Mass Spectrographic Analysis of Ta <sub>2</sub> O <sub>5</sub>	175
V	Mass Spectrographic Analysis of MgO (in ppm)	195
VI	Mass Spectrographic Analysis of CoO (in ppm)	195
VII	Composition Dependence of $\tilde{D}$ as a Function of Temperature and Oxygen Partial Pressure	202
VIII	Room Temperature Mechanical Properties of Ti-6Al-2Sn-4Zr-2Mo Alloy in the Stress-Relieved and Aged Conditions	223
IX	Peak Energies (in eV) of K <sub><math>\beta</math></sub> X-Ray Emission from Third-Period Metals	243
X	Calculated and Experimental Values for Change in Peak Energies of the K <sub><math>\beta</math></sub> Emission Spectra for Some Third-Period Metal Compounds	246

## SECTION I

### INTRODUCTION

Continued advancement in the provision of low cost, reliable, long life, high performance energy systems is critically dependent upon the availability and effective utilization of improved materials. At present the performance requirements of many systems have pushed currently available materials to the limit of their usefulness. The projected Air Force advancements in these systems make the availability of materials possessing high strength and chemical stability imperative; thus, the successful development of such materials is of fundamental importance to the Air Force mission.

The past two decades have seen spectacular alloy development payoffs, resulting in Ni- and Co-base superalloys capable of operation at  $\sim 1000^{\circ}\text{C}$ . However, severe oxidation and hot-corrosion problems with these alloy systems have been encountered; and, for the near term, it is expected that further efforts to improve these alloys will be primarily directed toward increasing the chemical stability with minimum sacrifice of hot strength. A better understanding of the mechanism of hot corrosion or accelerated oxidation will significantly hasten this progress.

Worthwhile as these advances will be, it is nevertheless clear that, for the intermediate and long term, radically new materials must be found. An exciting prospect for advanced structural high-temperature use is the application of ceramic and intermetallic materials, many of which combine extremely high strength and creep resistance with outstanding oxidation resistance. Si-base materials, for example, are finding increased usage where high temperature corrosion resistance and compressive strength are required. A further possibility which appears particularly promising is the incorporation of two or more materials into a composite, thereby taking maximum advantage of the desirable properties of the individual materials and at the same time allowing the composite structure to obviate some of the less favorable mechanical property aspects.

One of the most important contributions the materials scientist can make to the development of advanced high-temperature materials is to determine the

relationship which exists between the composition, microstructure, and defect structure of a material and its physical, chemical, and mechanical properties. By gaining a basic understanding of these relationships further improvements in material performance can be realized. Often these relationships are quite complex and their determination extremely difficult; however, for successful fabrication and utilization of reliable and consistent materials, a fundamental requirement is full knowledge of the material characteristics.

In this technical report, the results of investigations on materials behavior at high temperatures are presented. Investigations were conducted in five principle areas:

- 1) High-temperature oxidation of Si-base materials.
- 2) High-temperature corrosion of experimental Ni-Cr-Al alloys.
- 3) Transport properties of high-temperature oxides.
- 4) Mechanical properties and microstructure of high-temperature Ti alloys.
- 5) Electron-microprobe analysis of high-temperature materials.

A number of publications and presentations have resulted from these investigations:

J. W. Hinze, W. C. Tripp, and H. C. Graham, "Oxidation Behavior of  $\text{HfB}_2$ ," Paper No. 83-B-73 presented at the 75th Annual Meeting of the American Ceramic Society, Cincinnati, Ohio, April 29-May 3, 1973.

J. W. Hinze, W. C. Tripp, and H. C. Graham, "The High-Temperature Oxidation Behavior of a  $\text{HfB}_2$  + 20 v/o SiC Composite," submitted in July 1974 to J. Electrochem. Soc. for publication.

J. W. Hinze, W. C. Tripp, and H. C. Graham, "The High-Temperature Oxidation of Hot-Pressed Silicon Carbide," Paper No. 28-S2-74 presented at the 76th Annual Meeting of the American Ceramic Society, Chicago, April 28-May 2, 1974.

J. W. Hinze, W. C. Tripp, and H. C. Graham, "The High-Temperature Oxidation of Hot-Pressed Silicon Carbide," in Mass Transport in Ceramics (A. H. Heuer and A. R. Cooper, eds.), (Plenum Publishing Co., New York, in press). Presented at the 9th University Conference on Ceramic Science, Case Western Reserve University, Cleveland, Ohio, June 3-5, 1974.

W. C. Tripp and J. W. Hinze, "Oxide Scale Formation on Hot-Pressed  $\text{Si}_3\text{N}_4$ ," Presented at the American Ceramic Society, Cincinnati, Ohio, April 30-May 4, 1973.

W. C. Tripp and J. E. Stroud, "Interdiffusion in the Single-Crystal System Mg-Co-O," Presented at the American Ceramic Society, Cincinnati, Ohio, April 30-May 4, 1973.

W. C. Tripp, J. W. Hinze, and H. C. Graham, "Temperature and Pressure Dependence of Thick Scale Formation on Silicon," Presented at the 76th Annual Meeting of the American Ceramic Society, Chicago, Illinois, April 28-May 2, 1974.

J. Stroud, W. C. Tripp, and J. M. Wimmer, "The Defect Structure of  $Ta_2O_5$ ," J. Am. Ceram. Soc. 57, 172 (1974).

J. E. Stroud, W. C. Tripp, and J. W. Hinze, "High-Temperature Charge and Mass Transport in Vitreous Silica," Presented at the Electrochemical Society Meeting, San Francisco, Calif., May 12-17, 1974.

M. G. Mendiratta, "Tensile Properties to 650°C and Deformation Structures in a Precipitation-Strengthened Titanium Aluminum Alloy," Presented at the Fall Meeting of TMS-AIME, Chicago, Illinois, Oct. 1-4, 1973. Met. Trans. (May 1974).

M. G. Mendiratta, "Tensile Properties to 550°C and Microstructures in Quenched and Aged Ti-6Al-2Sn-4Zr-6Mo Alloy," Presented at the AIME Spring Meeting, Pittsburgh, Pa., May 1974.

M. G. Mendiratta, "Embrittlement of Ti-6Al-2Sn-4Zr-2Mo Alloy by  $\alpha_2$ -Phase Precipitation," Accepted for publication in Met. Trans.

A. F. Hampton, "High Temperature Oxidation Behavior of Some Experimental Ceramic-Based Composites," Presented at the 76th Meeting of the American Ceramic Society, Chicago, Ill., April 28-May 2, 1974.

A. F. Hampton, H. H. Davies, and H. C. Graham, "Some Observations on the High-Temperature Behavior of Ni8Cr6Al in a Variety of Corrosive Environments at 1000°F," to be presented at the International Symposium on Metal-Slag-Gas Reactions and Processes, Toronto, Canada, May 11-16, 1975.

A. F. Hampton, H. H. Davis, and H. G. Granam, "Severe Corrosive Attack in NiCrAl System. I, in C-Containing Environments," to be published.

A. F. Hampton, H. H. Davis, and H. G. Graham, "Severe Corrosive Attack in NiCrAl System. II, in S-Containing Environments," to be published.

R. H. Duff, "Chemical Species Identification in Ceramic Materials Using an Electron Microprobe," Presented at the 76th Annual Meeting of the American Ceramic Society, Chicago, Ill., April 28-May 2, 1974.

R. H. Duff, "Chemical Species Identification in an SEM by Changes in Emitted X-ray Energies," Presented at the 32nd Annual Meeting of the Electron Microscope Society of America, St. Louis, Mo., Aug. 13-16, 1974.

## SECTION II

### HIGH-TEMPERATURE OXIDATION OF SILICON-BASE MATERIALS

For the past several years, SRL has been investigating the oxidation behavior of a number of Si-base materials, the aim being to define the rate determining mechanism(s) of oxidation. These materials have a bright future in high-temperature energy systems such as MHD generators, rocket engines, re-entry vehicles, and advanced air-breathing propulsion systems. Desirable properties include retained strength at elevated temperatures, chemical inertness, thermal stability, high strength-to-weight ratio, and thermal shock resistance.

Among the materials studied were Si, SiC,  $\text{Si}_3\text{N}_4$ , and composites such as  $\text{HfB}_2 + \text{SiC}$ , and  $\text{Si}_3\text{N}_4 + \text{carbon glass}$ . In all cases  $\text{SiO}_2$  scales were formed upon oxidation, and, in most cases, parabolic oxidation kinetics were observed; nevertheless, activation energies for oxidation were much larger than those often quoted for the oxidation of Si. Activation energies of 28-30 kcal/mole have been reported in the literature<sup>(1-3)</sup> and elsewhere in this report for Si oxidation, whereas 70-122 kcal/mole was found in our laboratory for other Si base materials. Despite these large activation energies, the very low oxidation rates observed in our investigations suggested that the reactions were still controlled by oxygen diffusion through the  $\text{SiO}_2$  layer, even in the case of layered oxides where silica is the minor scale constituent. Such was the case for  $\text{HfB}_2 + \text{SiC}$  oxidation, where an activation energy of 106 kcal/mole was observed.

#### OXIDATION OF HOT-PRESSED SiC

Most investigations on SiC oxidation<sup>(4-10)</sup> have been conducted with powdered material because only recently have hot-pressing and crystal-growth techniques been successful in preparing bulk SiC of reasonable purity. Investigations in which activation energies have been reported are summarized in Table I. The large amount of scatter in the activation energies for oxidation of the powdered materials may be caused by partial fusing of the  $\text{SiO}_2$  scale surrounding each SiC particle during

TABLE I  
PUBLISHED ACTIVATION ENERGIES FOR POWDERED SiC OXIDATION

Investigator	$Q_k$ (kcal/mole)	Temperature (°C)
Jorgensen, Wadsworth, Cutler <sup>(4)</sup>	20	900-1600
Adamsky <sup>(5)</sup>	66	1200-1500
Nakatogawa <sup>(6)</sup>	60	1000-1200
Pultz <sup>(7)</sup>	151	1355-1445
Ervin <sup>(8)</sup>	50	1100-1300

oxidation, which, in turn, causes a reduction in surface area. This phenomenon might result in apparent weight gains (mass/unit area) and hence scaling-rate constants which are low. The rate at which the scale fuses would increase with temperature, resulting in activation energies for oxidation which may be lower than those observed if planar oxide growth is exhibited. In order to avoid the scale-fusing effect, a study of the oxidation behavior of hot-pressed silicon carbide was conducted.

#### Experimental

The Norton hot-pressed material used was theoretically dense and contained ~ 3 w/o  $Al_2O_3$  as a hot-pressing aid and ~ 1 w/o WC as a major impurity. Coupons ( $\sim 1.2 \times 0.5 \times 0.2$  cm) cut from the hot-pressed billet were abraded through 320-grit SiC paper. A metallurgical polish was also imparted to several of the samples to determine whether oxidation kinetics were a function of surface preparation. Samples were ultrasonically cleaned in acetone and methanol. The commercial grade  $O_2$  and  $O_2/Ar$  gas mixtures used were dried with anhydrous magnesium perchlorate. Oxidation experiments were conducted under dynamic flow conditions at a flow rate of  $\sim 60$  cm<sup>3</sup>/min at STP. The experiments were initiated by quickly lowering the abraded and cleaned SiC coupons into pre-established furnace environments. Sample weight gains were monitored continuously with either a Cahn RG electrobalance having a sensitivity of  $\pm 1$   $\mu$ g or an Ainsworth FV microbalance having a sensitivity of  $\pm 3$   $\mu$ g. The furnace-balance system has been described previously.<sup>(11)</sup> In



general, the oxidation experiments were conducted for a 24 hr period after which the oxidized samples were examined by using the standard microscopic and x-ray techniques.

## Results

Figure 1 presents the oxidation kinetics of SiC as a function of temperature in 150-torr O<sub>2</sub>. Oxidation kinetics were measured in the temperature range 1200–1550°C; the 1200° and 1550° data are not shown because they fall essentially on the abscissa and ordinate, respectively. The experiment at 1550°C lasted only 1/2 hr, after which scale rupture took place with subsequent breakaway oxidation. In all cases linear-parabolic oxidation kinetics were observed, as evidenced by the initial upward curvature of the parabolic plots, implying initial reaction control at the SiO<sub>2</sub>-gas or SiO<sub>2</sub>-matrix interface. The generalized parabolic rate equation,

$$\frac{1}{k_p} m^2 + \frac{1}{k_l} m = (t + t_0) \quad (1)$$

was used to obtain the linear and parabolic rate constants with the aid of a parabolic least-squares regression. The linear rate constants obtained were widely scattered, and no significant trend was observed with temperature. Thus, no attempt was made to plot or analyze this constant.

On the other hand, the parabolic rate constants obtained from the regression contained little scatter and were not far different than the slopes of the plots shown. For a given set of experimental conditions, the parabolic rate constant was not dependent upon SiC surface preparation. The parabolic rate constants obtained from these data are presented in the Arrhenius plot in Figure 2. The activation energy for oxidation in pure O<sub>2</sub> at 150 torr is ~108 kcal/mole in the high-temperature region--this value being much larger than the 20 kcal/mole often quoted in the literature. A relatively large number of oxidation experiments were conducted to increase the reliability of the reported activation energy. The activation energy for oxidation appears to decrease below 1300°C. This trend is real since oxidation rates are readily measurable down to ~1200°C with

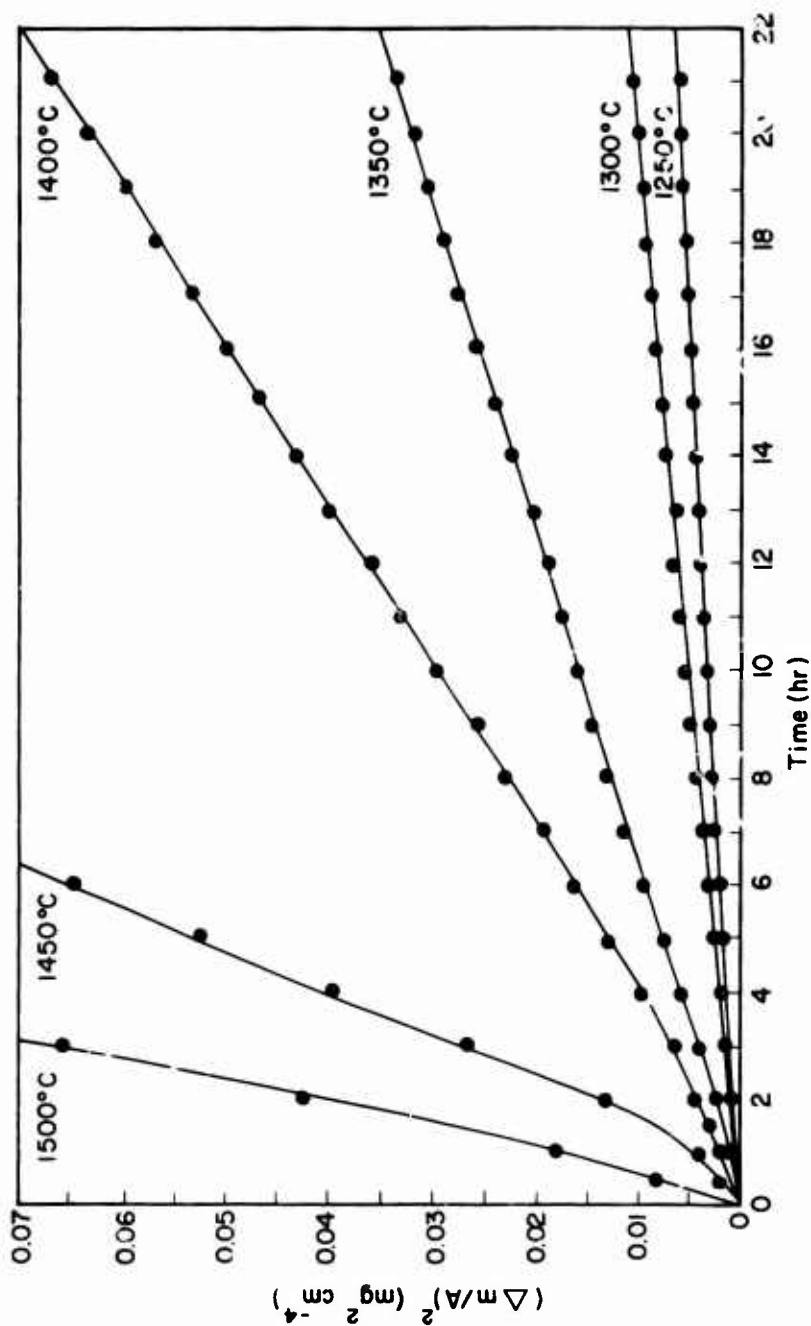


Figure 1. Temperature Dependence of the Weight Gain of SiC in 150 torr  $\text{O}_2$ .

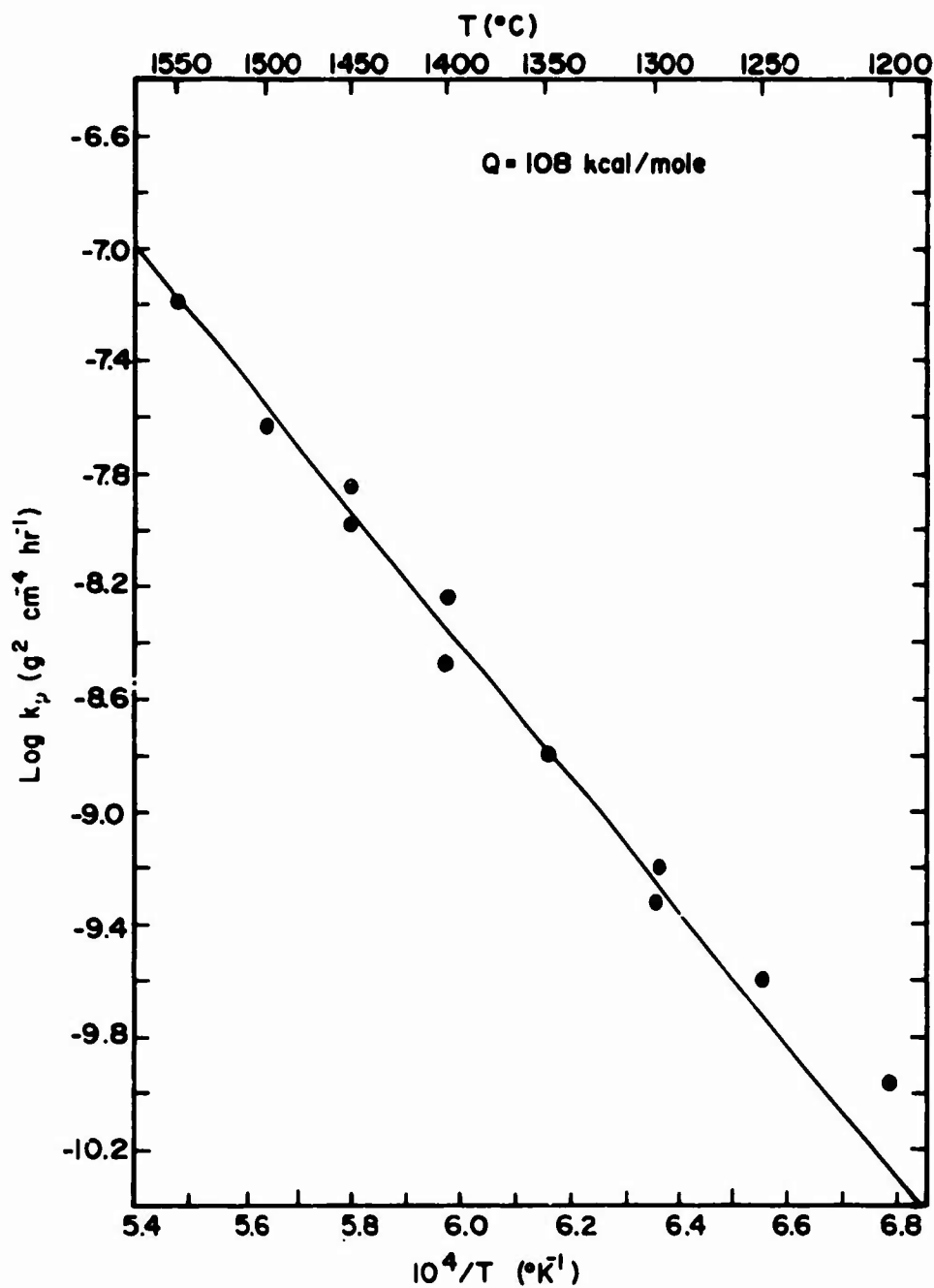


Figure 2. Arrhenius Plot of the Parabolic Rate Constants for the Oxidation of SiC in 150 torr O<sub>2</sub>.

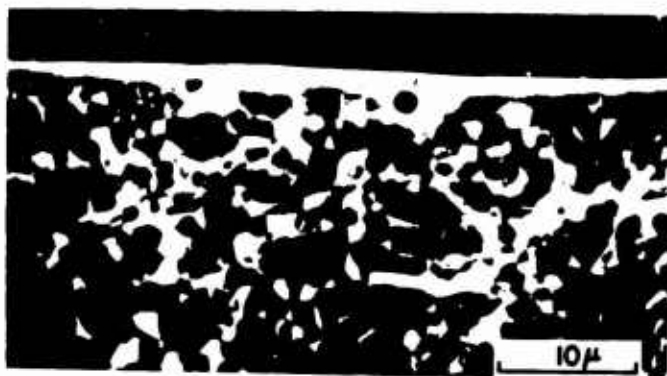
reasonable accuracy. The activation energy for oxidation of SiC may approach that of Si in the low-temperature region; however, this speculation could not be tested with the available balance system due to the very slow oxidation rates that would be observed.

Figure 3 shows SEM micrographs of the fractured cross section of SiC coupons oxidized for 24 hr in 150-torr O<sub>2</sub> at three temperatures. The oxide scales formed appear to be glassy even at 1500°C. Pores are present due to formation of CO and SiO at the SiC-SiO<sub>2</sub> interface during oxidation. X-ray analysis of the scales reveals an amorphous hump centered about the major cristobalite peak. X-ray scans of a number of standards consisting of various amounts of amorphous silica and cristobalite were compared with those of the oxide scales. The scales formed were found to consist of 90-95 w/o amorphous silica; the remainder was cristobalite, even at the high temperatures. The scales contained 4-6 w/o alumina with uniform distribution, with the source as the matrix material. No mullite was found in these glassy scales; however, in a number of experiments abnormally slow oxidation kinetics were observed. The scales formed in these experiments were dull and non-glassy in appearance, consisting of mullite and cristobalite. It is postulated that system contamination accelerated the mullite reaction in the scaling layer during these experiments, causing the altered oxidation behavior. However, neither spark-source mass spectrometry nor energy-dispersive x-ray analysis (EDAX) revealed the nature or the source of the contamination. Therefore, the kinetic data presented here are representative of the oxidation of SiC when amorphous SiO<sub>2</sub> scales are formed. When mullite-cristobalite scales are formed, oxidation kinetics are lower by over an order of magnitude but contain a large amount of scatter.

Figure 4 is a plot of the oxidation kinetics of SiC as a function of oxygen partial pressure at 1400°C and a total pressure of 150 torr. The reduced oxygen partial pressures were obtained by using suitable commercial O<sub>2</sub>/Ar bottled-gas mixtures from Air Products and Chemicals, Inc. Again, linear-parabolic oxidation kinetics were observed and no active oxidation was found, even in the 0.1% O<sub>2</sub>/Ar ( $P_{O_2} = 1.97 \times 10^{-4}$  atm) gas mixture. Data of this type were obtained at each of five temperatures ranging from 1300-1500°C. Results of these experiments are summarized in Figure 5,



1300°C, 24 hr.



1400°C, 24 hr.



1500°C, 24 hr.

Figure 3. SEM Micrographs of the Fractured Cross Sections of SiC Specimens Oxidized in 150 torr O<sub>2</sub>.

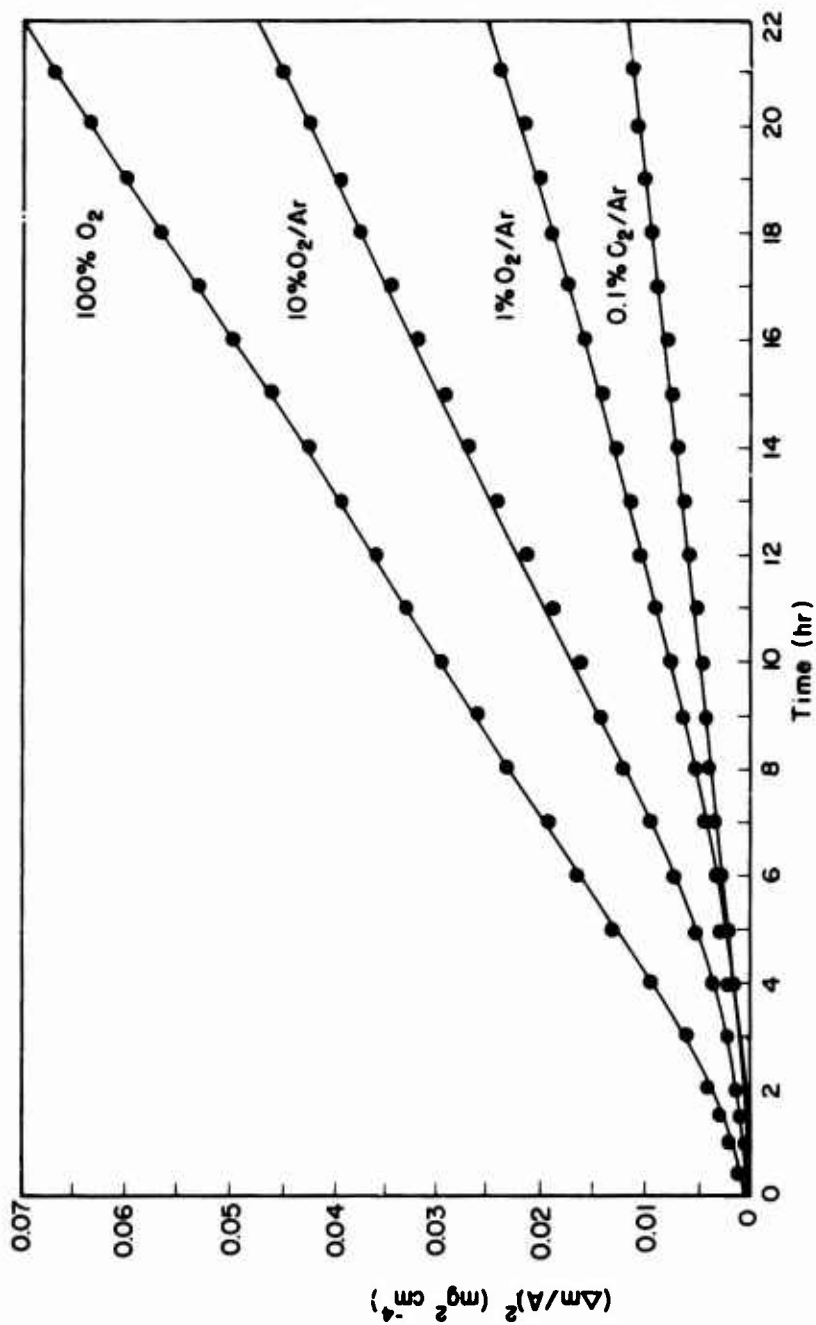


Figure 4. Oxygen Partial Pressure Dependence of the Weight Gain of SiC in  $\text{O}_2$  and  $\text{O}_2/\text{Ar}$  Gas Mixtures at  $1400^\circ\text{C}$  (Total Pressure = 150 torr).

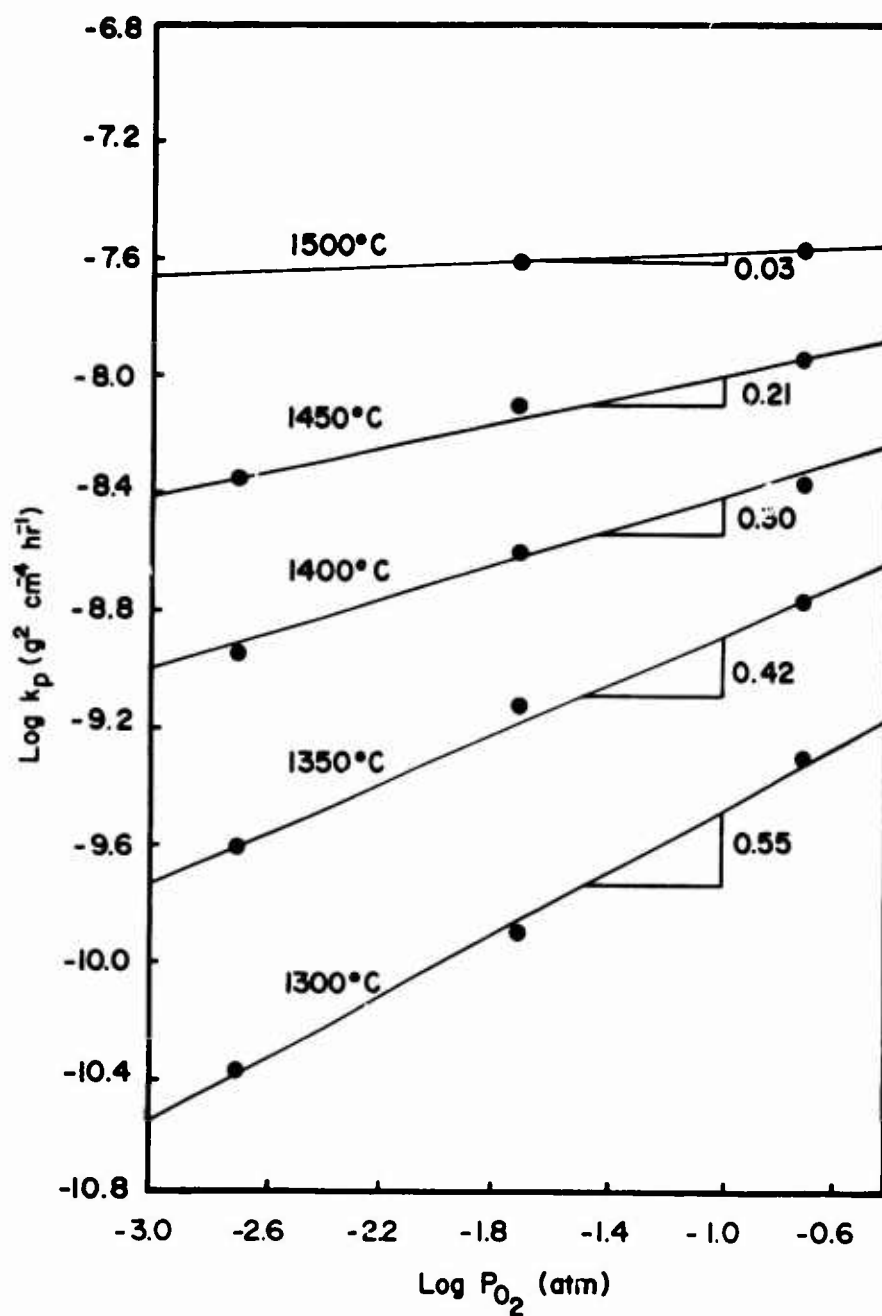


Figure 5. Oxygen Partial Pressure Dependence of the Parabolic Rate Constant for SiC in  $O_2$  and  $O_2/Ar$  Gas Mixtures (Total Pressure = 150 torr).



where the log of the parabolic rate constant has been plotted as a function of the log of the oxygen partial pressure. The salient feature of this plot is the increasing oxygen partial pressure dependence of the scaling rate constant with decreasing temperature. The parabolic rate constant is approximately proportional to  $P_{O_2}^{1/2}$  at 1300°C and nearly  $P_{O_2}$  independent at 1500°C. Only two data points were obtained at 1500°C because active oxidation behavior was found in the 1%  $O_2$ /Ar ( $P_{O_2} = 1.97 \times 10^{-3}$  atm) gas mixture.

### Discussion

The complicated pressure dependence of the scaling rate constant for silicon carbide does not permit straightforward determination of the oxidation mechanism. The increasing pressure dependence with decreasing temperature shown in Figure 5 suggests that no single mechanism predominates over the entire pressure and temperature range of this study. Oxygen transport through the scale by a neutral transport mechanism seems unlikely in view of the large activation energy for oxidation. A neutral transport mechanism would have an activation energy of <30 kcal/mole associated with it because no Si-O bonds are broken during the diffusional process. Thus, this activation energy would only be the sum of a mobility term and a neutral oxygen incorporation term, the latter being very small.<sup>(12)</sup> Transport by this mechanism would also give a linear or square root oxygen partial pressure dependence of the scaling-rate constant at all the temperatures studied. Instead, the activation energy for oxidation of 108 kcal/mole in 150 torr  $O_2$  found in the present study is in almost fortuitous agreement with the 100 kcal/mole necessary to create a vacancy in  $SiO_2$ .<sup>(13)</sup> In this case the activation energy for oxidation would involve the sum of a vacancy formation term ( $\sim 4$  eV), a term taking into account the oxygen pressure dependence of the vacancy concentration at the SiC- $SiO_2$  interface ( $\sim 1$  eV), and a vacancy mobility term. Oxidation by a vacancy mechanism, however, would require a  $P_{O_2}$ -independent scaling rate constant,<sup>(14)</sup> which is not observed experimentally except at 1500°C.

The most probable oxidation mechanism based upon the present findings is one involving a parallel flux of oxygen vacancies and atomic oxygen interstitials, the vacancy contribution having a large activation energy and

being  $P_{O_2}$  independent, the interstitial contribution having a low activation energy and being proportional to  $P_{O_2}^{1/2}$ . The overall scaling rate constant could then be written

$$k_T = k_V + k_n \quad (2)$$

$$k_T = k_V^0 \exp(-Q_V/RT) + k_n^0 P_{O_2}^{1/2} \exp(-Q_n/RT) \quad (3)$$

If  $Q_V = 9$  eV and  $Q_n = 2$  eV, the observed  $P_{O_2}^{1/2}$  dependence of the scaling rate constant would be obtained at 1300°C and  $P_{O_2}$  independence at 1500°C. However, the fit of the data from this model at the intermediate temperatures (1350-1450°) is not good, and the 9 eV for the vacancy diffusion term seems excessive in view of the 4 eV for the vacancy formation energy.

A rate determining mechanism involving outward diffusion of the CO or  $CO_2$  formed upon oxidation has been considered. A rather low activation energy for oxidation would be expected for this mechanism, again because the transport of a neutral species does not require bonds to be broken. A  $P_{O_2}$ -independent scaling rate constant would be predicted because only the concentration of dissolved CO at the SiC-SiO<sub>2</sub> interface would control the oxidation kinetics. Thus, this oxidation mechanism seems unlikely.

The effect of the Al found in the amorphous scales can be only a matter of speculation. The presence of this element may increase the activation energy for oxidation. Network-forming Al in silicate glasses is known to increase the activation energy for oxygen diffusion;<sup>(15)</sup> however, the concentration is usually around 10-20%.

#### OXIDATION OF HfB<sub>2</sub> + 20 v/o SiC

Early investigations by Kaufman et al.<sup>(16)</sup> on the oxidation of undoped diborides showed the oxidation resistance of HfB<sub>2</sub> to be superior to that of its Zr, Ti, Ta, and Nb counterparts based upon a comparison of the total

diboride recession after a 1 hr exposure to oxygen at temperatures ranging from 1300-2000°K. Later, Kaufman et al.<sup>(17)</sup> and Berkowitz-Mattuck<sup>(18)</sup> studied the oxidation rate of  $\text{HfB}_2$  and  $\text{ZrB}_2$  as a function of temperature and oxygen partial pressure in order to determine the mechanism of oxidation. The oxidation kinetics were observed to obey a parabolic rate law, and oxygen diffusion through the  $\text{HfO}_2$  layer was found to be rate determining. More recently, Clougherty et al.<sup>(19)</sup> investigated the oxidation behavior of  $\text{HfB}_2$  and  $\text{ZrB}_2$  containing additions of SiC as a function of temperature only, and total diboride recession was measured after 1 hr of oxidation. The SiC addition was found to increase the oxidation resistance; however, kinetic data were not obtained.

The oxidation of  $\text{ZrB}_2$  and  $\text{ZrB}_2 + 20 \text{ v/o SiC}$  has been investigated by Tripp et al.<sup>(20-22)</sup> as a function of temperature and oxygen partial pressure by thermogravimetric techniques. The oxidation reaction was found to be controlled by diffusion through a  $\text{SiO}_2$  scaling layer. In the present investigation, the oxidation behavior of  $\text{HfB}_2 + 20 \text{ v/o SiC}$  was studied as a function of temperature and oxygen partial pressure. The oxidation resistance of the  $\text{HfB}_2 + \text{SiC}$  composite was compared to that of its constituent components as well as its zirconium counterpart in order to define the rate determining oxidation mechanism.

### Experimental

The diboride composite was prepared by Man Labs, Inc. under contract with the Air Force Materials Laboratory and was provided by Mr. John Fentor (AFML/LP). The  $\text{HfB}_2 + 20 \text{ v/o SiC}$  powders had been hot pressed at 2200°C under a pressure of 3000 psi for 90 min, and the resulting billet was 88% dense. Coupons ( $\sim 1 \times 0.5 \times 0.1 \text{ cm}$ ) were cut from the billet, ground with 600-grit SiC paper, and ultrasonically cleaned in acetone and methanol.

Oxidation kinetics were determined by an oxygen-consumption technique<sup>(11,20-22)</sup> which is very useful for studying oxidation where one or more of the reaction products is volatile at sample temperature but condensable at lower temperatures. With this technique the volatile species are collected on the walls of a cold alumina crucible which is suspended over the sample,

and the weight of the sample and crucible is monitored continuously with time. In this way the weight gain due to the oxygen used to form both the solid and volatile products can be measured. The measurement of sample weight change alone does not give a true indication of the reaction kinetics because sample weight gains and losses occur simultaneously. In the present work nonvolatile  $\text{HfO}_2$  and  $\text{SiO}_2$  as well as volatile  $\text{B}_2\text{O}_3$  and  $\text{SiO}$  are formed. The  $\text{CO}$  and  $\text{CO}_2$  which are formed as oxidation products cannot be condensed on the cold crucible; however, their weight is only a small percentage of the total weight change.

The kinetics of total oxygen consumption were studied by using a Cahn RH electrobalance having a capacity of 100 g and a sensitivity of  $\pm 2 \mu\text{g}$ . The balance assembly has been described previously.<sup>(11,20)</sup> The diboride specimen and crucible were preheated for  $\sim 15$  hr in Ar at  $500^\circ\text{C}$  in the balance assembly. The furnace was then quickly heated to the desired temperature and the oxidant ( $\text{O}_2$ ,  $\text{O}_2/\text{Ar}$ , or  $\text{CO}/\text{CO}_2$ ) admitted into the furnace chamber until the desired total pressure was reached. In all cases the oxidation experiments were conducted in flowing gas at  $\sim 60 \text{ cm}^3$  (STP)/min.

Postoxidation analysis of the specimens consisted of x-ray analysis for determining scale constituents, microprobe analysis for elemental distribution, and optical and scanning electron microscopy for scale morphologies.

## Results

### Oxidation in Pure Oxygen

The oxidation behavior in pure oxygen was studied in the temperature range  $1200$ – $1550^\circ\text{C}$ ; the results of a typical experiment are shown in Figure 6. In all experiments rates of oxygen consumption were parabolic after an initial transient period, with the initial rapid kinetics being due to short-circuit diffusion (see Discussion Section). Scaling rate constants computed from the slopes of the parabolic plots are given in Arrhenius form in Figure 7. The activation energy for oxidation in the range  $1350$ – $1550^\circ\text{C}$  is  $106 \text{ kcal/mole}$  with

$$k_p = 1.62 \times 10^7 \exp(106,000/RT) \text{ g}^2 \text{ cm}^{-4} \text{ hr}^{-1} . \quad (4)$$

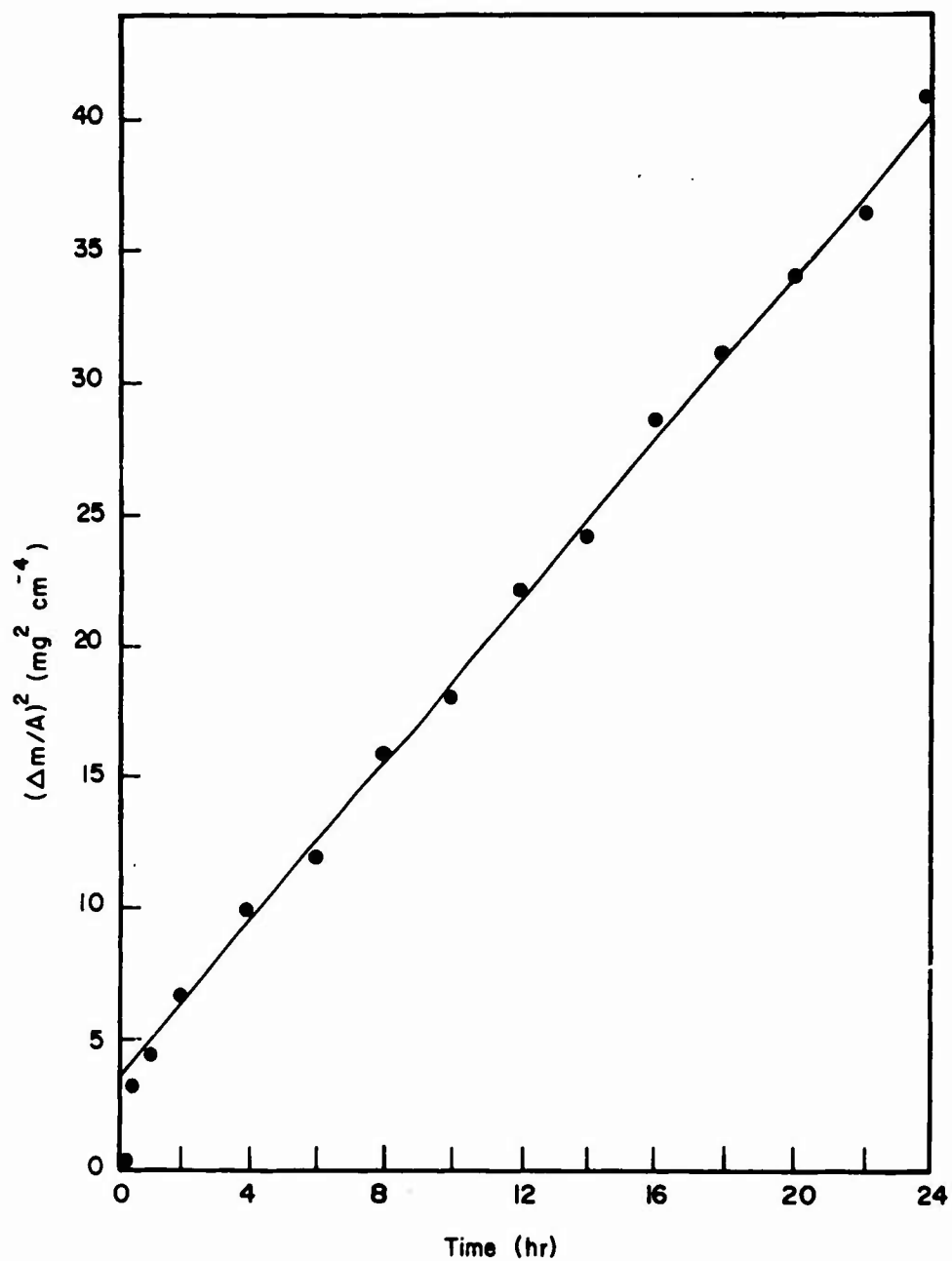


Figure 6. Typical Parabolic Plot of Kinetic Data for  $\text{HfB}_2 + \text{SiC}$  Oxidation at  $1500^\circ\text{C}$  in 250 torr  $\text{O}_2$ .

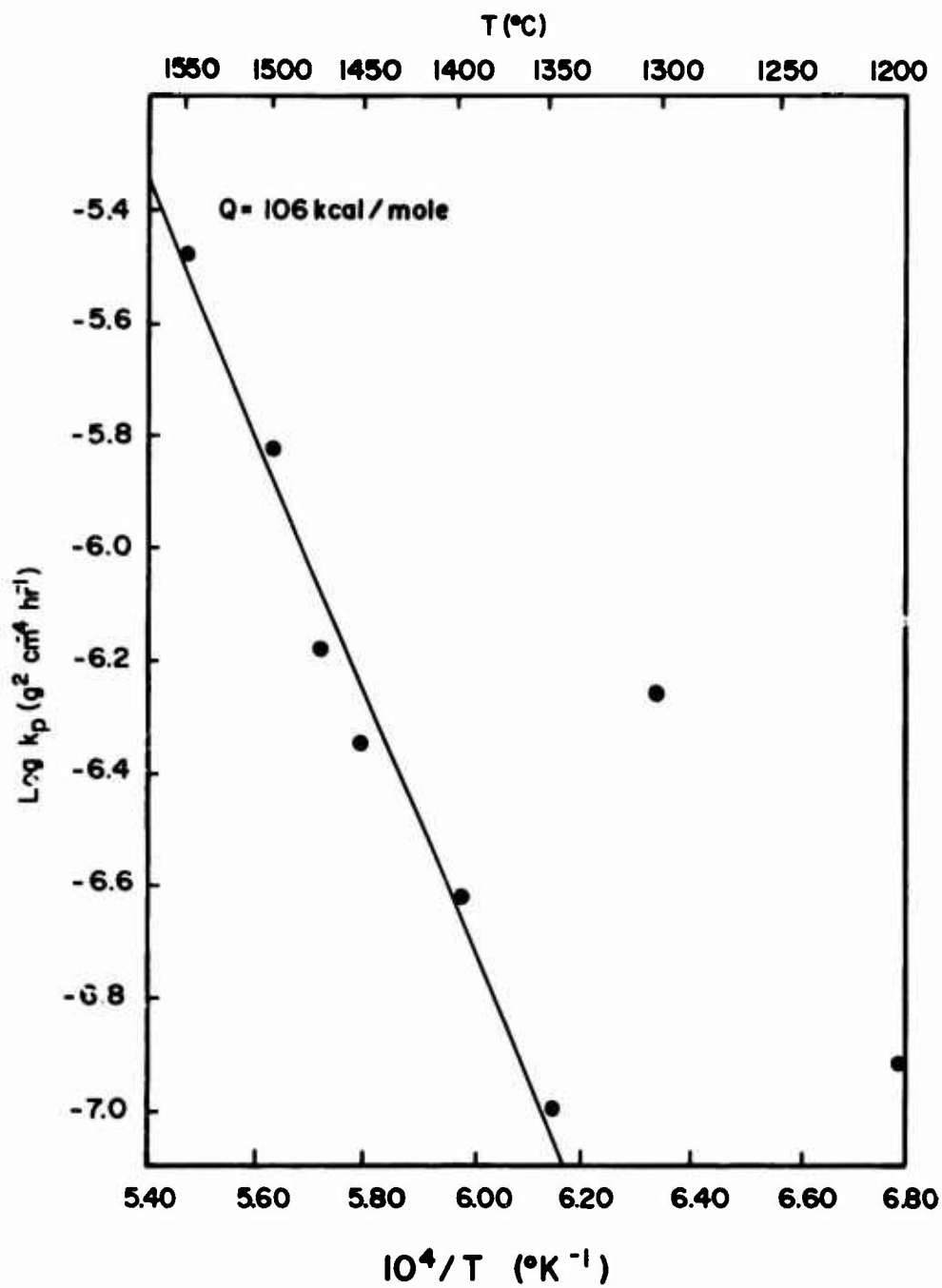


Figure 7. Arrhenius Plot of Parabolic Rate Constants for Total Oxygen Consumption of  $\text{HfB}_2 + \text{SiC}$  in 250 torr  $\text{O}_2$ .

The scaling rate increases abruptly below 1350°C due to selective oxidation of the  $\text{HfB}_2$  with very slow attack of the  $\text{SiC}$ ; i.e., only small amounts of  $\text{SiO}_2$  were found on the samples oxidized at these low temperatures. Therefore, the beneficial effect of the addition of  $\text{SiC}$  appears to be lost in this temperature range.

Figure 8 is an optical micrograph of the polished cross section of a sample oxidized for 24 hr at 1400°C in 250 torr oxygen. The scale formed consists of an amorphous  $\text{SiO}_2$  layer on top of a  $\text{HfO}_2$  layer and is typical of those formed in the high-temperature region. The  $\text{HfO}_2$  is porous and of uniform thickness with dark regions that are a combination of voids and  $\text{SiC}$  particles.

X-ray diffractometer analysis of the oxidized specimens indicated that monoclinic  $\text{HfO}_2$  and tetragonal  $\text{HfSiO}_4$  are the primary scale constituents. The expected amorphous silica hump and cristobalite peak could not be found with this technique. The location of the scale constituents was obtained by means of the electron-beam microprobe. Figure 9 is a schematic microprobe scan of the sample oxidized at 1400°C. The zone between 19 and 27  $\mu$  may be  $\text{HfSiO}_4$ ; however, since the intensity of the Hf peak varies throughout this range, the thickness of the  $\text{HfSiO}_4$  cannot be determined. The  $\text{HfSiO}_4$  probably exists as a very thin reaction layer between the  $\text{SiO}_2$  and  $\text{HfO}_2$  scaling layers.

#### Oxidation at Reduced Oxygen Partial Pressures

The oxygen partial pressure dependence of the rate of oxygen consumption was investigated at 1400°C. Reduced oxygen partial pressures in the range  $3.3 \times 10^{-1}$  to  $3.6 \times 10^{-9}$  atm were established with premixed  $\text{O}_2/\text{Ar}$  and  $\text{CO}/\text{CO}_2$  gas mixtures obtained from Air Products and Chemicals, Inc., with the total system pressure being maintained at 250 torr. A parabolic plot of oxygen consumption is presented in Figure 10. Oxidation kinetics are slower than parabolic in the  $\text{O}_2/\text{Ar}$  mixtures except at a  $P_{\text{O}_2}$  of  $3.2 \times 10^{-4}$  atm where rapid linear oxidation kinetics are exhibited. At this  $P_{\text{O}_2}$  active oxidation of the  $\text{SiC}$  occurs, with gaseous  $\text{SiO}$  being formed as the reaction product. A weight gain--rather than a weight loss--is observed because the volatile species is collected as

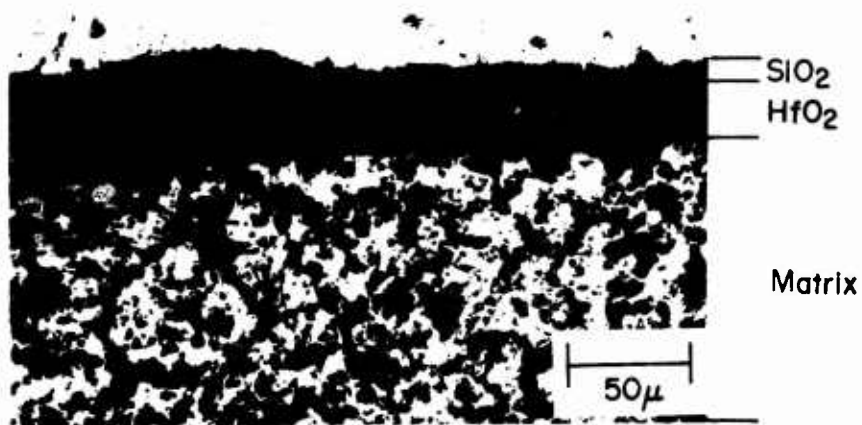


Figure 8. Optical Micrograph of a  $\text{HfB}_2 + \text{SiC}$  Specimen Oxidized at  $1400^\circ\text{C}$  in 250 torr  $\text{O}_2$  for 24 hr.



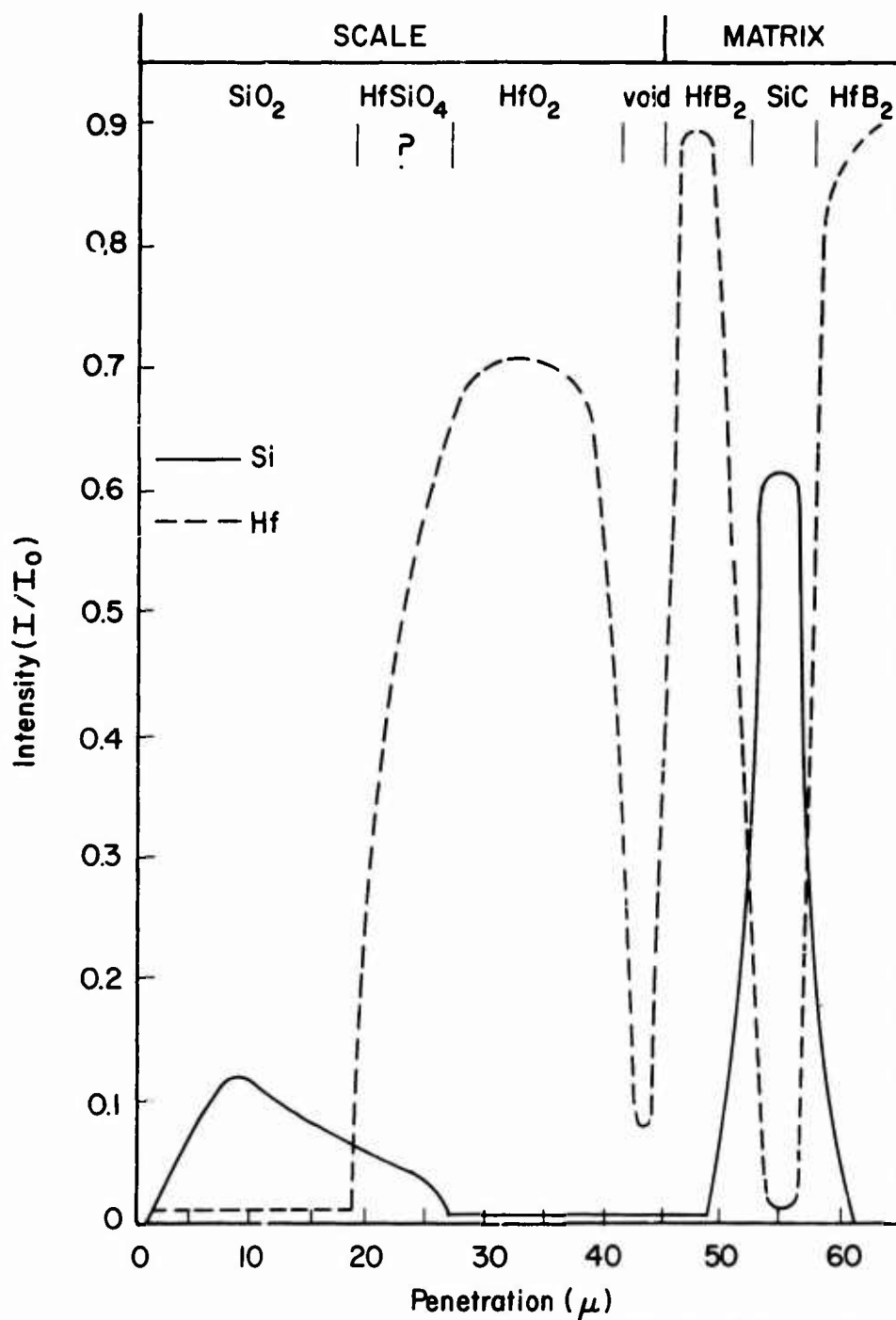


Figure 9. Electron-Beam Microprobe Scan of a HfB<sub>2</sub> + SiC Specimen Oxidized at 1400°C in 250 torr O<sub>2</sub> for 24 hr.

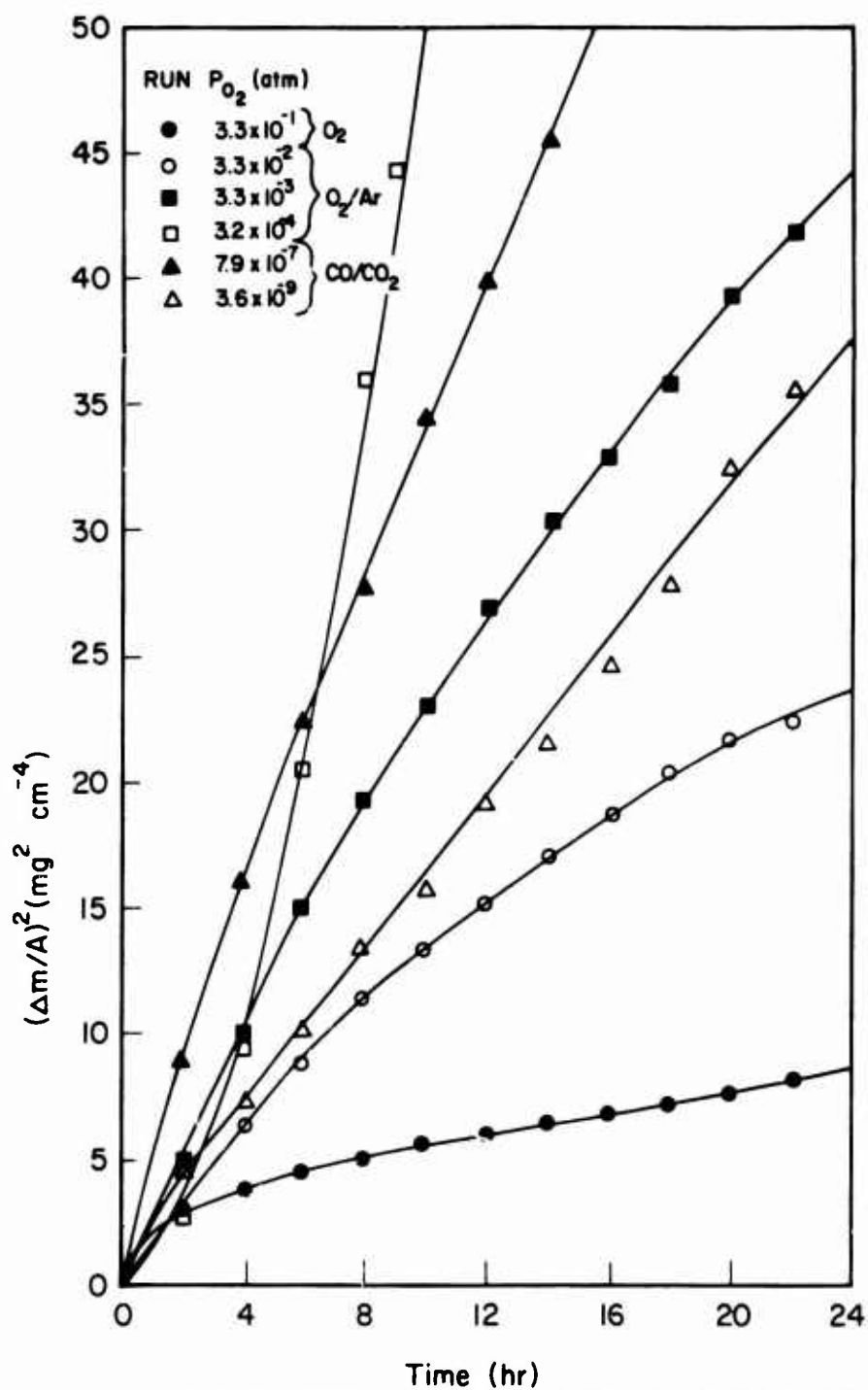


Figure 10. Total Oxygen Consumption of  $HfB_2 + SiC$  as a Function of Oxygen Partial Pressure at  $1400^\circ C$ .

SiO<sub>2</sub> on the cold crucible surrounding the HfB<sub>2</sub> + SiC sample. The rate of oxygen consumption is found to increase with decreasing P<sub>O<sub>2</sub></sub> in O<sub>2</sub>/Ar gas mixtures down to 3.2×10<sup>-4</sup> atm. Below this pressure CO/CO<sub>2</sub> gas mixtures were used, and the trend was reversed. The oxidation kinetics are parabolic in CO/CO<sub>2</sub> mixtures as in pure oxygen, indicating diffusion-controlled kinetics; however, the oxidation rates at the low oxygen partial pressures are much higher.

Figure 11 is a light micrograph of the sample oxidized at a P<sub>O<sub>2</sub></sub> of 3.2×10<sup>-4</sup> atm. As expected, the SiO<sub>2</sub> scale is absent and a thick HfO<sub>2</sub> layer has formed. The SiC particles have been depleted in the matrix due to rapid active oxidation [i.e., oxidation to form SiO(g)]. This micrograph is in contrast to that of the sample oxidized in pure oxygen (Figure 8) where no such depletion zone is present. Figure 12 is a comparison of scanning electron micrographs of specimens oxidized at 1400° in a P<sub>O<sub>2</sub></sub> of 3.3×10<sup>-1</sup> and 3.2×10<sup>-4</sup> atm. The specimen oxidized at the higher P<sub>O<sub>2</sub></sub> formed an apparently coherent HfO<sub>2</sub> scale beneath the SiO<sub>2</sub> layer. The HfO<sub>2</sub> layer which formed at the lower P<sub>O</sub> contains pores and pinholes through which SiO(g) escaped during oxidation and is much thicker.

Light micrographs of samples oxidized in CO/CO<sub>2</sub> mixtures are shown in Figure 13. The HfO<sub>2</sub> scale formed on these samples has a greater thickness than that formed in pure oxygen (twice as thick in 24 hr), and globules of SiO<sub>2</sub> rather than a coherent layer are formed on the HfO<sub>2</sub> layer. No active oxidation of the SiC particles was found, as evidenced by the absence of a SiC depletion zone near the matrix-oxide interface.

### Discussion

The parabolic oxidation kinetics observed in pure oxygen indicate that the oxidation reaction is diffusion controlled. Oxidation may be controlled by one of several mechanisms, including inward diffusion of oxygen through either the HfO<sub>2</sub> or SiO<sub>2</sub> layer or outward diffusion of a boron or carbon species through the HfO<sub>2</sub> or SiO<sub>2</sub>. Silicon is assumed to be immobile in SiO<sub>2</sub> relative to oxygen and is not considered as a diffusing species during oxidation. If the oxidation mechanism is via oxygen transport through the

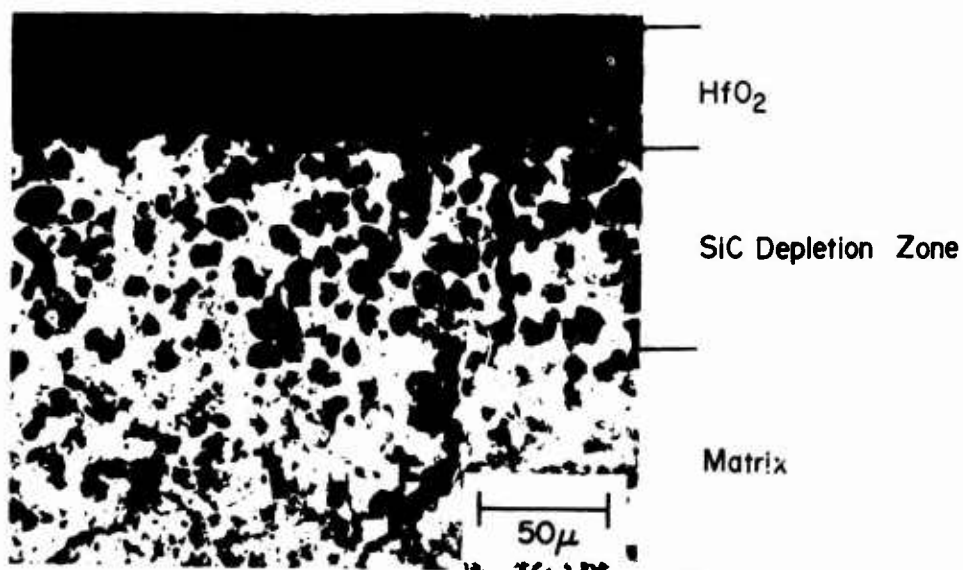
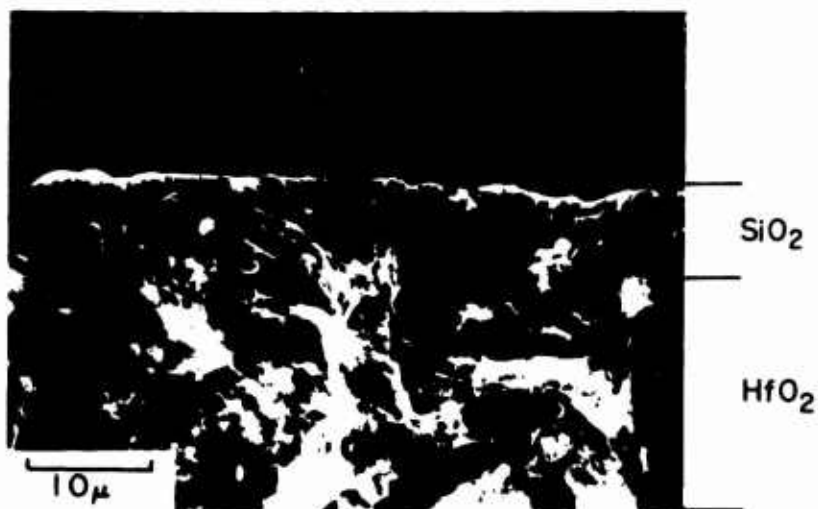
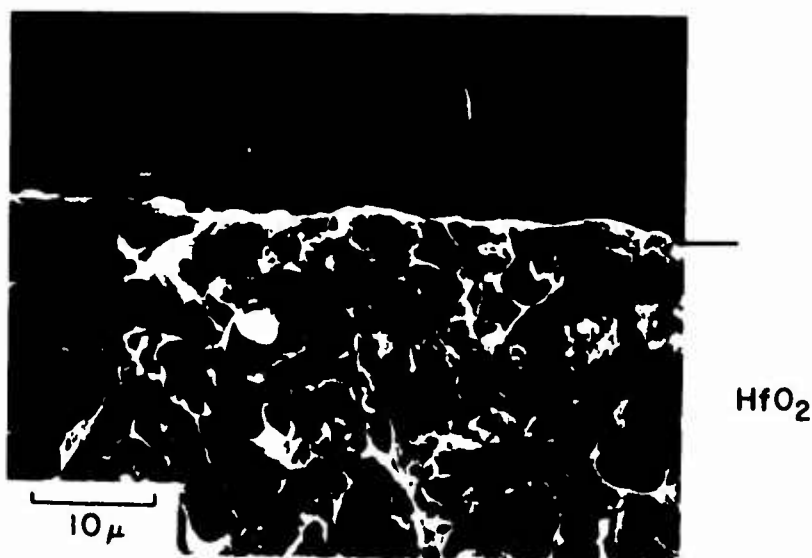


Figure 11. Light Micrograph of a HfB<sub>2</sub> + SiC Specimen Oxidized at 1400°C in 975 ppm O<sub>2</sub>/Ar ( $P_{O_2} = 3.2 \times 10^{-4}$  atm) for 24 hr.



$$P_{O_2} = 3.2 \times 10^{-1} \text{ atm}$$



$$P_{O_2} = 3.2 \times 10^{-4} \text{ atm}$$

Figure 12. SEM Micrographs Showing the Effect of Oxygen Partial Pressure on Oxide-Scale Morphologies. Specimens Were Oxidized at 1400°C for 24 hr.

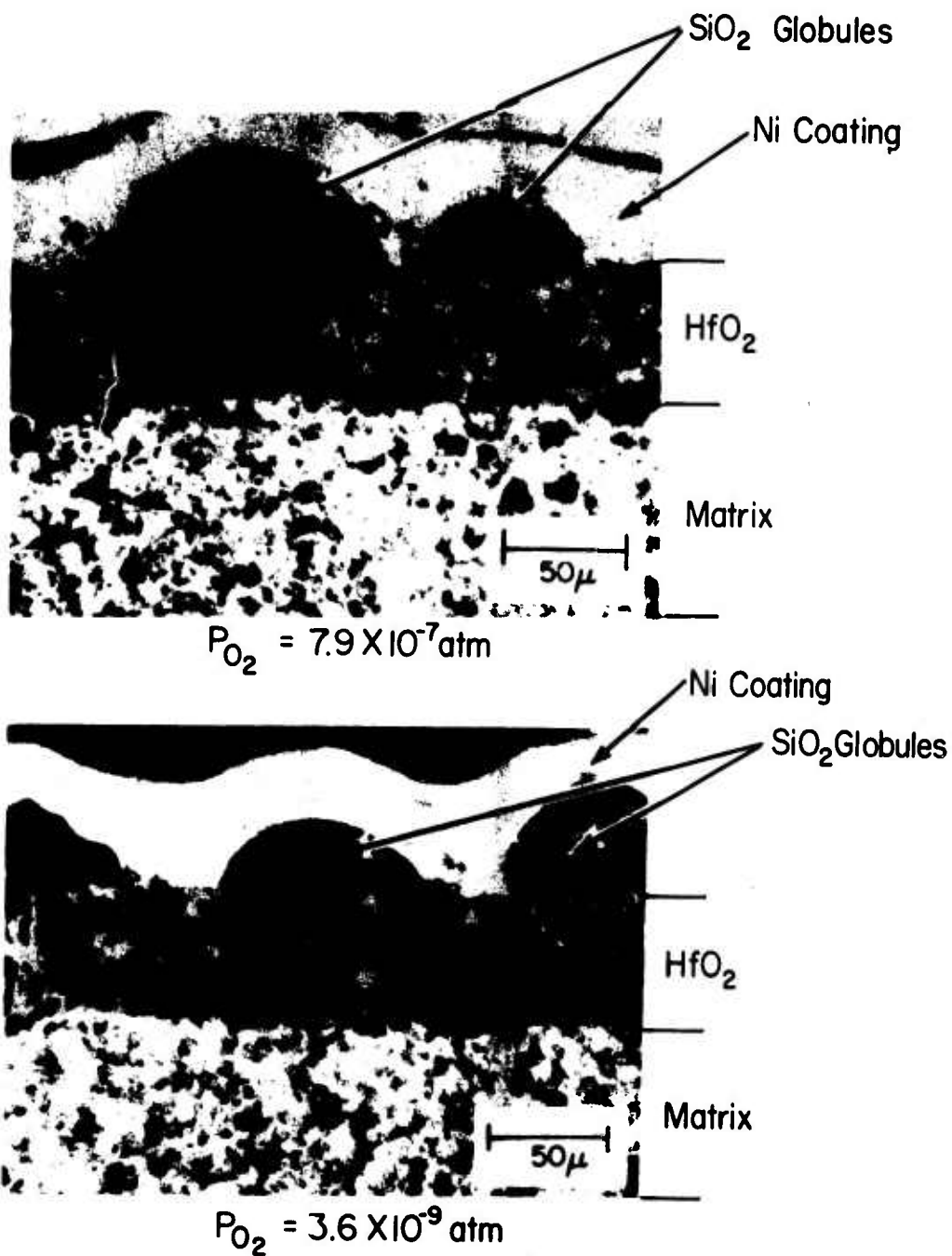
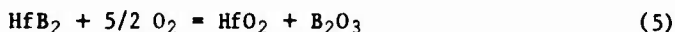


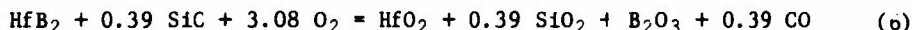
Figure 13. Light Micrographs of Two HfB<sub>2</sub> + SiC Samples Oxidized at 1400°C in CO/CO<sub>2</sub> Gas Mixtures for 24 hr.

HfO<sub>2</sub> scale, the oxidation rate and activation energy for oxidation should agree with previous results for Hf and HfB<sub>2</sub> oxidation. The rates of oxidation for HfB<sub>2</sub> + SiC, HfB<sub>2</sub>, and Hf in 250 torr O<sub>2</sub> are compared in Figure 14.

To compare the oxidation kinetics for the three materials, the rates of HfO<sub>2</sub> formation were computed from the experimental parabolic rate constants, on the assumption that the diboride materials oxidize stoichiometrically according to the reactions

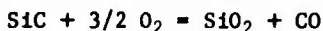


and



The low temperature (600-1200°C) data by Smeltzer and Simnad<sup>(23)</sup> for Hf oxidation were extended into the range of interest. For the oxidation of Hf and HfB<sub>2</sub>, the agreement in rates of HfO<sub>2</sub> formation and activation energies is quite good, which suggests that the oxidation mechanism is the same for the two materials. However, the SiC addition to the HfB<sub>2</sub> significantly reduces the rate of weight gain and increases the activation energy for oxidation. Although volume diffusion of oxygen through the HfO<sub>2</sub> layer was found to control the oxidation of Hf<sup>(23)</sup> and HfB<sub>2</sub>,<sup>(18)</sup> this mechanism is not rate determining during the oxidation of HfB<sub>2</sub> + SiC.

If the oxidation of HfB<sub>2</sub> + SiC is controlled by diffusion of oxygen through the SiO<sub>2</sub> scaling layer, the activation energy and kinetics of oxidation should agree with those of other silicon-base materials. Generally activation energies of 28-30 kcal/mole are reported for silicon oxidation in the range 800-1200°C.<sup>(1-3)</sup> However, in recent investigations on the oxidation of hot-pressed silicon carbide,<sup>(24-26)</sup> activation energies of 108-115 kcal/mole were reported. In Figure 15 the oxidation kinetics of HfB<sub>2</sub> + SiC are compared with those for SiC oxidation shown earlier. The rates of SiO<sub>2</sub> formation were compared for the two materials by using the stoichiometric oxidation reaction [Equation (6)] and the reaction



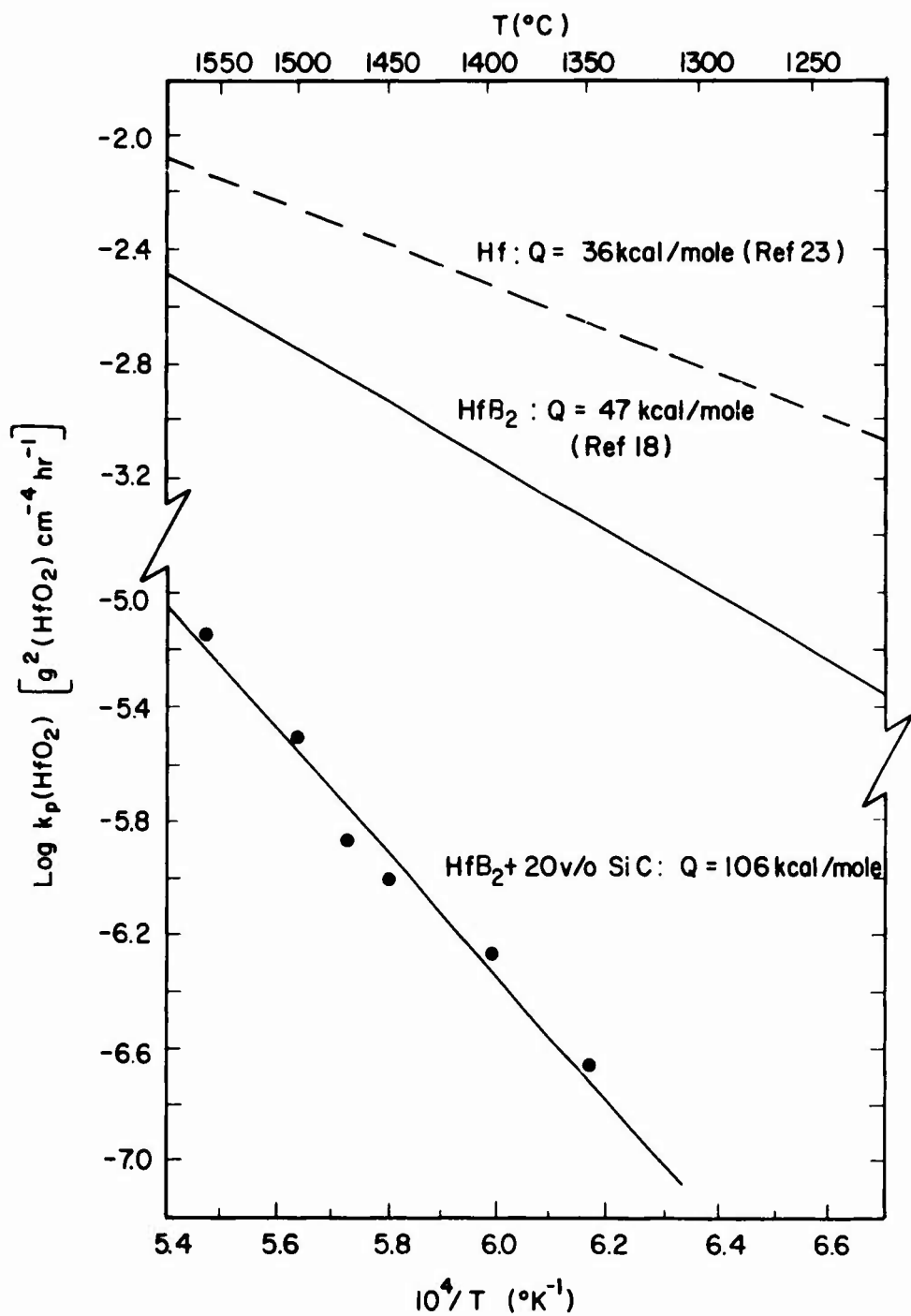


Figure 14. Comparison of the Rates of  $\text{HfO}_2$  Formation during Oxidation of  $\text{HfB}_2 + 20 \text{ v/o SiC}$ ,  $\text{Hf}$ , and  $\text{HfB}_2$  in 250 torr  $\text{O}_2$ .



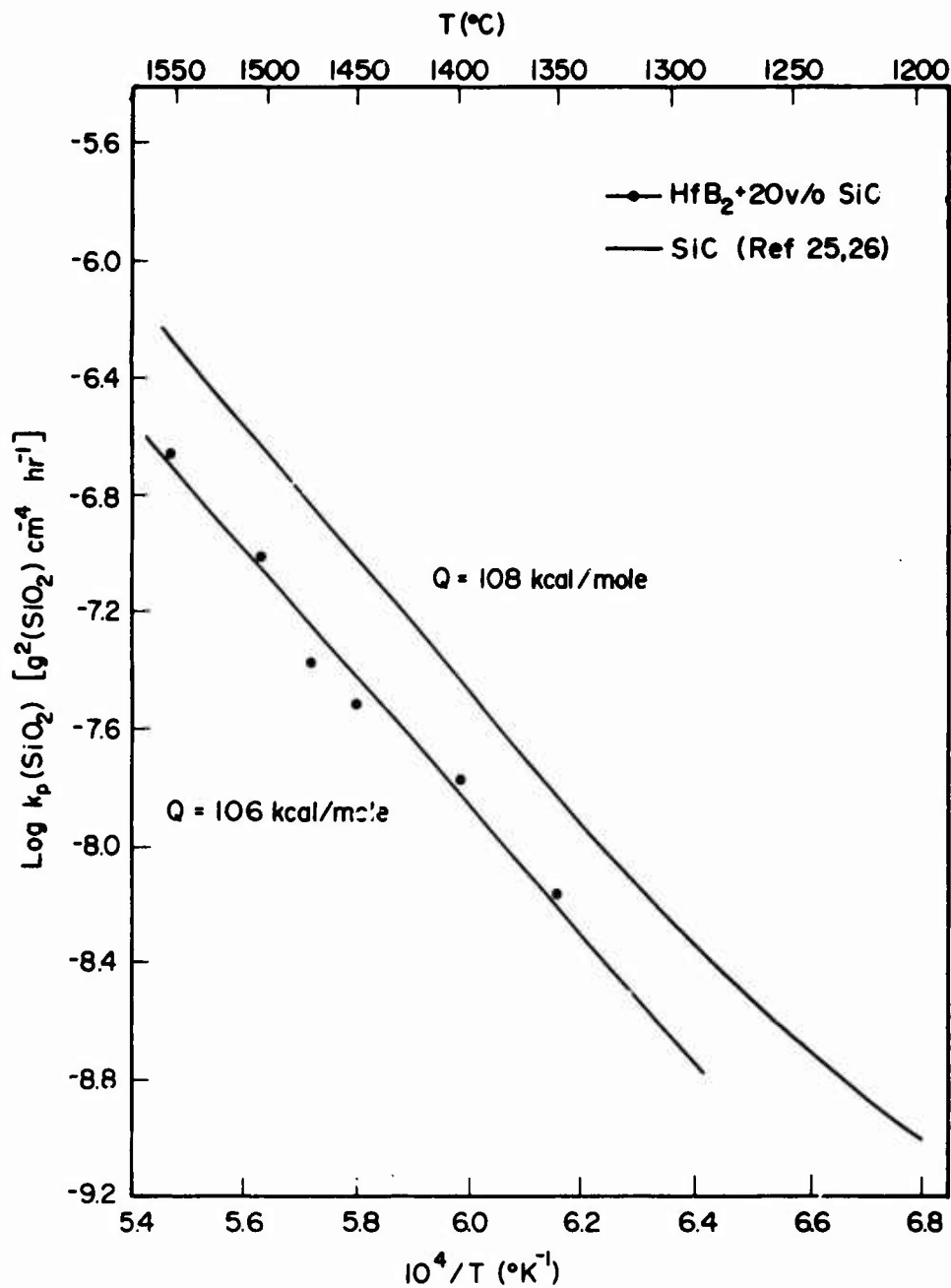


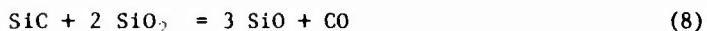
Figure 15. Comparison of the Rates of  $\text{SiO}_2$  Formation during Oxidation of  $\text{HfB}_2 + 20 \text{ v/o SiC}$  and Hot Pressed  $\text{SiC}$  in 250 torr  $\text{O}_2$ .

The correspondence in rates and activation energies is excellent, confirming that the oxidation mechanism is the same for the two materials. Therefore, outward diffusion of a boron species through the scale is eliminated as a possible rate controlling mechanism. For SiC oxidation (see this report pp. 4-14 and Ref. 25-26) a mechanism involving outward diffusion of a carbon species was shown to be unlikely. Instead, volume diffusion of oxygen through the scale was found to be rate controlling, with the valence of the oxygen species being indeterminate. Thus, in pure oxygen, the oxidation mechanism of both  $\text{HfB}_2 + \text{SiC}$  and SiC is inward diffusion of oxygen through the silica scale.

The oxygen partial pressure dependence of the oxidation rate is quite different for the two materials. At reduced oxygen partial pressure in  $\text{O}_2/\text{Ar}$  gas mixtures, the oxidation rate of SiC was parabolic and increased with  $P_{\text{O}_2}$ . In the present investigation the rate decreased with increasing  $P_{\text{O}_2}$  in the same mixtures. The rapid rate of oxidation at a  $P_{\text{O}_2}$  of  $3.2 \times 10^{-4}$  atm has already been interpreted in terms of active oxidation of the SiC particles in the  $\text{HfB}_2$  matrix. However, at larger oxygen partial pressures, no evidence for active oxidation was found. The downward curvature of the parabolic plots at these pressures suggests that the oxidation rate is controlled by oxygen diffusion along short-circuit paths through the  $\text{HfO}_2$  layer, the number of which decreases with time. Such short-circuit diffusion has been observed and interpreted by Smeltzer et al.<sup>(27)</sup> for the initial oxidation of Zr and Hf. If the rate of  $\text{SiO}_2$  formation decreases with decreasing  $P_{\text{O}_2}$  -- as observed for SiC oxidation -- it will take longer to form a coherent  $\text{SiO}_2$  layer at reduced  $P_{\text{O}_2}$ , and the short-circuit diffusion found initially in pure oxygen will occur for a longer period. Therefore, in  $\text{O}_2/\text{Ar}$  mixtures the oxidation mechanism is essentially the same as it is in pure oxygen except that the period of short-circuit diffusion is extended.

In  $\text{CO}/\text{CO}_2$  gas mixtures the oxidation rates were parabolic after a brief transient period, decreased with decreasing  $P_{\text{O}_2}$ , and were larger than in pure oxygen. The  $\text{SiO}_2$  formed in these mixtures appeared as globules and was not protective. Although the cause of the globule formation is not clear, volume oxygen diffusion through the  $\text{HfO}_2$  layer is believed to be rate determining in these mixtures. The parabolic rate constants obtained in these mixtures

agree well with those obtained by Kofstad and S. Espevik<sup>(28)</sup> for the low oxygen pressure high temperature oxidation of Hf. Active oxidation of the SiC particles was not observed in CO/CO<sub>2</sub> mixtures. In these mixtures the partial pressure of CO in the gas surrounding the sample is large, causing the active oxidation reactions



and



to be retarded or driven to the left.

The rates of total oxygen consumption of HfB<sub>2</sub> + SiC and ZrB<sub>2</sub> + SiC composites in 250 torr O<sub>2</sub> are compared in Figure 16. The 1400°C data for the ZrB<sub>2</sub>-base composite are those of Tripp et al.<sup>(22)</sup> converted to a parabolic plot. The initial rapid oxidation kinetics of the two composites are controlled by short-circuit diffusion through the inner HfO<sub>2</sub> or ZrO<sub>2</sub> scales; however, the reason for the large difference in initial oxidation rates is unknown. After

10 hr the oxidation rate of the ZrB<sub>2</sub> + SiC composite is only four times that of the HfB<sub>2</sub> + SiC. Since each composite contains ~ 28 m/o SiC, the stoichiometric oxidation reactions are essentially the same for the two materials. Hence, the rates of silica formation during oxidation can be compared directly and agree within a factor of four. The oxygen partial pressure dependences of the oxidation rates are also similar. Therefore, the same mechanism--initial short-circuit oxygen diffusion through the HfO<sub>2</sub> or ZrO<sub>2</sub> followed by oxygen diffusion through the SiO<sub>2</sub> scaling layer--controls the oxidation of the two materials.

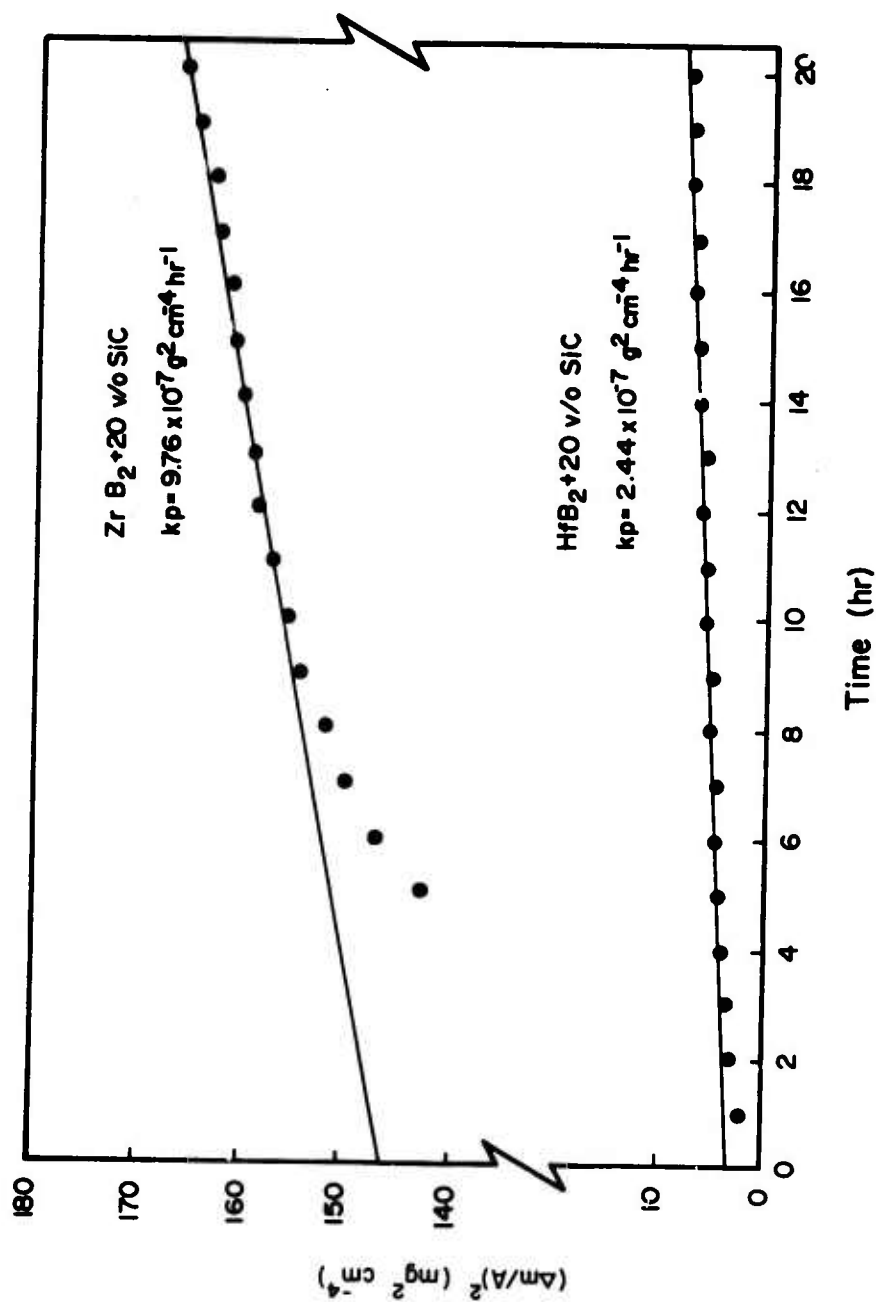


Figure 16. Comparison of the Rates of Total Oxygen Consumption for HfB<sub>2</sub> + 20 v/o SiC and ZrB<sub>2</sub> + 20 v/o SiC at 1400°C in 250 torr O<sub>2</sub>.

## OXIDATION OF $\text{Si}_3\text{N}_4$

Three forms of  $\text{Si}_3\text{N}_4$  have been investigated. Norton hot-pressed HS-130 was of major interest because of its superior strength and oxidation resistance. However, some weight change measurements were made on a reaction-sintered  $\text{Si}_3\text{N}_4$  and on HS-110, an earlier form of hot-pressed material.

### Reaction-Sintered $\text{Si}_3\text{N}_4$

Weight change data on Norton reaction-sintered  $\text{Si}_3\text{N}_4$  were nonreproducible. The technique used to initiate the reaction appeared to influence the kinetics. Several techniques were used in an attempt to obtain reproducible results. Figure 17 is an example of the results from these two techniques. The lower curve is the change in weight of a specimen lowered rapidly into the hot zone -- the method generally used in oxidation experiments. The upper curve is the data obtained from a sample annealed for several hours at  $600^\circ\text{C}$  in Ar before being lowered into the furnace hot zone. Figure 18 shows the behavior observed on five samples of reaction-sintered  $\text{Si}_3\text{N}_4$  oxidized at the same temperature and pressure. The magnitude of the initial weight changes observed varied considerably and all reaction appears to occur in the first few hours, with very little weight change being observed after the initial rapid reaction. Because of the difficulty in obtaining reproducible data on the oxidation behavior of reaction-sintered  $\text{Si}_3\text{N}_4$ , no further weight change studies were made.

### Norton HS-110 $\text{Si}_3\text{N}_4$

The first commercial hot-pressed  $\text{Si}_3\text{N}_4$  available was Norton HS-110, which was soon superseded by HS-130. HS-110 contains a higher percentage of additives than HS-130, with the major differences being the Ca content -- 0.5 w/o in HS-110 and 0.04 w/o in HS-130. Weight change data for hot-pressed HS-110 are shown in Figure 19. The abrupt change in slope of the  $1400^\circ$  curve is probably caused by scale spalling or cracking which results in an increase in rate due to the exposure of clean surfaces. Although this change of slope is not observed at higher temperature, the same scale spalling

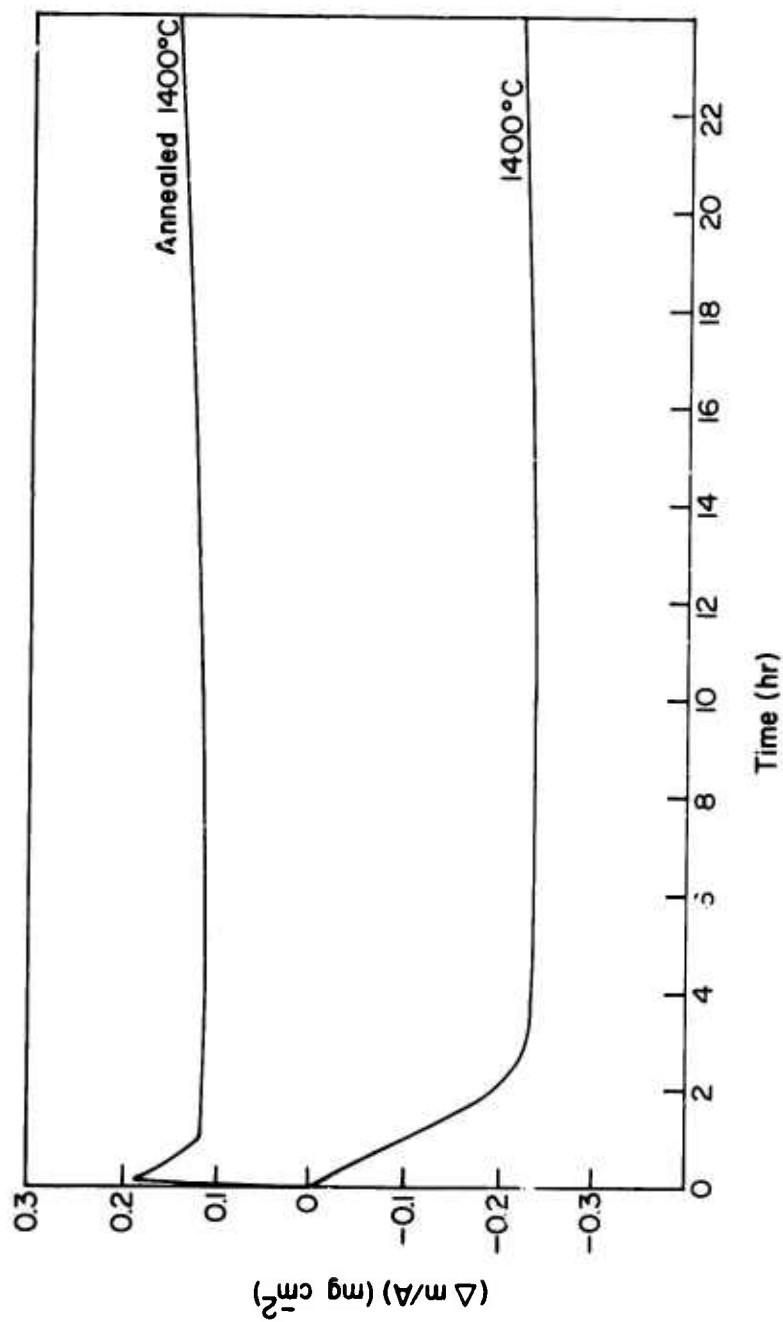


Figure 17. Oxidation Behavior of Reaction Bonded  $\text{Si}_3\text{N}_4$  in 150 torr  $\text{O}_2$  at  $1400^\circ\text{C}$ .

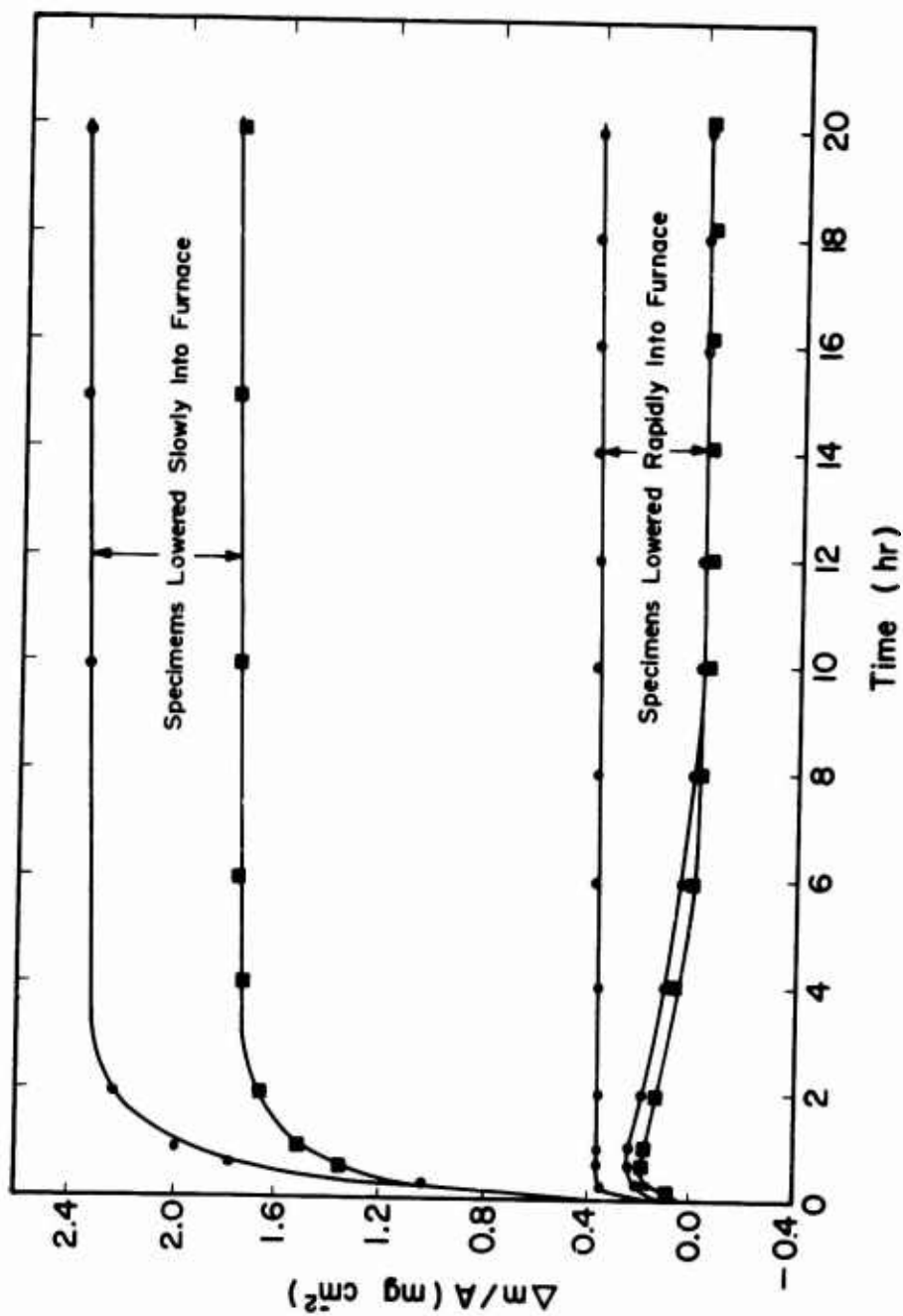


Figure 18. Oxidation of Reaction Sintered  $\text{Si}_3\text{N}_4$  at  $1300^\circ\text{C}$  in 150 torr  $\text{O}_2$ .

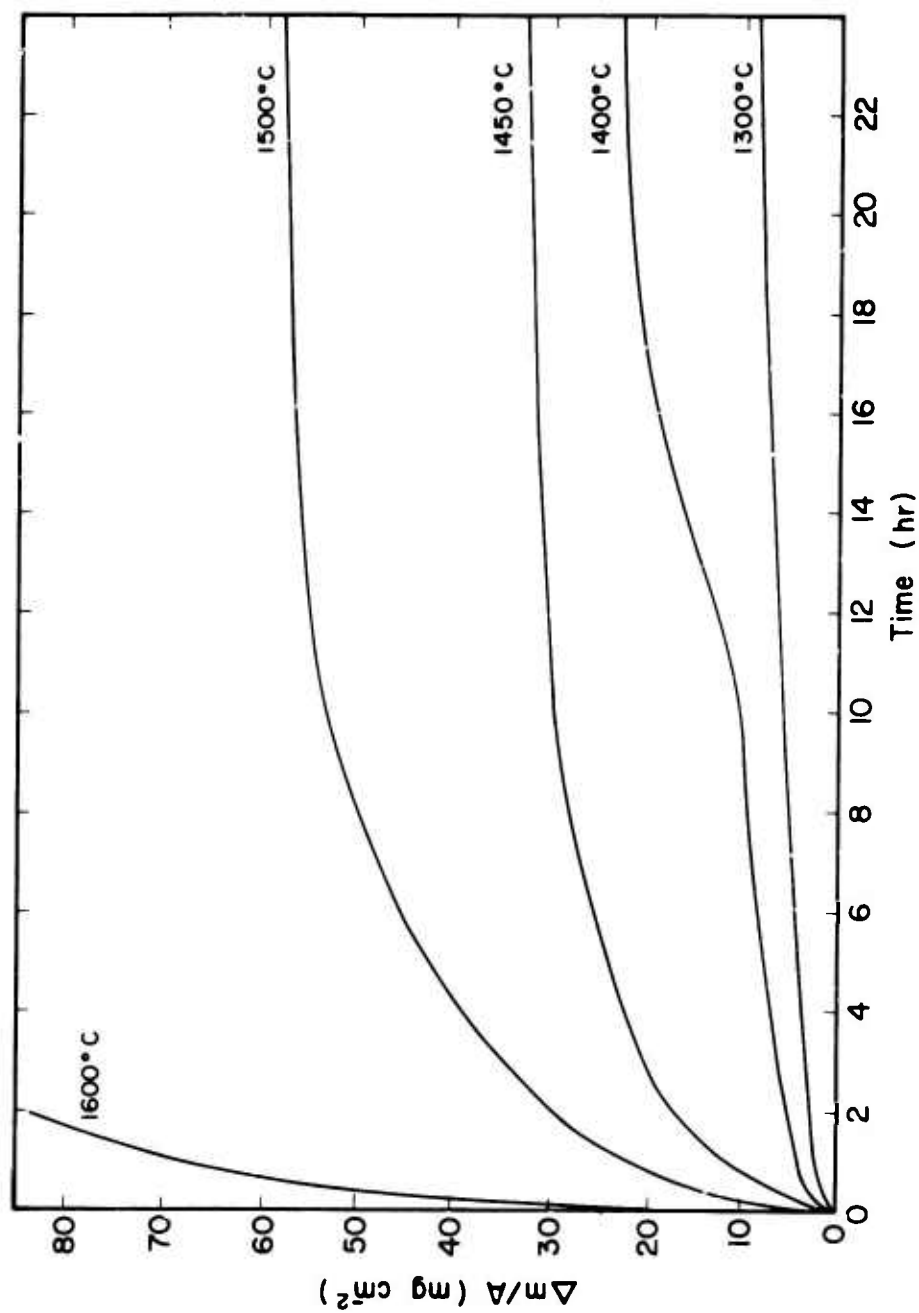


Figure 19. Weight Change Data for Norton HS-110  $\text{Si}_3\text{N}_4$  in 150 torr  $\text{O}_2$ .



process takes place as evidenced by small abrupt weight losses on the strip chart (too small to be shown on the graph).

This spalling of the scale accompanied by an increase in reaction rate appears to be less severe in  $O_2$  which has been dried by passing through a magnesium perchlorate filled drying tower. Figure 20 presents data from two samples oxidized in dried and undried  $O_2$ . The lower rate shown is probably the intrinsic oxidation behavior which would be expected under controlled experimental conditions. Figure 21 is a parabolic plot for two samples of HS-110 reacted in dry  $O_2$  at different temperatures. Good parabolic kinetics are observed, indicating that the reaction is diffusion controlled and that the scale is dense and adherent. Figure 22 is an Arrhenius plot of the parabolic rate constants for HS-110. An activation energy of 122 kcal/mole is calculated from the slope of the plot.

#### Norton HS-130 $Si_3N_4$

##### Oxidation Kinetics

Extensive oxidation studies were conducted on Norton HS-130 because this material shows the most promise for structural applications. Figure 23 is a comparison of the weight gains observed in HS-110 and HS-130 in dry  $O_2$  at  $1400^\circ C$ . The difference in rates is caused by differences in the composition of the scales formed, which is governed by that of the substrate.

Results of weight change measurements of HS-130 in the temperature range  $1300^\circ$  to  $1450^\circ C$  are shown in Figure 24. Data obtained at  $1500^\circ C$  are not shown because the ordinate scale of the graph will not accommodate the large weight gains observed at this temperature. Figure 25 is a parabolic plot of the data shown in Figure 24. The  $1500^\circ C$  data are shown in Figure 26. Parabolic kinetics were generally observed after ~ 1 hr of oxidation, indicating that a coherent scale is formed and the oxidation reaction is diffusion controlled.

An Arrhenius plot of the data at 150 torr  $O_2$  is shown in Figure 27. The parabolic rate constants were obtained from the slope of the linear portion

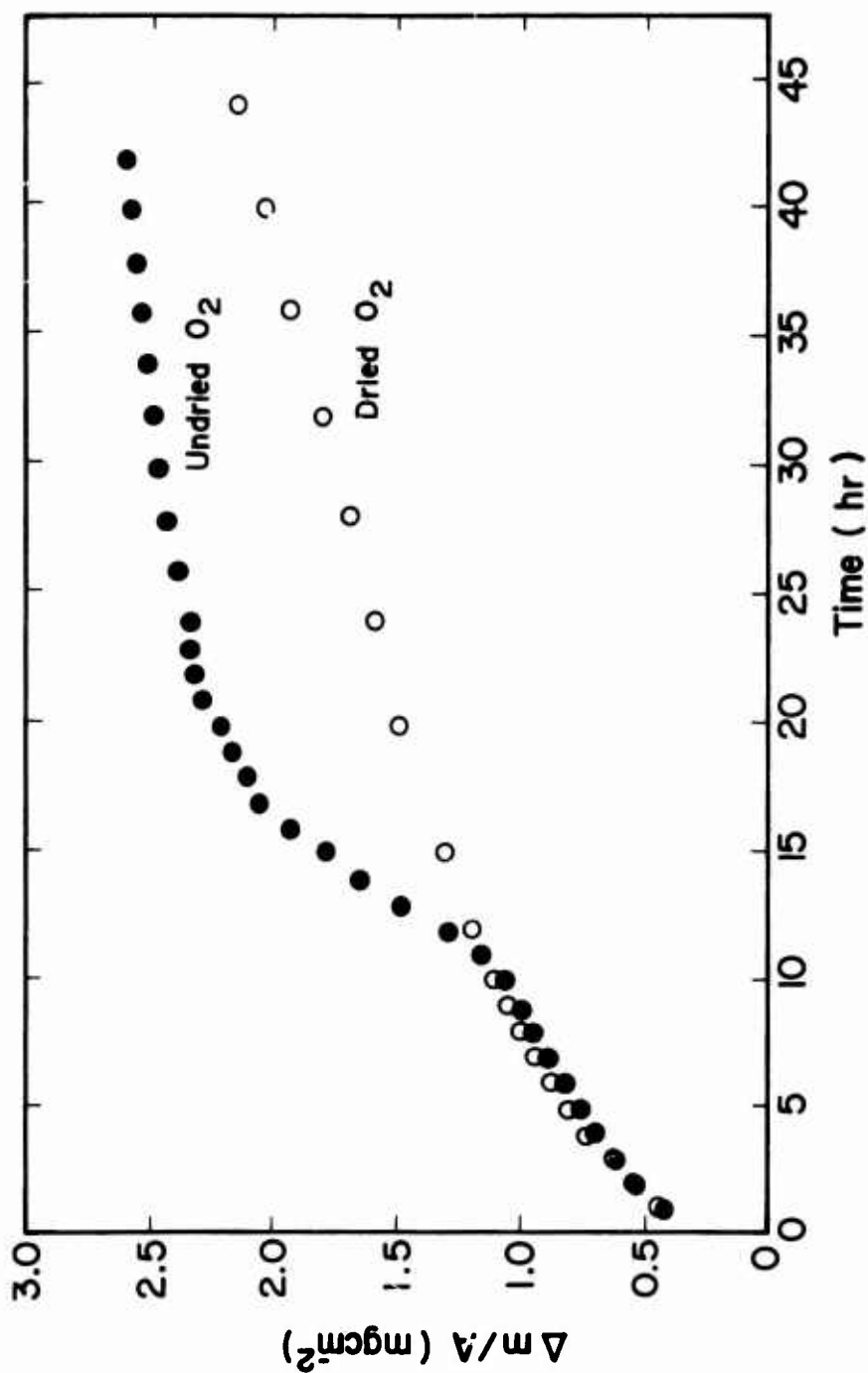


Figure 20. Hot-Pressed Norton HS-110 Si<sub>3</sub>N<sub>4</sub> Oxidized at 1400°C in Undried O<sub>2</sub> (●) and in Dried O<sub>2</sub> (○).

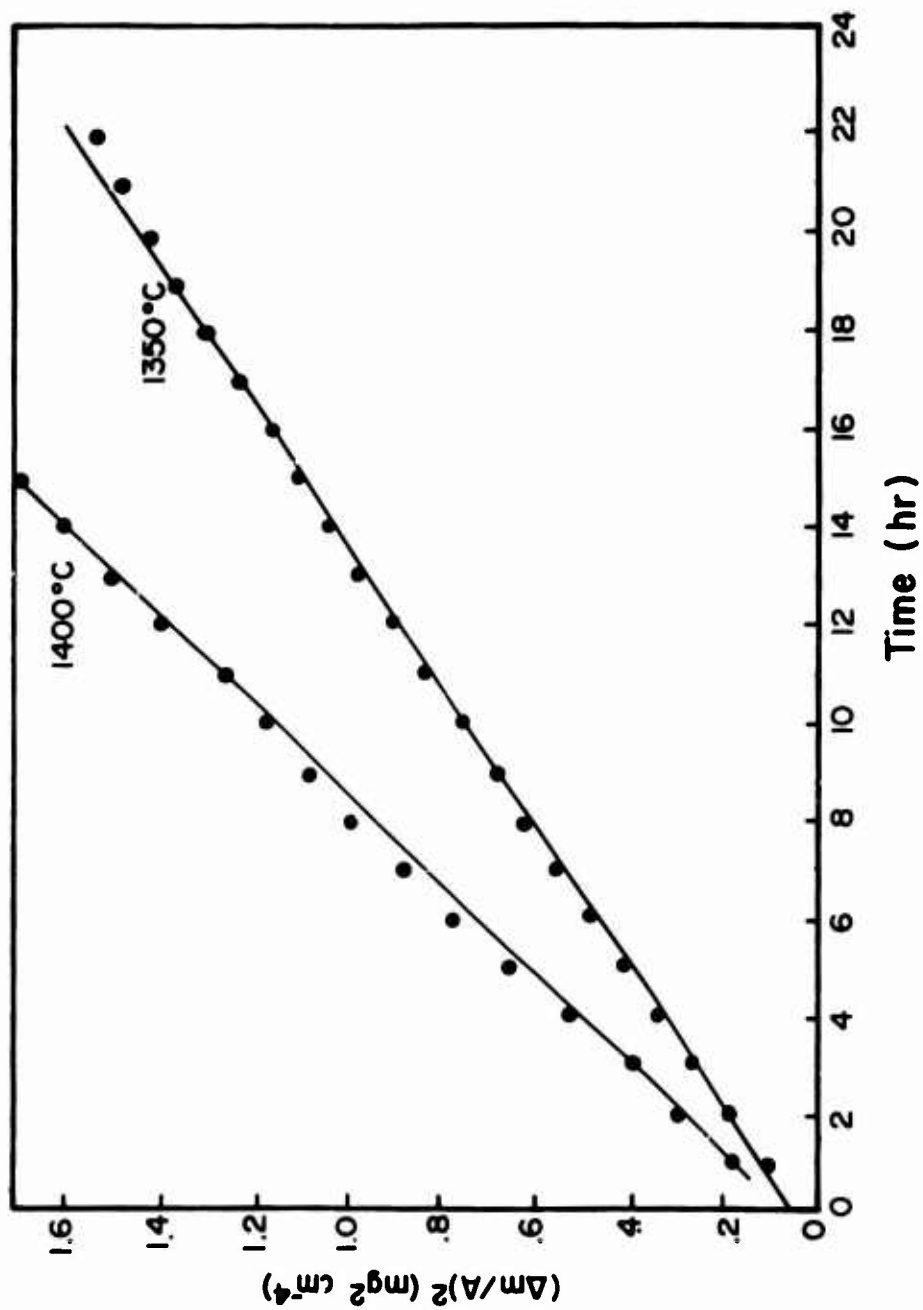


Figure 21. Parabolic Plot of Oxidation of Norton HS-110 Si<sub>3</sub>N<sub>4</sub> in 150 torr Dried O<sub>2</sub>.

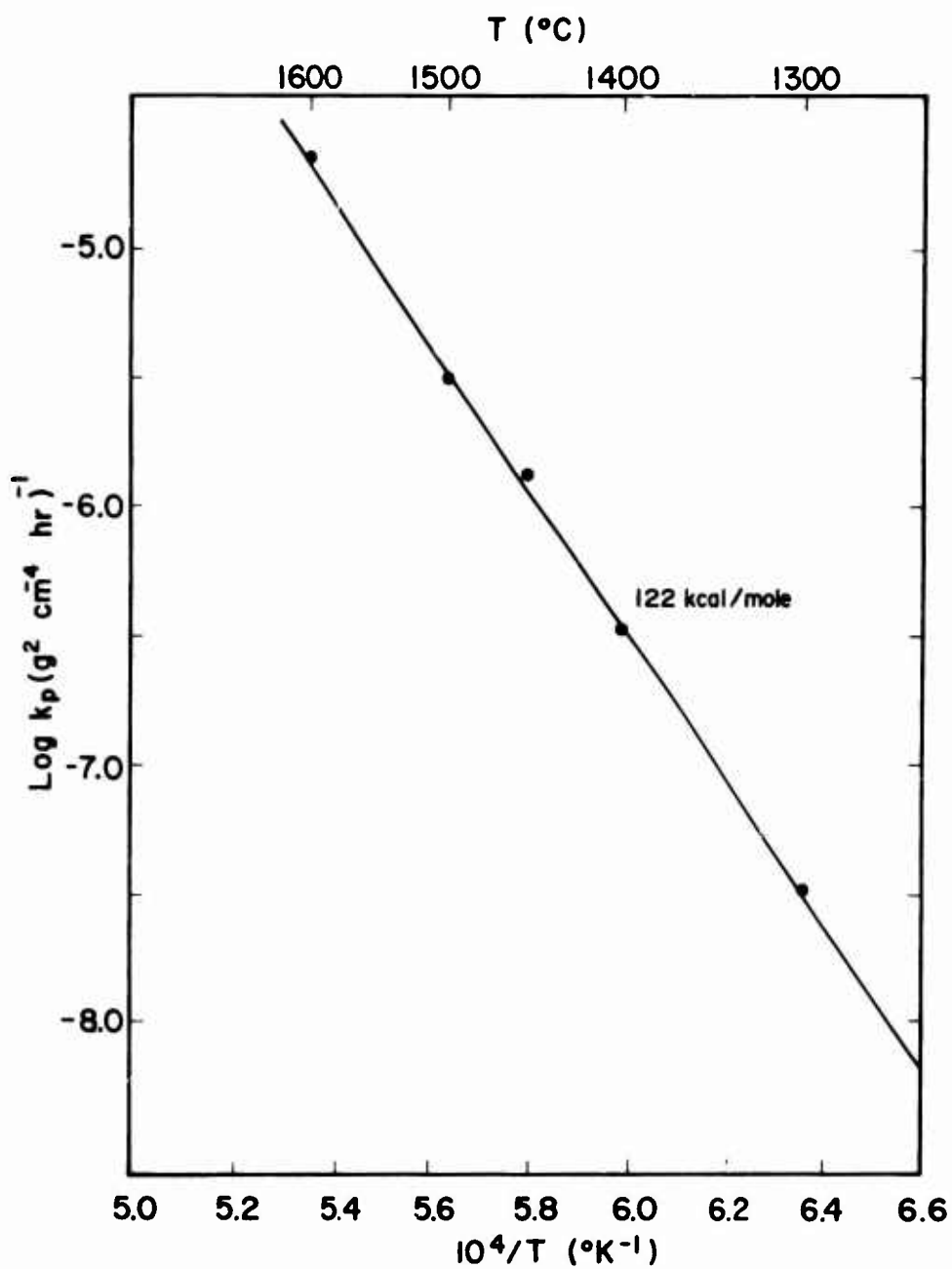


Figure 22. Arrhenius Plot of Parabolic Rate Constants for Norton HS-110 Hot Pressed  $\text{Si}_3\text{N}_4$  in 150 torr Dried  $\text{O}_2$ .

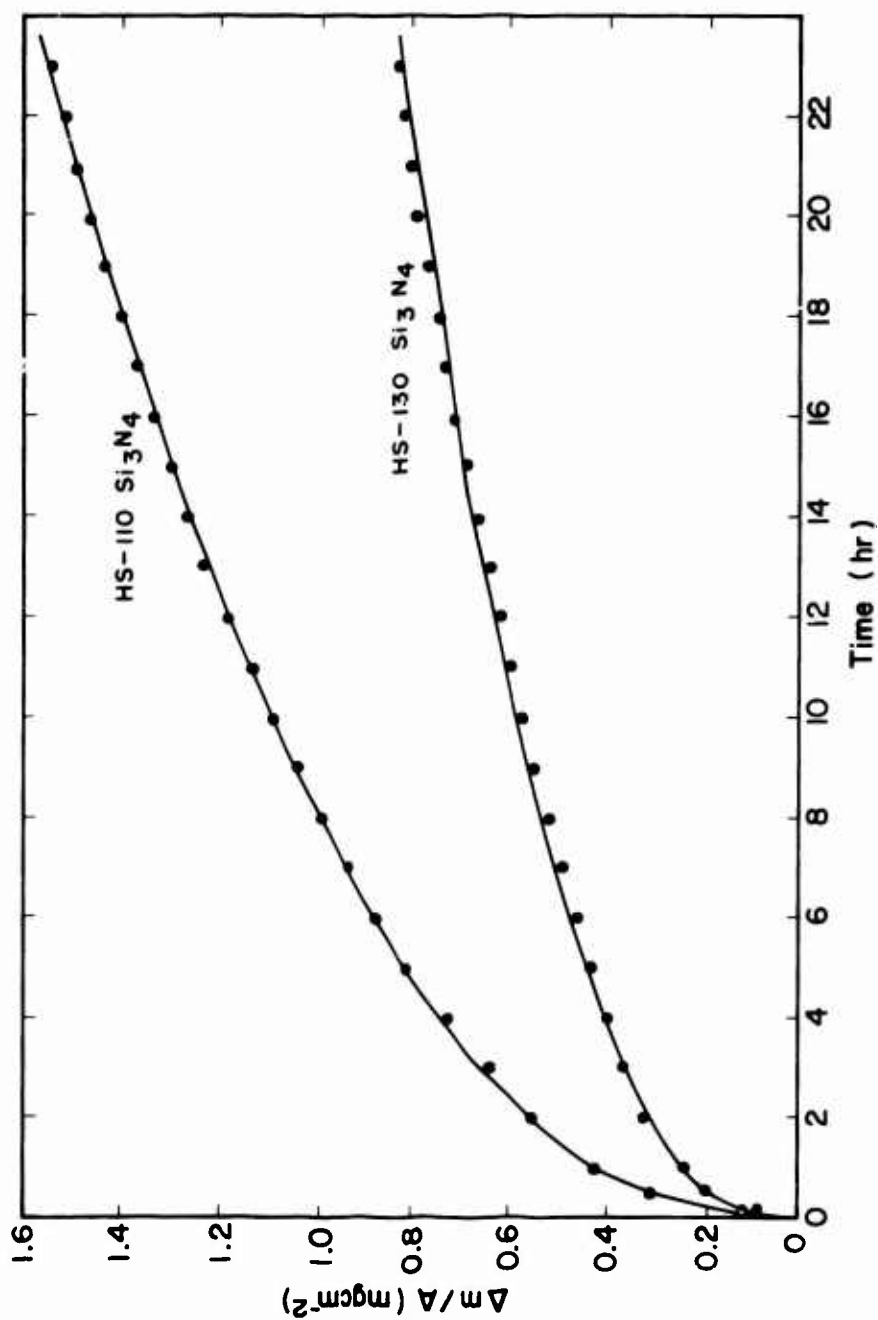


Figure 23. Comparison of the Oxidation Rate of Norton HS-110 and HS-130  $\text{Si}_3\text{N}_4$  at  $1400^\circ\text{C}$  in 150 torr Dried  $\text{O}_2$ .

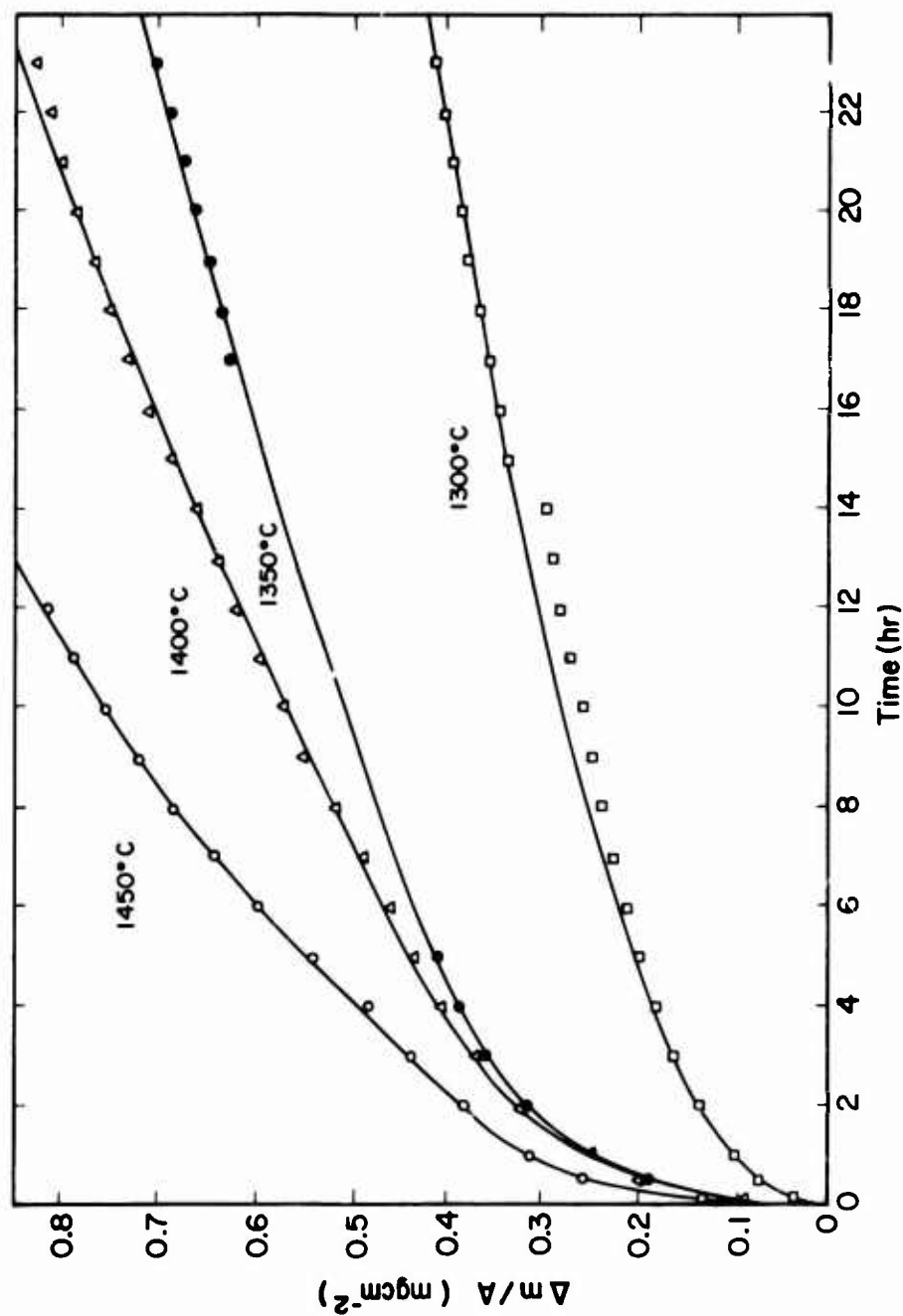


Figure 24. Weight-Change Data for Norton HS-130  $\text{Si}_3\text{N}_4$  in 150 torr  $\text{O}_2$ .

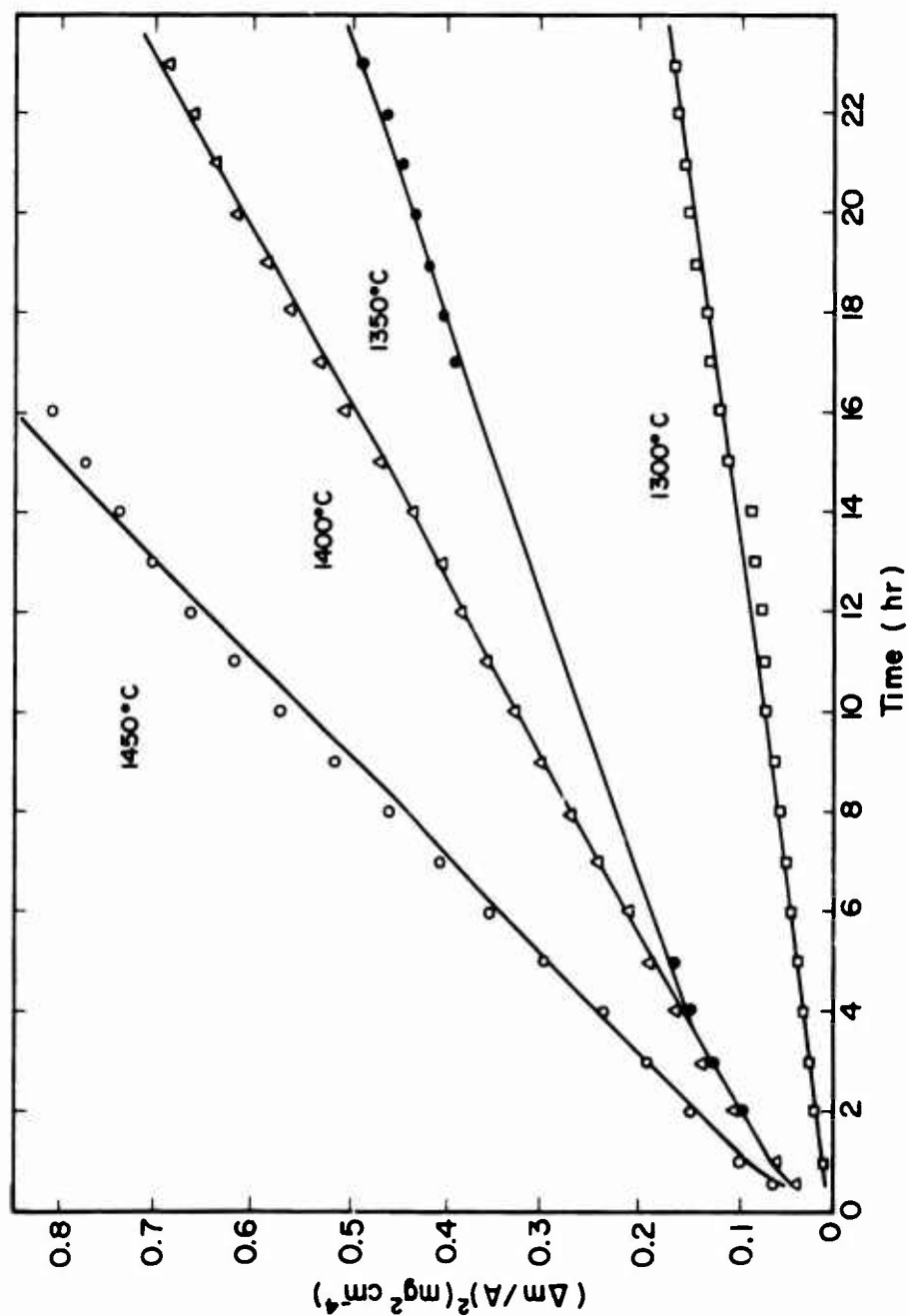


Figure 25. Parabolic Plot of Weight Change Data for Norton HS-130  $\text{Si}_3\text{N}_4$  in 150 torr  $\text{O}_2$ .

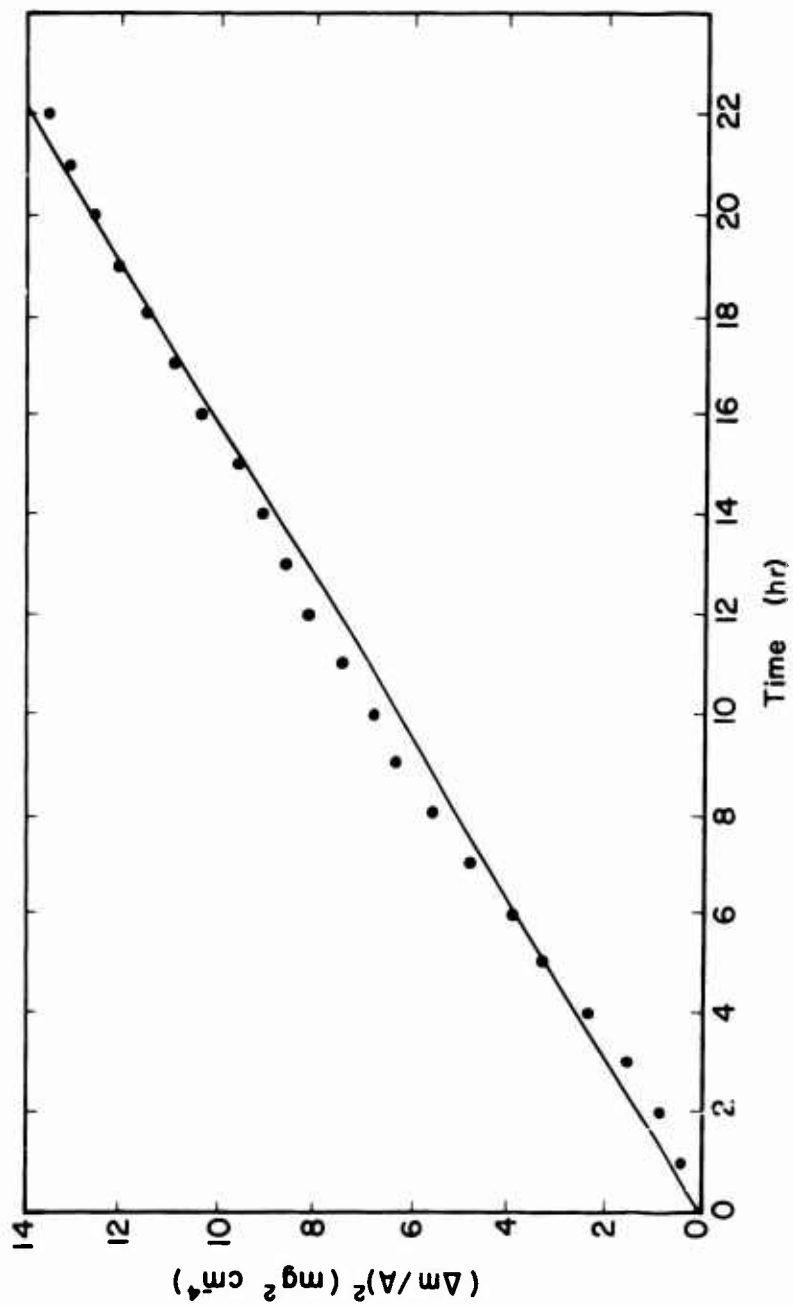


Figure 26. Parabolic Plot of Weight Change Data for Norton HS-130  $\text{Si}_3\text{N}_4$  at  $1500^\circ\text{C}$  in 150 torr  $\text{O}_2$ .



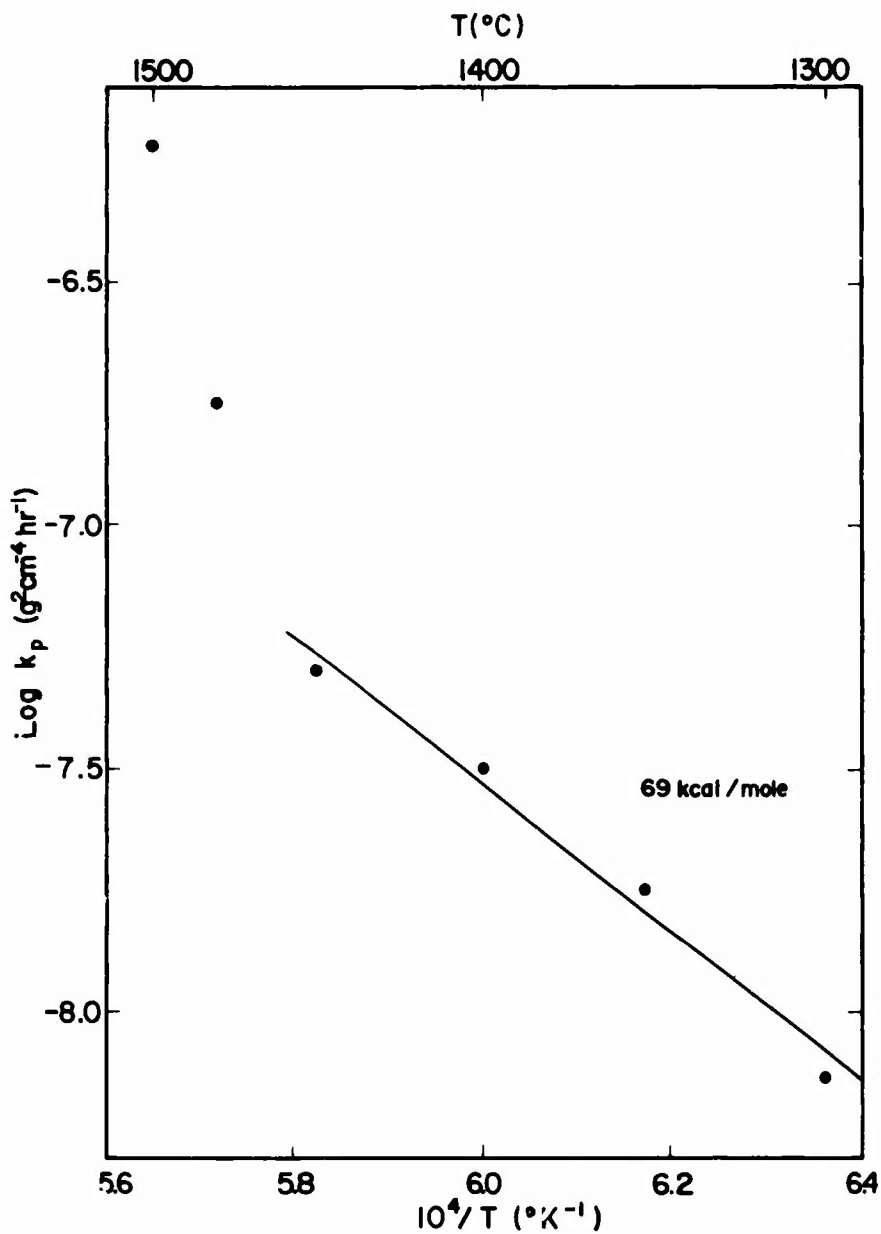


Figure 27. Arrhenius Plot of the Parabolic Rate Constants for Norton HS-130  $\text{Si}_3\text{N}_4$  in 150 torr  $\text{O}_2$ .

of each curve shown in Figures 25 and 26. Below 1450°C an activation energy of 3 eV (69 kcal/mole) was calculated. Above this temperature, a rapid increase in the reaction rate was observed. An extremely high activation energy of 12 eV was calculated from the three data points at 1450°, 1475°, and 1500°C. This energy is much too large to be associated with a simple diffusion controlled mechanism, and instead, probably represents a transition region between different reaction mechanisms.

Results of long time oxidation experiments conducted at 1350° and 1450°C are presented in Figures 28 and 29. At 1350°C initial parabolic kinetics were observed followed by a gradual increase in oxidation rate; after ~ 30 hr a higher parabolic rate was found. At 1450°C the opposite effect was observed. During both of these experiments, scale breakdown occurred after a sufficiently long reacting time, as evidenced by discontinuous weight losses on the strip-chart recorder (usually too small to be plotted on the graphs shown). This scale breakdown occurs at shorter times as the temperature is increased; at sufficiently long times at high temperature, a relatively high linear oxidation rate was observed. These increased rates of attack, occurring at the low flow rates used in these experiments, would be expected to be accelerated at higher flow rates.

The presence of H<sub>2</sub>O vapor in the reacting gas has been found to increase significantly the rate of oxidation of other Si-base materials. Although the oxidation rate increased when Si<sub>3</sub>N<sub>4</sub> was exposed to O<sub>2</sub> saturated at room temperature with H<sub>2</sub>O, the increase was not very large, as shown in Figure 30.

The  $P_{O_2}$  dependence of the oxidation rate was investigated in the range 75-600 torr by two techniques. In the first, pure oxygen was used, and total pressure was varied to give the desired  $P_{O_2}$ . Results from these experiments are shown in Figure 31 for total pressures of 75, 150, 300, and 600 torr. The data fall within the band indicated, and the small differences observed were not sufficient to indicate a  $P_{O_2}$  dependence. In the second technique, O<sub>2</sub>/N<sub>2</sub> and O<sub>2</sub>/Ar mixtures were used at 600 torr total pressure. The desired  $P_{O_2}$  was obtained by varying the O<sub>2</sub>/N<sub>2</sub> or O<sub>2</sub>/Ar ratio. Figure 32 shows

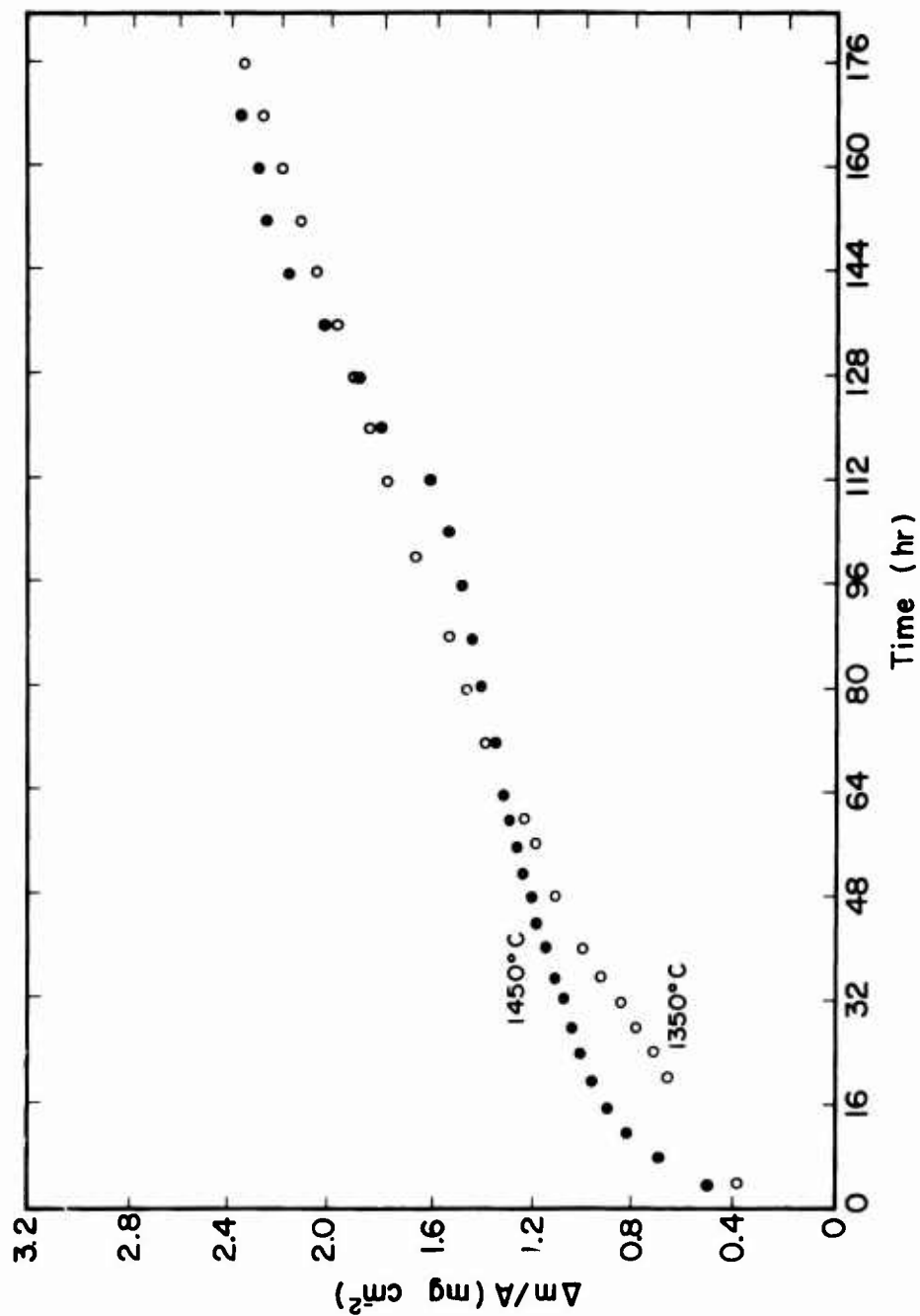


Figure 28. Long Time Weight Change Data of Norton HS-130  $\text{Si}_3\text{N}_4$  in 150 torr  $\text{O}_2$ .

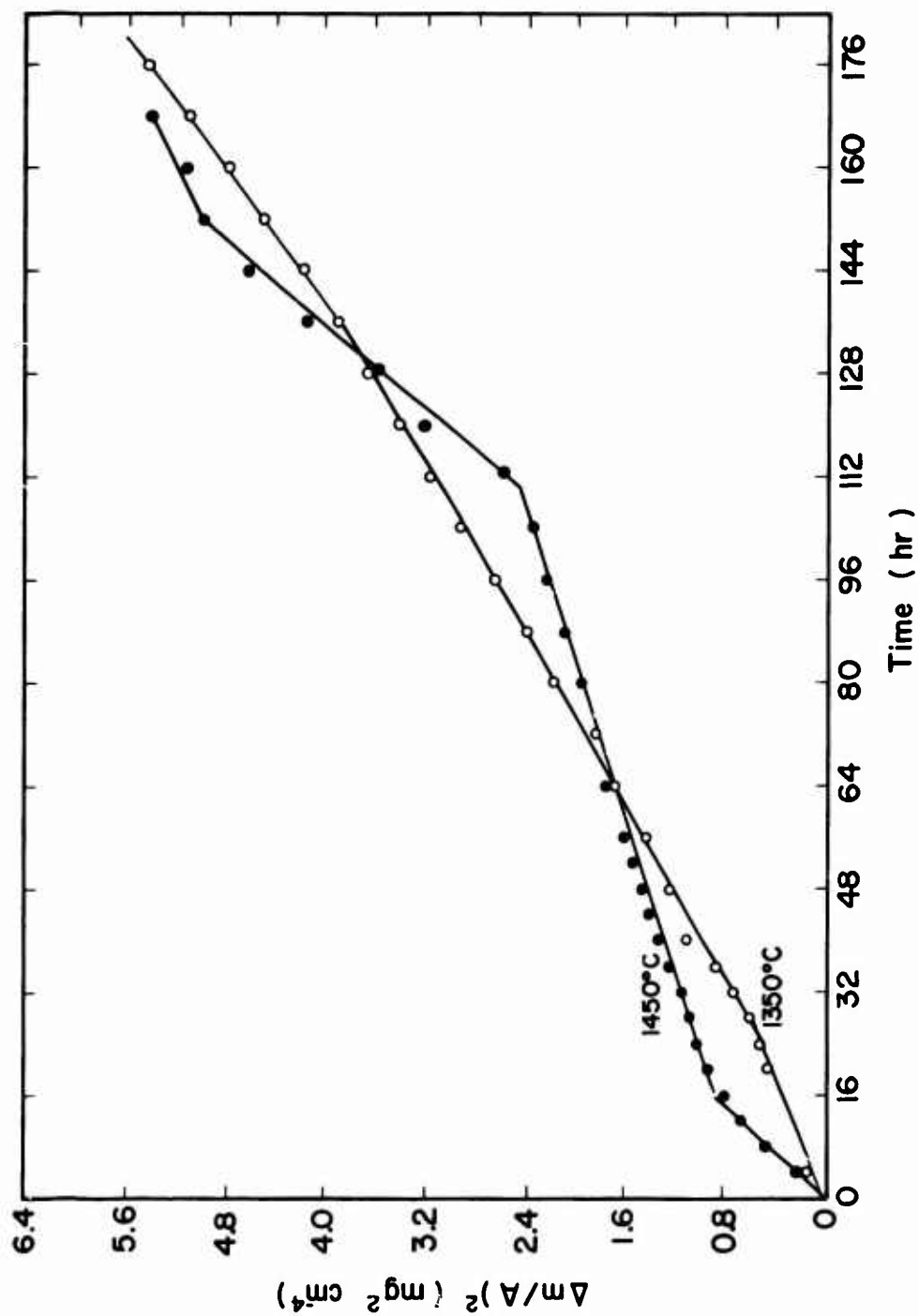


Figure 29. Parabolic Plot of Long Time Weight Change Data of Norton HS-130  $\text{Si}_3\text{N}_4$  in 150 torr  $\text{O}_2$ .

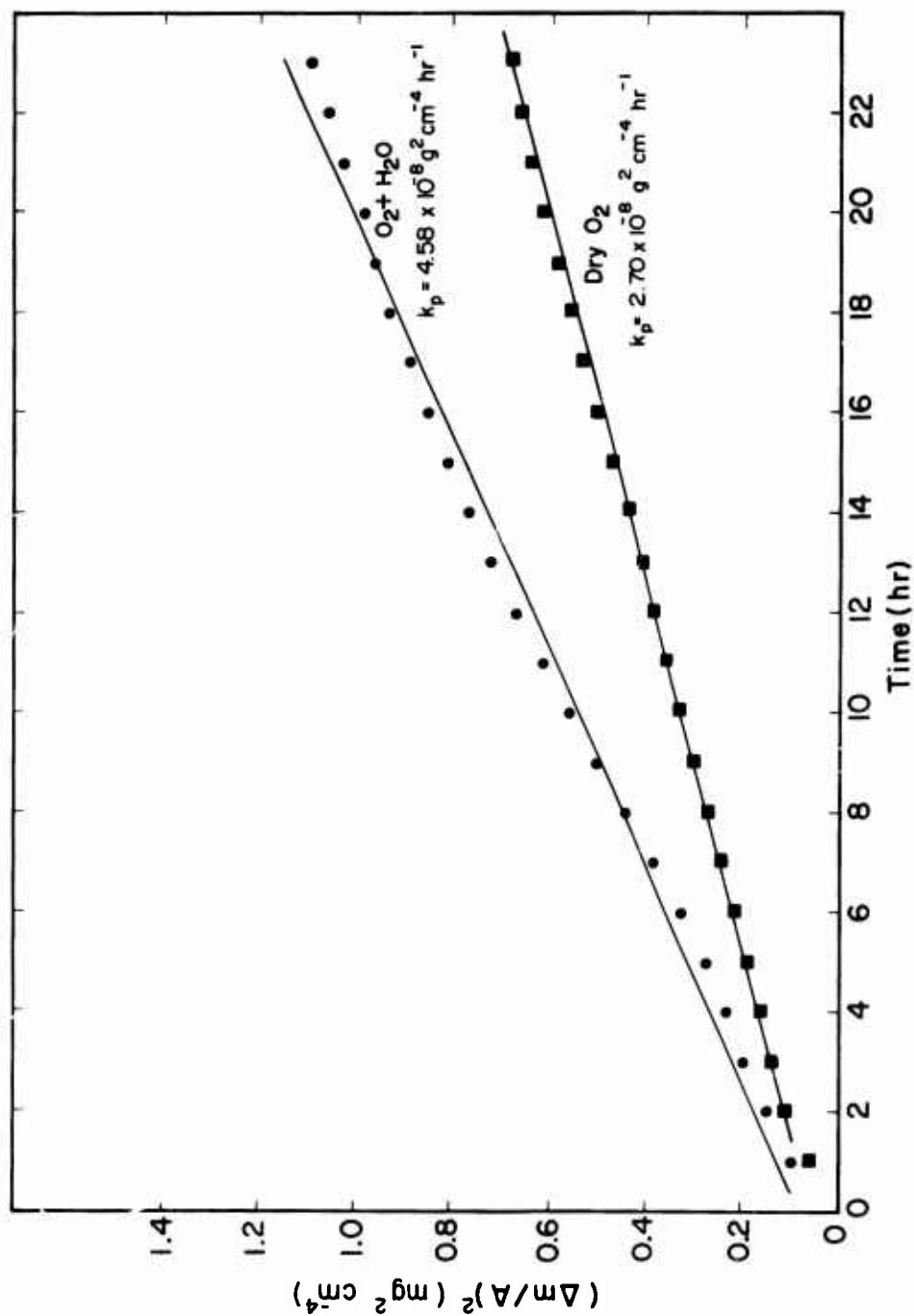


Figure 30. Comparison of Oxidation Rate of Norton HS-130  $\text{Si}_3\text{N}_4$  in  $\text{H}_2\text{O} + \text{O}_2$  and Dry  $\text{O}_2$  at  $1400^\circ\text{C}$  (Total Pressure = 150 torr).

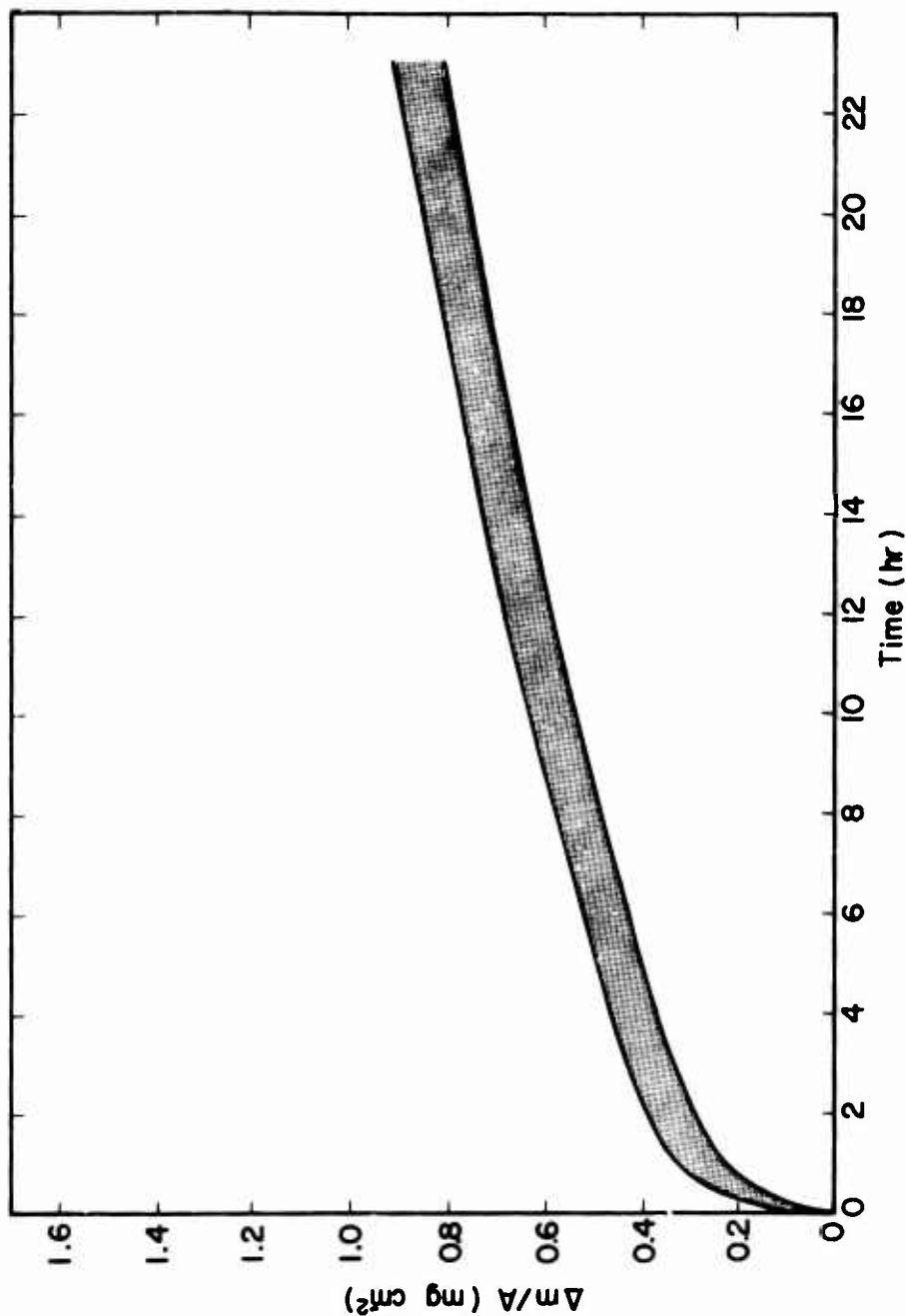


Figure 31. Weight-Change Data of Norton HS-130  $\text{Si}_3\text{N}_4$  in the Range 75 to 600 torr  $\text{O}_2$  at  $1400^\circ\text{C}$ .

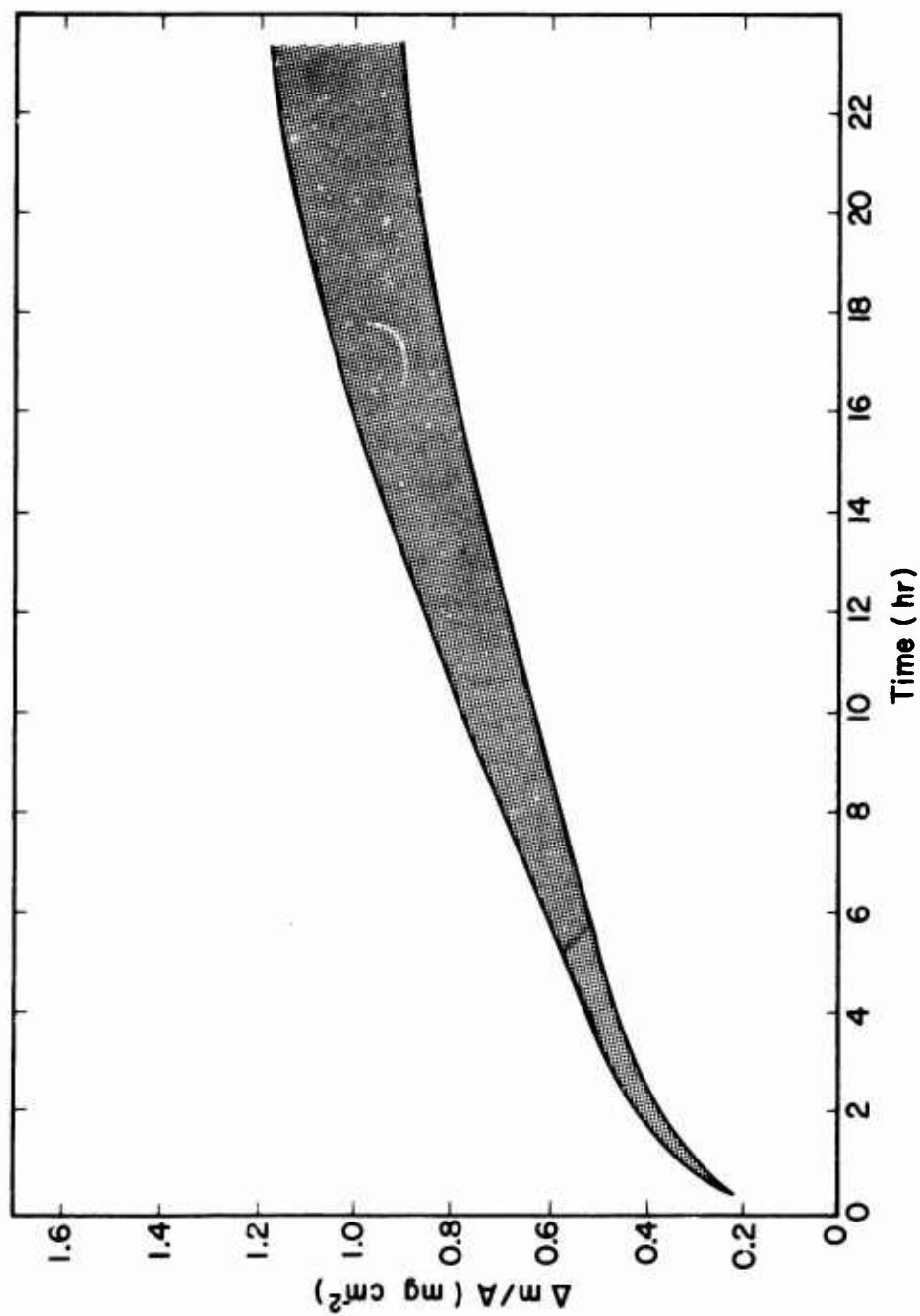


Figure 32. Weight Change Data of Norton HS-130  $\text{Si}_3\text{N}_4$  in the Range 75 to 600 torr Using  $\text{O}_2/\text{N}_2$  Mixtures at  $1400^\circ\text{C}$  (Total Pressure = 600 torr).

the results of these measurements, and, again, no pressure dependence was found over the same  $P_{O_2}$  range (i.e., 75-600 torr  $O_2$ ).

$Si_3N_4$  forms a protective  $SiO_2$  coating during oxidation at high oxygen partial pressures; however, active oxidation--i.e., the formation of  $SiO(g)$ --is expected to occur at low oxygen partial pressures. Both Wagner<sup>(29)</sup> and Gulbranson<sup>(30)</sup> have formulated theories to explain the active oxidation of Si. Gulbranson<sup>(30)</sup> has also extended his theory to SiC active oxidation. Based on Gulbranson's theory, active oxidation is expected to occur at oxygen pressures below  $10^{-4}$  atm at 1400°C for  $Si_3N_4$ . Four specimens were oxidized in different CO/ $CO_2$  mixtures which established oxygen partial pressures between  $10^{-6}$  and  $10^{-9}$  atm. Active oxidation is characterized by sample weight losses; however, from the results shown in Figure 33 no such weight losses were observed. The rates measured in the four gas mixtures were independent of  $P_{O_2}$ ; however, they were less than those obtained in  $O_2$  or  $O_2/N_2$  gas mixtures. Further work revealed that active oxidation occurred at an oxygen partial pressure of  $10^{-12}$  atm. Upon increasing the oxygen partial pressure, no weight gain indicating a transition from active to passive oxidation was observed until a  $P_{O_2}$  of  $10^{-7.4}$  atm was reached. At  $P_{O_2} = 10^{-7.4}$  atm no change in weight was observed; this would indicate a transition region from active to passive behavior between  $P_{O_2} = 10^{-8}$  and  $10^{-7.4}$  atm.

Figure 34 summarizes the  $P_{O_2}$  dependence of the oxidation kinetics in  $O_2$ ,  $O_2/N_2$ ,  $O_2/Ar$  and CO/ $CO_2$  atm at 1400°C. The oxidation kinetics are essentially  $P_{O_2}$  independent; however, rates in CO/ $CO_2$  mixtures are somewhat lower than those in pure  $O_2$ , which are, in turn, somewhat lower than those in  $O_2/N_2$  mixtures.

#### Oxide Scale Constituents and Morphologies

X-ray diffraction data have shown the composition of the scales to consist of  $\alpha$ -cristobalite and magnesium silicate. To determine the composition more accurately, a microprobe study was made. Results for samples oxidized between 1300° and 1500°C for 24 hr in 150 torr  $O_2$  are shown schematically in Figure 35. The significant increase in scale thickness and the slight difference in composition at 1475° and 1500°C are consistent with the upward



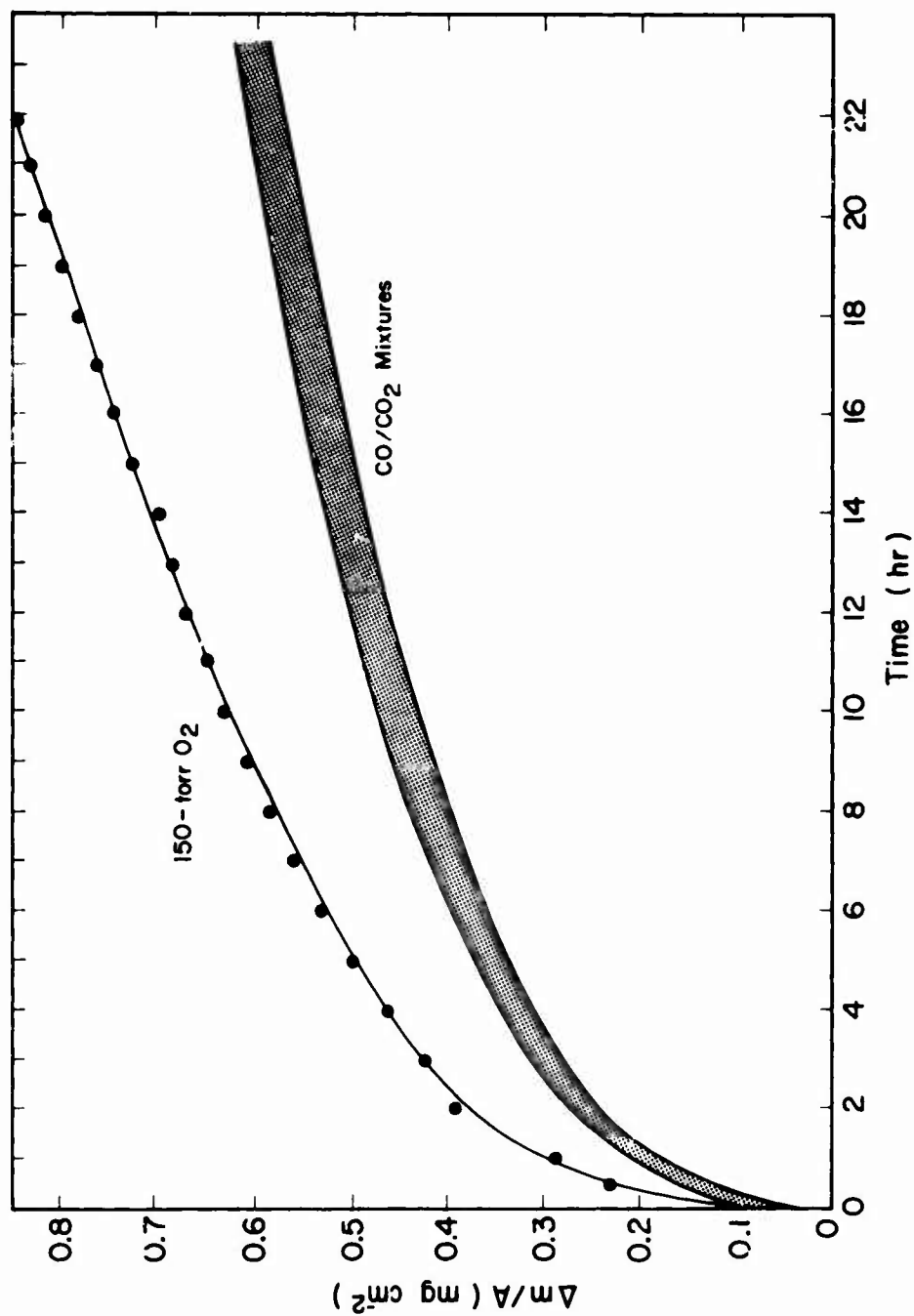


Figure 33. Weight Change Data of Norton HS-130 Si<sub>3</sub>N<sub>4</sub> in 10<sup>-6</sup> to 10<sup>-9</sup> atm O<sub>2</sub> Using CO/CO<sub>2</sub> Mixtures at 1400°C.

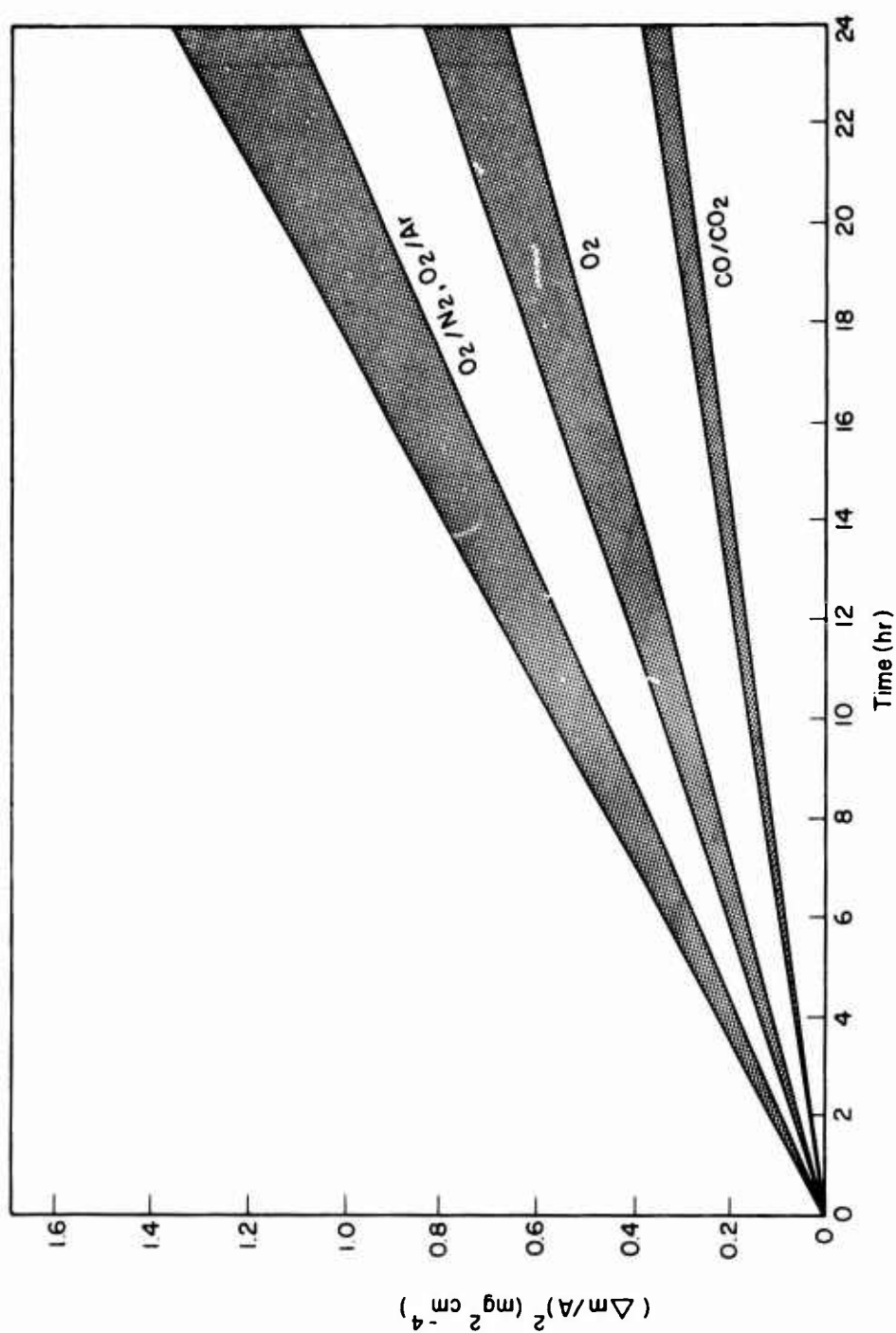


Figure 34. Parabolic Plot of Weight Change Data for  $\text{Si}_3\text{N}_4$  Oxidized at  $1400^\circ\text{C}$  in  $\text{O}_2$ ,  $\text{O}_2/\text{N}_2$ ,  $\text{O}_2/\text{Ar}$ , and  $\text{CO/CO}_2$  Mixtures.

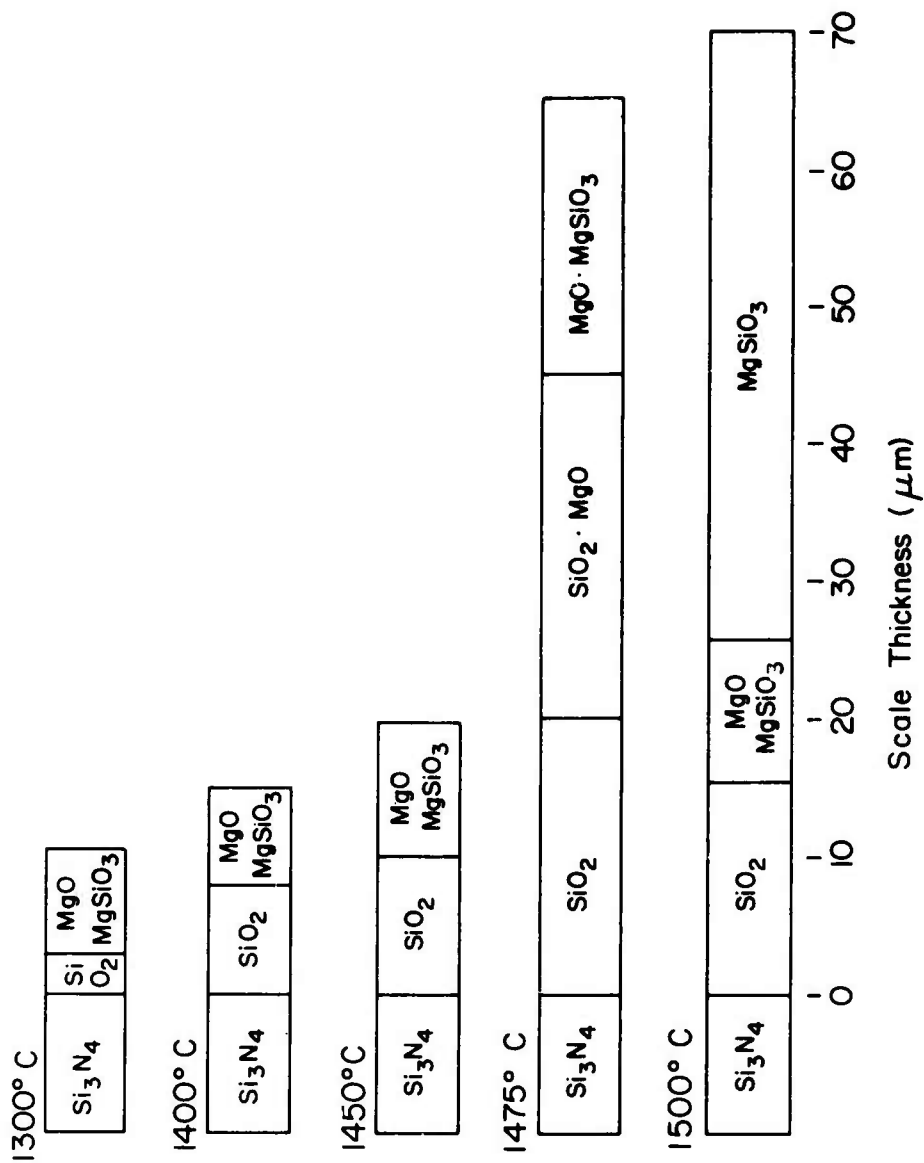


Figure 35. Microprobe Analysis of Scale Composition for Specimens Oxidized in 150 torr  $O_2$  for 24 hr.

break at 1450°C in the Arrhenius plot shown in Figure 27. In all cases a layer of  $\text{SiO}_2$  was found at the nitride-oxide interface. In this area of the scale the concentration of Mg, as well as Ca, Al, and Fe, common impurities in  $\text{Si}_3\text{N}_4$ , was less than 1%, similar to the concentrations measured in the nitride. Outside of this  $\text{SiO}_2$  layer, large concentrations of Mg were found together with Si (and oxygen). Ca, Al, and Fe were still present but at no increased concentration, except at the outer surface where a significant increase in Ca was observed.

Quantitative microprobe analysis showed the ratio of Mg/Si to increase with temperature. The results for scales formed in 600 torr  $\text{O}_2$  on three specimens after 24 hr of reaction and on one specimen after 194 hr (at 1350°C) are as follows:

	<u>1300°</u>	<u>1400°</u>	<u>1450°</u>	<u>1350'</u>
Si (wt %)	27.40 $\pm$ 2.8	27.89 $\pm$ 0.5	30.05 $\pm$ 0.6	28.07 $\pm$ 0.76
Mg (wt %)	17.37 $\pm$ 2.0	21.96 $\pm$ 0.5	26.68 $\pm$ 1.5	16.80 $\pm$ 0.5
O (by difference)	55.23	50.15	46.26	55.12

These data were obtained by point counting at different locations in the scale and utilizing a computer program (MAGIC<sup>(31)</sup>) to average and correct the data, using MgO and  $\text{SiO}_2$  as standards.

On a sample oxidized at 1500°C in 600 torr  $\text{O}_2$ , accurate analysis was difficult because of gross irregularities in the scale. However, the Mg content appeared to be quite low (10%), although the reaction rate was abnormally fast. The reason for this low concentration is undoubtedly the limited source of MgO in the matrix.

Figure 36 shows optical micrographs of the scales formed in 150 torr  $\text{O}_2$  after 24 hr of reaction. The scales formed over the temperature range 1300° to 1475°C exhibit a change in morphology with increasing temperature. A large thickness increase is observed at 1475°C, and the scale appears to be very porous.



1300°C



1400°C



1450°C



1475°C

Figure 36. Optical Micrographs of the Scales Formed on  $\text{Si}_3\text{N}_4$  Oxidized in 150 torr  $\text{O}_2$  for 24 hr.

One of the major differences in the scales formed below 1450° and above 1450° was the granular or crystalline nature at the lower temperatures and the glassy appearance above 1450°C. Scanning electron micrographs of scales formed in each region are shown in Figures 37 and 38. The cracks, clearly visible in the micrographs of the surface, probably are formed upon cooling. The scale is known to be coherent at temperature as evidenced by the observed parabolic oxidation kinetics.

#### Oxygen Pressure Dependence of Scale Morphologies

Experiments were conducted in oxygen at 75, 150, 300, and 600 torr  $O_2$  at 1400°C by varying the total pressure. Weight-change measurements clearly showed that the reaction rate was not  $P_{O_2}$  dependent (Figure 31). The scales formed at 1400°C after 24 hr of reaction at these four different pressures were consistent with this observation. The scales shown in Figure 39 appear to be similar in structure and to have the same thickness.

Experiments were also conducted at 75, 150, and 300 torr  $P_{O_2}$ , using  $O_2/N_2$  mixtures at a total pressure of 600 torr. Rates of oxidation in these mixtures were somewhat larger than those in pure  $O_2$  at reduced total pressure as shown in Figure 34. Figure 40 is a comparison of the scales formed at 1400°C after 24 hr of exposure to 75 torr  $O_2$  + 525 torr  $N_2$  and to 75 torr  $O_2$  only. The scanning electron micrographs of the scales formed in these mixtures show differences in structure. The scale formed on the specimen exposed to the  $O_2 + N_2$  mixture contains large voids and has a much more glassy appearance than the scale formed on the specimen oxidized in pure  $O_2$ . When the  $P_{N_2}$  in the ambient is large, apparently the nitrogen formed at the nitride-oxide interface upon oxidation cannot escape as readily as when the  $P_{N_2}$  in the ambient is low. Therefore,  $N_2$  is trapped in the scale, as evidenced by the gas pockets and the increased weight gain observed. In Figures 41 and 42 similar scale morphology is exhibited.

Since the addition of  $N_2$  to the  $O_2$  ambient increased the oxidation rate,  $N_2$  was added to the  $CO/CO_2$  mixtures to determine whether the same behavior would occur. Figure 43 shows the results for a  $CO/CO_2$  mixture at 150 torr and the same  $CO/CO_2$  mixture at 150 torr plus 450 torr of  $N_2$ . In both cases,



Surface

Reproduced from  
best available copy.



Scale

Matrix

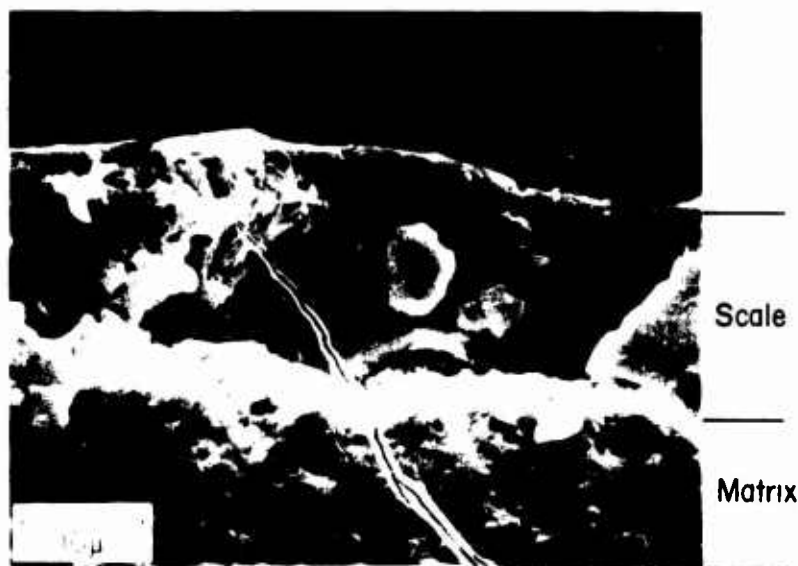
10 μ

Fractured Cross Section

Figure 37. Scanning Electron Micrographs of the Scales Formed on  $\text{Si}_3\text{N}_4$  after 24 hr of Reaction in 150 torr  $\text{O}_2$  at  $1400^\circ\text{C}$ .



Surface



Fractured Cross Section

Figure 38. Scanning Electron Micrographs of the Scales Formed on  $\text{Si}_3\text{N}_4$  after 24 hr of Reaction in 150 torr  $\text{O}_2$  at  $1475^\circ\text{C}$ .



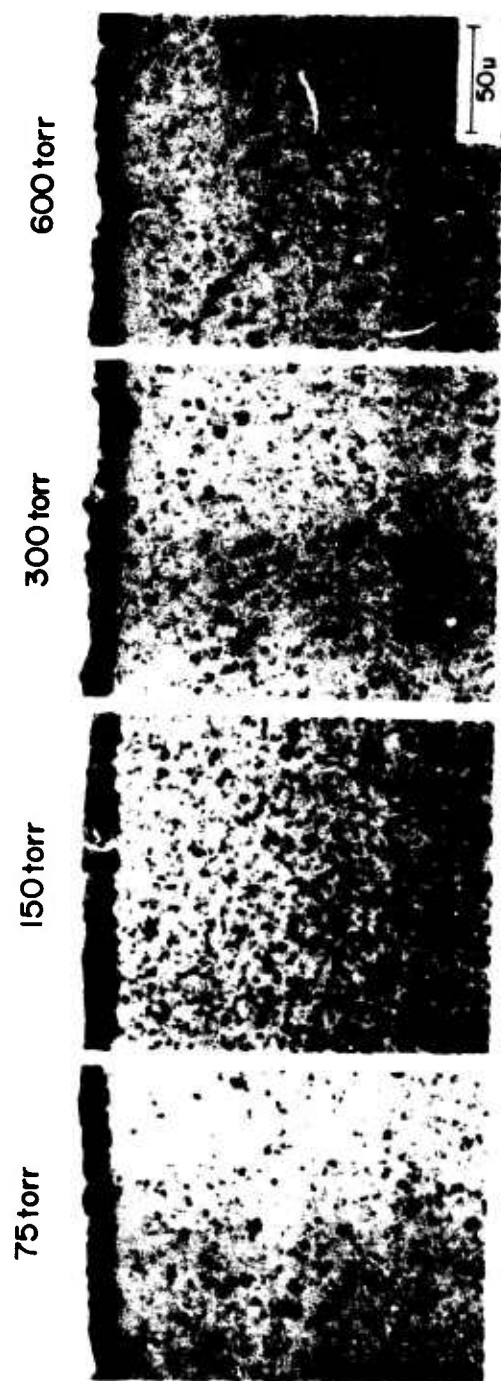


Figure 39. Optical Micrographs of Scales Formed on  $\text{Si}_3\text{N}_4$  after 24 hr of Reaction in 75, 150, 300, and 600 torr  $\text{O}_2$  at  $1400^\circ\text{C}$ .

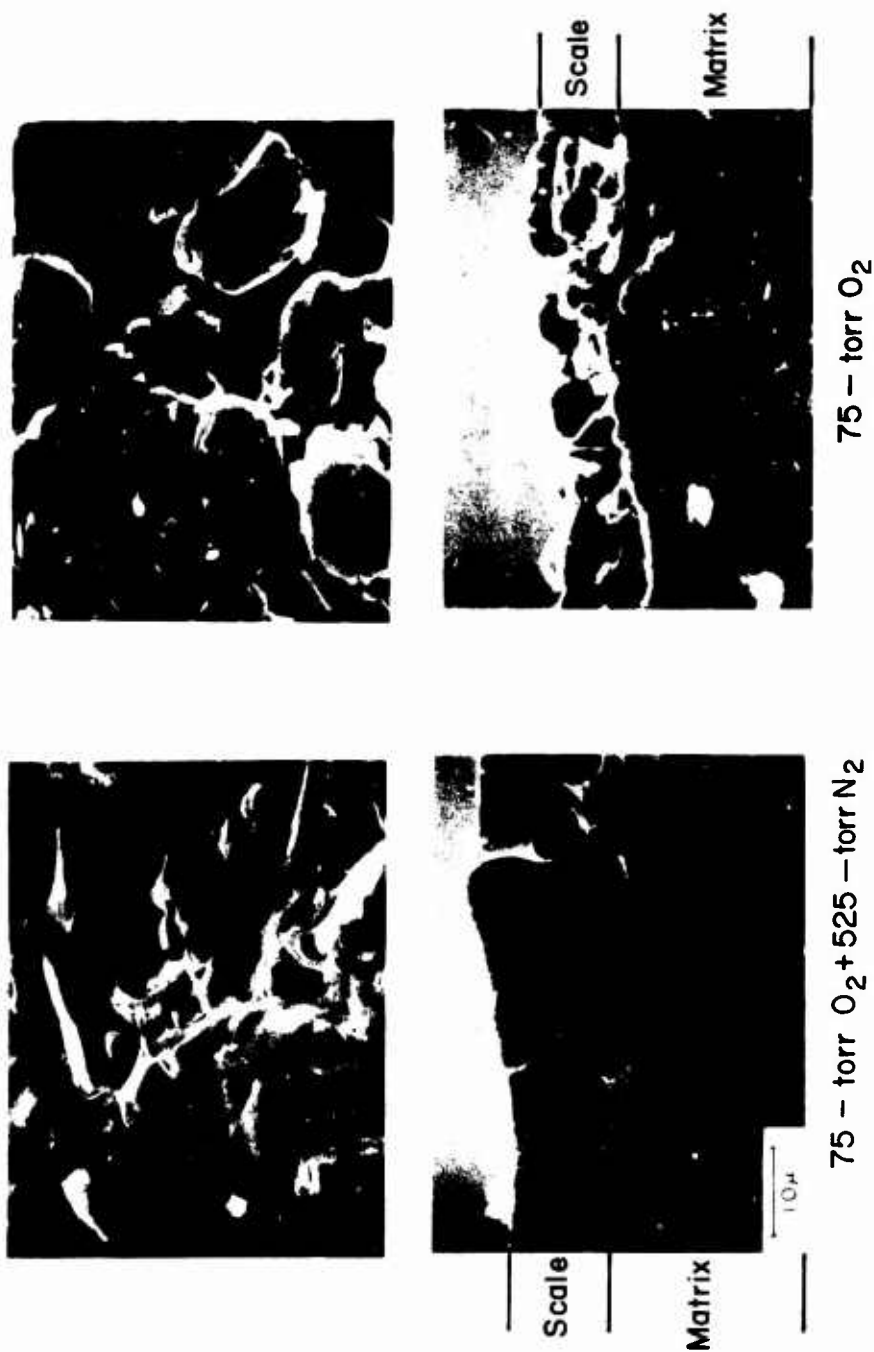


Figure 40. Scanning Electron Micrographs of the Scales Formed on  $Si_3N_4$  in  $O_2$  and in  $O_2/N_2$  Gas Mixtures after Reaction for 24 hr at  $1400^\circ C$ .

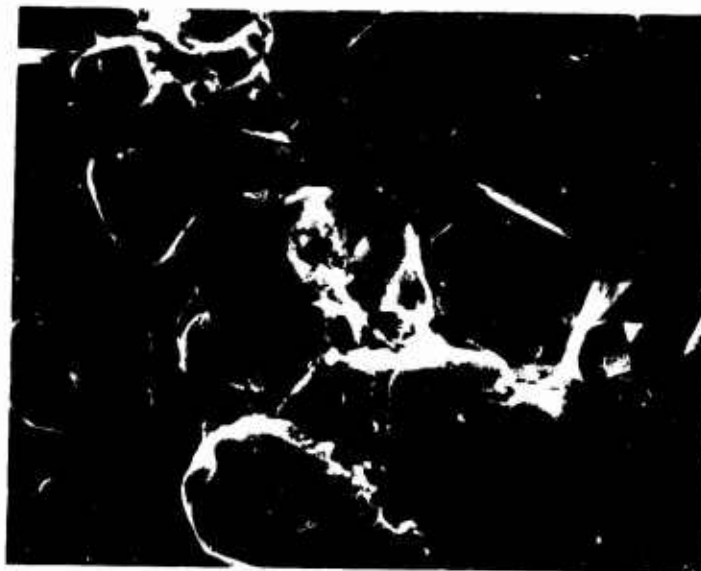


Figure 41. Scanning Electron Micrograph of the Scale formed on  $\text{Si}_3\text{N}_4$  after 24 hr of Reaction in 150 torr  $\text{O}_2$  and 450 torr  $\text{N}_2$  at  $1400^\circ\text{C}$ .

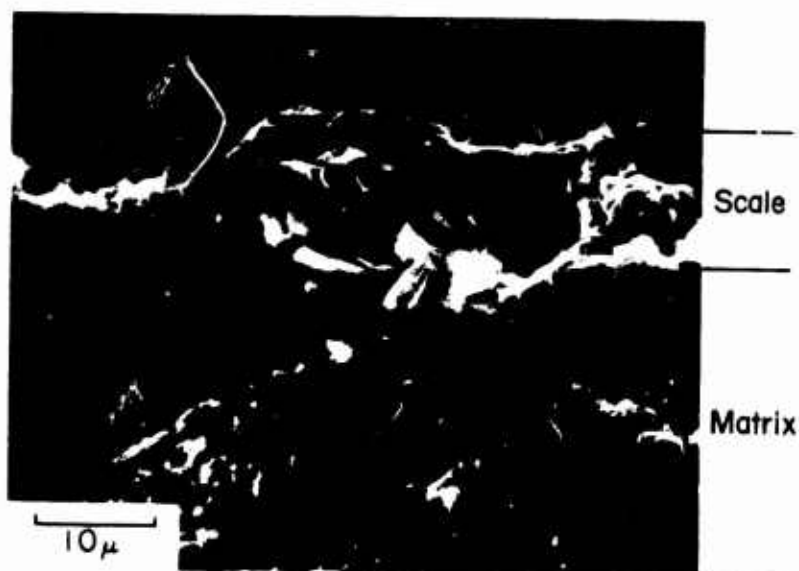


Figure 42. Scanning Electron Micrographs of the Scale Formed on  $\text{Si}_3\text{N}_4$  after 24 hr of Reaction in 300 torr  $\text{O}_2$  and 300 torr  $\text{N}_2$  at  $1400^\circ\text{C}$ .

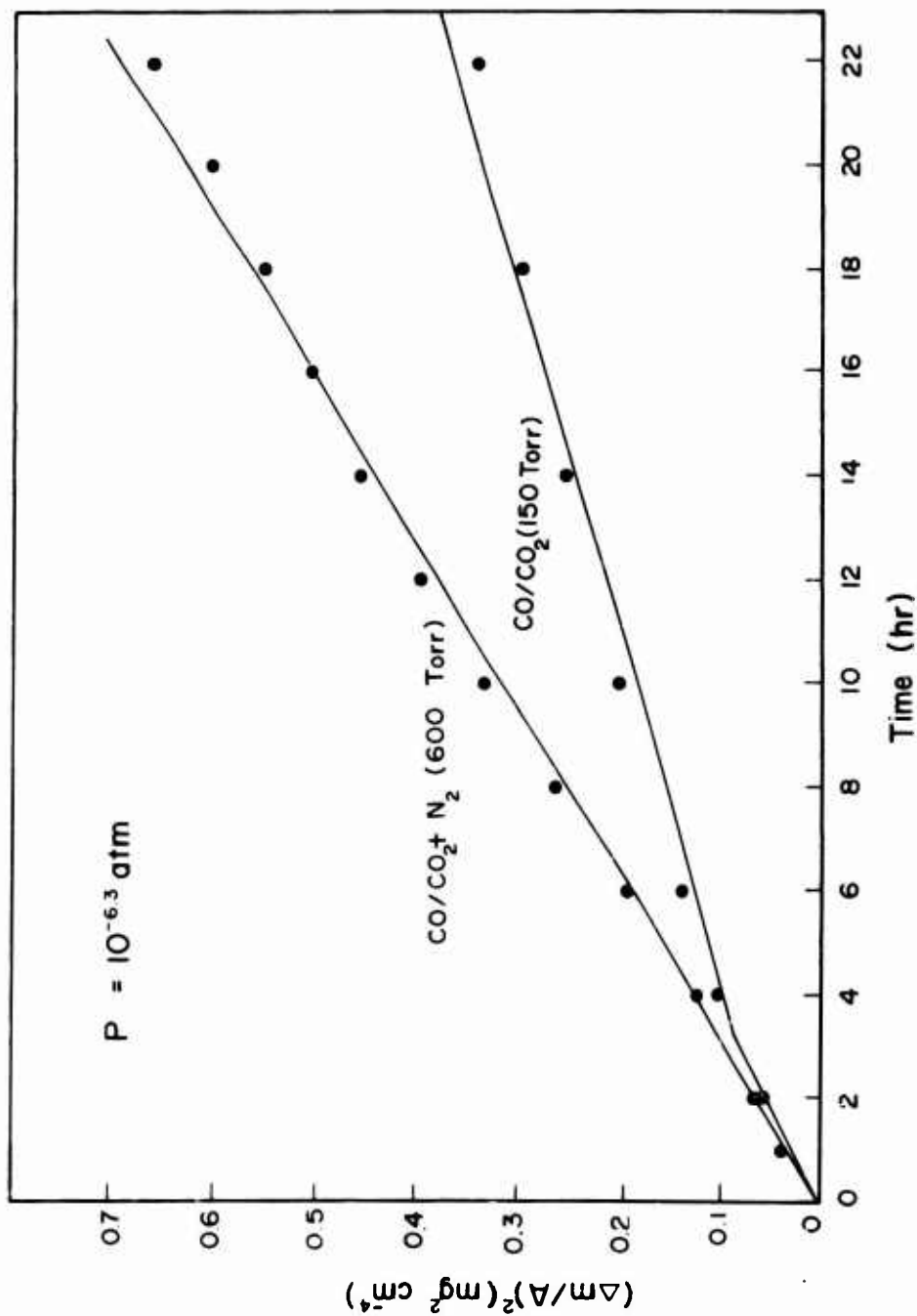
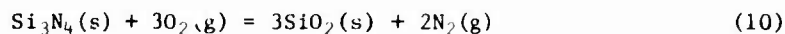


Figure 43. Parabolic Plot of Weight Change Data for  $\text{Si}_3\text{N}_4$  Oxidized at  $1400^\circ\text{C}$  in  $\text{CO}/\text{CO}_2$  and  $\text{CO}/\text{CO}_2/\text{N}_2$  Mixtures.

$P_{O_2} = 10^{-6.3}$  atm; as expected, an increase in rate was observed because the nitrogen is trapped in the scale. Scales formed in  $CO/CO_2 + N_2$  are shown in Figure 44.

#### Influence of $N_2$ on the Oxidation Behavior

In order to determine the amount of nitrogen retained in the scale upon oxidation, let us consider the stoichiometric oxidation reaction for  $Si_3N_4$  -- assuming for simplicity that  $MgO$  is present neither in the base material nor in the scale. The reaction can be written as



The measured weight change,  $m(ox)$  is related to the amount of oxygen gained and the amount of nitrogen lost by the equation

$$m(ox) = m(O_2) - (1-\alpha) m(N_2) \quad (11)$$

where  $\alpha$  is the fraction of nitrogen formed upon oxidation which is retained in the scale and  $m(O_2)$  and  $m(N_2)$  are, respectively, the weights of  $O_2$  and  $N_2$ . Two limiting cases of Equation (11) are readily apparent. When  $\alpha = 1$  (i.e., when all of the nitrogen formed upon oxidation is retained in the scale), the second term in Equation (11) vanishes and

$$m(ox) = m(O_2) \quad (12)$$

In the second case, when  $\alpha = 0$  (i.e., when all of the nitrogen formed upon oxidation escapes to the ambient), Equation (11) becomes

$$m(ox) = m(O_2) - m(N_2) \quad (13)$$

As an example of the second case (i.e., when all the  $N_2$  escapes), the following quantities can be calculated for every  $mg/cm^2$  gain in weight measured:

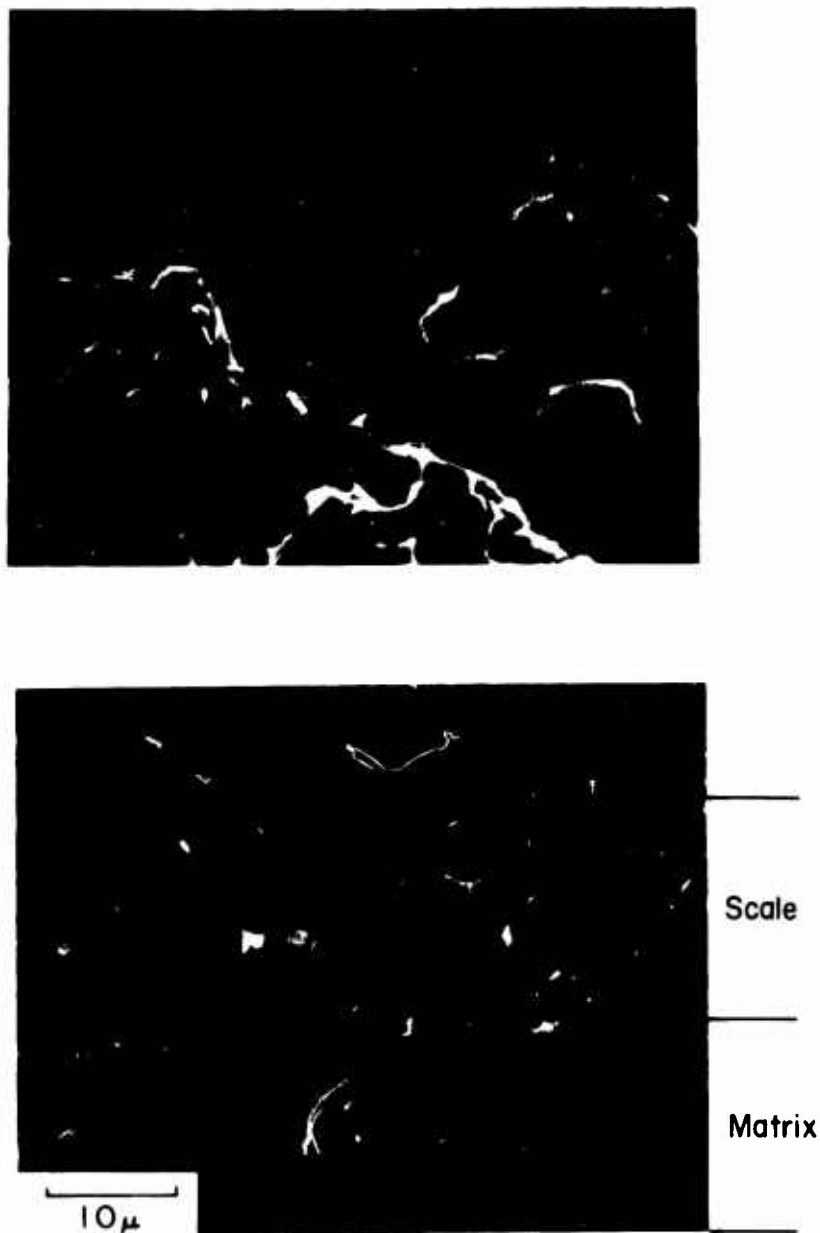


Figure 44. Scanning Electron Micrographs of the Scale Formed on  $\text{Si}_3\text{N}_4$  after 24 hr of Reaction in  $\text{CO}/\text{CO}_2 + \text{N}_2$  at  $1400^\circ\text{C}$  ( $\text{CO}/\text{CO}_2 = 150$  torr,  $\text{N}_2 = 450$  torr;  $P_{\text{O}_2} = 10^{-6}$  atm).

- 2.38 mg/cm<sup>2</sup> of O<sub>2</sub> is reacted.
- 1.38 mg/cm<sup>2</sup> of N<sub>2</sub> is released.
- 4.46 mg/cm<sup>2</sup> of SiO<sub>2</sub> is formed.
- 3.47 mg/cm<sup>2</sup> of Si<sub>3</sub>N<sub>4</sub> is consumed.

Therefore, for every mg/cm<sup>2</sup> of weight gain, the amounts of Si<sub>3</sub>N<sub>4</sub> consumed and SiO<sub>2</sub> formed are large.

In comparison to the first case (i.e., when all the N<sub>2</sub> formed is retained in the scale), a 1 mg/cm<sup>2</sup> gain in weight represents the following:

- 1 mg/cm<sup>2</sup> of O<sub>2</sub> reacted
- 0.58 mg/cm<sup>2</sup> of N<sub>2</sub> formed (and retained)
- 1.87 mg/cm<sup>2</sup> of SiO<sub>2</sub>
- 1.46 mg/cm<sup>2</sup> of Si<sub>3</sub>N<sub>4</sub> consumed

In reality, some N<sub>2</sub> will be retained and some lost (i.e., 0 < α < 1). The exact amount can be determined from scale etching experiments.

#### Scale Etching Experiments

From scale etching experiments, it is possible to measure the amount of nitride consumed and also the weight of the scale formed. Such measurements will enable calculation of the fraction of N<sub>2</sub> formed during oxidation which is retained in the scale. Let

- $m_0$  = weight of Si<sub>3</sub>N<sub>4</sub> sample before reaction
- $m_R$  = weight of sample and scale after reaction
- $m_f$  = weight of Si<sub>3</sub>N<sub>4</sub> remaining after scale etching
- $m(\text{ox})$  = measured weight gain recorded during oxidation (should agree with  $m_R - m_0$ )
- $m(\text{scale}) = m_R - m_f$  (determined by weighing oxidized sample and sample after removing scale)
- $m(\text{Si}_3\text{N}_4) = m_0 - m_f$  = nitride consumed in reaction
- $m(\text{O}_2)$  = oxygen consumed in reaction
- $m(\text{SiO}_2) = \text{SiO}_2$  formed during reaction
- $m(\text{N}_2) = \text{N}_2$  formed during reaction



$M(\text{Si}_3\text{N}_4)$  = molecular weight of  $\text{Si}_3\text{N}_4$

$M(\text{SiO}_2)$  = molecular weight of  $\text{SiO}_2$

$M(\text{N}_2)$  = molecular weight of  $\text{N}_2$

Since  $m(\text{Si}_3\text{N}_4)$  can be measured ( $= m_0 - m_f$ ), one can calculate the following quantities assuming the stoichiometric oxidation reaction [Equation (10)] to be valid:

$$m(\text{SiO}_2) = \frac{m(\text{Si}_3\text{N}_4)}{M(\text{Si}_3\text{N}_4)} \cdot 3M(\text{SiO}_2) \quad (14a)$$

$$m(\text{N}_2) = \frac{m(\text{Si}_3\text{N}_4)}{M(\text{Si}_3\text{N}_4)} \cdot 2M(\text{N}_2) \quad (14b)$$

$$m(\text{O}_2) = \frac{m(\text{Si}_3\text{N}_4)}{M(\text{Si}_3\text{N}_4)} \cdot 3M(\text{O}) \quad (14c)$$

Equation (11) can be solved for  $\alpha$ , the fraction of  $\text{N}_2$  trapped in the scale

$$\alpha = \frac{m(\text{ox}) + m(\text{N}_2) - m(\text{O}_2)}{m(\text{N}_2)} \quad (15a)$$

or, equivalently,

$$\alpha = \frac{m(\text{scale}) - m(\text{SiO}_2)}{m(\text{N}_2)} \quad (15b)$$

The results of the etching experiments are presented in Table II. A considerable amount of scatter in the data is apparent. The cause of the scatter is probably the large amounts of  $\text{MgSiO}_3$  present in the scales but not taken into account in the calculations. Columns 3 and 4 should agree because the data in both columns are supposedly a measurement of the net weight gained during reaction. However, the data presented in column 3,  $m(\text{ox})$  are from in situ balance measurements made at temperature. Whereas the data in column 4 are calculated from weighings made after the sample had been cooled to room temperature and consequently would be affected by any  $\text{N}_2$  loss due to scale cracking or spalling of the scale. The calculations in column 8 were made using the in situ weight data and those in column 9 from the before and after weighing. However, Table II does indicate that

TABLE II  
SCALE ETCHING EXPERIMENTS FOR CALCULATION OF PERCENT  $N_2$  RETAINED IN SCALES

Sample and Experimental Condition	(1) $m$ (Si $N_4$ ) *	(2) $m$ (scale)	(3) $m$ (ox)	(4) $m_K - m_O$	(5) $m(O)$	(6) $m(SiO_2)$	(7) $m(N_2)$	(8) $\% \times 100$ (Eq 15a)	(9) $\% \times 100$ (Eq 15b)
No. 108 75-torr O + 525-torr Ar 1400°C - 24 hr	2.632	3.547	0.900	0.957	1.805	3.384	1.053	14.0%	15.5
No. 107 150-torr O + 450-torr Ar 1400°C - 24 hr	2.658	3.615	1.085	0.957	1.823	3.417	1.063	30.5%	18.6
No. 109 300-torr O + 300-torr Ar 1400°C - 24 hr	2.686	3.640	1.075	0.953	1.842	3.453	1.074	28.5%	18.4
No. 114 150-torr O 1400°C - 24 hr	2.686	3.605	0.919	0.919	1.842	3.453	1.074	14.0%	14.1
No. 115 600-torr O 1400°C - 24 hr	2.833	3.823	1.065	0.991	1.943	3.642	1.133	22.5%	16.0
No. 116 150-torr O + 450-torr N 1400°C - 24 hr	2.333	3.353	1.053	1.020	1.599	2.999	0.933	41.4%	37.9

\* All mass quantities in units of mg cm<sup>-2</sup>

significant amounts of nitrogen are trapped in the scale. Because of the large amounts calculated, the nitrogen is probably in the dissolved form rather than in the gaseous state.

#### Summary and Conclusions

The high-temperature oxidation behavior of three forms of  $\text{Si}_3\text{N}_4$  was investigated--reaction-sintered  $\text{Si}_3\text{N}_4$ , hot-pressed Norton HS-110, and hot-pressed Norton HS-130. Of the three materials, the HS-130 displayed the best oxidation resistance; therefore, most experiments were conducted to characterize the oxidation behavior of this important high-temperature material. For HS-130 the oxidation kinetics were found to be diffusion controlled, and the activation energy was 69 kcal/mole below 1450°C. Above 1450°C relatively rapid kinetics were observed, even though the reaction remained diffusion controlled. The scales which formed consisted of  $\alpha$  cristobalite adjacent to the  $\text{Si}_3\text{N}_4$  matrix and  $\text{MgSiO}_3$  (enstatite) near the ambient scale interface. Scale morphologies were dependent upon temperature, oxygen partial pressure, and  $\text{N}_2$  content of the ambient. Scale etching experiments indicated that a large concentration of nitrogen is present in the scale, probably in the dissolved form.

## OXIDATION BEHAVIOR OF A Si-SiC COMPOSITE

Considerable work is in progress<sup>(32-34)</sup> to determine the feasibility of using ceramic-fiber-reinforced ceramics to overcome the problems that arise when attempts are made to employ brittle ceramic materials where mechanically and thermally induced tensile loads are experienced. To date, dense SiC and Si<sub>3</sub>N<sub>4</sub> are among the leading candidate materials for such high-temperature structural applications. It may be hypothesized that through the incorporation of a suitable second phase dispersion or fiber of one ceramic into a dense matrix of a suitable recipient ceramic, both the fracture energy and strength increase. In addition, if the solute ceramic involved exhibits greater thermal conductivity, the thermal conductivity of the resulting composite may be significantly greater than that of the matrix or solvent ceramic. Fracture energies of many ceramics have been increased,<sup>(32,33)</sup> often however without increase in room-temperature strength, and improvements in the high-temperature strength and thermal conductivity have also been obtained. Even with the attainment of improved mechanical properties by use of composites, investigations must be performed to determine whether the oxidation characteristics of the composite are satisfactory. The following is a brief report on studies of the oxidation characteristics of a Si/SiC composite provided by Dr. W. B. Hillig of The General Electric Company, Schenectady, New York.

### Experimental

The composite consisted of SiC braid in a Si matrix, and the as-received specimens were rectangular coupons with dimensions 1 x 0.5 x 0.1 cm. The direction of the SiC braid was approximately normal to the main faces of the coupon. A suspension hole was drilled ultrasonically through the coupons, which were then abraded through 600-grit SiC paper and cleaned ultrasonically. Dimensions and specimen weights were recorded and the sample degreased with alcohol and dried prior to insertion into the thermobalance.

The oxidation kinetics were studied by continuous gravimetric measurements on an Ainsworth Series-1000 Electrobalance. The tests were performed in flowing bottled oxygen ( 100 cc/min) at 150 torr total pressure in the temperature range 1200-1500°C. Exposure times were generally on the order of 100 hr. The use of a side-arm insertion-retrieval arrangements facilitated direct lowering of the specimen into the test environment and, upon completion of the test, rapid removal and cooling. In addition to conventional weight change measurements, oxygen-consumption techniques for measuring weight change plus condensable vapor species were employed. (11,20-22)

The oxidized samples and reaction products were characterized by means of x-ray diffraction techniques, metallographic examination, scanning electron microscopy (SEM), and electron-microprobe analysis.

#### Materials Characterization

The as-received composite was characterized via x-ray diffraction and electron-microprobe analysis. Diffraction results indicated predominantly Si and  $\alpha$ -SiC; in addition, a hump between 14 and 25° (2 $\theta$ ) was indicative of amorphous silica, and a series of unidentifiable weak peaks appeared between 38 and 43° (2 $\theta$ ). Electron-microprobe analysis indicated the presence of impurity levels of Al and Fe associated with the regions immediately adjacent to the SiC fibers, with an order of magnitude greater concentration of these elements in these areas than in the Si matrix.

The macroscopic appearance of the composite coupons is shown in Figure 45 (note the gross nature of the composite). The individual SiC braid bundles (appearing as dark annuli) are 1 mm in diam, composing about 60% of material volume.

Figure 46 presents optical micrographs of the matrix microstructure in the as-received condition; the silica parent matrix is the smooth bright region on the right.

Figure 47 shows SEM micrographs of a fracture surface of as-received material in a  $\beta$ -braid region. The channels, which extend to the specimen



Figure 45. Macroscopic Appearance of Composite Coupons Used in Oxidation Studies.

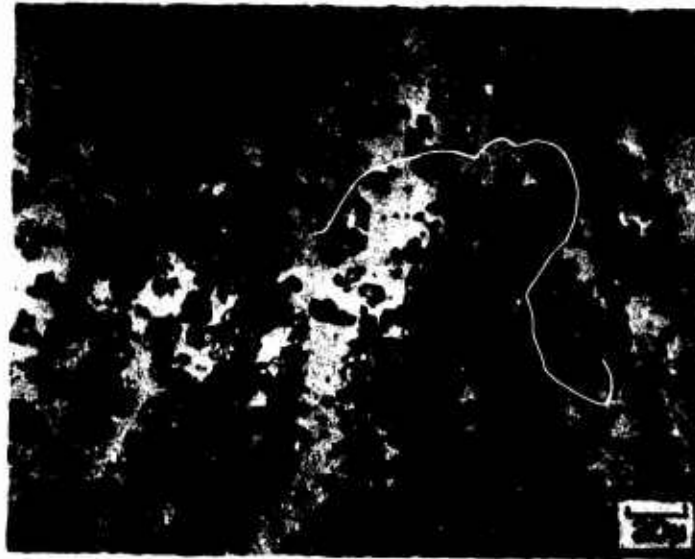
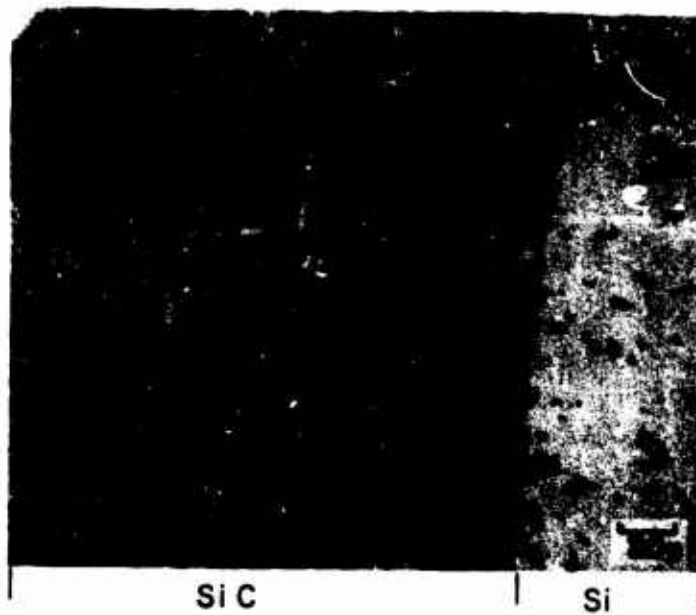


Figure 46. Optical Micrographs of a Cross Section of Composite Coupon Showing Si Matrix (Light Region on the Right) and SiC Fiber Region.

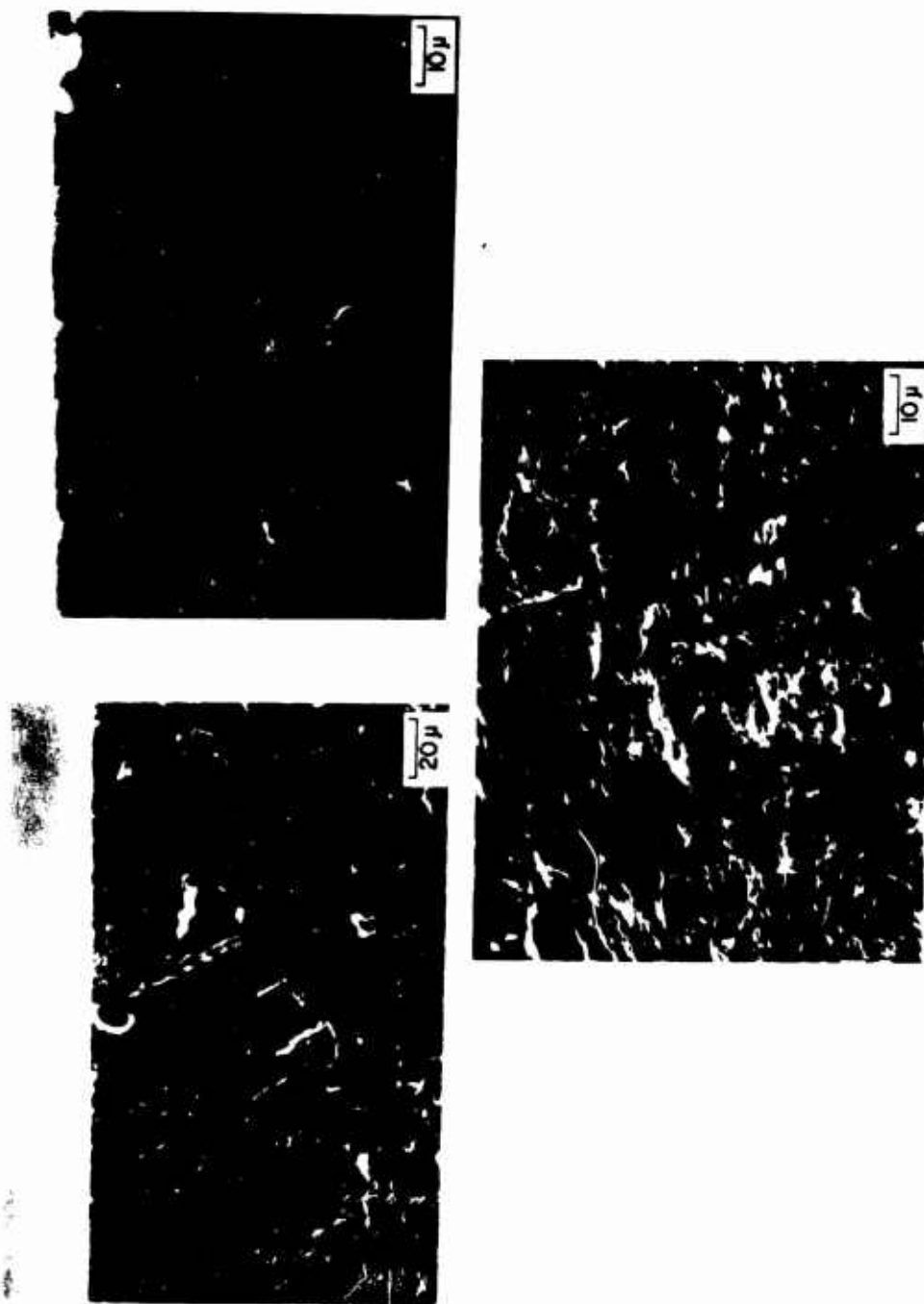


Figure 47. Fracture Surface of As-Received Composite in SiC Fiber Region.



surface, are assumed to result from the tearing out or fracture of individual fibers comprising the SiC braid. Figure 48 shows the SiC braid/Si matrix interface of a fractured sample; the Si is the smooth region on the left-hand side of the micrograph.

X-ray images of the as-received material are shown in Figure 49. The smooth central region is the Si; the SiC braid is on either side. Appreciable impurity levels of Fe and Al were found to be associated with the SiC fibers.

### Results and Discussion

The oxidation kinetics of the material in terms of weight change per unit surface area as a function of exposure time are represented in Figure 50 in the temperature range 1200-1500°C. Figure 51 is a parabolic plot of the weight gain as a function of time to elucidate any conformance to parabolic kinetics. Excellent parabolic kinetics were displayed at all temperatures after an apparent induction period of ~ 2-3 hr. In the initial seconds of the reaction, a large weight loss was exhibited by all samples.

Included in Figures 50 and 51 are data from oxygen-consumption measurements made at 1400 and 1500°C. At 1400°C no appreciable condensable vapors were apparent. In reality, the oxygen consumption was lower than the apparent weight change; this was assigned to experimental error (probably due to sample variations) and it is concluded that no appreciable vapor loss was occurring. However, at 1500°C a significant amount of condensate was measured (probably condensation of Si vapor, since the melting point of Si is 1410°C). The accelerated nature of oxidation at 1500°C and subsequent metallographic examination suggest an increasing loss of integrity of the matrix-fiber interface at this temperature. The oxidation rate for the composite was considerably greater than that of either pure compact Si or SiC. Figure 52 presents the parabolic rate constants for oxidation of the Si/SiC composite as a function of  $1/T$  compared to those for Si and SiC, described elsewhere in this report. The activation energy obtained from an Arrhenius plot was 40.1 kcal/mole, which is near the value of 28 kcal/mole reported



Figure 48. Fractured Composite Sample in Region of Si/SiC Interface (Si is Smooth Region on the Left).

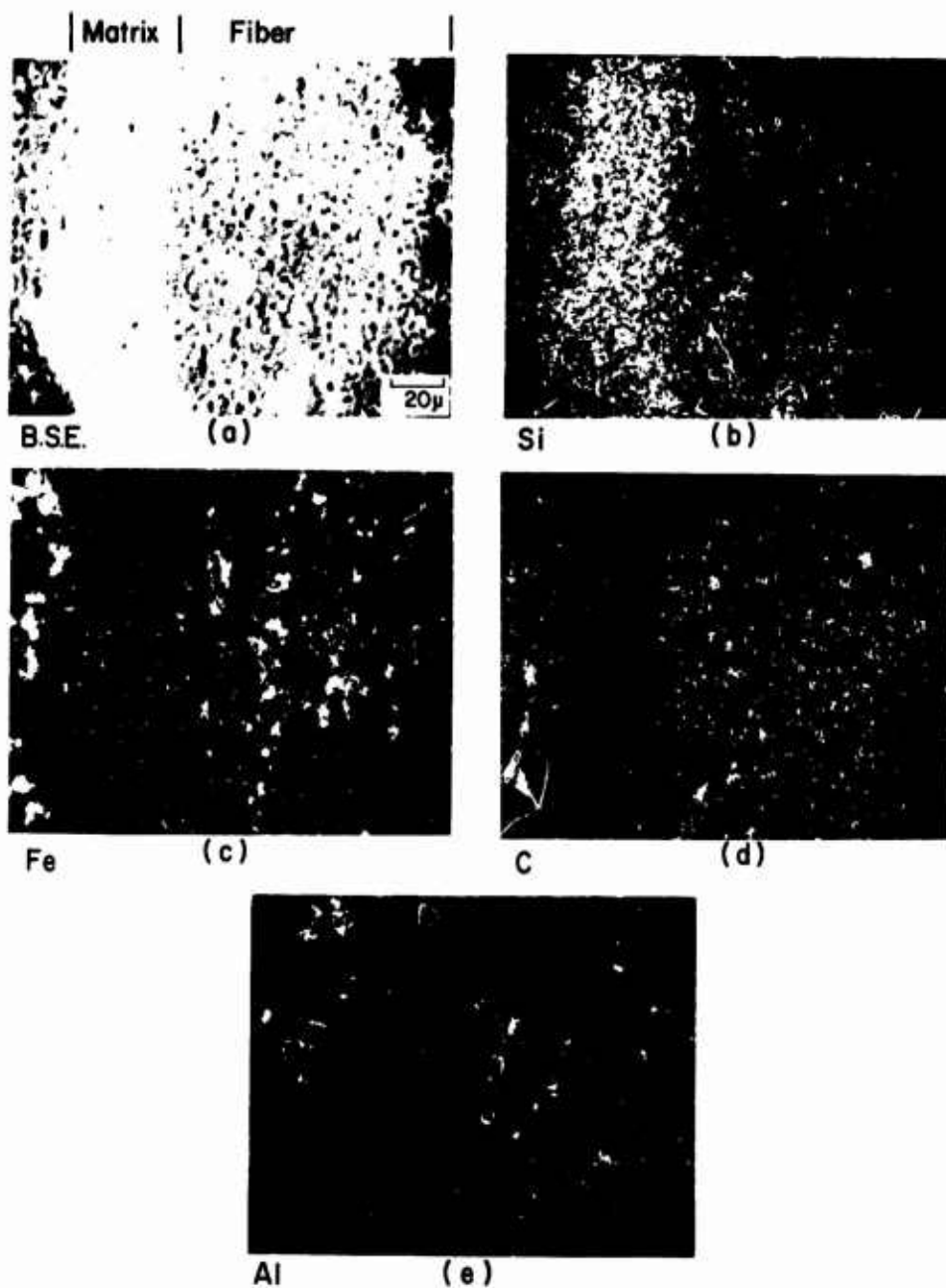


Figure 49. Microprobe X-Ray Scans of Cross Section of As-Received Composite Material.

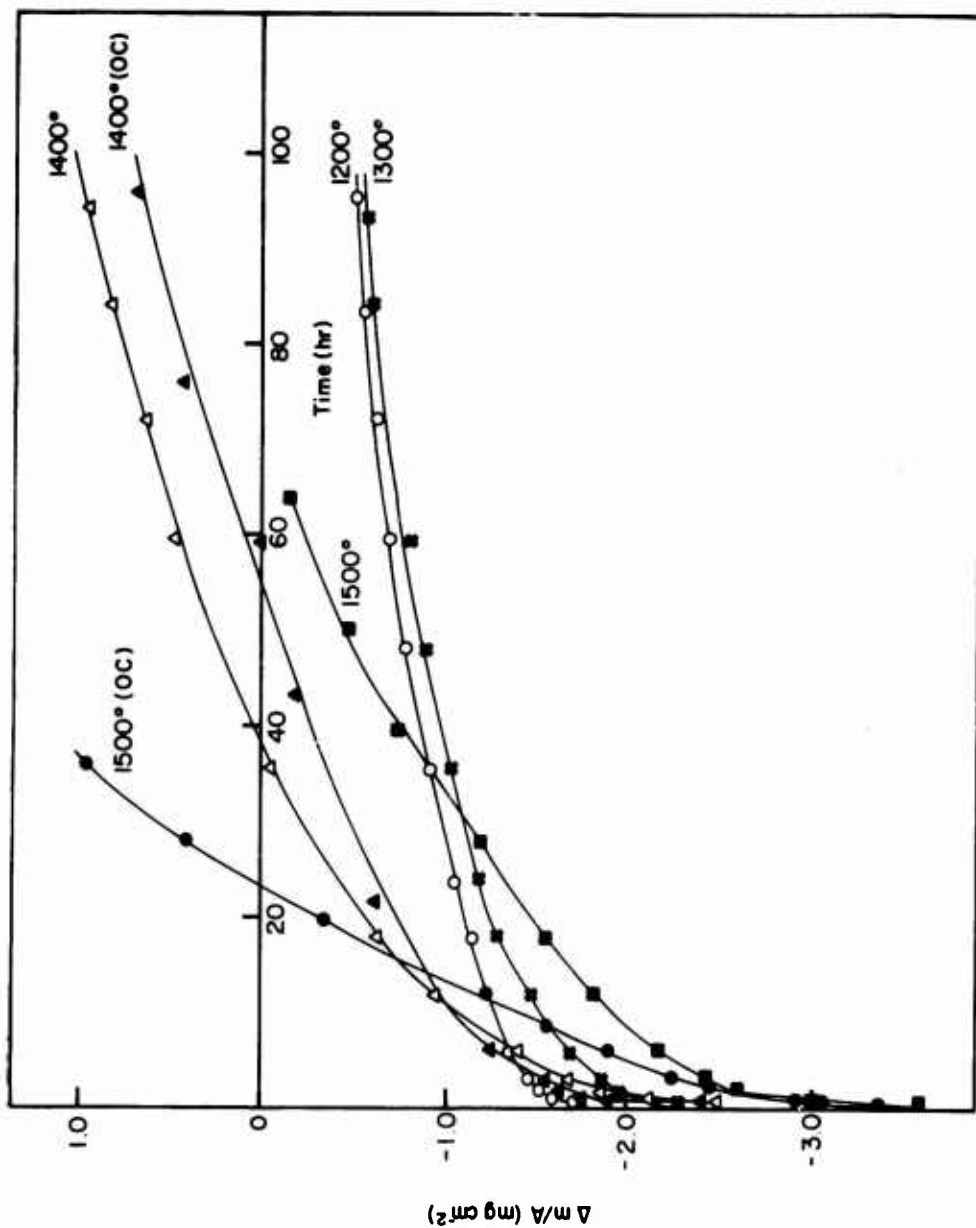


Figure 50. Observed Sample Weight Gain and Oxygen Consumption (OC) as a Function of Exposure Time during Oxidation of Si/SiC Composite at Various Temperatures in Pure Flowing  $\text{O}_2$  at an Ambient Pressure of 150 torr.

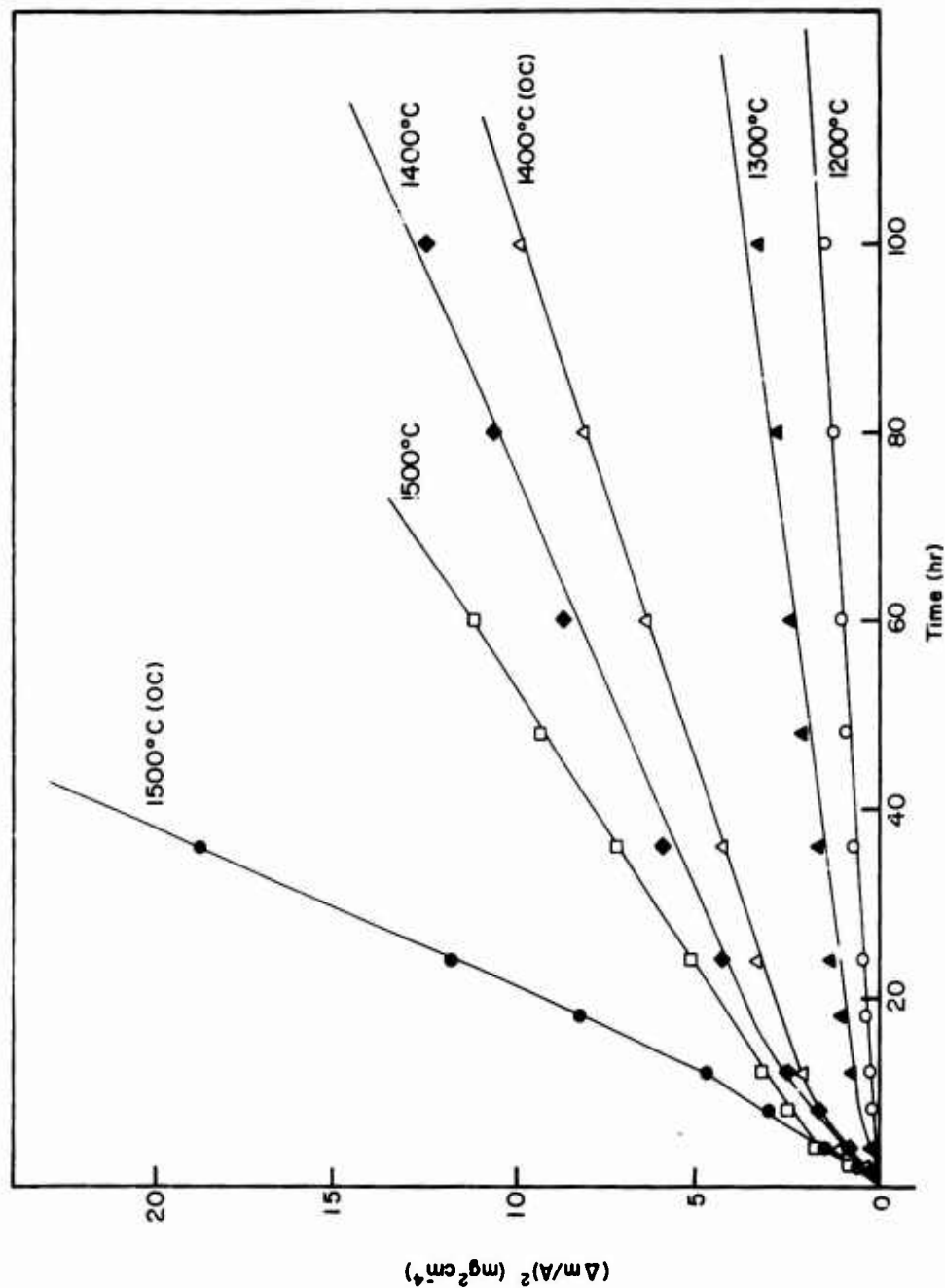


Figure 51. Parabolic Plot of Sample Weight Change and Oxygen Consumption (OC) as a Function of Exposure Time during Oxidation of Si/SiC Composite at Various Temperatures in Pure Flowing  $O_2$  at an Ambient Pressure of 150 torr.

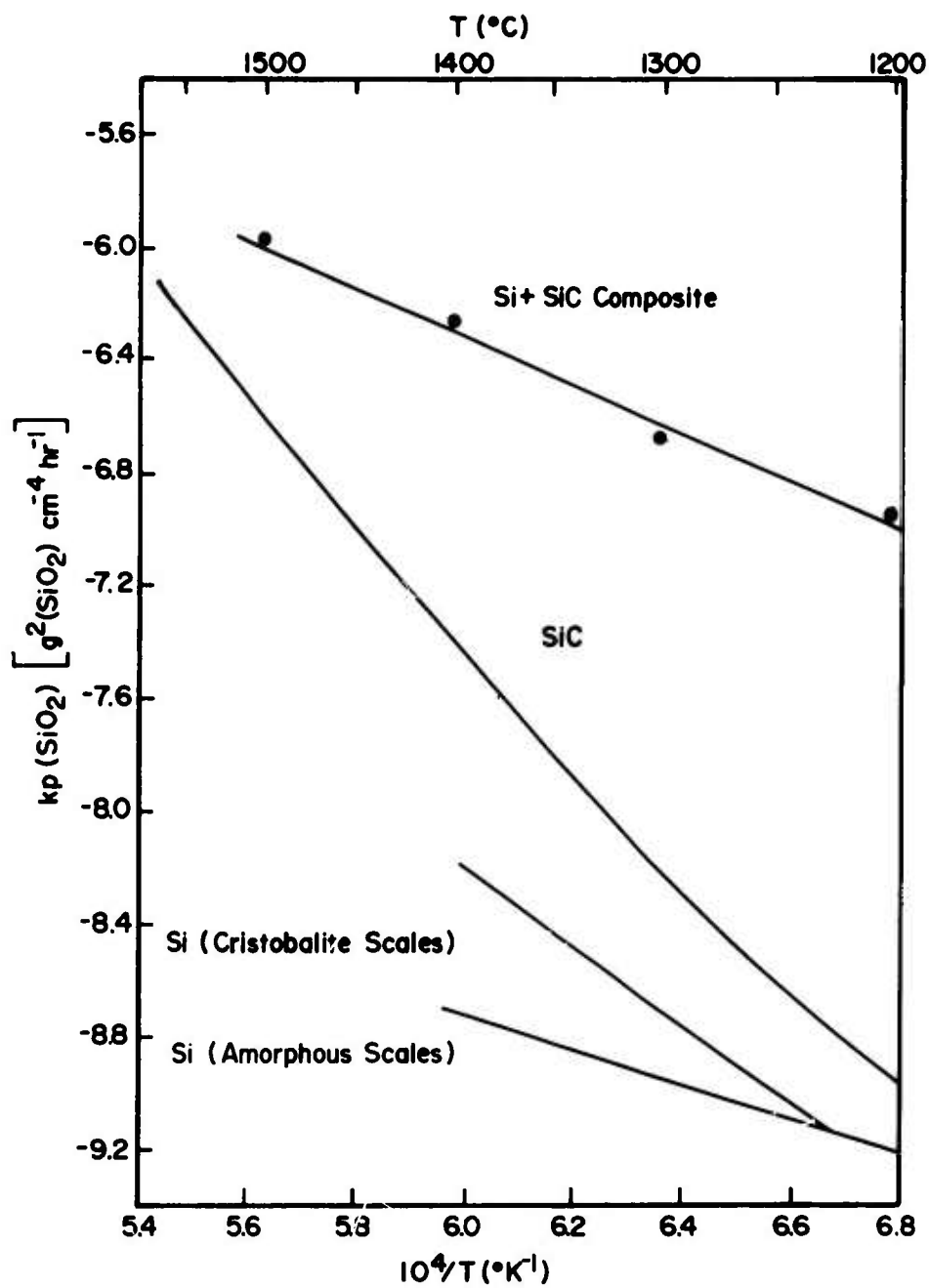


Figure 52. Arrhenius Plot of the Scaling-Rate Constant for the Si+SiC Composite Compared with Si and SiC.

for Si when amorphous  $\text{SiO}_2$  scales are formed, but lower than that for hot-pressed SiC.

X-ray diffraction of the oxidized samples revealed the presence of only  $\alpha$ -cristobalite in the scale; the amorphous hump and the unidentified peaks between  $38$  and  $43^\circ$  ( $2\theta$ ) had disappeared, and no oxycarbides or silicates were present. The scales formed on the composite were dense and very adherent as might be expected from the protective kinetics, even for extended exposure times.

Figure 53 is a fracture cross section of the oxide scale and matrix after exposure at  $1200^\circ\text{C}$  for 100 hr. The compactness and adherence of the scale are self-evident. The difference in oxidation rates of the Si and SiC regions under these conditions is apparent. The different oxidation rates of the Si and SiC regions are displayed more clearly in Figure 54(a) and (b); the specimen was oxidized at  $1400^\circ\text{C}$  for 70 hr. The increased thickness of the oxide scale over the SiC braid relative to the Si region is evident, and the oxide scale is apparently compact [Figure 54(c)]. Electron-microprobe analysis of a cross section of a specimen oxidized at  $1200^\circ\text{C}$  is presented in Figure 55. The Fe and Al in the braid (right-hand side) and the segregation of these elements into the oxide scale are apparent.

The preceding micrographs and microprobe analysis were typical for oxidized specimens exposed in the temperature range  $1200$ – $1400^\circ\text{C}$ . At  $1500^\circ\text{C}$  there were regions of very nonuniform scale thickness and matrix degradation. The remaining figures show specimens which were oxidized at  $1500^\circ\text{C}$  in an attempt to elucidate further localized degradation of the matrix. Figure 56 presents macrographs of specimens exposed at  $1500^\circ\text{C}$  for (b) 12 min and (c) 20 hr as compared to one exposed at  $1400^\circ$  for (a) 50 hr; the increased attack of the material at  $1500^\circ\text{C}$  is evident. The bubbles in Figure 56(b) are evidence of the early evolution of liquid Si and its vaporization at this temperature, as confirmed by the condensable vapor technique and elemental analysis. For longer exposure times, when an  $\alpha$ -cristobalite layer covers the specimen, the eruptions were less in evidence. The surface

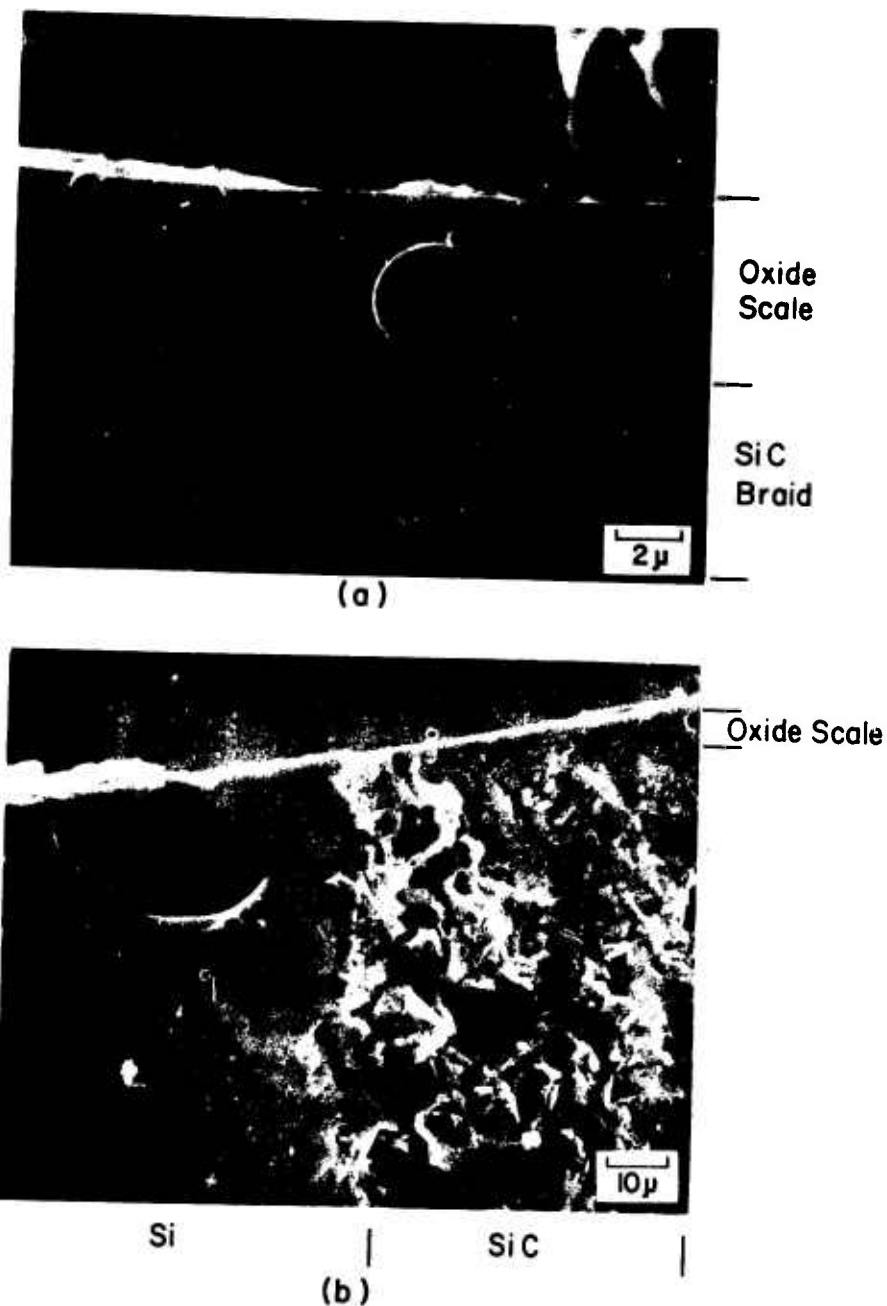


Figure 53. Microstructure of Cross Section of Composite after 100 hr Exposure at 1200°C. (a) Oxide Scale over SiC Braid Region. (b) Oxide Scale in Region of Si/SiC Interface (Si is Smooth Region on Left).



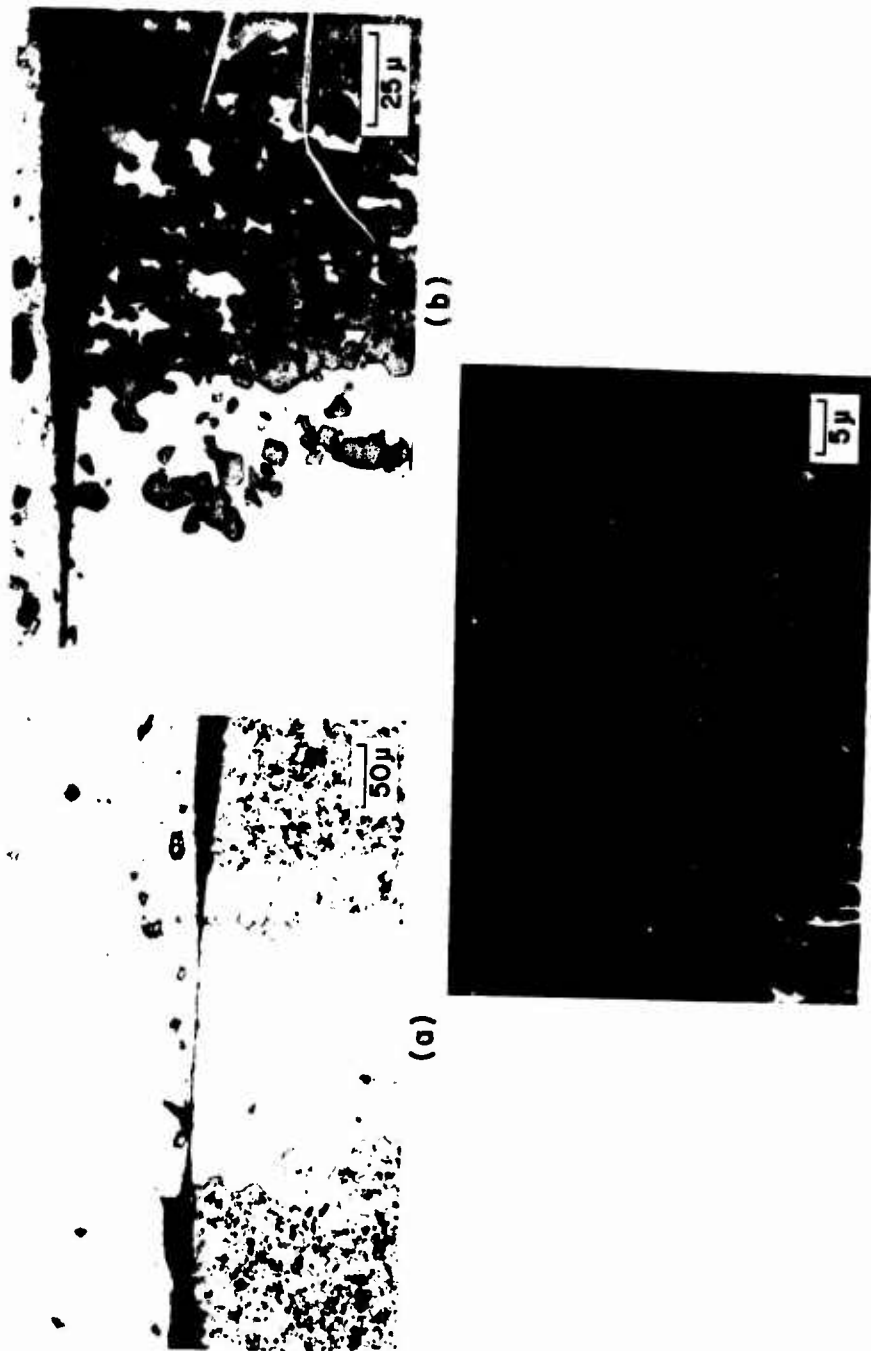


Figure 54. Microstructure of Cross Section of Composite Oxidized at 1400°C for 100 hr. (a) and (b) Optical Micrographs of Oxide Scale over Si/SiC Regions. (c) Fracture Surface of Oxide Scale over SiC Region.



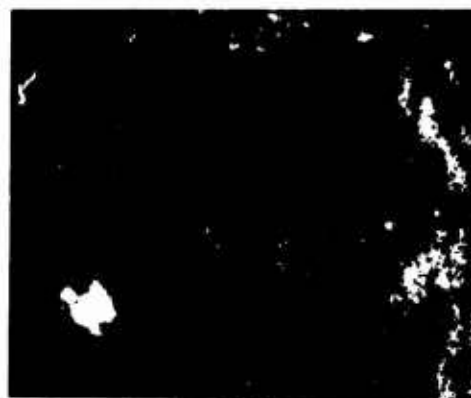
B.S.E. (a)



Si (b)



C (c)



Fe (d)



Al (e)

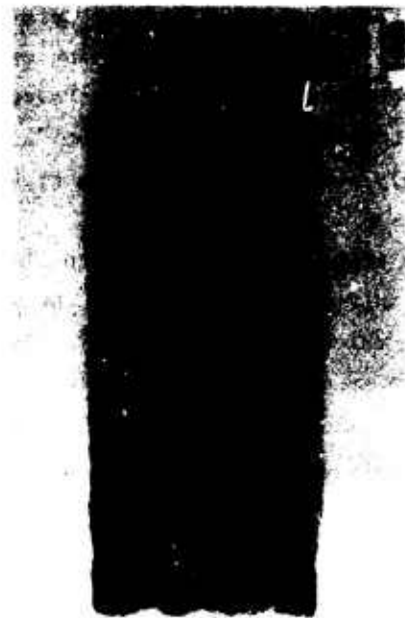
Figure 55. Cross Section of Composite Oxidized at 1200°C for 100 hr.



1400°C, 70hr.  
(a)



1500°C, 12 min.  
(b)



1500°C, 20hr  
(c)

Figure 56. Macrographs of Surface Topography of Composite Coupons Oxidized at 1400°C and 1500°C.

of this specimen is shown at higher magnification in Figure 57, and the molten nature of many regions and evidence of gaseous evolution can be observed. The scale formed at 1500°C is much less uniform and compact and the matrix surface more irregular than following exposure at lower temperatures. The comparative maximum scale thickness over the SiC braid was 6-8  $\mu$  at 1200°C and 30-35  $\mu$  at 1500°C. The apparent "sealing" of the fiber channels is increasingly evident at 1500°C (see Figure 58).

X-ray images of a cross section of a sample oxidized at 1500°C are presented in Figures 59 and 60 for two regions displaying uniform and irregular scale thickening, respectively. As found previously in the lower-temperature specimens, segregation of the Fe and Al to the surface and into the silica scale has occurred. Figure 61 presents evidence at 1500°C that some localized preferential oxidation of SiC fibers may be occurring in the matrix immediately above the fiber tips, with oxide scale penetration to the channel tip vacated by the SiC fiber on fracture. Confirmation of the presence of SiO<sub>2</sub> at the channel tip was provided by soft x-ray spectra analysis of Si, which can be used to determine the oxidation state and the chemistry of the species involved (discussed in final section of this report).

#### Summary and Conclusions

The oxidation kinetics of the composite material, in general, obeyed a parabolic rate law in the temperature range 1200-1500°C in pure flowing oxygen. The oxidation resistance of the material was appreciably inferior to that of either Si or SiC, the rate constant for the composite was more than an order of magnitude higher than that for Si or SiC. However, the activation energy was significantly lower than that for hot-pressed SiC. An explanation for the higher oxidation rate of the composite is not immediately available. The behavior may arise from modification of the chemical potentials of the reactive species (with subsequent effect upon material transport phenomena) or the presence of Al and Fe impurities in the SiC fibers (with subsequent effect upon the morphology and growth mechanism of the silica scale). Alternatively, the behavior may result from an inherent characteristic of the microstructure of composite materials. The observed



Reproduced from  
best available copy.



Figure 57. Surface Topography of Composite Oxidized at 1500°C for 20 hr.



Figure 58. Fracture Surface of Composite after Oxidation at 1500°C for 20 hr Showing Fiber Pullout and Apparent "Sealing" of Fiber Tip.

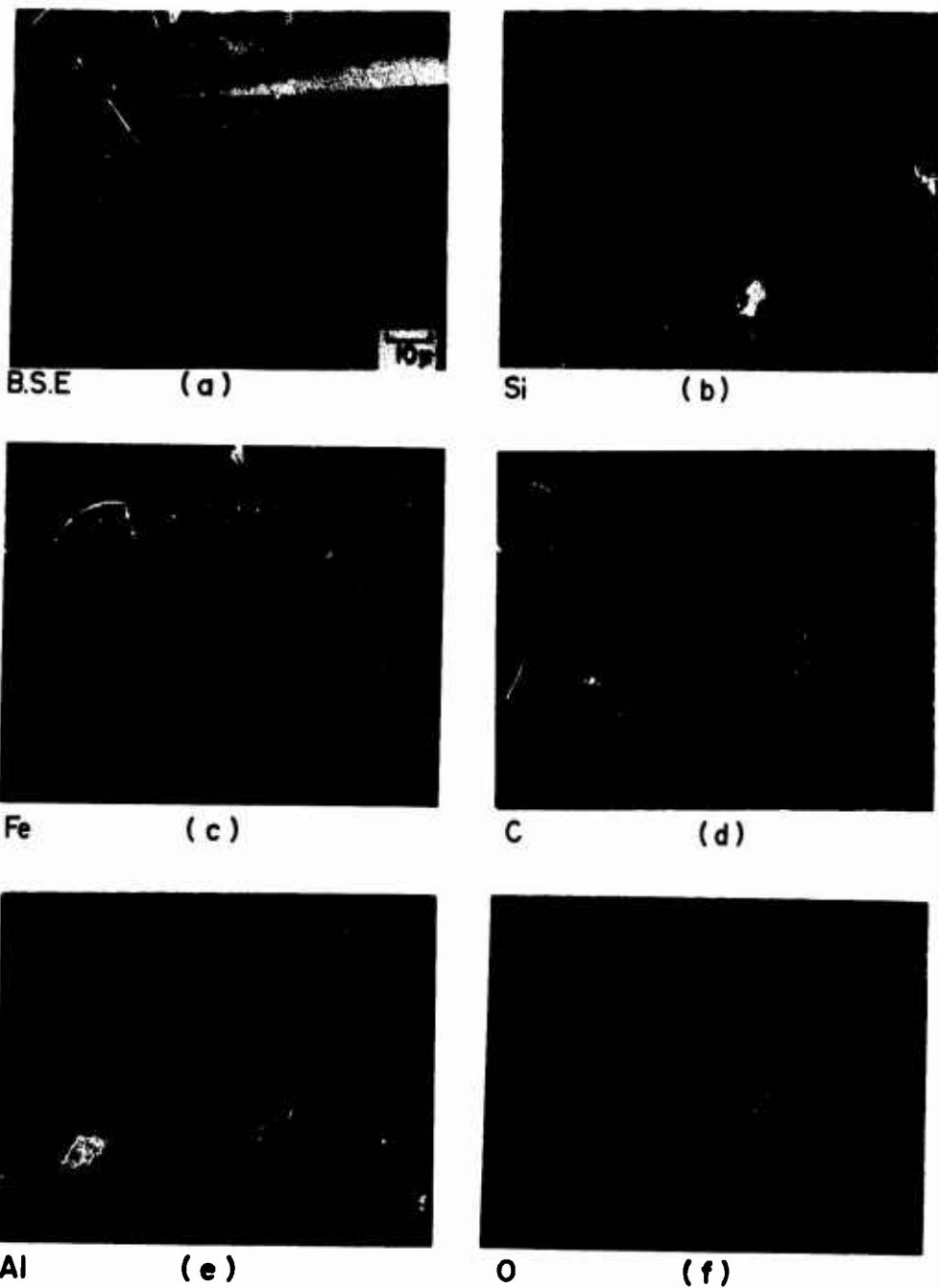


Figure 59. Cross Section of Composite Oxidized at 1500°C for 20 hr.

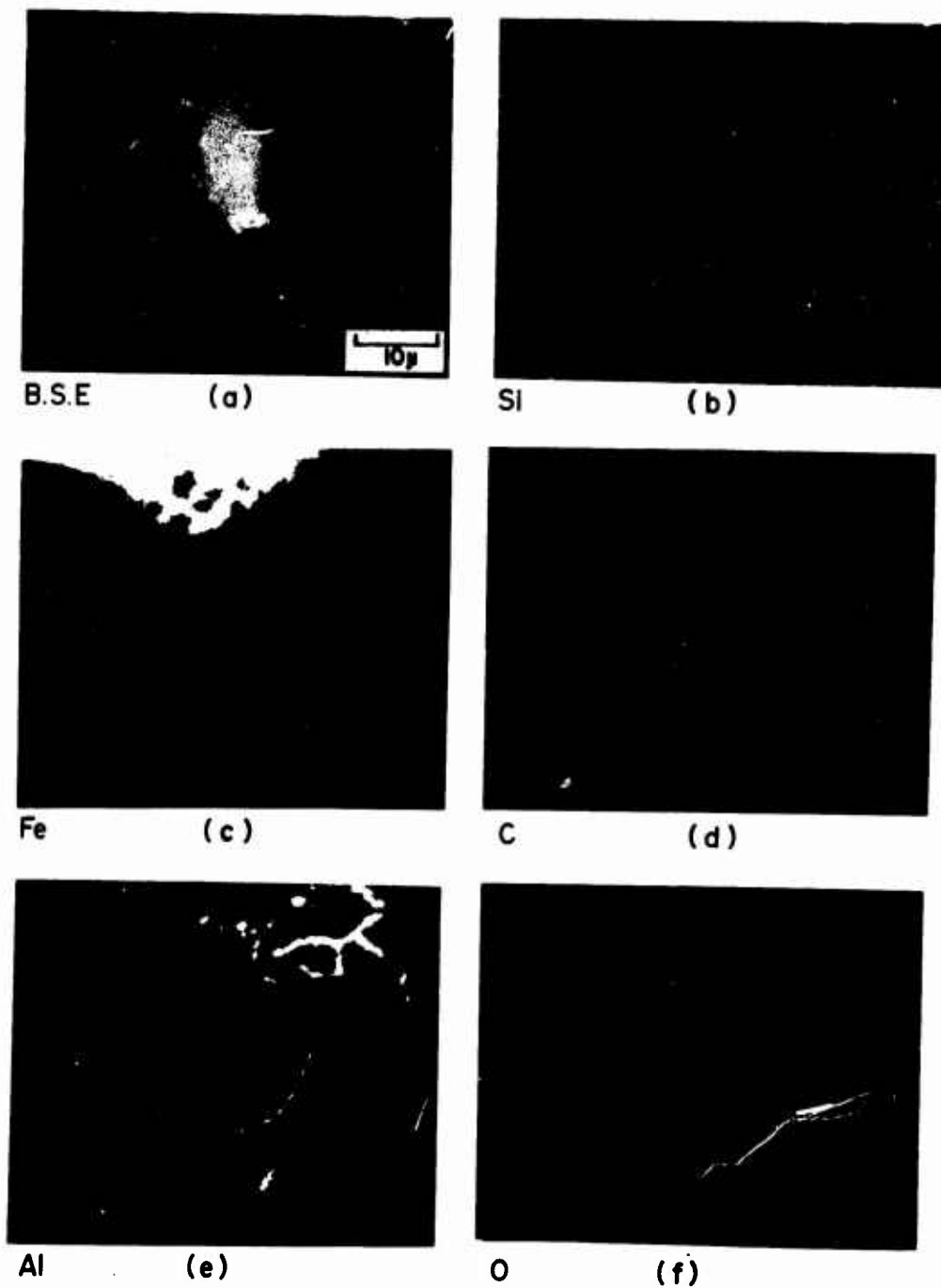


Figure 60. Cross Section of Composite Oxidized at 1500°C for 20 hr.



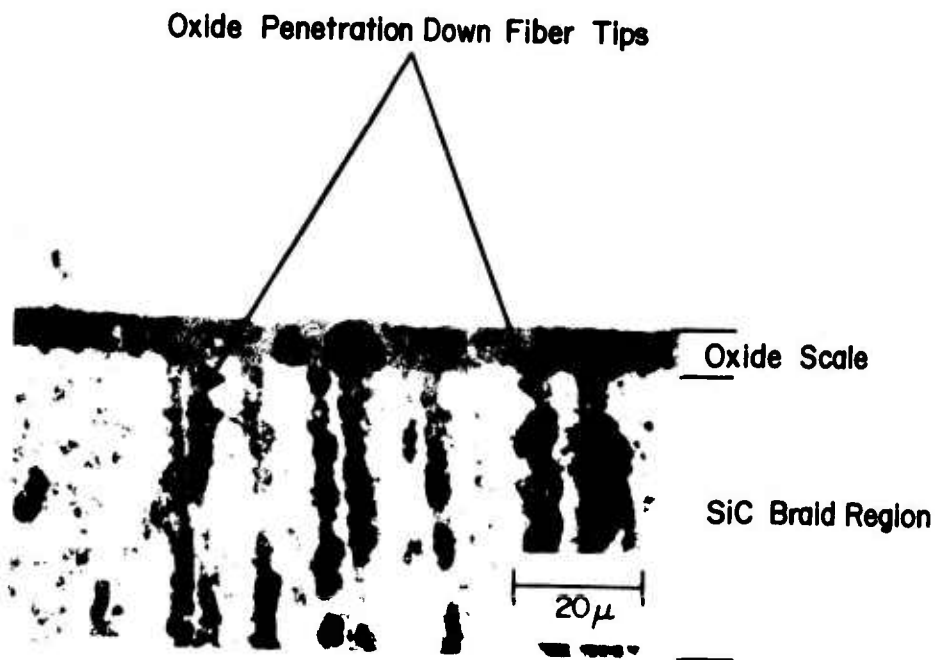


Figure 61. Optical Micrograph of Cross Section of Composite Coupon Oxidized at 1500°C for 20 hr, Showing Evidence of Oxidation Penetration above SiC Fiber Channels.

difference in thickness of the silica layer formed over the Si and SiC regions may be explainable on the basis of impurity effects in the SiC. It was found that impurity levels of Fe and Al were present in the SiC fibers of the as-received material; and, upon oxidation, appreciable segregation of these elements into the growing oxide scale was observed. Only  $\alpha$ -cristobalite could be identified from the x-ray diffraction patterns, no silicates were in evidence.

Integrity of the composite material was maintained up to 1400°C; in excess of this temperature, molten Si was evolved, and accelerated degradation of the matrix ensued. However, even at 1500°C no widespread degradation of the matrix material was observable after a 100 hr exposure.

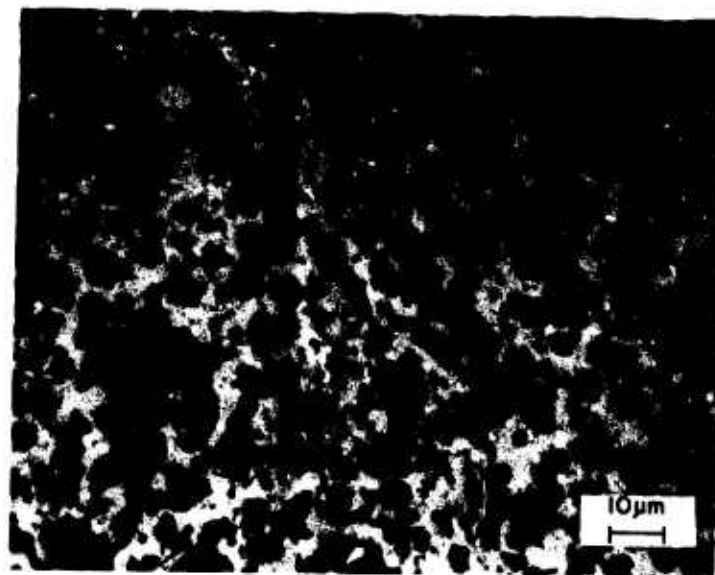
Further work must be performed before a full understanding of the effects of Fe and Al impurities in the matrix on the growth mechanism and morphology of a silica scale<sup>(35-37)</sup> can be gained.

#### OXIDATION OF SiC-MULLITE COMPOSITES

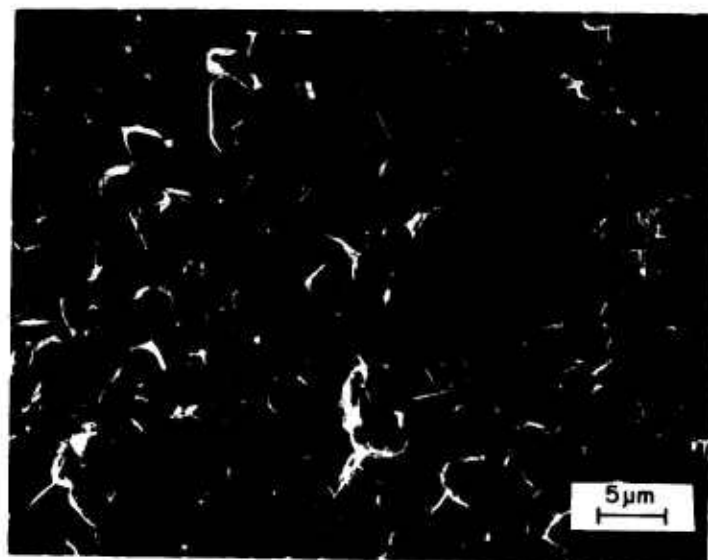
In the present investigation the oxidation behavior of SiC + 3 w/o mullite and SiC + 20 w/o mullite composites was investigated. This study was one part of the work unit, the aim of which was to gain a working knowledge of various composites through the investigation of their high-temperature oxidation behavior. The materials evaluated to date include Si/SiC and Si<sub>3</sub>N<sub>4</sub> modified with (SiO<sub>2</sub> + C).

#### Experimental

The composites were obtained from R. L. Crane at the Air Force Materials Laboratory. Two compositions were studied--silicon carbide with 3 w/o and 20 w/o additions of mullite. These composites were formed as an intimate mixture of small particle size powder by hot pressing. Figure 62 indicates the microstructural appearance of the as-received composite (a) in the optical metallograph and (b) on the scanning electron microscope (SEM). Samples were prepared as rectangular coupons (1 x 0.5 x 0.1 cm), abraded through 600-grit SiC paper, and ultrasonically cleaned in



(a)



(b)

Figure 62 . Optical Micrograph (a) and SEM Micrograph (b) of "As-Received" Composite Material, SiC-20 w/o Mullite.

acetone and methanol. Dimensions and weights were obtained prior to insertion in an Ainsworth Series-1000 Electrobalance. The tests were performed over the temperature range 1300°-1575°C in flowing pure oxygen [100 cm<sup>3</sup>/min(STP)] at system pressure of 150 torr for exposure times of the order of 70-100 hr. The oxidized samples and reaction products were characterized by x-ray diffraction techniques, metallographic examination, scanning electron microscopy, and electron microprobe analysis.

### Results and Discussion

Both compositions oxidized according to a parabolic rate law between 1300 and 1570°C. The kinetic curves are presented in Figures 63 and 64. In general the SiC-3 w/o mullite oxidized at a lower rate than the 20 w/o composition. An Arrhenius-type plot is shown in Figure 65 for the two materials. The activation energies for oxidation were nearly equal for the two materials-- ~ 80-90 kcal/mole.

Table III presents the weight gain per unit surface area observed in a 24 hr exposure for the composites and for SiC and Si<sub>3</sub>N<sub>4</sub>.

TABLE III

WEIGHT GAIN PER UNIT SURFACE AREA FOR SiC + 3 w/o MULLITE AND SiC + 20 w/o MULLITE COMPARED TO Si AND NORTON HS-130 Si<sub>3</sub>N<sub>4</sub>

[24 hr (mg cm<sup>-2</sup>) in flowing pure O<sub>2</sub>, 150 torr]

T(°C)	SiC	Si <sub>3</sub> N <sub>4</sub>	SiC 3 w/o mullite	SiC 20 w/o mullite
1300	0.12	0.42	0.41	0.63
1400	0.35*	0.83	1.36	1.88
1500	0.78*	3.80	2.09	2.87

\* Data for SiC and Si<sub>3</sub>N<sub>4</sub> presented elsewhere in this report.

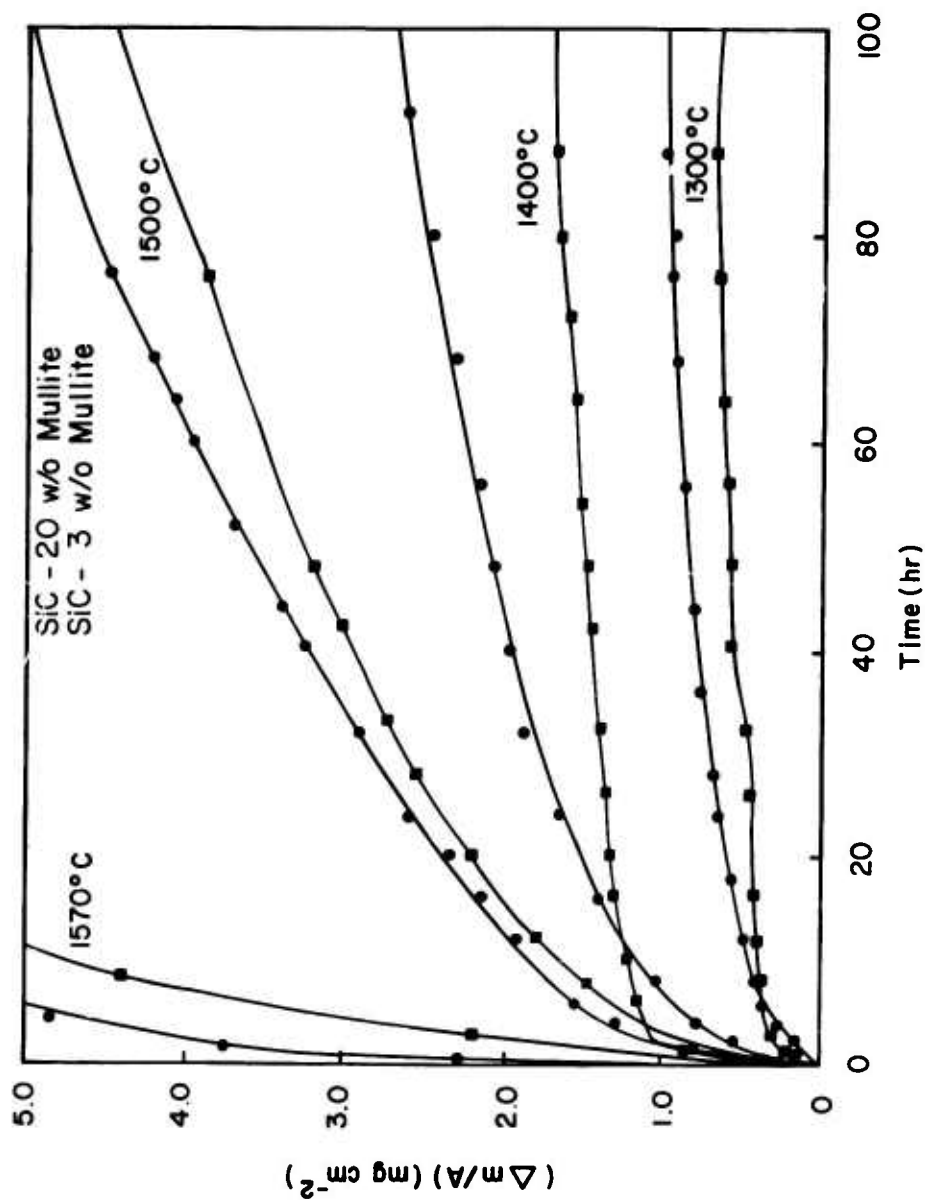


Figure 63. Observed Weight Change as a Function of Exposure Time During Oxidation of SiC-Mullite Composites at Various Temperatures in Pure Flowing  $O_2$  (Total Pressure = 150 torr).

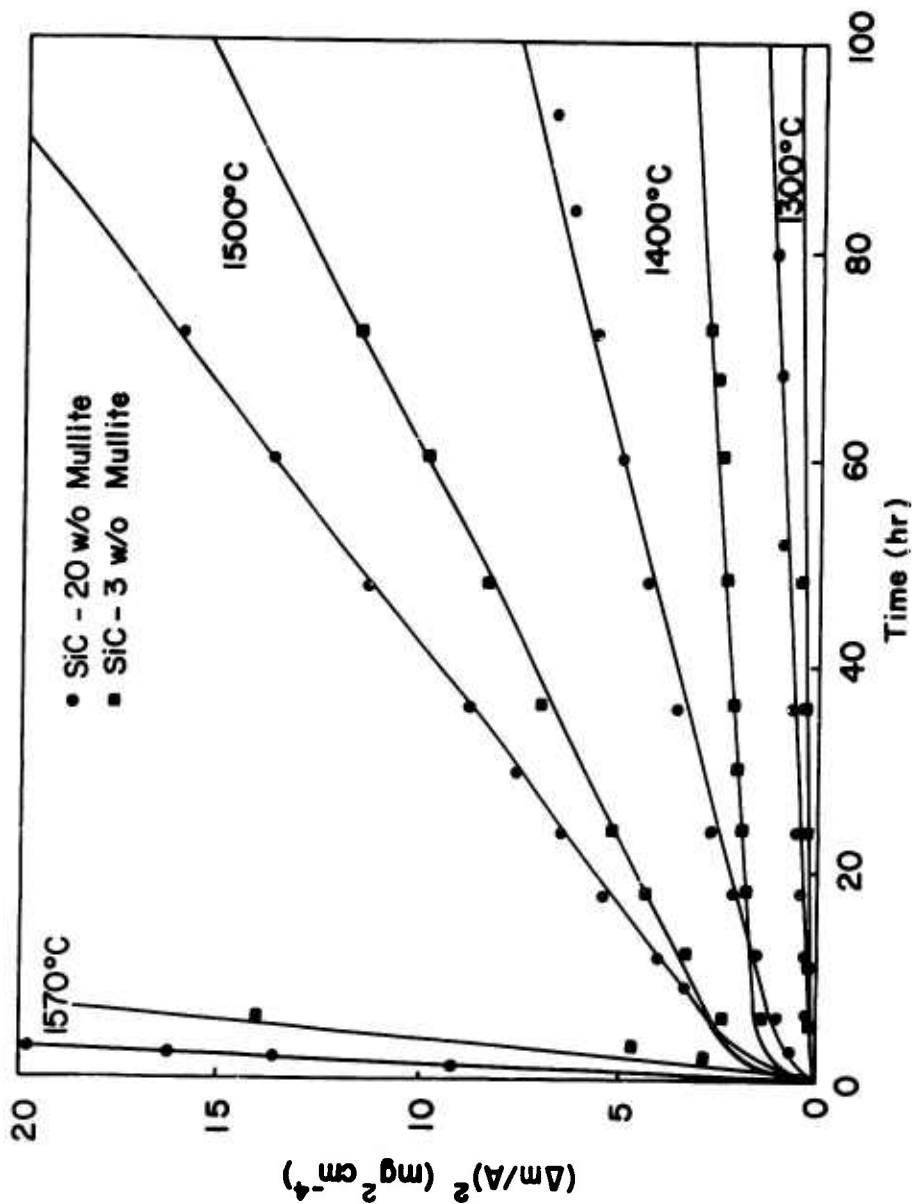


Figure 64. Parabolic Plot of Sample Weight Change Data as a Function of Exposure Time during Oxidation of SiC-Mullite Composites at Various Temperatures in Pure Flowing  $\text{O}_2$  (Total Pressure = 150 torr).

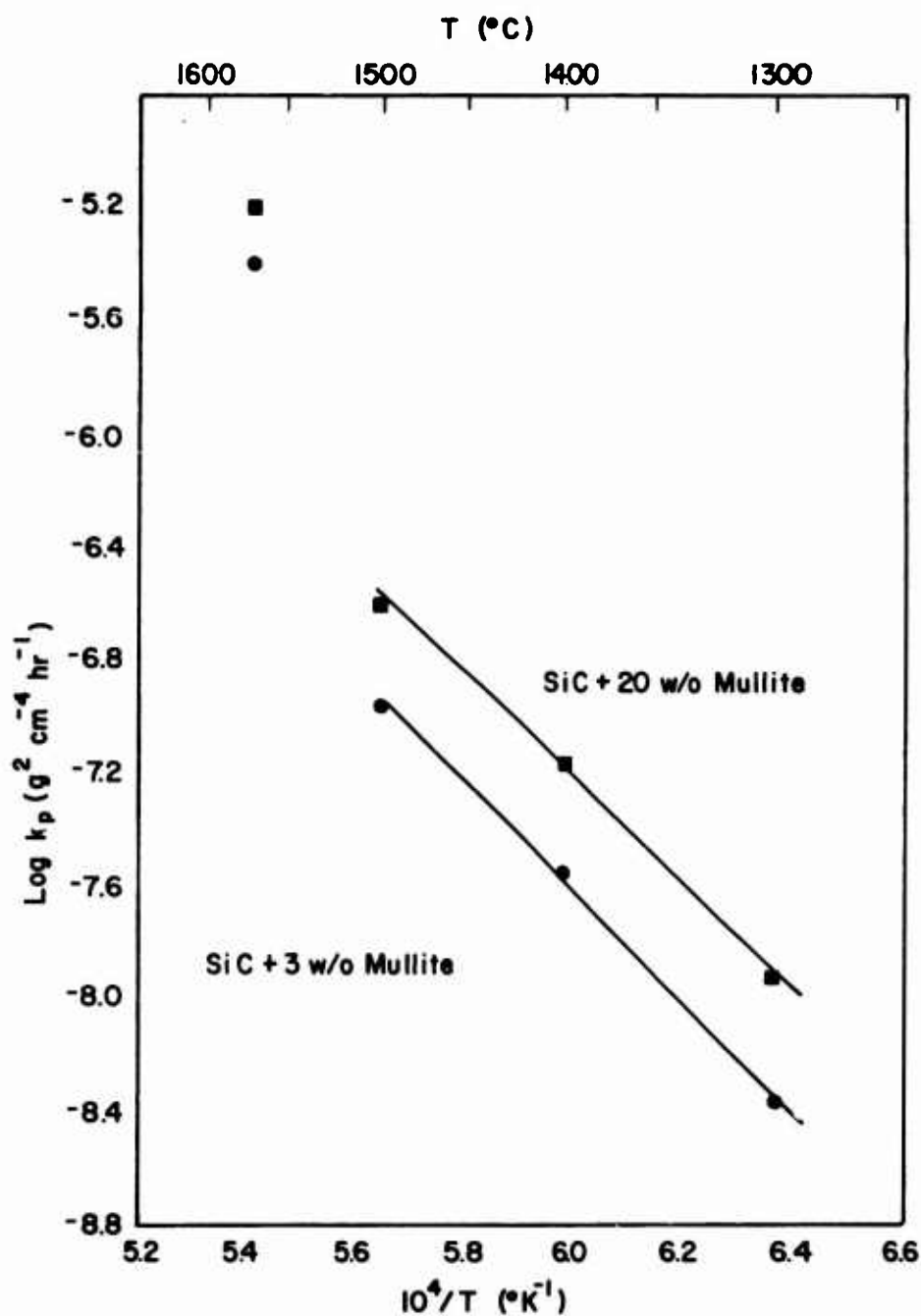


Figure 65. Arrhenius Plot of the Parabolic Rate Constants for SiC-Mullite Composites.

In order to obtain a truer evaluation of the composite performance relative to Si, SiC, and  $\text{Si}_3\text{N}_4$ , a procedure has been adopted whereby rates of recession for the materials can be compared, with allowance for any inert phase present in the matrix or gaseous species evolved. A derivation of the calculations will not be presented at this time; however, the necessary assumptions will be described briefly. The basic assumptions made are 1) the material oxidizes stoichiometrically, 2) the scale and matrix are free of porosity, 3) phases such as mullite are present as inert fillers, and 4) all the gaseous species formed leave the scale. The recession rates have been computed with these assumptions and are plotted as the logarithm of recession rate as a function of  $1/T$  in Figure 66. It is obvious that the oxidation resistance of the composites is inferior to that of SiC (an order of magnitude in recession rate). The 3 w/o composition is more resistant than hot-pressed  $\text{Si}_3\text{N}_4$ , and the 20 w/o composition and  $\text{Si}_3\text{N}_4$  display similar recession rates.

Typical cross sections of the oxide scale grown on the composites are presented in Figure 67. The scales grown below  $1500^\circ\text{C}$  were relatively compact and adherent to the composite matrix. The presence of the inert mullite particles in the oxide scales is revealed in Figures 67a and b; the mullite in the parent SiC effectively acts as an inert filler. Following exposure at the higher temperature  $1575^\circ\text{C}$  and to a lesser extent at  $1500^\circ\text{C}$ , the appearance of large voids was observed upon metallographic examination. These voids appeared to be in the proximity of the scale-matrix interface and are shown in Figure 67d. They could be associated with gaseous buildup and release at the scale-matrix interface. X-ray image micrographs from the electron microprobe analysis are presented in Figure 68 for a sample of SiC-20 w/o mullite oxidized at  $1400^\circ\text{C}$ . The Al in the matrix associated with the mullite particles is localized in intense regions, whereas in the oxide scale a relatively uniform intensity of signal was obtained. This does not agree with the optical micrograph, Figure 67, where a plate-like second phase is observable in the oxide scale. It is also of interest to note that the C image shows the presence of C in the scale, although at a diminished level compared to the matrix. These probe data were typical of the oxide scales formed at all temperatures.



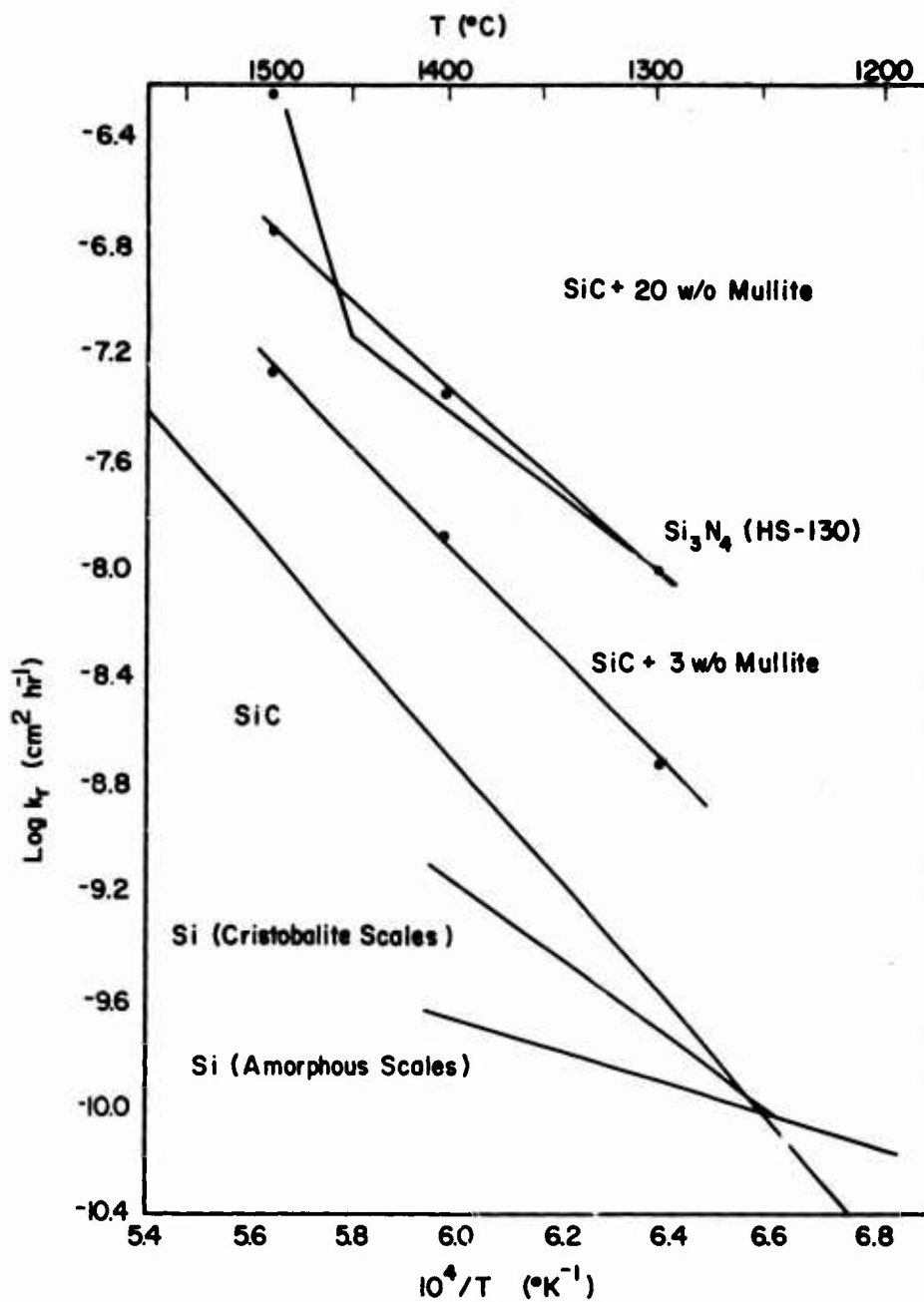


Figure 66. Plot of the Normalized Recession Rates for SiC-Mullite Composites Compared with Those Obtained for Si, SiC, and Norton HS-130  $\text{Si}_3\text{N}_4$  Described Elsewhere in this Report.



SiC-20 w/o mullite, 1500°C, 60 hrs

(a)



SiC-20 w/o mullite, 1400°C, 100 hrs

(b)



SiC-3 w/o mullite, 1300°C, 80 hrs

(c)



SiC-3 w/o mullite, 1570°C, 100 hrs

(d)

Figure 67. Optical and SEM Micrographs of Cross Sections of Oxidized Composite Samples.

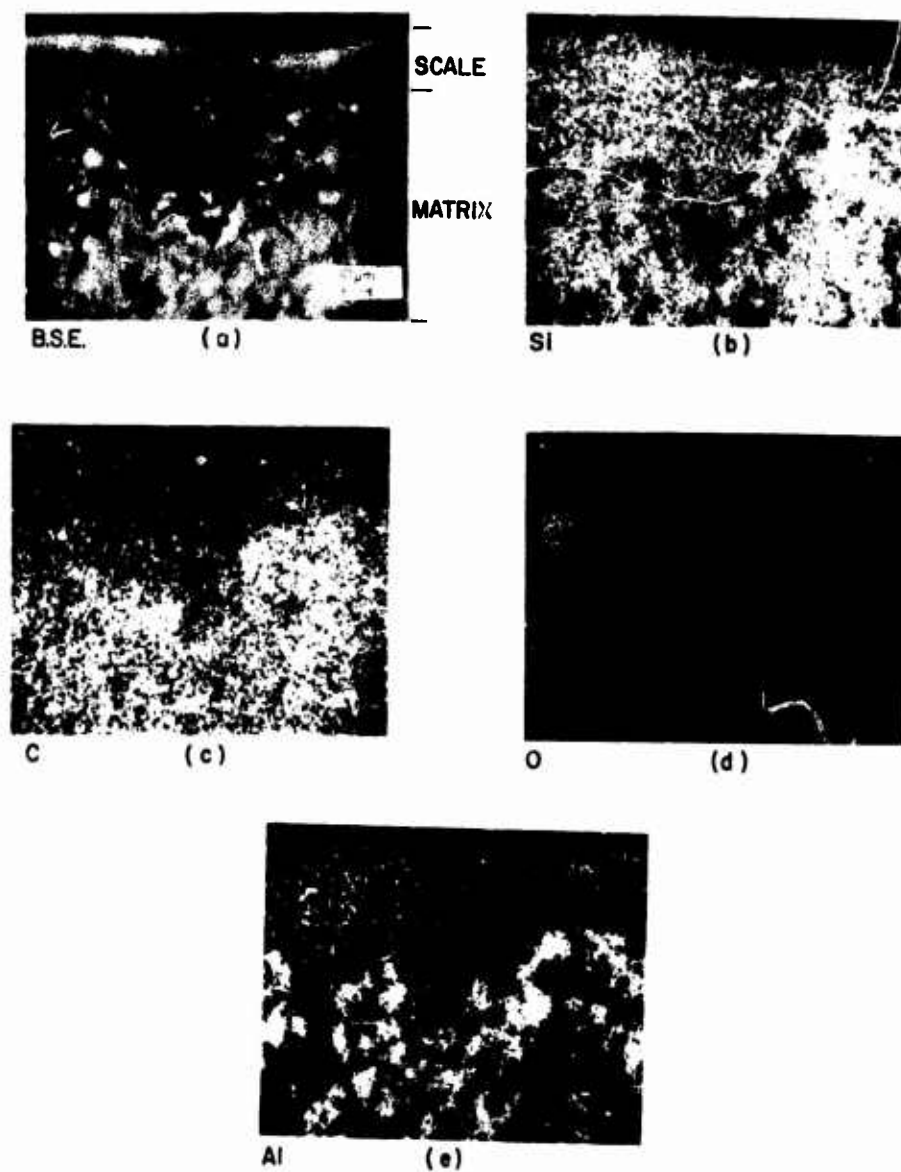


Figure 68. Cross Section of Scale Formed on SiC-20 w/o Mullite after 100 hr in 150 torr  $O_2$ .

## Summary and Conclusions

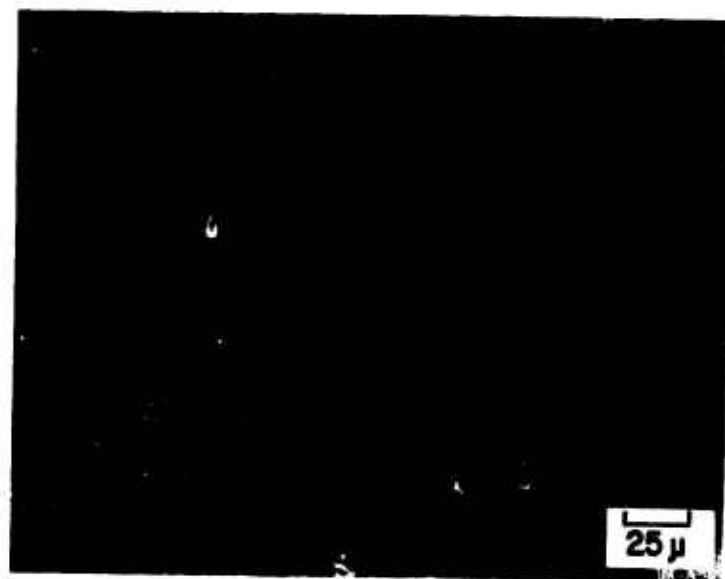
From the oxidation kinetics obtained in this investigation, it is concluded that the oxidation resistance of the SiC + 3 w/o mullite composite is superior to that of the SiC + 20 w/o mullite composite. The 3 w/o mullite material is superior to  $\text{Si}_3\text{N}_4$  in oxidation resistance; however, it has lower oxidation resistance than hot-pressed SiC without mullite additions. The 3 w/o mullite material does appear to have superior oxidation resistance to both  $\text{Si}_3\text{N}_4$  and SiC at very high temperatures ( $\sim 1500$ – $1550^\circ\text{C}$ ). On an absolute scale the recession rates for all the materials shown in Figure 66 are extremely low. Therefore, all of the materials are suitable for high temperature applications from the standpoint of their oxidation resistance.

## OXIDATION OF A $\text{Si}_3\text{N}_4$ + "BLACK GLASS" COMPOSITE

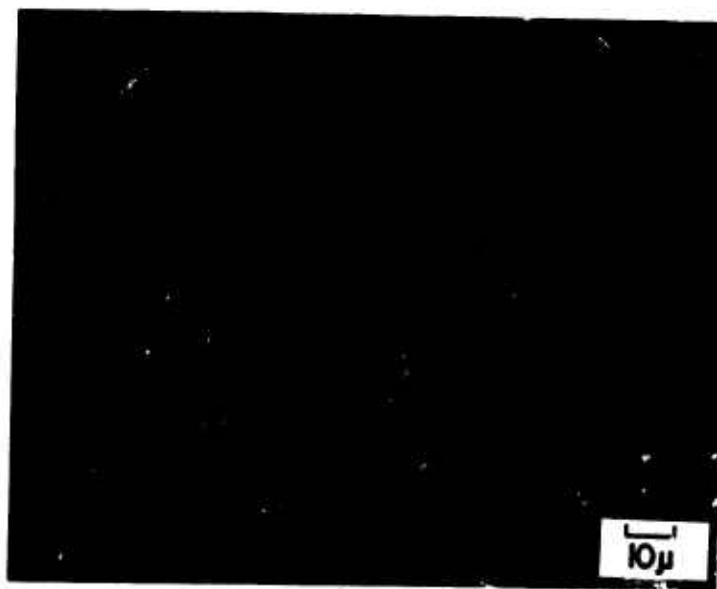
A devitrification-resistant glass having good mechanical strength and thermal stability has recently been developed and patented by Crandall and Smith at IIT Research Institute.<sup>(38)</sup> Carbon and  $\text{SiO}_2$  were heat treated in an oxygen free atmosphere to produce a carbon containing glass of composition 66%  $\text{SiO}_2$  + 33% C which resists devitrification.<sup>(38)</sup> This glass, henceforth to be referred to as "black glass," is microscopically indistinguishable from silica. Black glass was found to be devitrification resistant at hot-pressing temperatures approaching  $1250^\circ\text{C}$ , and was more viscous and possessed greater thermal stability than pure vitreous silica while retaining comparable strength properties. In the present investigation the effect of black glass additions on the oxidation behavior of  $\text{Si}_3\text{N}_4$  was studied.

## Experimental

Two compositions of  $\text{Si}_3\text{N}_4$  + black glass were investigated, 80%  $\text{Si}_3\text{N}_4$  + 20% black glass (designated as 20BG) and 70%  $\text{Si}_3\text{N}_4$  - 30% black glass (designated as 30BG). These materials were fabricated at IIT Research Institute and supplied by W. B. Crandall. The black glass was not uniformly distributed throughout the material, as can be seen in the micrographs presented in Figure 69, where black glass agglomerations (dark phase) are exhibited. X-ray analysis indicated that the as-received material is predominantly  $\beta$   $\text{Si}_3\text{N}_4$ , containing a significant amount of  $\alpha$ -cristobalite and small amounts of  $\alpha$ - $\text{Si}_3\text{N}_4$  and  $\text{Si}_2\text{ON}_2$ .



(a)



(b)

Figure 69. Microstructure of the As-Received  $\text{Si}_3\text{N}_4$  + Black Glass Composites Revealing Black-Glass Agglomerations.

Oxidation samples cut from the hot-pressed billets were rectangular or disc shaped. The coupons were abraded through 600-grit SiC, and ultrasonically cleaned in acetone and methanol, and the dimensions and weights were recorded prior to insertion into the thermobalance. Sample weight changes were monitored continuously by an Ainsworth 1000 Electrobalance. Experiments were conducted in dry oxygen at 150 torr in the temperature range 1300-1570°C. Oxidized samples and reaction products were characterized by x-ray diffraction, optical microscopy, SEM, and microprobe analysis.

### Results and Discussion

Typical weight gain data are presented in Figures 70 and 71 for the 20BG and 30BG material, respectively. After an induction period, the kinetics of oxidation are parabolic. Results of vapor-condensation experiments (shown only for 30BG) indicated that no condensable vapor species were evolved from either material within the experimental temperature range.

Figure 72 is an Arrhenius plot of the  $k_p$  data for the 20BG and 30BG material compared with data for HS-130  $Si_3N_4$  given elsewhere in this report. The 20BG material exhibited good oxidation resistance at 1500°C and above, whereas both the 30BG material and  $Si_3N_4$  exhibit accelerated oxidation rates. At lower temperatures the performance of the three materials are comparable.

Figure 73 presents macrophotographs of the two black glass modified materials following 100 hr exposures at 1500°C. Evidence of the superior performance of the 20BG material is quite obvious. An optical micrograph of the cross sections of the scale formed on the 20BG following exposure at 1570°C is shown in Figure 74--the scale is very uniform, compact, and adherent.

Figure 75 presents the cross section of a 20BG coupon which had been oxidized at 1500°C, together with x-ray images from the electron microprobe. Agglomeration of the black glass is evident, and of special note is the appreciable segregation of various impurity elements into the growing oxide scale.

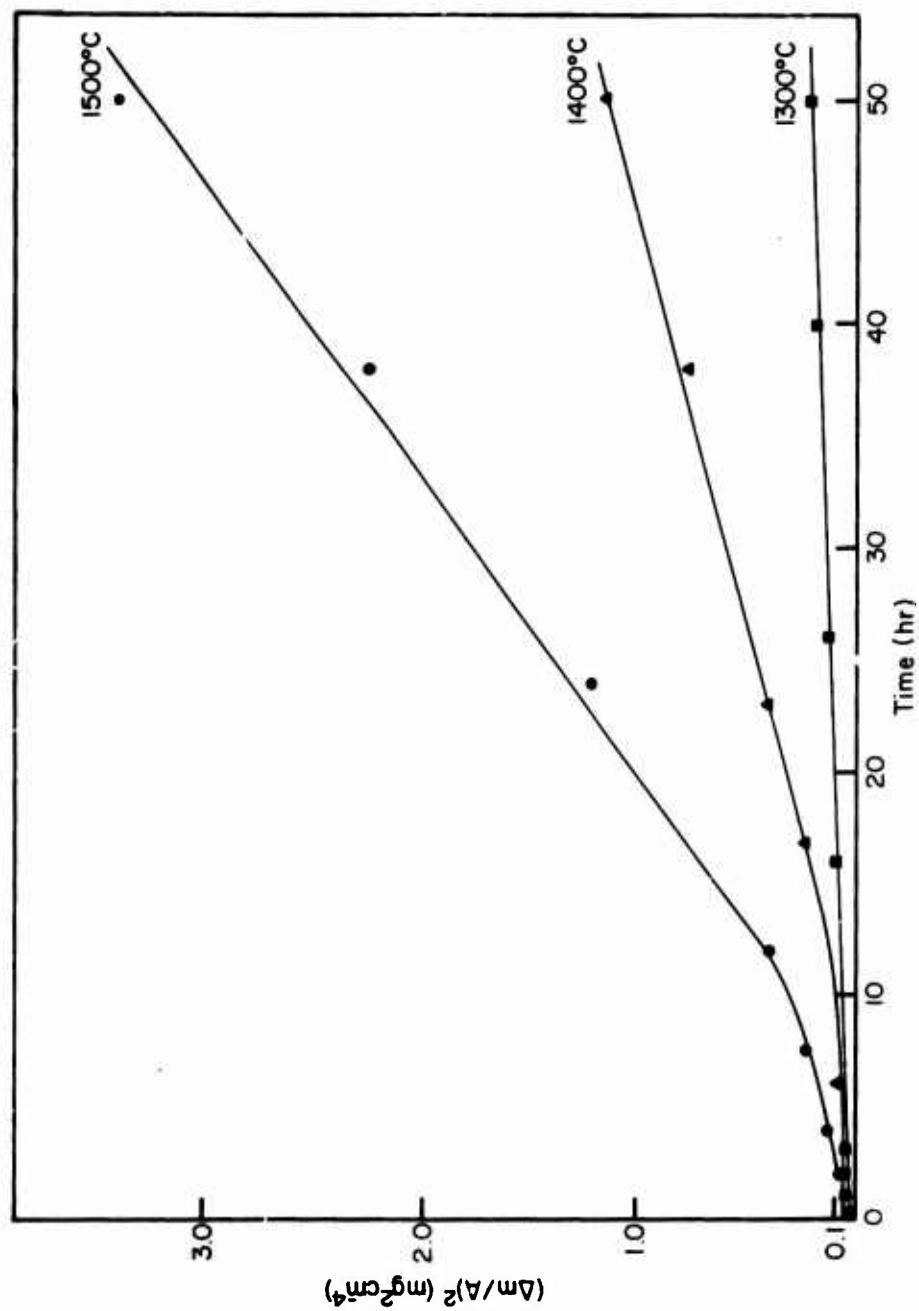


Figure 70. Parabolic Plot of Weight Change as a Function of Time for 20BG Material.

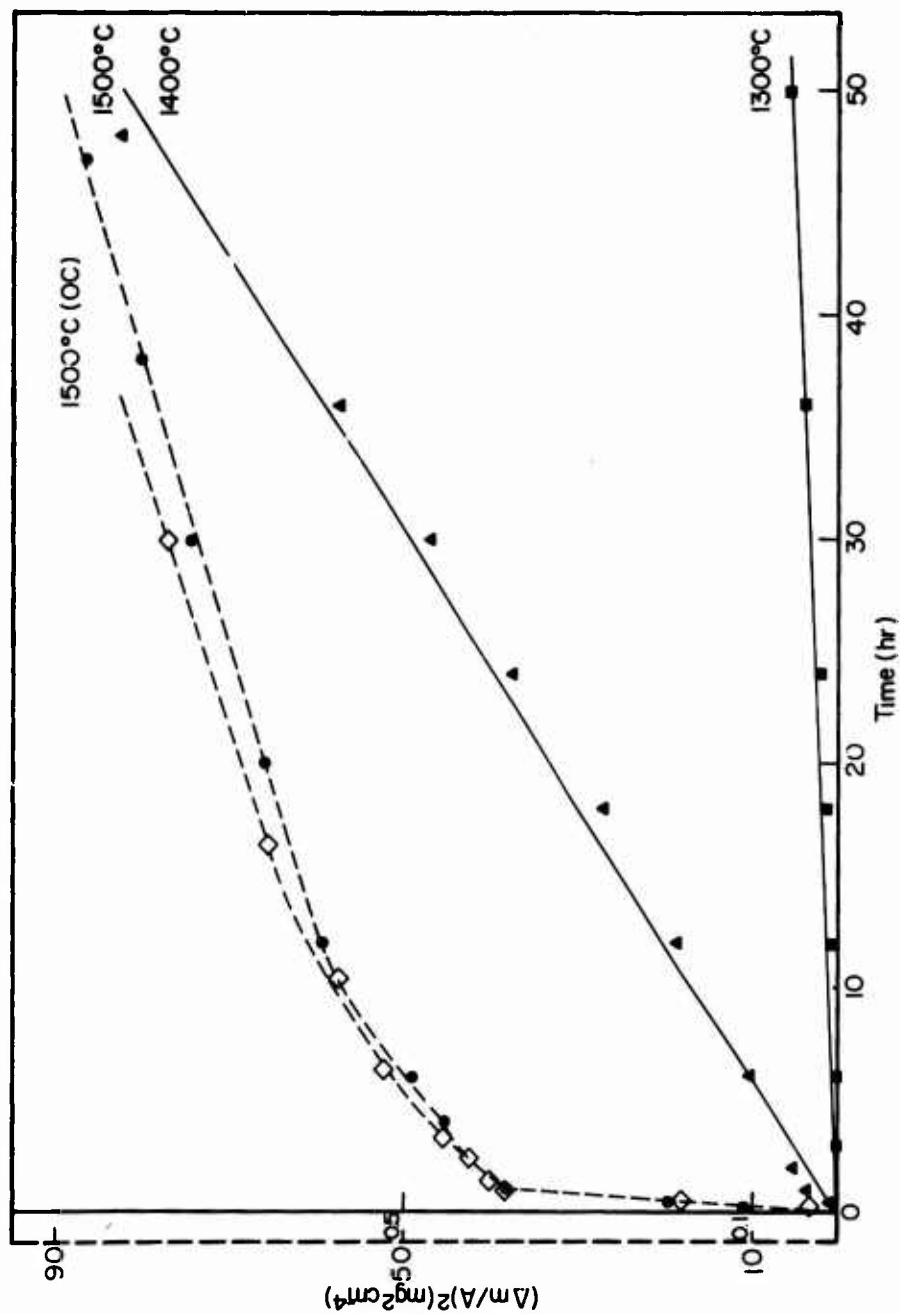


Figure 71. Parabolic Plot of Sample Weight Change and Oxygen Consumption (OC) as a Function of Time for 30BG Material.



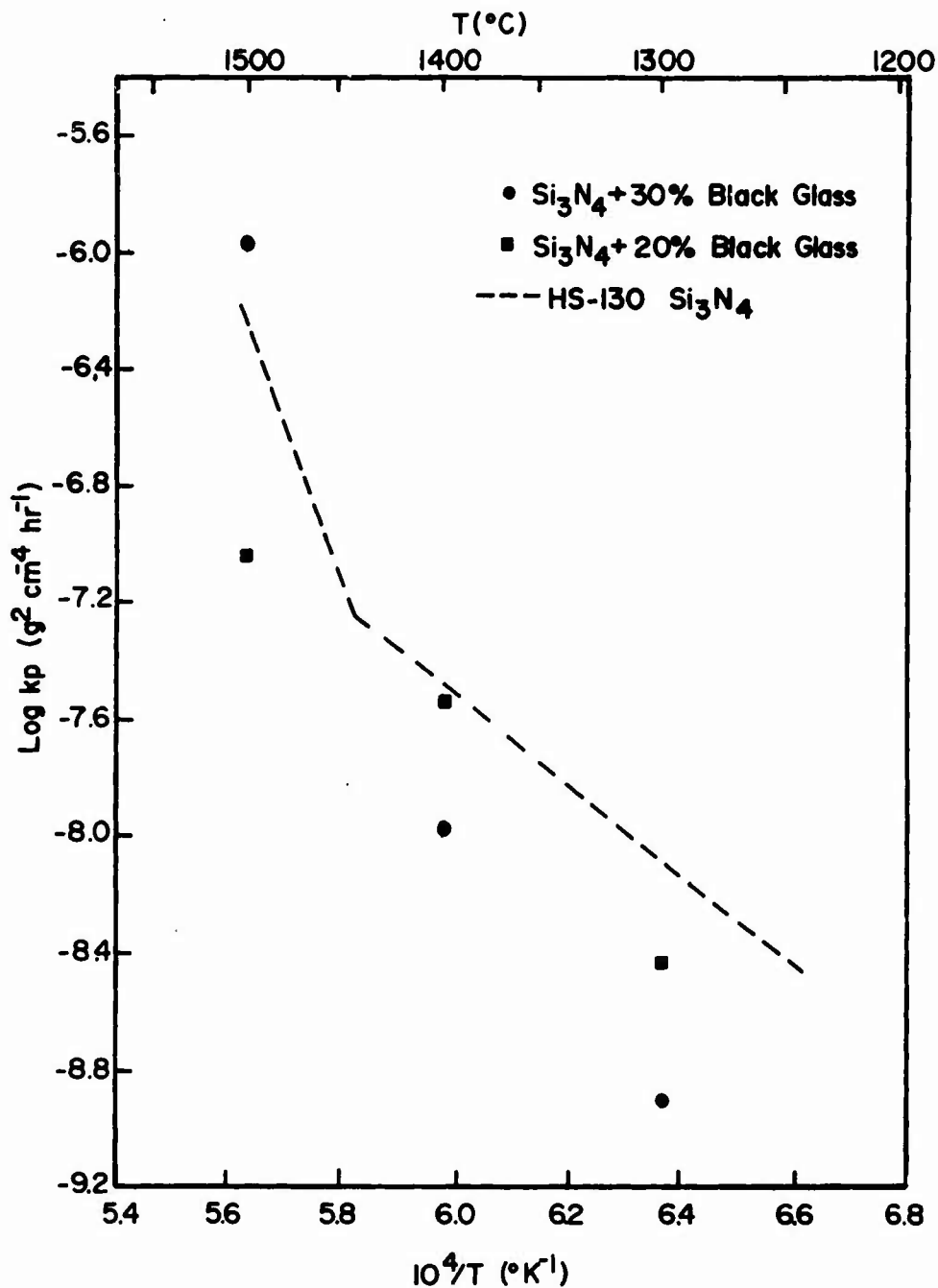
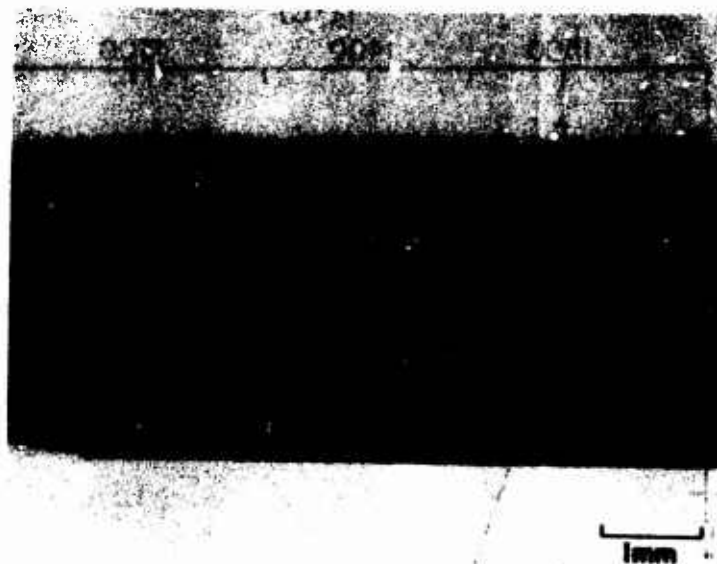


Figure 72. Arrhenius Plot of the Scaling-Rate Constant for 20 BG and 30 BG Material Compared with Norton HS-130 Si<sub>3</sub>N<sub>4</sub>.



**20 BG**



**30 BG**

Figure 73. Macrophotographs of 20BG and 30BG Specimens Oxidized at 1500°C for 100 hr.

Reproduced from  
best available copy.



Figure 74. Light Micrograph of 20BG Specimen Oxidized at 1570°C for 100 hr.

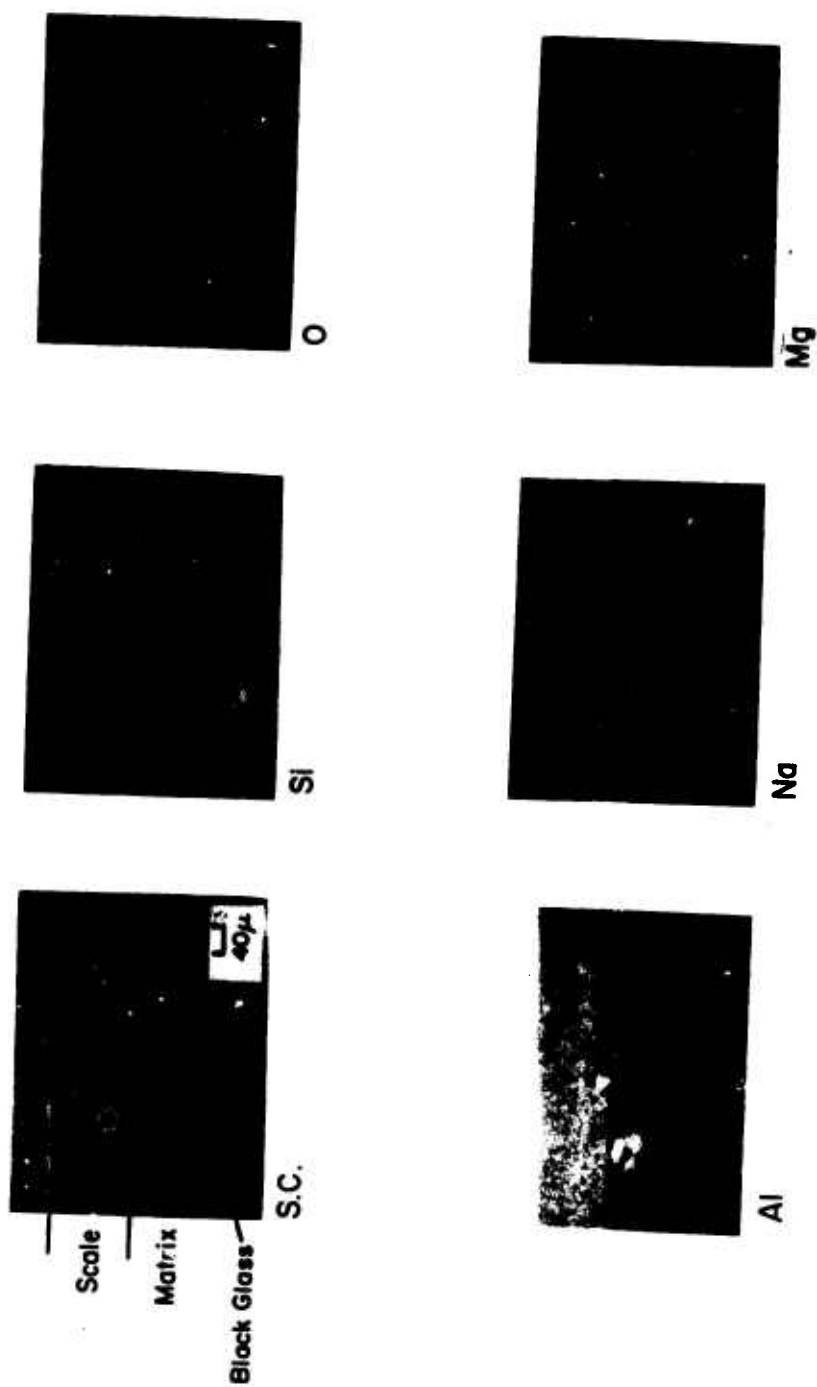


Figure 75. Microprobe Analysis of 20BG Specimen Oxidized at 1500°C for 100 hr.

X-ray diffraction of the reaction products confirmed that the oxide scales formed on 20BG had not devitrified even at temperatures greater than 1500°C, whereas devitrification of the scales formed on 30BG and  $\text{Si}_3\text{N}_4$  had occurred.

Considerable differences in the porosity of the 20BG and 30BG material were found. Porosity decreased with increasing hot-pressing temperature. In an attempt to elucidate the role of porosity, the oxidation behavior of a series of samples of the two materials having differing porosities was studied briefly. These studies showed that the rate of weight gain for the two materials increased as the porosity decreased (density increased) at temperatures in the range 1400°-1570°C. The cause of this behavior is unknown at the present time. The macroscopic appearance of the samples oxidized at 1500°C is shown in Figure 76.

An evaluation of the relative oxidation resistance of the 20BG material, SiC, and  $\text{Si}_3\text{N}_4$  was performed at 1500°C and 1570°C. The macroscopic appearance of the oxidized samples is shown in Figure 77. The superior performance of the black glass modified  $\text{Si}_3\text{N}_4$  (20BG) is visually evident and is consistent with the kinetic data. The SiC and  $\text{Si}_3\text{N}_4$  had been oxidized for 12 hr and the 20BG for 100 hr. The silica scales formed on the SiC and  $\text{Si}_3\text{N}_4$  had devitrified, whereas no devitrification was observed in the silica scale formed on the 20BG material.

#### Summary and Conclusions

Modification of  $\text{Si}_3\text{N}_4$  with additions of a devitrification-resistant carbon containing glass produced significantly improved oxidation resistance over HS-130  $\text{Si}_3\text{N}_4$  at high temperatures ( $\geq 1500^\circ\text{C}$ ). Reasons for the improved oxidation resistance are not clear; however, it is believed that oxygen transport is retarded because of the incorporation of a higher viscosity glass into the growing oxide scales. Silica scales formed on the 20BG and 30BG materials generally exhibited improved devitrification resistance to higher temperatures than scales formed on HS-130  $\text{Si}_3\text{N}_4$ , which was especially true for the 20BG material. At 1570°C the silica scale which formed on the 20BG material remained essentially amorphous, even after a 100 hr exposure.

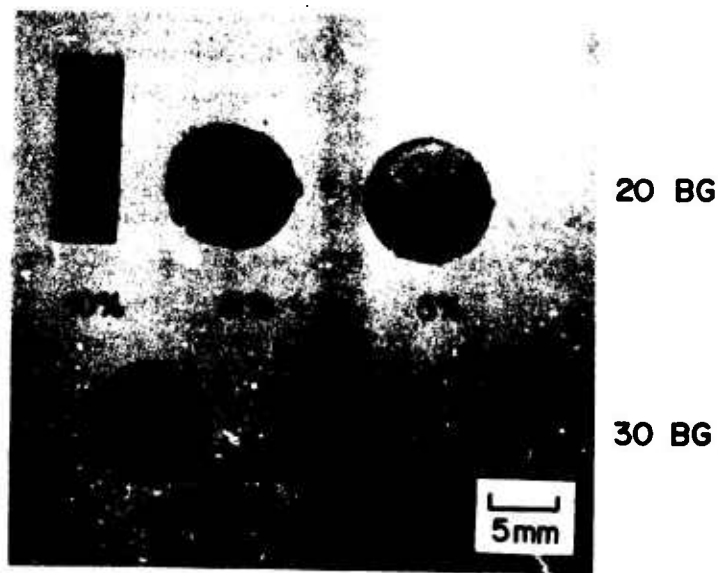
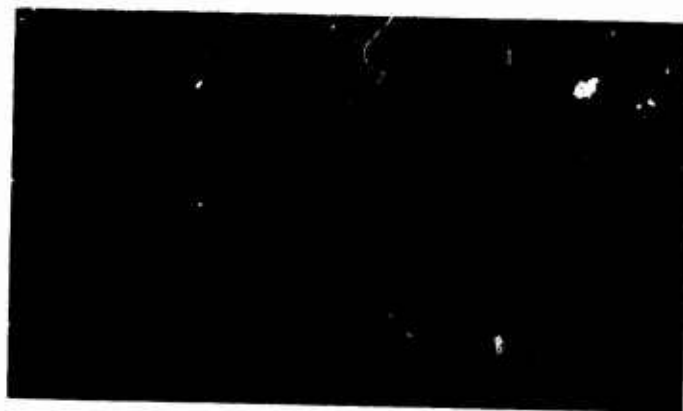


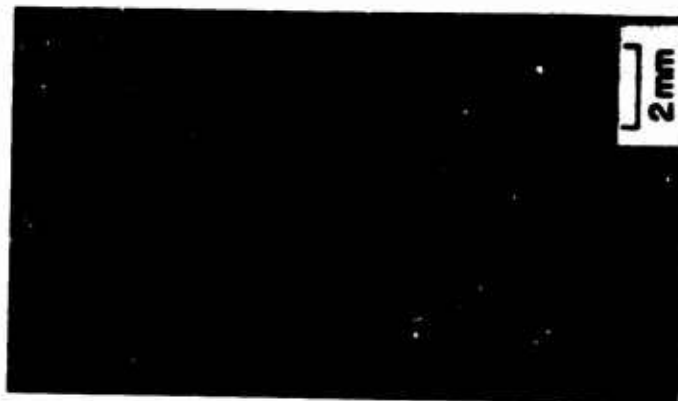
Figure 76. Macrophotographs of Oxidized Specimens Revealing the Effect of Porosity on Scale Morphologies.



20 BG 1500°C, 100 hr



SiC 1500°C, 12 hr



Si<sub>3</sub>N<sub>4</sub> 1500°C, 12 hr

Figure 77. Macrophotographs Comparing Scale Morphologies on Specimens Oxidized at 1500°C.

## OXIDATION OF Si AT HIGH TEMPERATURES

Studies on the oxidation behavior of SiC, Si<sub>3</sub>N<sub>4</sub>, HfB<sub>2</sub>+ SiC, and other Si-base materials have been described in previous sections of this report. Oxidation kinetics were found to be controlled by diffusion through a coherent SiO<sub>2</sub> scale. Activation energies for oxidation ranged from 70 to 110 kcal/mole, and oxygen partial pressure dependences of the scaling rate constants varied with material. In these investigations the activation energies for oxidation did not agree with the 28-30 kcal/mole reported in the literature for the oxidation of Si<sup>(1-3)</sup> nor did the P<sub>O<sub>2</sub></sub> dependence of the scaling rate constant approach the linear or 3/4 power dependence reported for Si.<sup>(1,39)</sup>

Three possible explanations can be offered for these disparities. First, investigations of Si oxidation generally have been conducted in the range 800-1200°C because Si wafers were usually oxidized in this range during preparation of thermal SiO<sub>2</sub> films for semiconductor applications. However, investigations on the oxidation of other Si-base materials have typically been conducted in the temperature range of their application, 1200-1550°C. It was possible that the activation energy for oxidation of Si in this temperature range would be larger than 28-30 kcal/mole, or alternatively that the activation energy for oxidation of other Si-base materials would have approached 28-30 kcal/mole if the studies could have been conducted at lower temperatures.

Secondly, investigations of Si oxidation in general have been conducted with ultrapure material and in pure oxygen environments. Although the latter criterion was approached for the oxidation of the Si-base materials described earlier, the former criterion was not met because only very impure materials were available for study--generally with impurity contents in the percent range. Some of these impurities were found to segregate in the SiO<sub>2</sub> scaling layers formed upon oxidation and may have altered the oxidation mechanism.

Thirdly, the scales formed on other Si-base materials have seldom been completely amorphous. Generally, scales consisted of cristobalite and



amorphous  $\text{SiO}_2$  in addition to silicates and other oxides. In previous studies on Si oxidation, only amorphous  $\text{SiO}_2$  scales were formed. Therefore, it is possible that at higher temperatures cristobalite instead of amorphous  $\text{SiO}_2$  will form on silicon, causing oxidation kinetics to agree with those of other Si-base materials.

In the present investigation the oxidation behavior of Si was investigated at temperatures approaching its melting point ( $\sim 1410^\circ\text{C}$ ). Pure Si and pure  $\text{O}_2$  environments were used in order to obtain baseline data for assessing the effect of impurities and scale devitrification on the oxidation kinetics.

### Experimental

High purity, semiconductor grade Si wafers were obtained--phosphorus doped, n-type  $\sim 5\Omega$  cm wafers having (100) faces from Texas Instruments and similarly doped wafers having (111) faces from Crystec (Wilmington, Ohio). Discs ( $\sim 1.3$  cm diam.  $\times 0.1$  cm thick) were cut from the wafers, polished on both sides through  $0.25 \mu$  diamond paste, and ultrasonically cleaned in acetone and methanol prior to each oxidation experiment.

The commercial grade oxygen used in this study was dried by using two techniques. In the first, the oxygen was passed over a magnesium-perchlorate dessicant in a closed tube; in the second the oxygen was dried by passing it through a liquid nitrogen cold trap, and the boil-off was used in the experiments. The water vapor pressure in  $\text{O}_2$  dried by this latter technique is extremely low,  $\sim 2 \times 10^{-19}$  torr. (40)

The thermobalance system used in this investigation has been described previously. (41) It consists of an Ainsworth FV microbalance atop a resistance heated, alumina tube furnace. In order to avoid oxidation of the tungsten heating elements, the furnace chamber surrounding the elements is held under high vacuum. This vacuum also minimizes the possibility of water vapor diffusion through the furnace tube into the reaction zone.

Each experiment was initiated by lowering a polished and cleaned Si coupon into the furnace hot zone, which was maintained at forepump vacuum. The sample was actively oxidized for several minutes in order to remove several hundred micrograms of Si by desorption of SiO. The purpose of this pretreatment was to establish an ultrapure SiO<sub>2</sub> free Si surface condition prior to the oxidation experiment. The Si coupon was raised from the hot zone, the desired environment was established, and the coupon was again lowered into the hot zone to initiate the experiment.

### Results and Discussion

Studies were conducted in the temperature range 1200-1390°C. In the experiments, oxidation kinetics were parabolic, and only slight deviations were observed. Figure 78 is an Arrhenius plot of the scaling rate constants obtained from the slopes of the parabolic data plots. The data were obtained in dried O<sub>2</sub> at 600 torr total pressure. In a number of experiments, cristobalite scales [SiO<sub>2</sub>(c)] were formed upon oxidation; however, in most experiments amorphous SiO<sub>2</sub> scales [SiO<sub>2</sub>(a)] were formed. When SiO<sub>2</sub>(c) scales formed, oxidation rates were more rapid and were characterized by a larger activation energy than when SiO<sub>2</sub>(a) scales formed, with activation energies for oxidation of ~ 65 kcal/mole for the former and ~ 28 kcal/mole for the latter.

Light micrographs of the surfaces of four samples having cristobalite and amorphous SiO<sub>2</sub> scales are presented in Figure 79. Figures 79(a) and (b) reveal the nature of the scales obtained during oxidation at 1340 and 1390°C, respectively where cristobalite has been formed; the cristobalite consists of large equiaxed grains. In contrast Figures 79(c) and (d) reveal the scales obtained during oxidation at 1350 and 1390°C, respectively, which consist entirely of amorphous SiO<sub>2</sub>. The "worm-like" structure, shown in Figure 79(c) and to a lesser extent in Figure 79(d), is the Si surface beneath the transparent SiO<sub>2</sub>(a) scale as it appears after the active-oxidation pretreatment. X-ray diffractometer scans revealed very strong cristobalite peaks for the samples shown in Figures 79(a) and (b), whereas a large amorphous hump and only a very weak cristobalite peak were found for the samples shown in Figures 79(c) and (d).

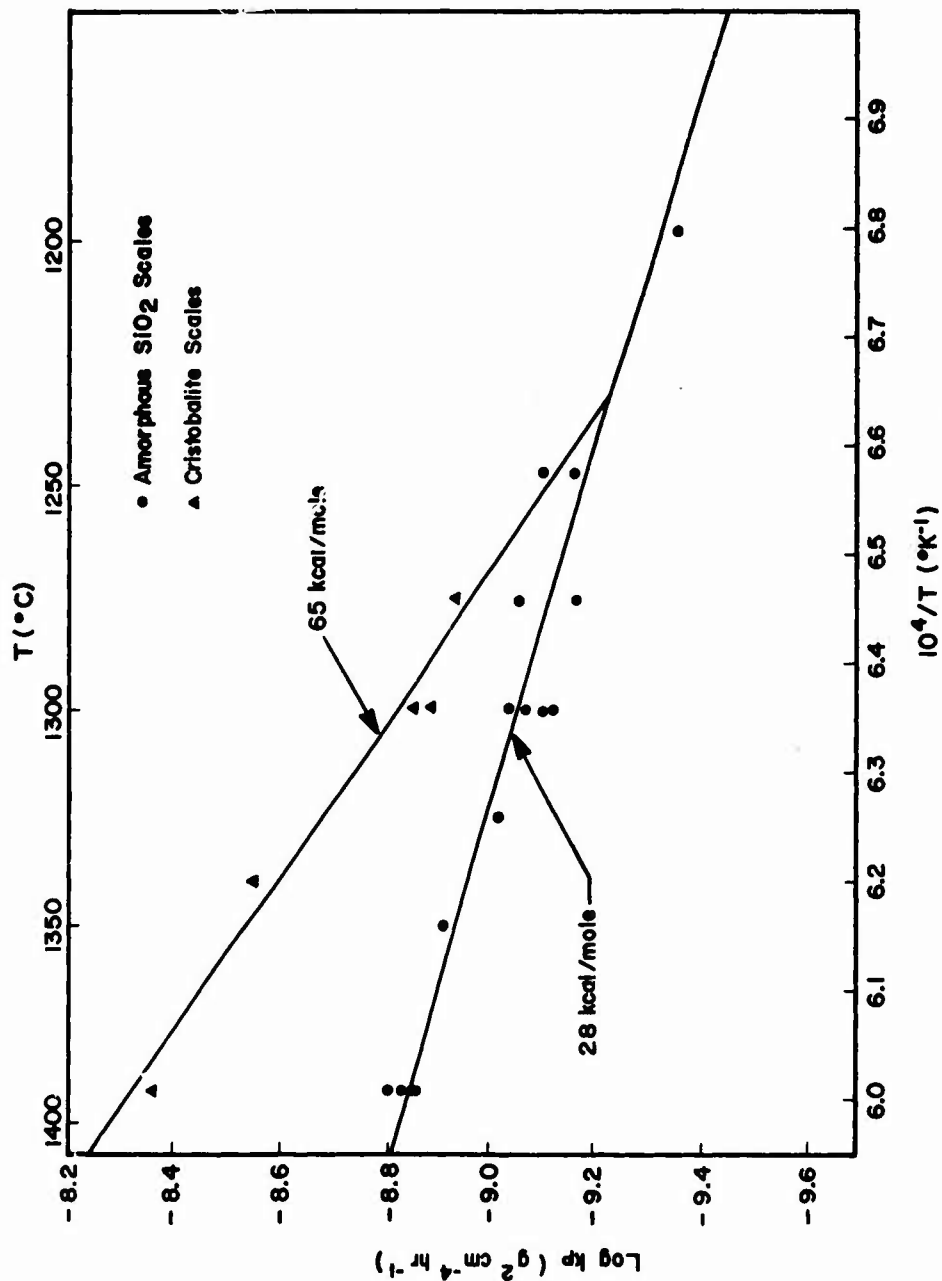


Figure 78. Arrhenius Plot of Parabolic Rate Constants for the Oxidation of Si in 500 torr O<sub>2</sub>.

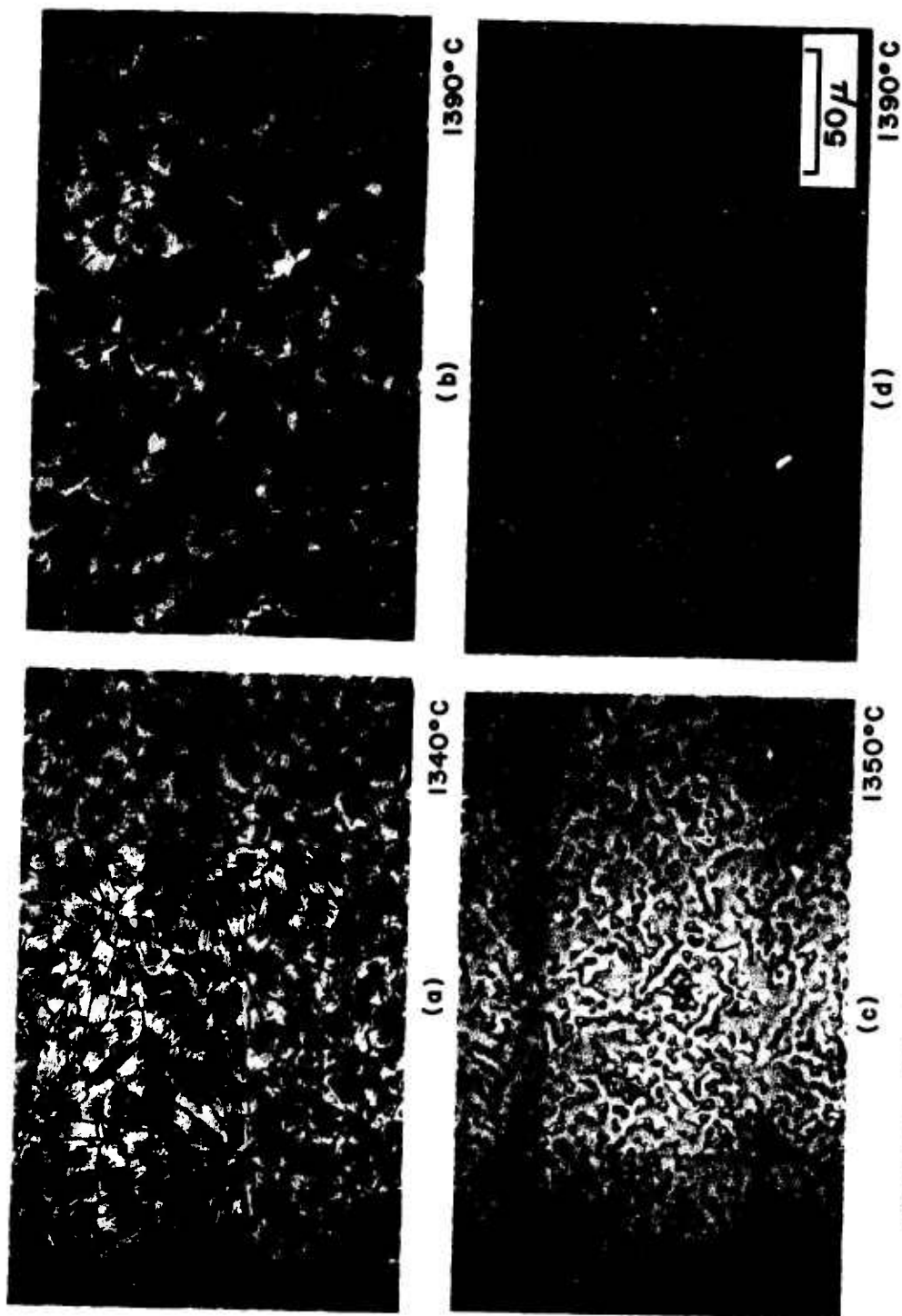


Figure 79. Light Micrographs of Sample Surfaces Revealing Two Types of Scales Formed on Si during Oxidation in 600 torr  $C_2$ .

Spark source mass spectrometer analyses of samples which had formed the two types of scales shown in Figure 79 were conducted to determine whether impurity elements had caused devitrification. Significant amounts of Fe (~ 30 ppm) were found in the  $\text{SiO}_2(\text{c})$  scales, whereas the  $\text{SiO}_2(\text{a})$  scales had negligible bulk impurity content.

The oxygen-pressure dependence of the scaling rate constant was obtained at  $1300^\circ\text{C}$  by varying the total pressure of oxygen. The results are shown in Figure 80, where  $\log k_p$  is plotted as a function of  $\log P_{\text{O}_2}$ . A  $3/4$  power  $P_{\text{O}_2}$  dependence is found whether the scale is amorphous or crystalline. This dependence is quite similar to the strong  $P_{\text{O}_2}$  dependence obtained by Ligenza and Spitzer ( $4/5$  power)<sup>(39)</sup> and by Deal and Grove (linear)<sup>(1)</sup> for the oxidation of Si and to the linear dependence on  $P_{\text{O}_2}$  of the oxygen permeability in amorphous  $\text{SiO}_2$  obtained by Norton;<sup>(12)</sup><sup>2</sup> these investigations were conducted at lower temperatures.

Figure 81 compares the oxidation results obtained in this investigation with those of previous investigations at lower temperatures. In the latter, oxidation kinetics were obtained by measuring  $\text{SiO}_2$  thickness as a function of time in 1 atm  $\text{O}_2$ . In order to make a direct comparison, these data were converted to weight gain data and the present results were extrapolated to 1 atm  $\text{O}_2$  by using the observed  $3/4$  power  $P_{\text{O}_2}$  dependence. Excellent agreement with previous investigations is found for experiments in which amorphous  $\text{SiO}_2$  scales are formed. Therefore the 28-30 kcal/mole activation energy for oxidation is valid to the melting point of Si whenever amorphous scales are formed. The activation energy observed when  $\text{SiO}_2(\text{c})$  scales are formed is probably impurity sensitive and its magnitude dependent upon the incubation period required to form cristobalite.

Figure 82 summarizes the results of the present investigation as well as those reported in earlier sections of this report for other Si-base materials. The rates shown were calculated from the experimental weight change data extrapolated to 150 torr  $\text{O}_2$ , with the assumption that the materials oxidize stoichiometrically and that all of the gaseous products

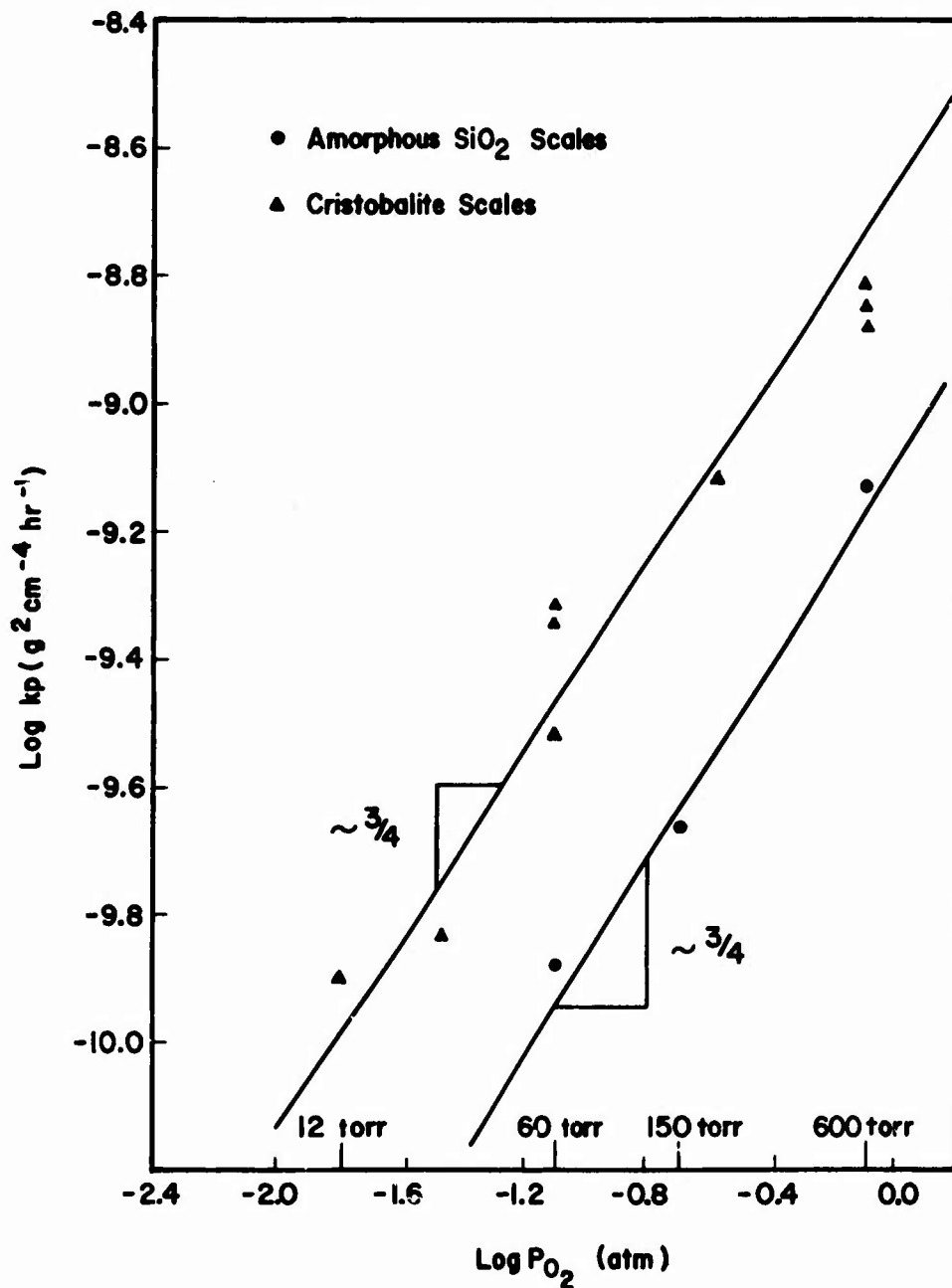


Figure 80. Oxygen Pressure Dependence of the Scaling Rate Constant for Si Oxidation at 1300°C.

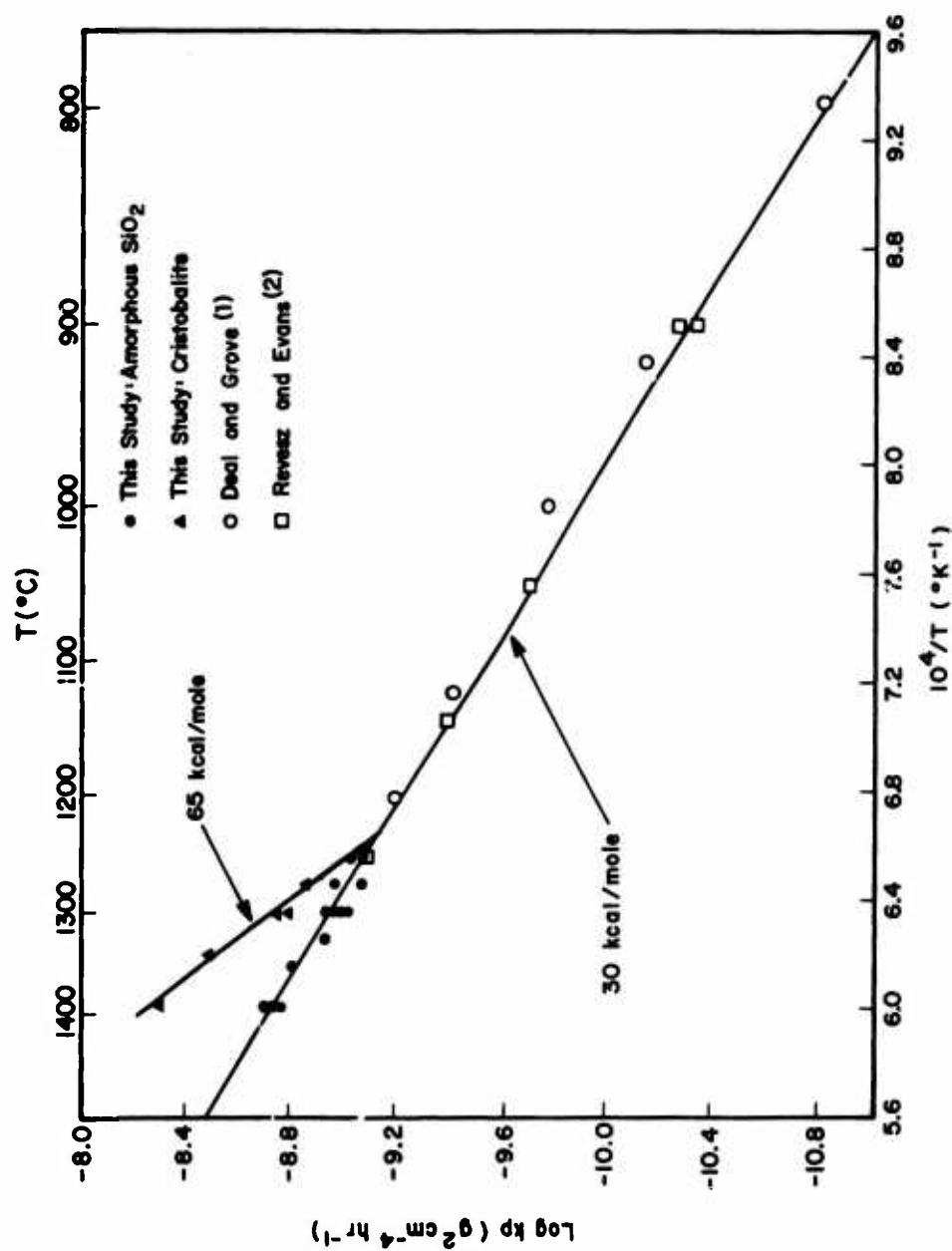


Figure 81. Comparison of the Oxidation Kinetics Obtained in This Investigation with Those in Previous Studies at Lower Temperatures in 1 atm O<sub>2</sub>.

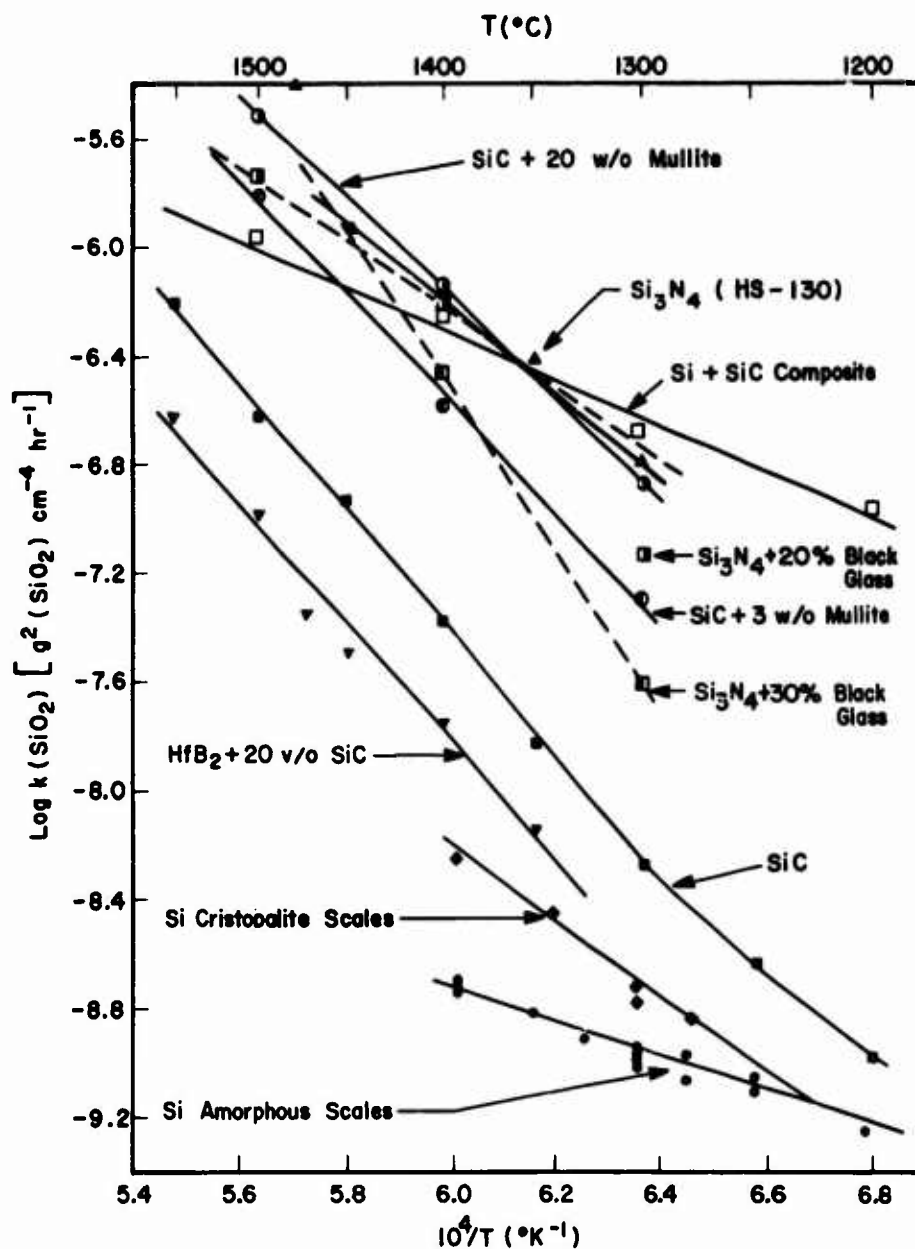


Figure 82. Comparison of the Oxidation Kinetics Obtained in This Investigation with Those of Other Si-Base Materials Presented in This Report.



formed upon oxidation are lost to the ambient. In order to permit a valid comparison, all of the data were converted to a common denominator; i.e., a  $\text{SiO}_2$  formation rate basis. In the temperature range shown, the activation energy for oxidation is quite large--except for Si when  $\text{SiO}_2(\text{a})$  is formed and for the Si/SiC composite. As expected, the rate of  $\text{SiO}_2$  formation for Si oxidation falls well below that of the other materials, probably due to the high purity of Si.

#### Summary and Conclusions

The oxidation behavior of Si was investigated at temperatures approaching the melting point of Si. The oxidation kinetics obtained when amorphous  $\text{SiO}_2$  scales are formed are in excellent agreement with kinetics obtained in previous investigations at lower temperatures. In a number of experiments, more rapid oxidation kinetics were observed due to the formation of cristobalite scales. The mechanism of cristobalite formation during these experiments is unknown; however, the small amounts of Fe found in the  $\text{SiO}_2(\text{c})$  scales probably caused scale devitrification. The high activation energy for oxidation of Si when  $\text{SiO}_2(\text{c})$  scales are formed is typical of other Si base materials described in previous sections of this report which suggests that scale devitrification and localized impurities in the scales formed on these latter materials cause the large activation energies for oxidation and rapid oxidation kinetics.

### SECTION III

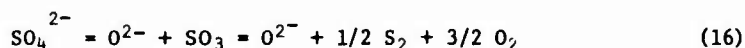
#### HIGH-TEMPERATURE CORROSION OF EXPERIMENTAL Ni-Cr-Al ALLOYS

##### INVESTIGATION OF THE MECHANISM OF SODIUM SALT INDUCED ACCELERATED OXIDATION OF Ni-BASE ALLOYS

In gas turbines the phenomenon termed "hot corrosion" or--more accurately-- "accelerated oxidation" is now generally accepted to arise from the deposition of  $\text{Na}_2\text{SO}_4$  resulting from ingested salts in the engine and sulfur resulting from the combustion of fuel.<sup>(42,43)</sup> Until recently the corrosion and oxidation resistance of superalloys had not been a design criterion so long as resistance to the environment was afforded up to the temperature at which the strength of the material was maintained. For Ni base superalloys containing 20 w/o Cr, this temperature was approximately 900°C; however, when the development of gas turbine materials having increased strength characteristics became necessary, the increased strength was achieved by adding Al and Ti, thereby increasing the amount of  $\gamma'$  hardening ( $\gamma'$  is an ordered intermetallic  $\text{Ni}_3\text{Al}$  or  $\text{Ni}_3\text{Ti}$ ) in the Ni base alloys. Unfortunately, to accommodate an increase in the maximum solubility of Ti or Al necessitated a decrease in the Cr content to ~10 w/o with resultant loss of high temperature hot corrosion resistance. Further increases in the inlet temperature to achieve improved efficiency would magnify the inadequacies of present day coated superalloys in terms of resistance to high temperature corrosive environments.

To date most accelerated oxidation studies have been conducted with  $\text{Na}_2\text{SO}_4$  as the condensed salt. Goebel and Pettit<sup>(44)</sup> recently presented a theory of accelerated oxidation of superalloys in  $\text{Na}_2\text{SO}_4$  environments which is gaining widespread acceptance. The following mechanistic interpretation has been offered: During the initial stages of oxidation of Ni-Cr-Al superalloys in the presence of  $\text{Na}_2\text{SO}_4$ , some  $\text{Al}_2\text{O}_3$ ,  $\text{Cr}_2\text{O}_3$ , and  $\text{NiO}$  are formed at the alloy- $\text{Na}_2\text{SO}_4$  interface. Sulfur leaves the sulfate and diffuses into the alloy; subsequently, internal sulfides of Cr are formed in the alloy matrix.

This process increases the oxygen ion  $O^{2-}$  activity in the  $Na_2SO_4$  to a level sufficient to flux basically the  $NiO$ ,  $Cr_2O_3$ , and  $Al_2O_3$ , according to the equations: <sup>(44-45)</sup>



The fluxed ions can decompose in the  $Na_2SO_4$  away from the alloy-sulfate interface (where the  $O^{2-}$  concentration is reduced) to form discontinuous particles of  $NiO$  and  $Al_2O_3$ . The fluxing reactions are similar; all occur because  $O^{2-}$  ions in the sulfate react with the oxides. However, for  $NiO$  and  $Al_2O_3$ , in general, sulfur must be removed from the sulfate in order to increase the  $O^{2-}$  activity to a sufficiently high level for the reaction to take place. In the case of an  $Al_2O_3$  forming alloy, the  $AlO_2^-$  which forms according to Eq. (17) will diffuse away from the oxide-sulfate interface to a region of lower  $O^{2-}$  activity in the sulfate. The  $O^{2-}$  activity in this region will not be sufficient to support the  $AlO_2^-$ . Therefore, the  $AlO_2^-$  will decompose to form  $Al_2O_3$  as a porous, nonprotective oxide. This type of degradation does not occur in  $Cr_2O_3$  scales because the  $O^{2-}$  activity in the  $Na_2SO_4$  is sufficient to stabilize the  $CrO_4^{2-}$  ion. The  $Cr_2O_3$  can become basically fluxed according to Eq. (19) without the occurrence of the reaction in Eq. (16). Only a small amount of  $Cr_2O_3$  scale can be fluxed before its solubility limit in  $Na_2SO_4$  is reached. Therefore, the protective  $Cr_2O_3$  scale remains stable, except for the small amount dissolved in the  $Na_2SO_4$ .

Seybolt <sup>(46,47)</sup> has suggested that the most critical step in the initiation of accelerated oxidation is the step involving internal Cr sulfide formation in the alloy matrix rather than the basic fluxing step. It is believed that these sulfides are preferentially oxidized, which allows sulfur to penetrate the alloy further, establishing a self-regenerative cycle. In the present

investigation the oxidation of two experimental Ni-Cr-Al alloys was investigated in carbonate and nitrate environments as well as in sulfate environments in order to determine whether the presence of sulfur is necessary to initiate accelerated oxidation.

### Experimental

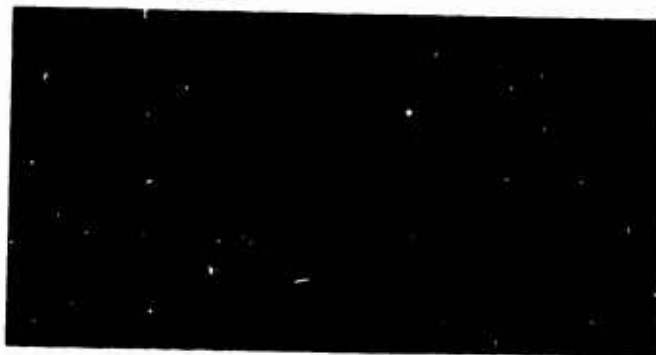
Two experimental alloys were used in this investigation, Ni8Cr6Al and Ni8Cr6Al0.2Y. Both are  $Al_2O_3$  formers and should be particularly vulnerable to hot salt environments. The Y was added to the second alloy to increase scale adherence.<sup>(48)</sup> Sample coupons ( $\sim 1 \times 0.6 \times 0.1$  cm) were abraded through 600-grit SiC and ultrasonically cleaned in acetone and methanol. Figure 83 presents the microstructures of the as received materials.

The laboratory technique used simulated, in part, accelerated oxidation and consisted of spraying a sodium salt coating-- $Na_2SO_4$ ,  $Na_2CO_3$ , or  $NaNO_3$  of equal molarity--onto the specimens and subsequently oxidizing at elevated temperatures in static  $O_2$  at 150 torr total pressure. Sample weight change was monitored continuously with time by using a Cahn RG electrobalance. The oxidized samples were examined by x-ray diffraction, microscopy, and electron microprobe analysis techniques.

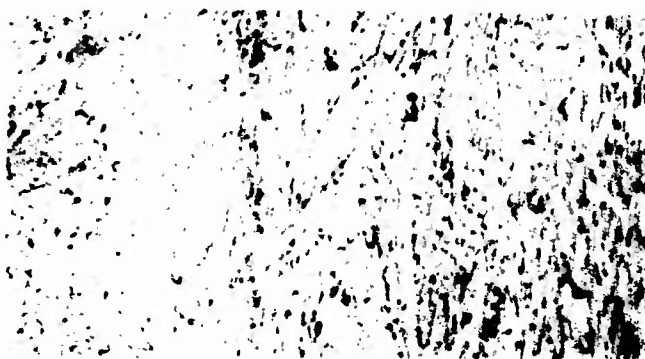
### Results and Discussion

Figure 84 is a comparison of the weight gain data as a function of time for  $Na_2SO_4$  coated and uncoated alloys in  $O_2$  at 1000°C. A thin protective  $Al_2O_3$  scale was formed on the uncoated specimens; NiO was the predominant oxide formed on the coated specimens, although some  $Al_2O_3$  was present after extended exposure times. The micrographs presented in Figures 85 and 86 reveal the presence of internally precipitated sulfides in the alloy matrix. For long exposures the rate of weight gain decreases to approach that of the uncoated alloy. It appears that the  $Na_2SO_4$  initially inhibits the formation of a protective  $Al_2O_3$  scale on the alloy; however, after long exposure times the  $Na_2SO_4$  is lost because of vaporization and basic fluxing, and subsequently

Reproduced from  
best available copy.



(a)



(b)

Figure 83. Representative Microstructures of Ni8Cr6Al and Ni8Cr6Al0.2Y.  
Magnification X55.

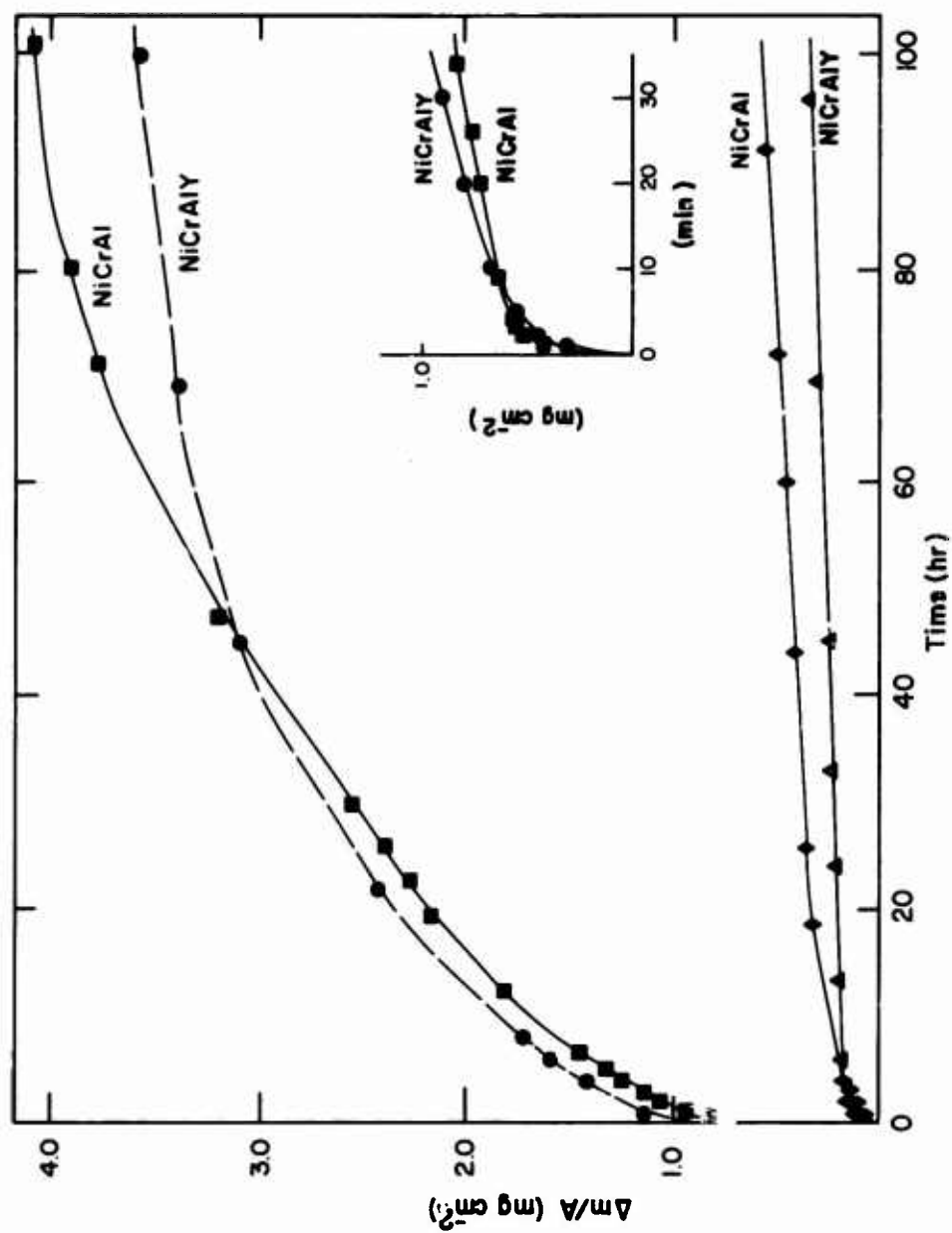


Figure 84. Observed Weight Gain as a Function of Exposure Time During the Oxidation of Na<sub>2</sub>SO<sub>4</sub> Coated Ni<sub>8</sub>Cr<sub>6</sub>Al and Ni<sub>8</sub>Cr<sub>6</sub>Al<sub>0.2</sub>Y Alloys at 1000°C in 150 p.p.m. O<sub>2</sub>.



20 $\mu$

Figure 85. Microstructure of Cross Section of  $\text{Na}_2\text{SO}_4$  Coated Ni8Cr6Al after 100 hr Exposure at 150 torr  $\text{O}_2$  at  $1000^\circ\text{C}$ . Note Sulfides Precipitated in Matrix.



10 $\mu$

Figure 86. Microstructure of Cross Section of  $\text{Na}_2\text{SO}_4$  Coated Ni8Cr6Al after 30 min Exposure in 150 torr  $\text{O}_2$  at  $1000^\circ\text{C}$ . Scale Has Spalled Revealing Sulfide Precipitates in Matrix.

a protective  $\text{Al}_2\text{O}_3$  layer forms. Figure 87 presents microprobe x-ray scans of the scale formed on Ni8Cr6Al after 30 min of accelerated oxidation; the presence of a porous scale within the  $\text{Na}_2\text{SO}_4$  slag and internal sulfides in the alloy matrix are apparent. Figure 88 presents microprobe x-ray scans for the same alloy after a 100 hr exposure; no evidence of  $\text{Na}_2\text{SO}_4$  remains.

In order to determine whether the presence of sulfur is necessary for initiation of accelerated oxidation, samples were coated with either  $\text{Na}_2\text{CO}_3$  or  $\text{NaNO}_3$  and exposed under identical environmental conditions. The kinetic curves and micrographs for the  $\text{Na}_2\text{CO}_3$  coated samples are presented in Figures 89 and 90. The constitution and morphology of the carbonate coated oxidized samples were similar to those for sulfate coated samples. The predominant oxide identifiable by x-ray diffraction of the scales was again  $\text{NiO}$ , and the kinetic curves showed that a distinct accelerated form of oxidation had transpired. In comparison to the sulfate coated samples, no internal precipitates could be found in the alloy matrix (see Figure 90). Therefore, it appears that internal precipitate formation is an unnecessary step for the initiation of accelerated oxidation of these alloys and that a fluxing process must have occurred.

The duration of accelerated oxidation for the  $\text{Na}_2\text{CO}_3$  coated samples was significantly less than for  $\text{Na}_2\text{SO}_4$  coated samples. This is explained on the basis of the difference between the rates of vaporization of the two salts. Vaporization data as a function of temperature and ambient oxygen pressure were obtained by coating coupons of Pt with the two salts and monitoring the weight loss in a thermobalance. The vaporization rate of  $\text{Na}_2\text{SO}_4$  was found to be lower than that for  $\text{Na}_2\text{CO}_3$ ; therefore, the sulfate simply remains for a longer period than the carbonate, enabling accelerated oxidation to occur longer.

The  $\text{NaNO}_3$  coated samples, after a weight loss period of ~1-2 min oxidized at rates similar to those for the uncoated alloys in pure  $\text{O}_2$  (Figure 91). The scale consisted of a continuous layer of  $\text{Al}_2\text{O}_3$  containing Ni and Cr probably in solution (Figure 92). The absence of accelerated oxidation probably was caused by the decomposition of the  $\text{NaNO}_3$  into its elements occurring before accelerated oxidation could take place.





B.S.E. (a)



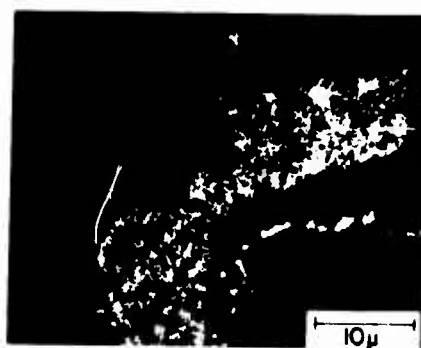
Ni (b)



Al (c)



Cr (d)



S (e)

Figure 87. Cross Section of Scale Formed on  $\text{Na}_2\text{SO}_4$  Coated N18Cr6Al Oxidized in 150 torr  $\text{O}_2$  for 30 min at  $1000^\circ\text{C}$ .

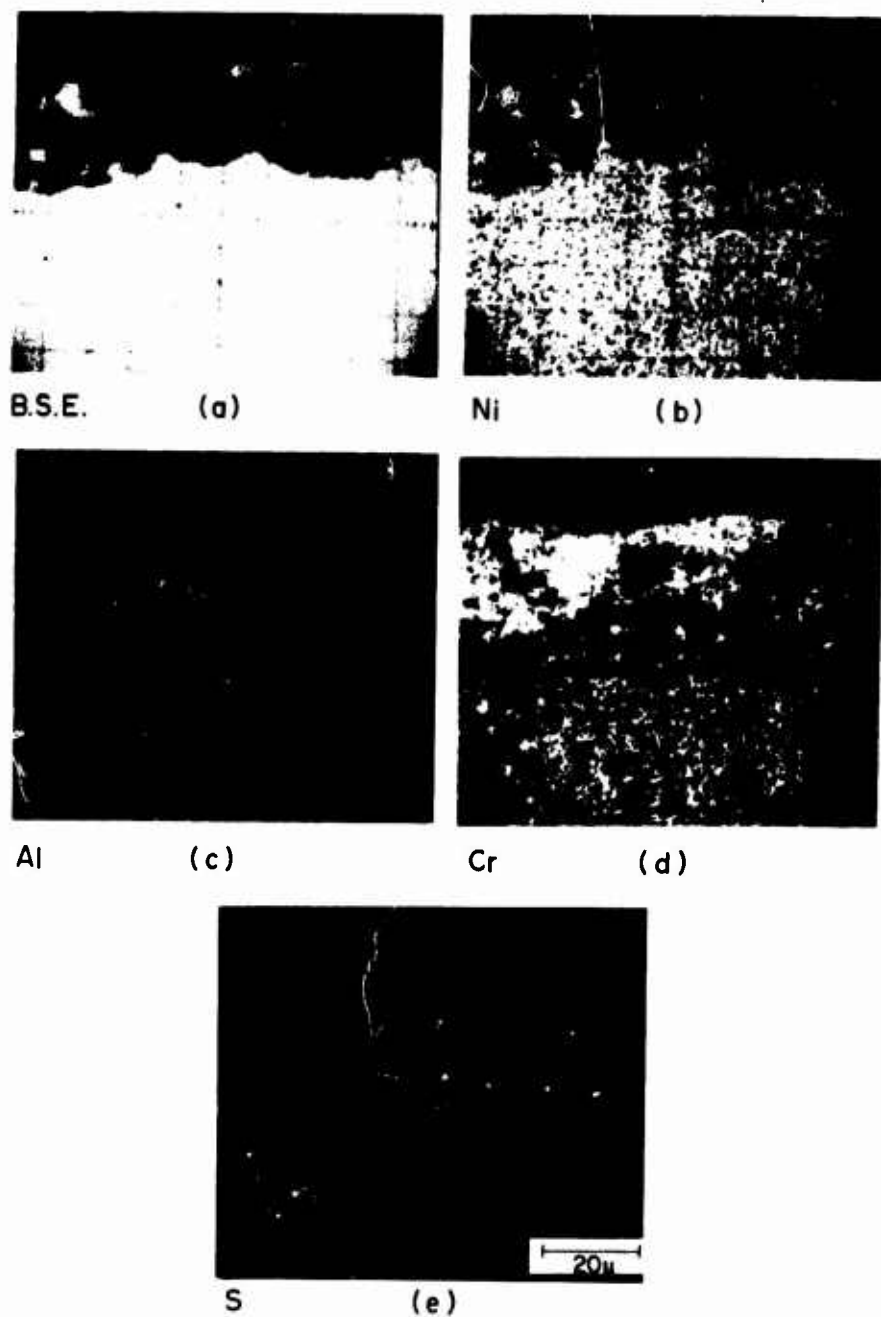


Figure 88. Cross Section of Scale Formed on  $\text{Na}_2\text{SO}_4$  Coated Ni8Cr6Al Oxidized in 150 torr  $\text{O}_2$  for 100 hr at  $1000^\circ\text{C}$ .

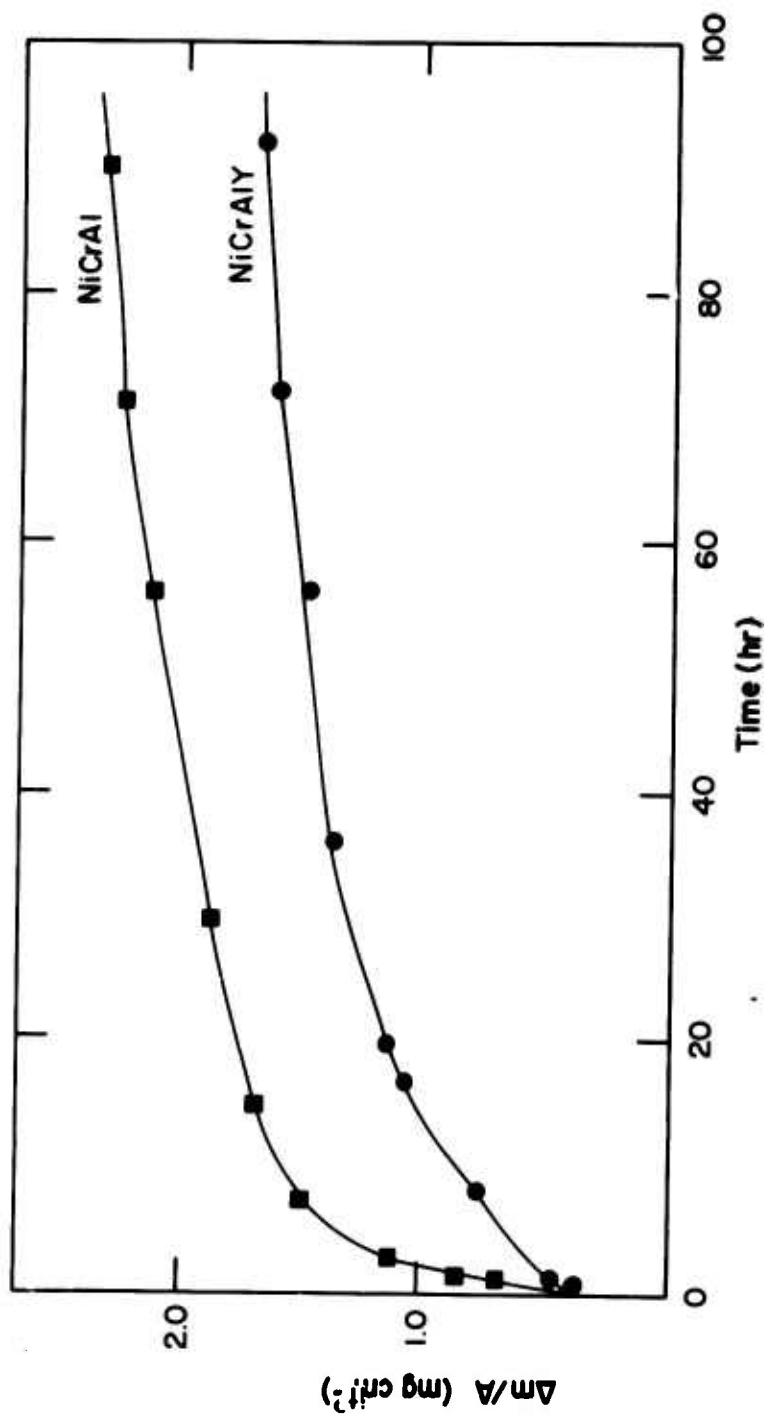


Figure 89. Observed Weight Gain as a Function of Exposure Time During the Oxidation of Na<sub>2</sub>CO<sub>3</sub> Coated Ni8Cr6Al and Ni8Cr6Al0.2Y at 1000°C in 150 torr O<sub>2</sub>.

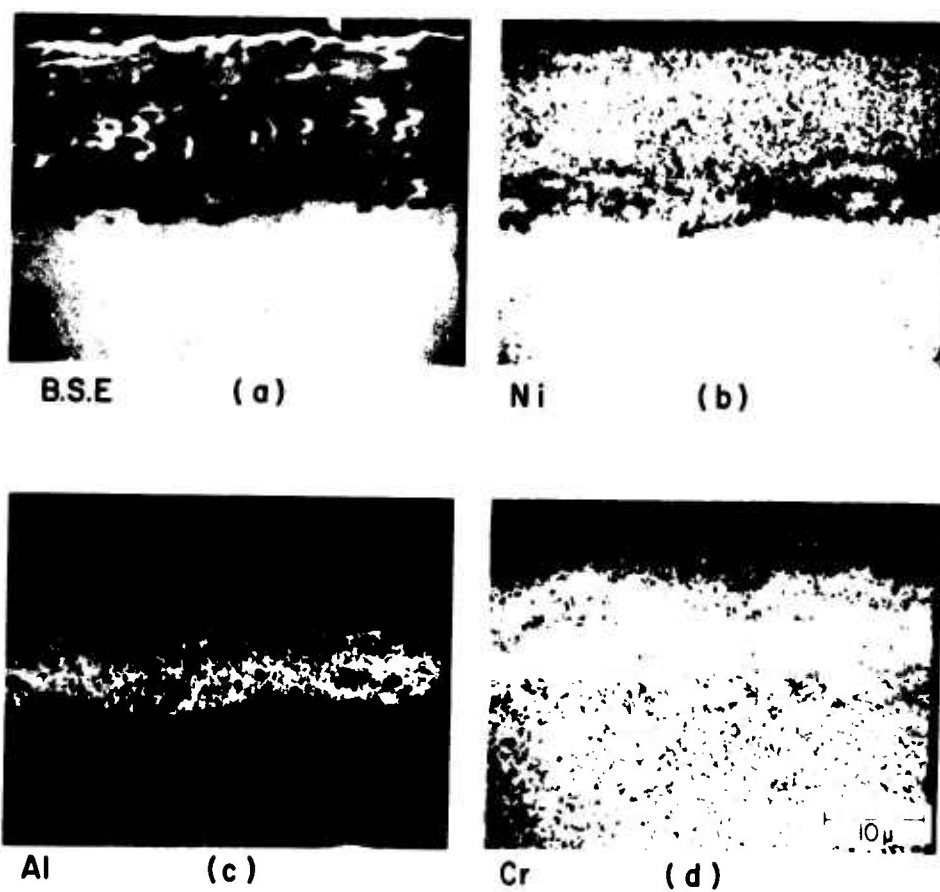


Figure 90. Cross Section of Scale Formed on  $\text{Na}_2\text{CO}_3$  Coated Ni8Cr6Al after 100 hr in 150 torr  $\text{O}_2$  at  $1000^\circ\text{C}$ .

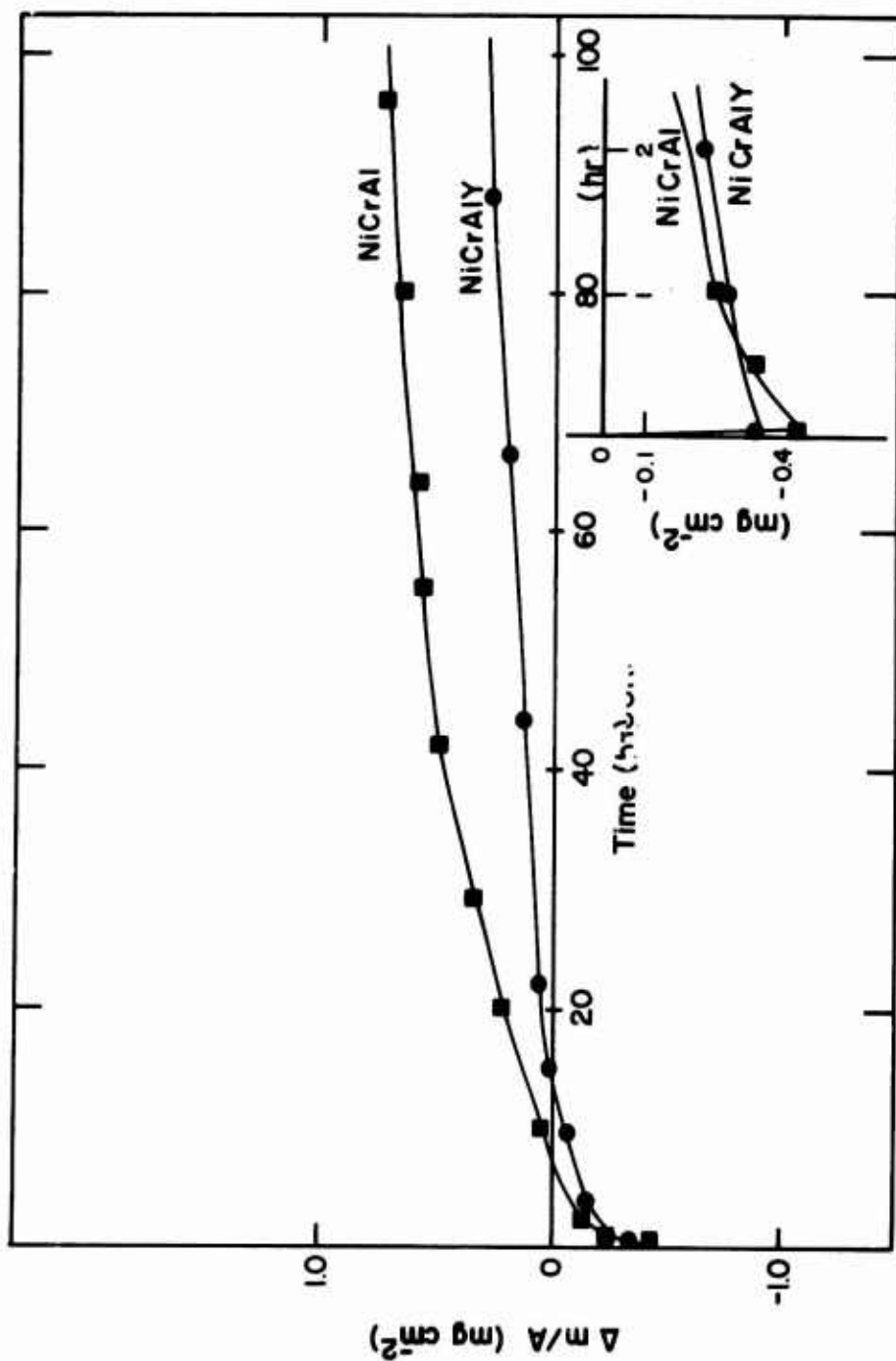


Figure 91. Observed Weight Gain as a Function of Exposure Time during Oxidation of  $\text{NaNO}_3$  Coated Ni8Cr6Al and Ni8Cr6Al0.2Y at  $1000^\circ\text{C}$  in 150 torr  $\text{O}_2$ .

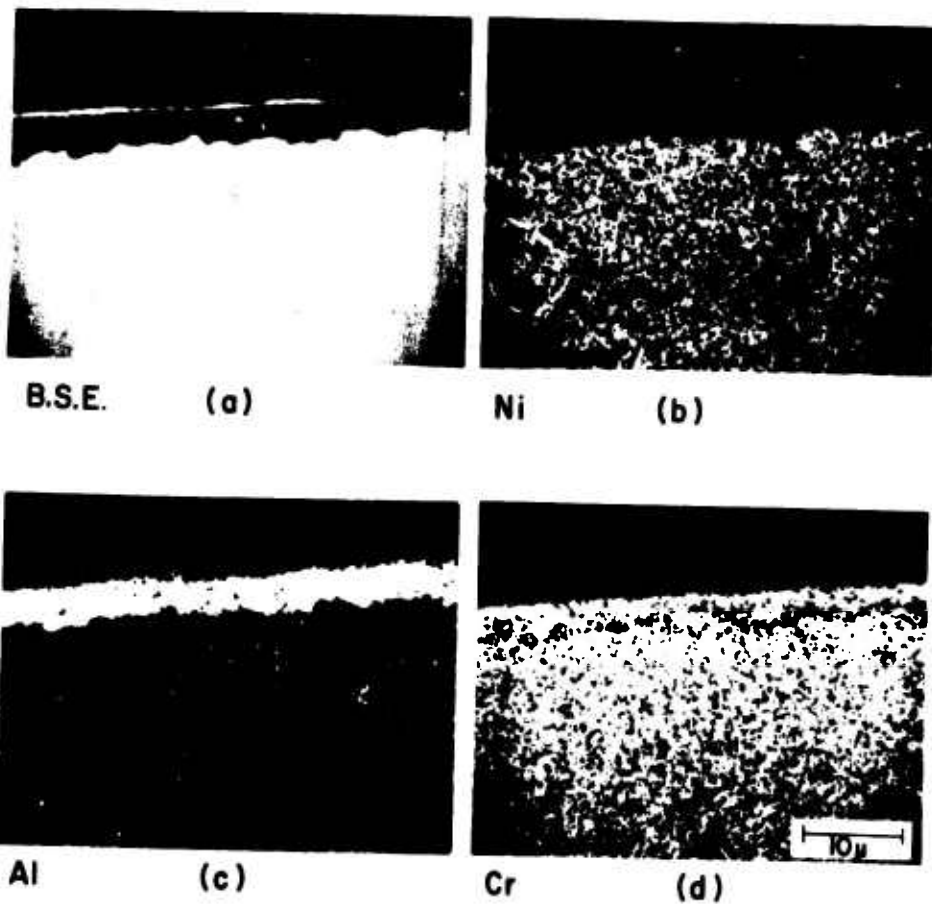


Figure 92. Cross Section of Scale Formed on  $\text{NaNO}_3$  Coated Ni8Cr6Al after 150 hr in 150 torr  $\text{O}_2$  at  $1000^\circ\text{C}$ .

## Summary and Conclusions

The above results appear to refute the hypothesis<sup>(46,47)</sup> that the critical step in accelerated oxidation is the formation of internal sulfides. No evidence of internal precipitates was found in oxidized alloys which had been coated with  $\text{Na}_2\text{CO}_3$ . Therefore, internal precipitate formation was not a necessary step for the initiation of accelerated oxidation. Instead, accelerated oxidation was caused by a basic fluxing mechanism.

### DEGRADATION OF Ni8Cr6Al AT 1000°C IN GASEOUS ENVIRONMENTS CONTAINING CARBON OR SULFUR

Degradation of superalloys has become an increasingly important problem as gas turbine environments have become more severe. Several types of alloy degradation can occur, depending upon the use temperature and corrosive environment. The purely oxidizing environment, i.e., air or oxygen, causes the least severe degradation because the  $\text{Al}_2\text{O}_3$  layer which forms on the alloy upon oxidation has extremely low diffusivities for O and Al ions. An important limitation of these  $\text{Al}_2\text{O}_3$  scales is their tendency to spall upon thermal cycling; and techniques are now being developed to prevent such spalling.<sup>(48)</sup>

A much more severe environment than air or oxygen is one which contains hot-salts, e.g.,  $\text{NaCl}$ ,  $\text{Na}_2\text{SO}_4$ ,  $\text{Na}_2\text{CO}_3$ . As described earlier these salts deposit on the normally protective  $\text{Al}_2\text{O}_3$  surrounding the alloy. Local dissolution of the oxide ensues through either basic fluxing in which  $\text{NaAlO}_2(l)$  is formed or acidic fluxing in which  $\text{Al}_2(\text{SO}_4)_3(l)$  is formed.<sup>(44)</sup> The result is the formation of a porous, nonprotective oxide which allows rapid attack of the alloy to take place. Results of experiments conducted in hot salt environments have already been presented in this report.

Highly reducing environments (i.e., environments which contain low oxygen pressures) containing  $\text{H}_2$ , C, and S can also be particularly destructive. Protective scales do not form in these environments; instead, the C and S penetrate deep within the metal and form internal carbides and sulfides.

Since a number of nickel sulfides are in liquid form at moderate temperatures ( $\sim 850$ – $900^\circ\text{C}$ ),  $\text{H}_2/\text{H}_2\text{S}$  attack of Ni-base superalloys can cause rapid deterioration of their mechanical properties.

The present investigation was conducted in order to characterize the attack of an experimental Ni-Cr-Al alloy (an alloy which is generic to the superalloys) in highly reducing environments containing  $\text{H}_2$ , C, and S. In particular the high temperature corrosion behavior of Ni-8w/o Cr-6w/o Al in  $\text{CO}/\text{CO}_2$  and  $\text{H}_2/\text{H}_2\text{S}$  environments was investigated at  $1000^\circ\text{C}$ .

### Experimental

Sample coupons ( $\sim 1 \times 0.6 \times 0.1$  cm) were abraided through 600-grit SiC, measured for surface area, ultrasonically cleaned in acetone and methanol, and weighed prior to exposure to the corrosive environment. Laboratory grade  $\text{O}_2$ ,  $\text{CO}/\text{CO}_2$ , and  $\text{H}_2/\text{H}_2\text{S}$  gases were used. The coupons were quickly lowered into the preestablished corrosive environment at 150 torr total pressure. The kinetics of attack were monitored continuously with an electrobalance having a sensitivity of  $\sim 10$ – $20$   $\mu\text{g}$ . Details of the furnace-balance system used in this study have been given previously.<sup>(11)</sup> The corrosion products and morphologies were characterized by x-ray diffraction, microscopy, and electron microprobe analysis techniques.

### Results and Discussion

#### Degradation in $\text{CO}/\text{CO}_2$ Environments

A  $\text{CO}/0.45$  v/o  $\text{CO}_2$  gas mixture, which establishes an equilibrium  $P_{\text{O}_2}$  of  $10^{-18}$  atm at  $1000^\circ\text{C}$  was used. Figure 93 presents light micrographs depicting the nature of attack after a 100 hr exposure at  $1000^\circ\text{C}$ . Figure 93(a) reveals the depth of carbon penetration; grain boundary and intragranular carbides are formed throughout the sample. A noncoherent porous oxide scale was formed consisting of external  $\text{Cr}_2\text{O}_3$  islands containing free Ni particles and an internal porous  $\text{Al}_2\text{O}_3$  scale. Free Ni rather than NiO was found because the ambient  $P_{\text{O}_2}$  was less than the equilibrium  $P_{\text{O}_2}$  for NiO formation, but



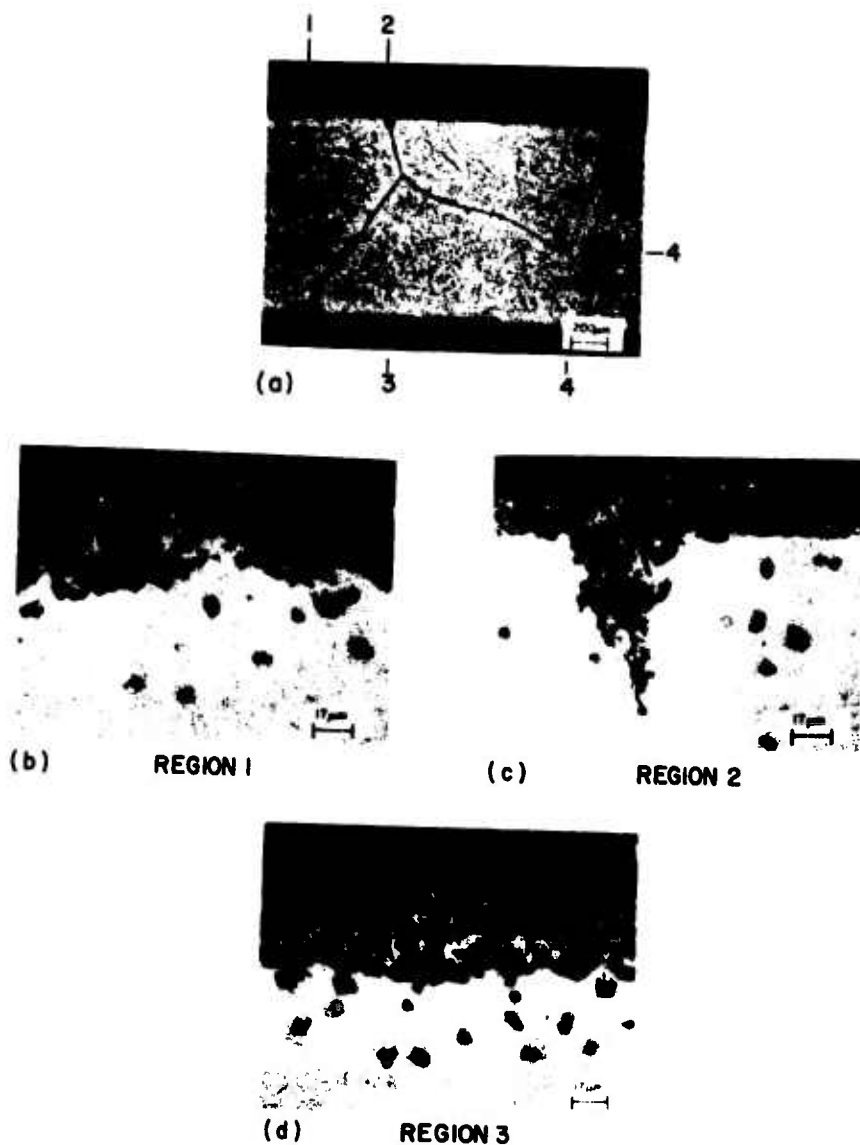


Figure 93. Optical Micrographs of Specimen Exposed to a CO/CO<sub>2</sub> Environment for 100 hr at 1000°C.

greater than that for  $\text{Cr}_2\text{O}_3$  and  $\text{Al}_2\text{O}_3$  formation. The attack is nonuniform and particularly extensive at the grain boundaries, as shown in Figure 93 (c) (Region 2). Figures 94-97 present microprobe scans for four regions similar to those shown in Figure 93(a) (Regions 1-4), confirming the presence of an internal  $\text{Al}_2\text{O}_3$  layer, the presence of an outer Al-rich  $\text{Cr}_2\text{O}_3$  layer containing the Ni particles, and the irregular nature of the attack.

Figure 97 is a microprobe scan of Region 4 confirming the presence of grain boundary and intragranular Cr carbides. SEM-energy-dispersive analysis of x-rays has revealed that the triple-point regions consist exclusively of Cr carbides and that the region surrounding these carbides is depleted in Cr and enriched in Al.

#### Degradation in $\text{H}_2/\text{H}_2\text{S}$ Environments

A  $\text{H}_2/5.18 \text{ v/o } \text{H}_2\text{S}$  mixture which establishes a  $P_{\text{S}_2}$  of  $1.5 \times 10^{-2}$  atmat at  $1000^\circ\text{C}$  was used. Figure 98 presents two micrographs depicting the extensive attack which is found after a 1 hr exposure. As shown in Figure 98(a), the attack was relatively uniform, except for the presence of stringers in advance of the reaction front. Figures 98(b) and 99 reveal the typical corrosion microstructure, consisting of internal Cr sulfide stringers in advance of a Ni sulfide (probably  $\text{Ni}_3\text{S}_2$ ) reaction front. The Ni sulfide contains Ni particles as well as large Al-rich Cr sulfide blocks. A thick  $\text{Al}_2\text{O}_3$  scale containing Cr, Ni, and S was formed on top of the Ni sulfide layer by oxidizing in pure  $\text{O}_2$  for 15 hr after the 42 min exposure to  $\text{H}_2/\text{H}_2\text{S}$ .

#### Comparison of Corrosion Rates and Microstructures in $\text{O}_2$ , $\text{Na}_2\text{SO}_4/\text{O}_2$ , $\text{CO}/\text{CO}_2$ , and $\text{H}_2/\text{H}_2\text{S}$ Environments

Figure 100 compares the corrosion rates and microstructure of Ni8Cr6Al in  $\text{O}_2$ ,  $\text{Na}_2\text{SO}_4/\text{O}_2$ ,  $\text{CO}/\text{CO}_2$ , and  $\text{H}_2/\text{H}_2\text{S}$  environments at  $1000^\circ\text{C}$ . Oxidation kinetics in pure  $\text{O}_2$  were extremely slow because of the formation of a coherent-protective  $\text{Al}_2\text{O}_3$  scale on the alloy surface [Figure 100 (a)]. The parabolic rate constant is  $8 \times 10^{-11} \text{ g}^2\text{cm}^{-4}\text{sec}^{-1}$ , which is in agreement with published values. (48,49)

Reproduced from  
best available copy.

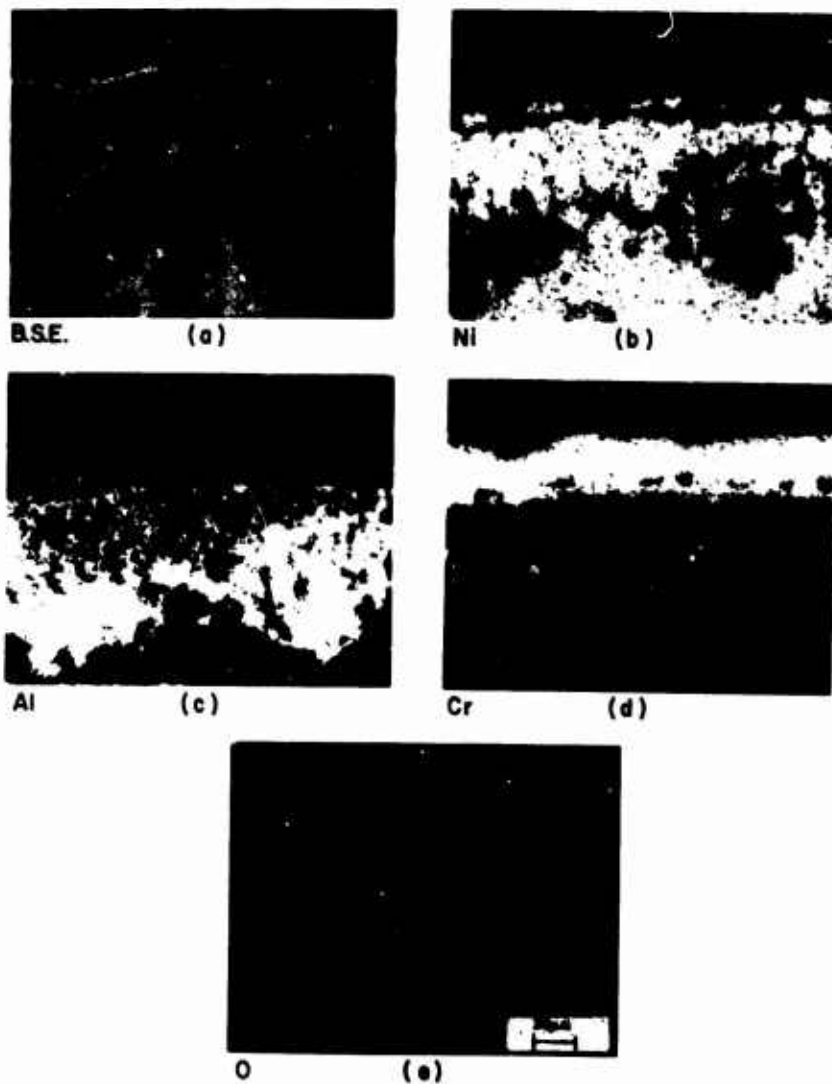


Figure 94. Microprobe Scans of Region 1 in the Preceding Figure  
Depicting Thick Al Rich  $\text{Cr}_2\text{O}_3$  Layer with  $\text{Al}_2\text{O}_3$  Internal  
Oxidation.

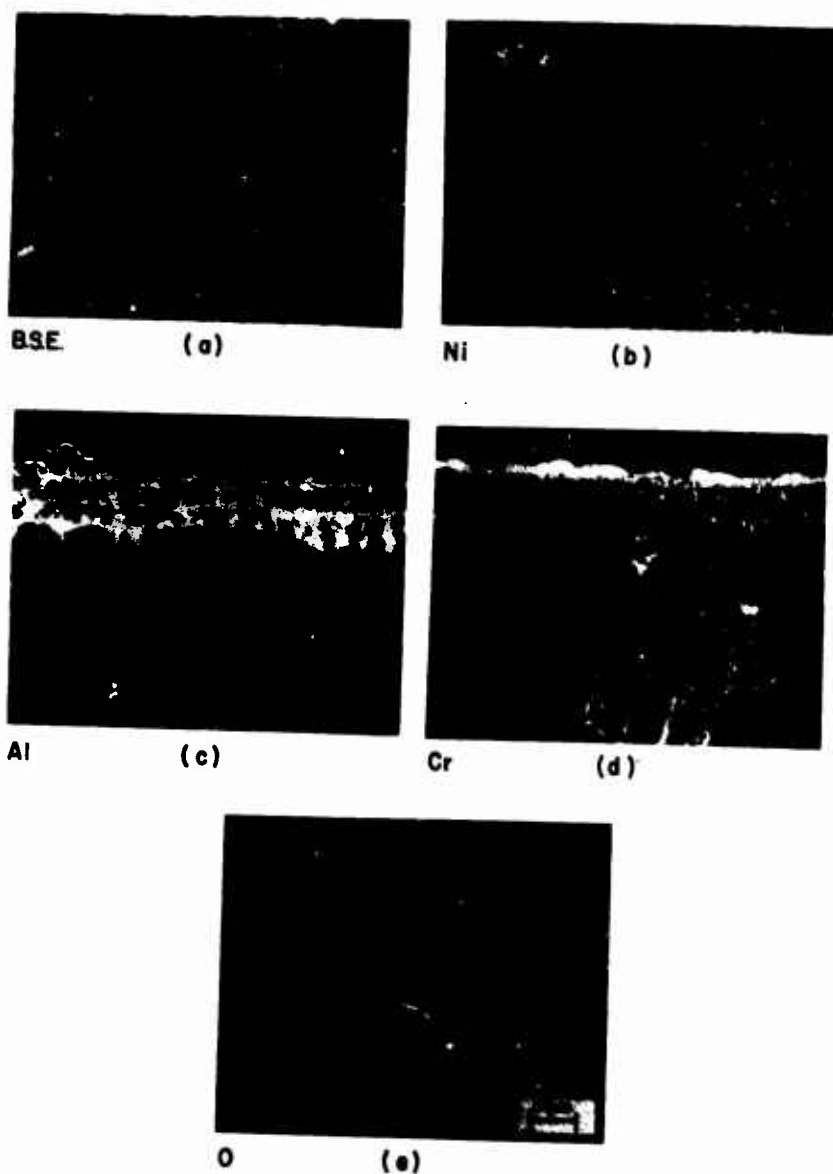
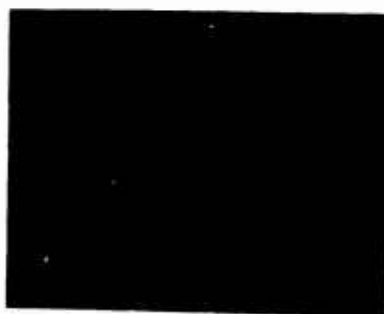


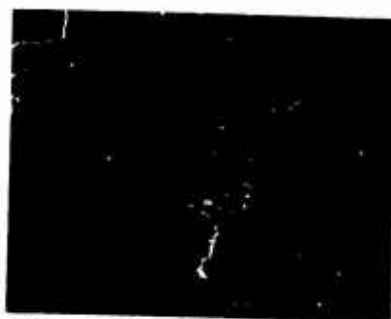
Figure 95. Microprobe Scans of Region 3 in Figure 93 Depicting Multiple Internal  $\text{Al}_2\text{O}_3$  Layers.



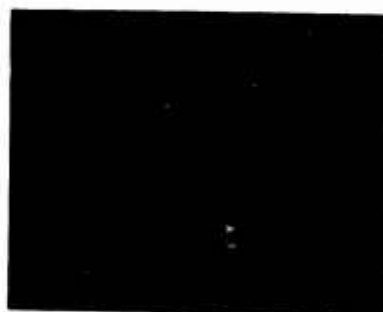
B.S.E. (a)



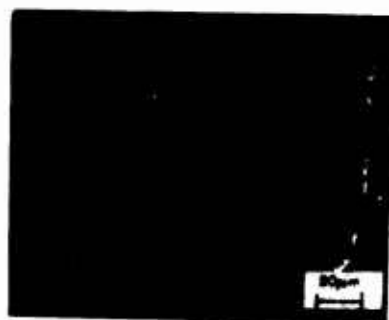
Ni (b)



Al (c)



Cr (d)



O (e)

Figure 96. Microprobe Scans of Region 2 in Figure 93 Depicting Grain Boundary Penetration of  $\text{Al}_2\text{O}_3$ .

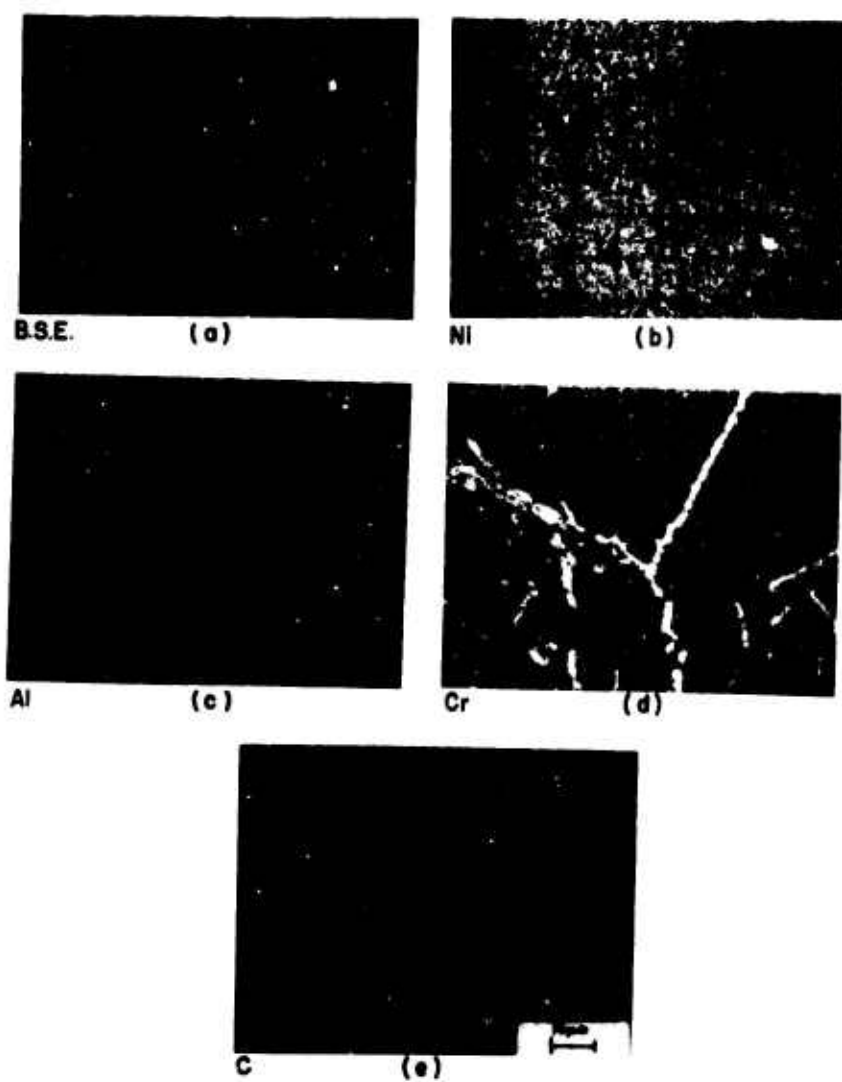
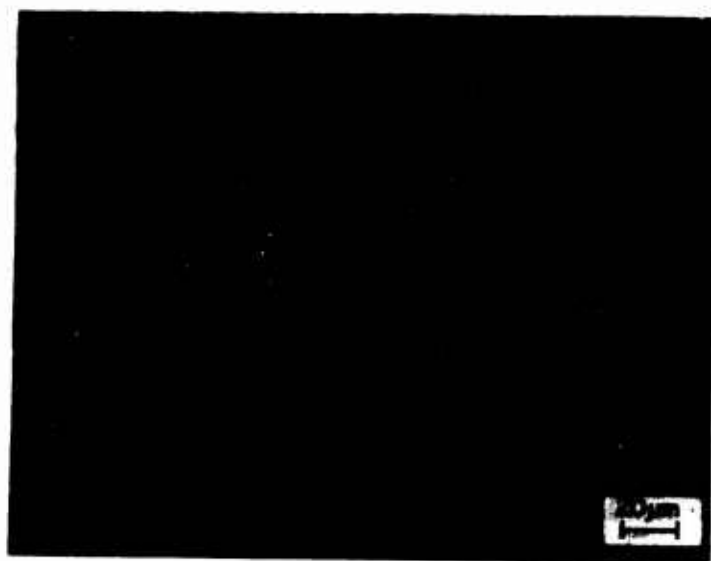


Figure 97. Microprobe Scans of Region 4 in Figure 93 Revealing Grain Boundary and Intragranular Carbides.



(a)



(b)

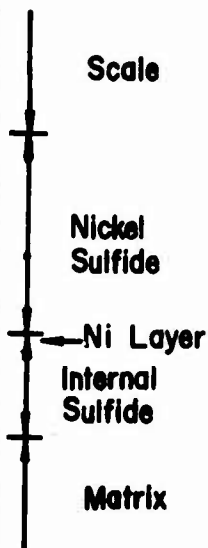


Figure 98. Optical Micrographs Showing the Formation of Sulfides after a 1 hr Exposure to a  $H_2/H_2S$  Environment at  $1000^\circ C$ .

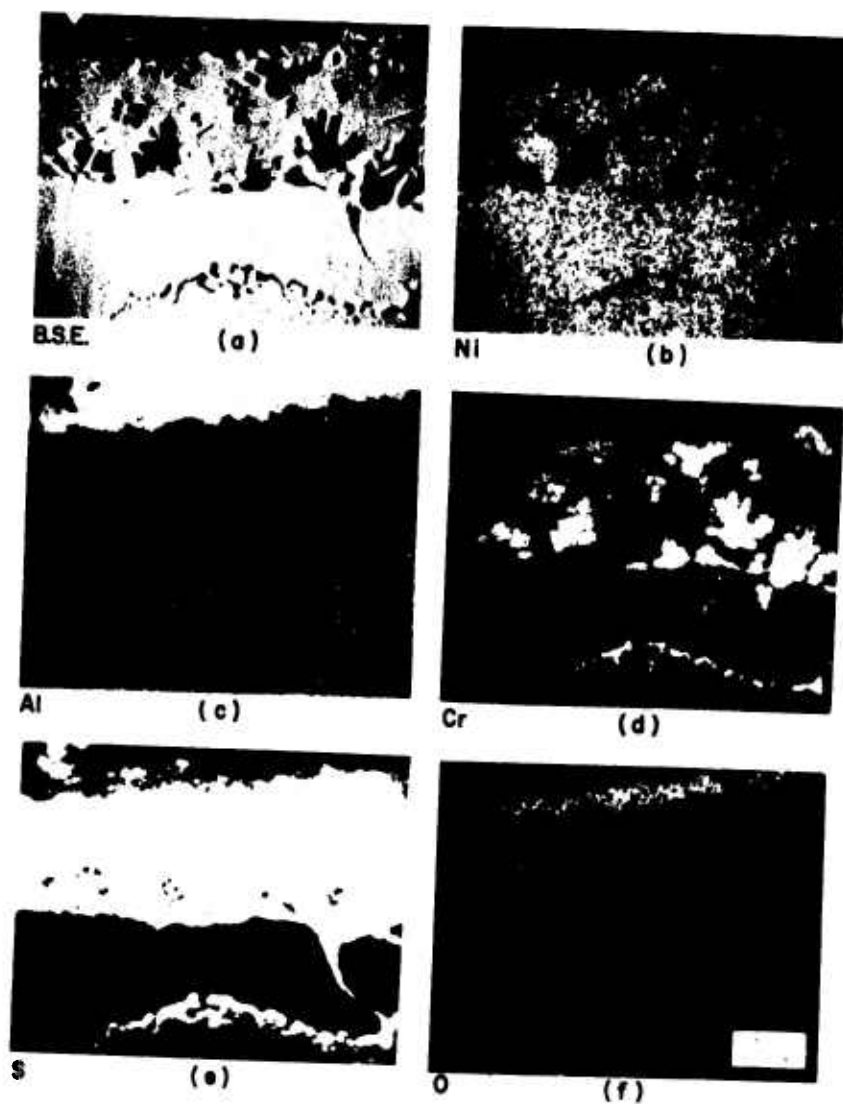


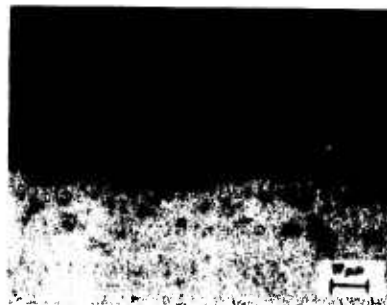
Figure 99. Microprobe Scans of Sulfidized Region after 42 min in  $H_2/H_2S$  Followed by a 15 hr Exposure to  $O_2$  at  $1000^\circ C$ . Note the Thick  $Al_2O_3$  Scale Formed.



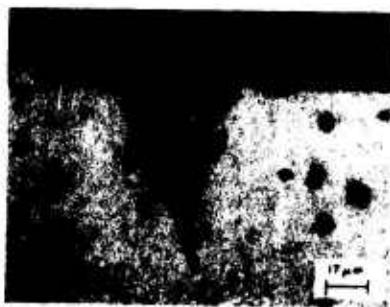
Reproduced from  
best available copy.



(a)  $O_2$ , 100 hr



(b)  $Na_2SO_4/O_2$ , 100hr



(c)  $CO/CO_2$ , 100hr



(d)  $H_2/H_2S$ , 0.5hr

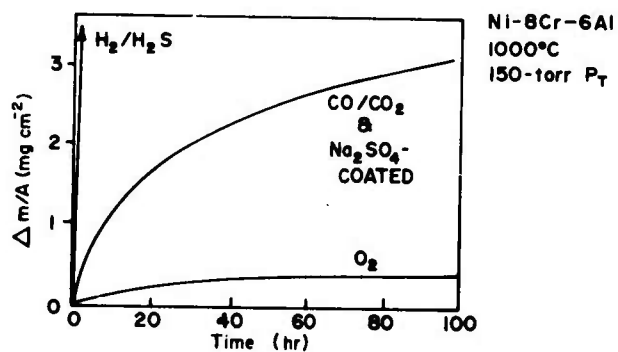


Figure 100. Comparison of Corrosion Rates and Microstructures for Specimens Exposed to  $O_2$ ,  $Na_2SO_4/O_2$ ,  $CO/CO_2$ , and  $H_2/H_2S$  Environments at 1000°C.

The kinetics of attack for  $\text{Na}_2\text{SO}_4$  coated samples described earlier in this report were more rapid than those in pure  $\text{O}_2$  due to the basic fluxing<sup>(44)</sup> of the scale in which liquid  $\text{NaAlO}_2$  is formed. The outer scale shown in Figure 100(b) is a porous  $\text{Al}_2\text{O}_3$  layer containing Na; the inner scale is a thin protective layer of  $\text{Al}_2\text{O}_3$  not fluxed by the hot salt. Internal Cr sulfides are found in the alloy matrix.

Oxidation kinetics in  $\text{CO}/\text{CO}_2$  environments were essentially the same as those in  $\text{Na}_2\text{SO}_4$  environments. The scales (as described earlier) consisted of external Al-rich  $\text{Cr}_2\text{O}_3$  islands containing Ni particles atop a porous  $\text{Al}_2\text{O}_3$  subscale. The oxide scale was nonprotective. The nonlinear reaction kinetics shown in Figure 100 are probably controlled by carbon diffusion along grain boundaries in the alloy matrix.

Oxidation kinetics in  $\text{H}_2/\text{H}_2\text{S}$  environments were extremely rapid and were probably controlled by S diffusion through the liquid Ni sulfide layer shown in Figure 100(d). Sulfides were found at great depths in the alloy matrix indicating that S diffusion was extremely rapid.

#### Summary and Conclusions

The high temperature corrosion of an experimental Ni-Cr-Al alloy was investigated in  $\text{CO}/\text{CO}_2$  and  $\text{H}_2/\text{H}_2\text{S}$  environments at  $1000^\circ\text{C}$ . Rapid rates of attack were observed in both environments; however, the  $\text{H}_2/\text{H}_2\text{S}$  environment is more severe, probably because of liquid sulfide formation on the alloy surface. Internal carbides and sulfides were found at great depths within the alloy matrix. A comparison between rates of attack and corrosion microstructures was made for four environments,  $\text{O}_2$ ,  $\text{Na}_2\text{SO}_4/\text{O}_2$ ,  $\text{CO}/\text{CO}_2$  and  $\text{H}_2/\text{H}_2\text{S}$ . The rates of attack in  $\text{H}_2/\text{H}_2\text{S}$  were much more rapid than those in the other environments. The rates in  $\text{Na}_2\text{SO}_4/\text{O}_2$  and  $\text{CO}/\text{CO}_2$  were nearly equal, and the rates in pure  $\text{O}_2$  were considerably lower than those in the more severe environments.

## SECTION IV

### TRANSPORT PROPERTIES OF HIGH-TEMPERATURE OXIDES

#### HIGH-TEMPERATURE ELECTRICAL PROPERTIES OF $\text{SiO}_2$

Of fundamental importance to the understanding of the oxidation of silica-forming materials is the elucidation of the mechanism of oxygen transport through  $\text{SiO}_2$ . This goal has proved to be an elusive one; at present, there is little agreement on either the atomistic interpretation of the phenomenon or the reliability of the various experimental methods available for its study. This situation is aggravated by the complexities of the Si-O phase diagram and the fact that the results of many past studies of "vitreous silica" are not directly comparable because the investigators used dissimilar types of silica.

The electrical properties of  $\text{SiO}_2$  have been of interest since at least 1886 when Jacques Curie measured the direct current resistivity of natural quartz crystals. This and other early measurements were sufficient to indicate the major features of conduction in this material, such as the dependence of the resistivity on total time of current flow. Curie was able to quantify the exponential nature of this dependence, while Warburg and Tegetmeier clearly demonstrated that the major contribution to conduction was the transport of sodium impurity ions. Transport of sodium has also been observed in most types of vitreous silica; therefore, to obtain any useful information concerning the mechanism of oxygen transport in  $\text{SiO}_2$  through the observation of electrical phenomena, sample material of unusual purity must be used, or experiments in which the impurity-ion conduction is minimized must be conducted. Experimental techniques have been used to minimize the impurity effect since ultrahigh purity  $\text{SiO}_2$  was not available until recently.

Recently, techniques have been developed for preparation of ultrapure  $\text{SiO}_2$  having negligible hydroxyl and metallic impurity contents. The purpose of the present investigation was to make high-temperature electrical measurements on this ultrapure material to determine the conductivity parameters necessary to predict the magnitude of oxygen permeation through  $\text{SiO}_2$ , and to predict the effect of dopant additions to the  $\text{SiO}_2$  network.

## Results

Electrical properties such as total ac conductivity, oxygen gradient emf, and Wagner dc polarization conductivity<sup>(50)</sup> were investigated in the temperature range 1300-1550°C on disc-shaped SiO<sub>2</sub> samples (~1.1 cm diam and 0.5 cm thickness). The synthetic SiO<sub>2</sub> (obtained from Thermal Syndicate) was amorphous and of ultrahigh purity, containing only trace amounts of metallic and hydroxyl ions.

### AC Conductivity Measurements

AC conductivity measurements were made on symmetric cells of the type Pt|P<sub>O<sub>2</sub></sub>|SiO<sub>2</sub>|P<sub>O<sub>2</sub></sub>|Pt|, in which the P<sub>O<sub>2</sub></sub> was established with the use of dried O<sub>2</sub>/Ar and CO/CO<sub>2</sub> gas mixtures. A three terminal, guarded electrode technique employing Pt electrodes was used to ensure measurement of bulk conductivity. Figure 101 is a plot of log  $\sigma_T$  vs 1000/T at an oxygen partial pressure of 10<sup>-1</sup> atm at 760 torr total pressure. The activation energy changes rapidly from the low-temperature value of 0.72 eV (or ~17 kcal/mole) to ~2.93 eV (or ~68 kcal/mole). The lower value is probably representative of the activation energy of the mobility of the impurity controlled species. Figure 102 is a plot of the ac conductivity as a function of P<sub>O<sub>2</sub></sub> at two temperatures. Three distinct conductivity-P<sub>O<sub>2</sub></sub> domains are apparent: (1) a relatively P<sub>O<sub>2</sub></sub>-independent conductivity region which dominates most of the P<sub>O<sub>2</sub></sub> range especially at 1400°C, (2) a low-P<sub>O<sub>2</sub></sub> region where the conductivity approaches a P<sub>O<sub>2</sub></sub><sup>-1/4</sup> dependence, and (3) a high-P<sub>O<sub>2</sub></sub> region where the conductivity approaches a P<sub>O<sub>2</sub></sub><sup>1/4</sup> dependence. The appearance of a three-domain log  $\sigma_T$  vs log P<sub>O<sub>2</sub></sub> plot suggests that SiO<sub>2</sub> is an impurity controlled ionic conductor over a broad P<sub>O<sub>2</sub></sub> range. Deviations from ionic character appearing at very low P<sub>O<sub>2</sub></sub>'s are due to electron conductivity, and those at the high P<sub>O<sub>2</sub></sub>'s are due to hole conductivity.

### Oxygen-Gradient EMF Measurements

In order to test this hypothesis, oxygen-gradient emf measurements were made on cells of the type Pt|P<sub>O<sub>2</sub></sub>(I)|SiO<sub>2</sub>|P<sub>O<sub>2</sub></sub>(II)|Pt. If the open circuit emf of

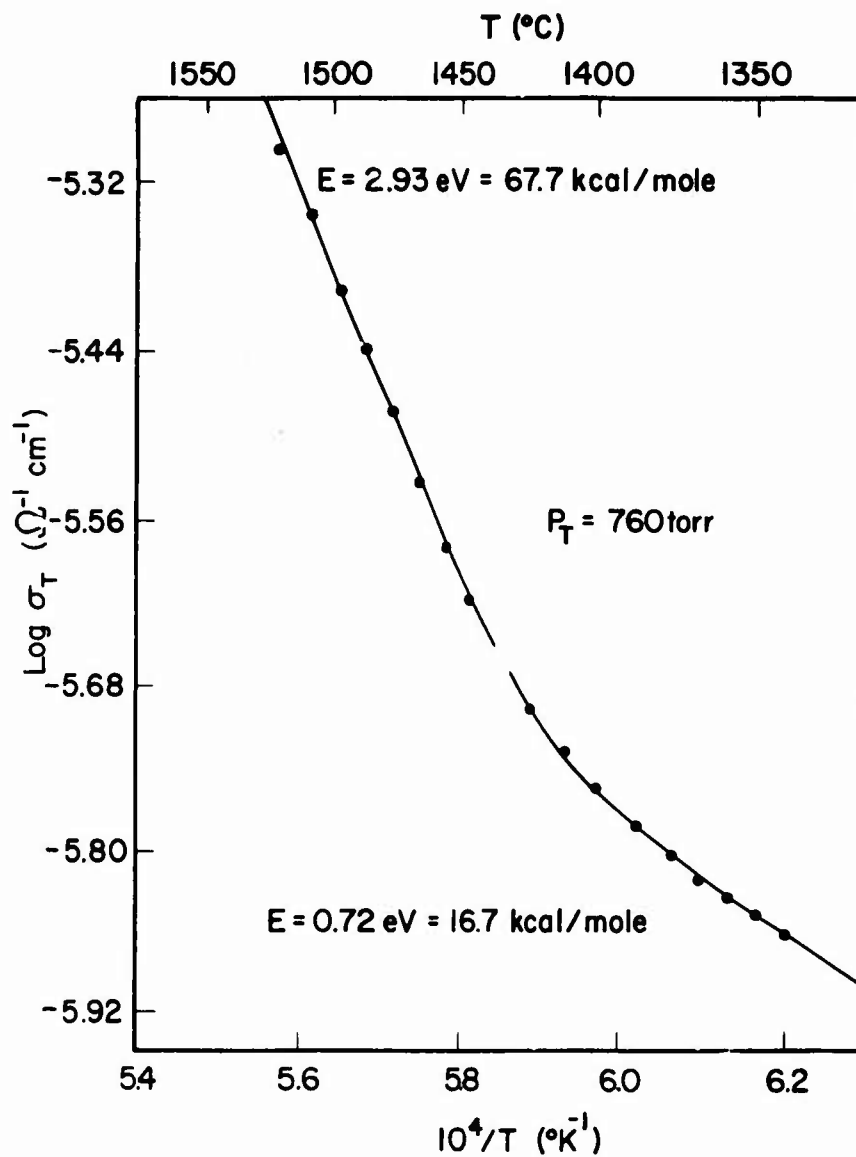


Figure 101. Total ac Conductivity in  $\text{SiO}_2$  as Function of Temperature at  $P_0 = 10^{-1}$  atm.

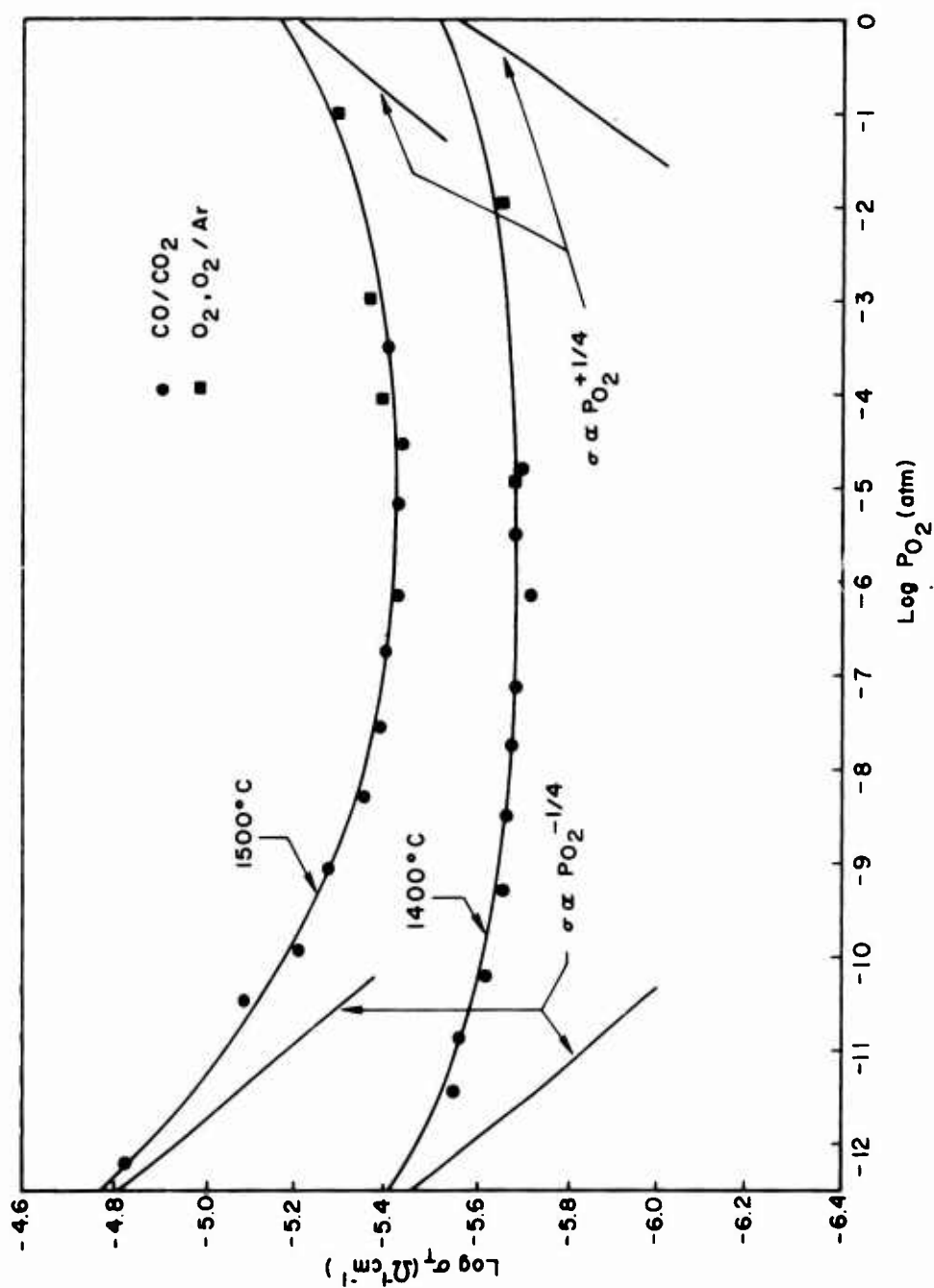


Figure 102. Plot of  $\text{Log } \sigma_T$  as a Function of  $\text{Log } P_{O_2}$  at 1400 and 1500°C, Revealing Mixed Ionic and Electronic Character of  $\text{SiO}_2$ .

this cell is measured and  $P_{O_2}(I)$  and  $P_{O_2}(II)$  are varied, the average ionic transference number ( $\bar{t}_{ion}$ ) can be determined from the relation

$$\bar{t}_{ion} = E_{oc}/E_{TH} \quad (20)$$

where  $E_{oc}$  is the measured open circuit emf and  $E_{TH}$  is the thermodynamic emf given by the equation

$$E = (RT/4F) \log [P_{O_2}(II)/P_{O_2}(I)] \quad (21)$$

where  $R$  is the gas constant,  $T$  is the temperature,  $F$  is Faraday's constant, and  $P_{O_2}(II)$  and  $P_{O_2}(I)$  are the  $P_{O_2}$ 's in the two separate cell compartments. Figure 103 presents a summary of the results of this experiment. The circles represent the experimental data, and the curve corresponds to predictions based upon the ac conductivity data in Figure 102. The agreement between data and predictions confirms the assumption that  $SiO_2$  is a mixed conductor over a broad range of  $P_{O_2}$ .

#### Wagner DC-Polarization Measurements

In order to determine the nature of electronic conduction in  $SiO_2$  Wagner<sup>(50)</sup> dc-polarization measurements in a helium ambient were made on cells of the type Pt,  $M, M_xO | SiO_2 | Pt$ , where the  $M, M_xO$  correspond to the metal-metal oxide coexistence electrodes  $Co/CoO$ ,  $Ta/Ta_2O_5$ , or  $V/V_2O_3$ . These electrodes serve to establish reversible  $P_{O_2}$ 's over a broad range down to the decomposition pressure of  $SiO_2$ . The Pt electrode at the right-hand side of the cell is nonreversible, i.e., blocking to ionic currents. An effective  $P_{O_2}$  can be established at this electrode by applying a constant voltage to the cell. After voltage is applied, the measured current will decay with time to a steady state value which corresponds to the electronic current, given by the equation

$$I = - \frac{RT}{FL} \left\{ \sigma_n^0 \left[ 1 - \exp(-EF/RT) \right] + \sigma_p^0 \left[ \exp(EF/RT) - 1 \right] \right\} \quad (22)$$

where  $I$  is current density,  $L$  is the  $SiO_2$  thickness,  $\sigma_n^0$  and  $\sigma_p^0$  are, respectively, the electron and hole conductivities at the  $P_{O_2}$  corresponding to the

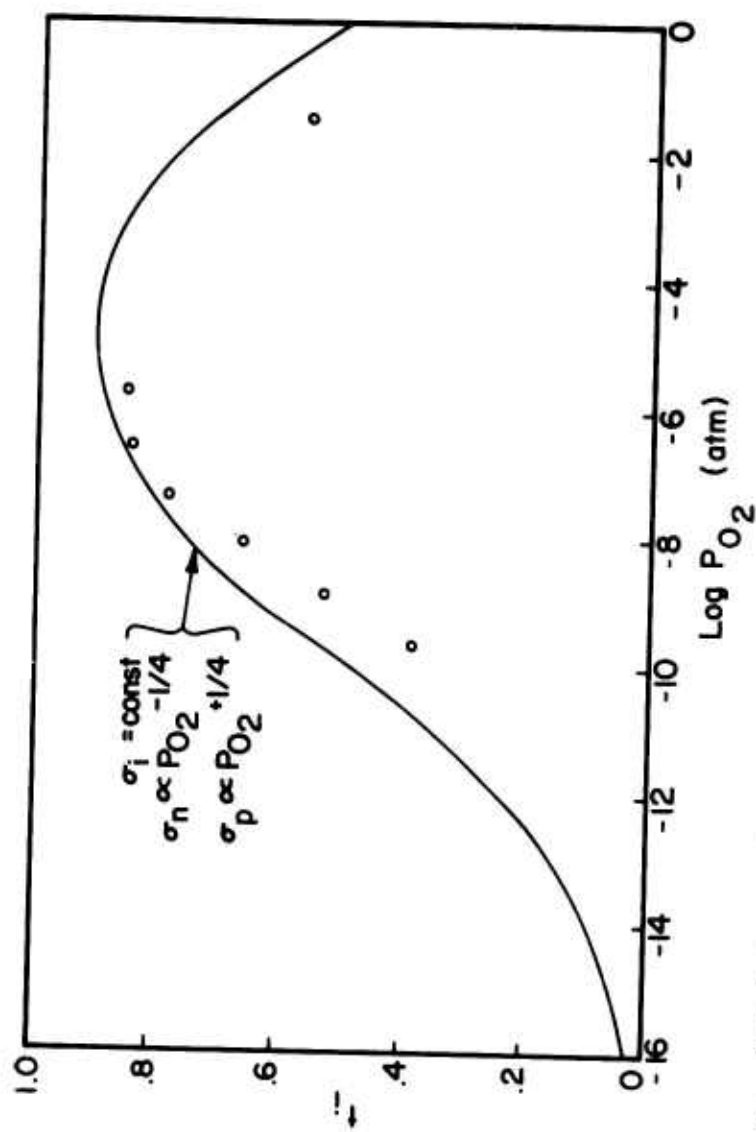


Figure 103. Plot of  $t_i$  as a function of  $\text{Log } P_{O_2}$  for  $\text{SiO}_2$  at  $1500^\circ\text{C}$ . Solid line is  $t_i$  predicted from the conductivity data in Figure 102.



to the reversible electrode, and  $E$  is the applied voltage. The electron and hole conductivities can be obtained from the electronic current through a linearization process developed by Patterson, Bogren, and Rapp.<sup>(51)</sup> By plotting the parameter  $I/[\exp(u)-1]$  vs  $\exp(u)$  (where  $u = EF/RT$ ),  $\sigma_n^0$  and  $\sigma_p^0$  can be obtained from the slope and intercept, respectively. Such a linearization is illustrated in Figure 104, where  $\sigma_n^0$  and  $\sigma_p^0$  are found to be  $10^{-4.863}$  and  $10^{-10.845} \text{ ohm}^{-1} \text{ cm}^{-1}$ , respectively. Figure 105 is a plot of  $\log \sigma_n$  and  $\log \sigma_p$  (different scales) vs  $1000/T$  for the three reversible electrodes used in this study. The electron and hole conductivity values for each electrode were extrapolated to a  $P_{O_2}$  of  $10^{-15}$  atm assuming +1/4 and -1/4 power dependences on the  $P_{O_2}$ . The activation energies for electron and hole conduction at constant  $P_{O_2}$  are obtained from the slopes of the curves shown in Figure 105 and are 5.16 eV for electron conduction and 3.15 eV for hole conduction.

Although  $\sigma_n$  and  $\sigma_p$  are  $P_{O_2}$  dependent, their product is not, due to the cancellation of the +1/4 and -1/4 power  $P_{O_2}$  dependences. The  $\sigma_n \sigma_p$  product is essentially the np product multiplied by a mobility factor. Since the mobilities are weakly temperature dependent over the temperature range of this investigation, a plot of  $\sigma_n \sigma_p$  vs  $1/T$  should give the activation energy for the np product, i.e., the band gap energy at 0°K. A value of 8.31 eV has been calculated from Figure 106, where the  $\sigma_n^0 \sigma_p^0$  product has been plotted for each reversible electrode used.

### Discussion

The data obtained from the above types of experiments exhibit excellent internal consistency. The activation energy for hole conduction obtained from the dc polarization measurements is in good agreement with the high-temperature activation energy for the ac conductivity obtained in Figure 101. The ionic transference number obtained from the emf measurements is in agreement with predictions based upon the ac conductivity data shown in Figure 102. The band gap energy of 8.31 eV is in good agreement with low-temperature predictions by Ishikawa et al.<sup>(52)</sup>

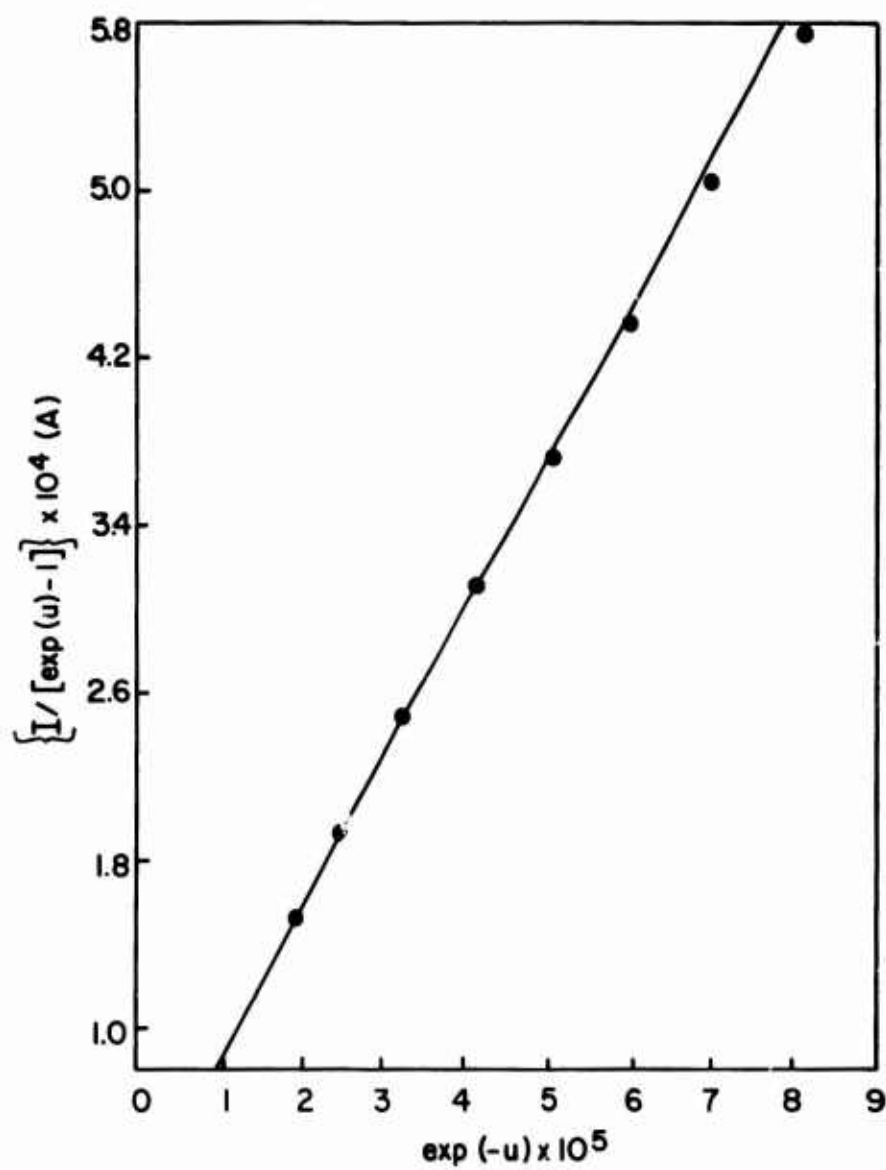


Figure 104. DC Polarization Data: Observed Current ( $I$ ) as Function of Applied Voltage ( $u$ ).

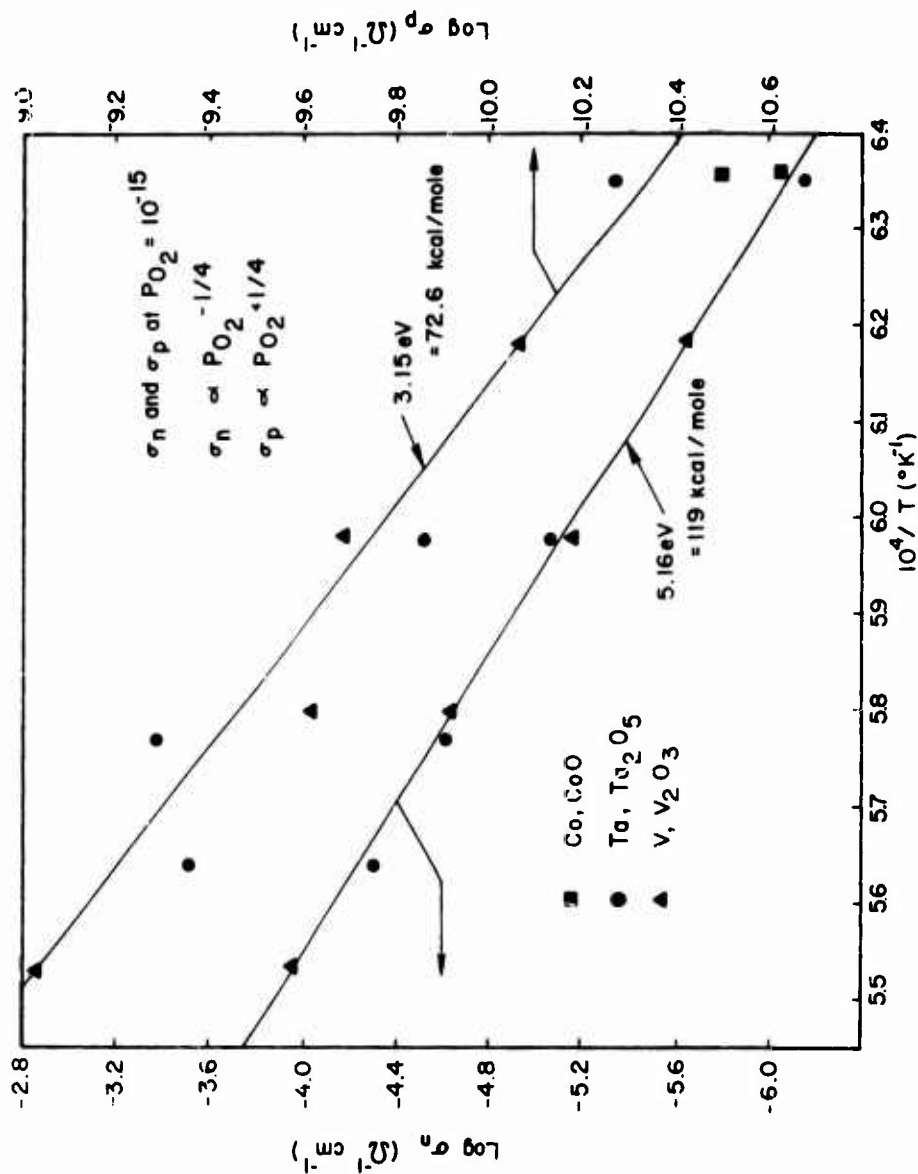


Figure 105. Plot of  $\text{Log } \sigma_n$  and  $\text{Log } \sigma_p$  as a Function of  $1/T$  at  $P_{O_2} = 10^{-15}$  atm.

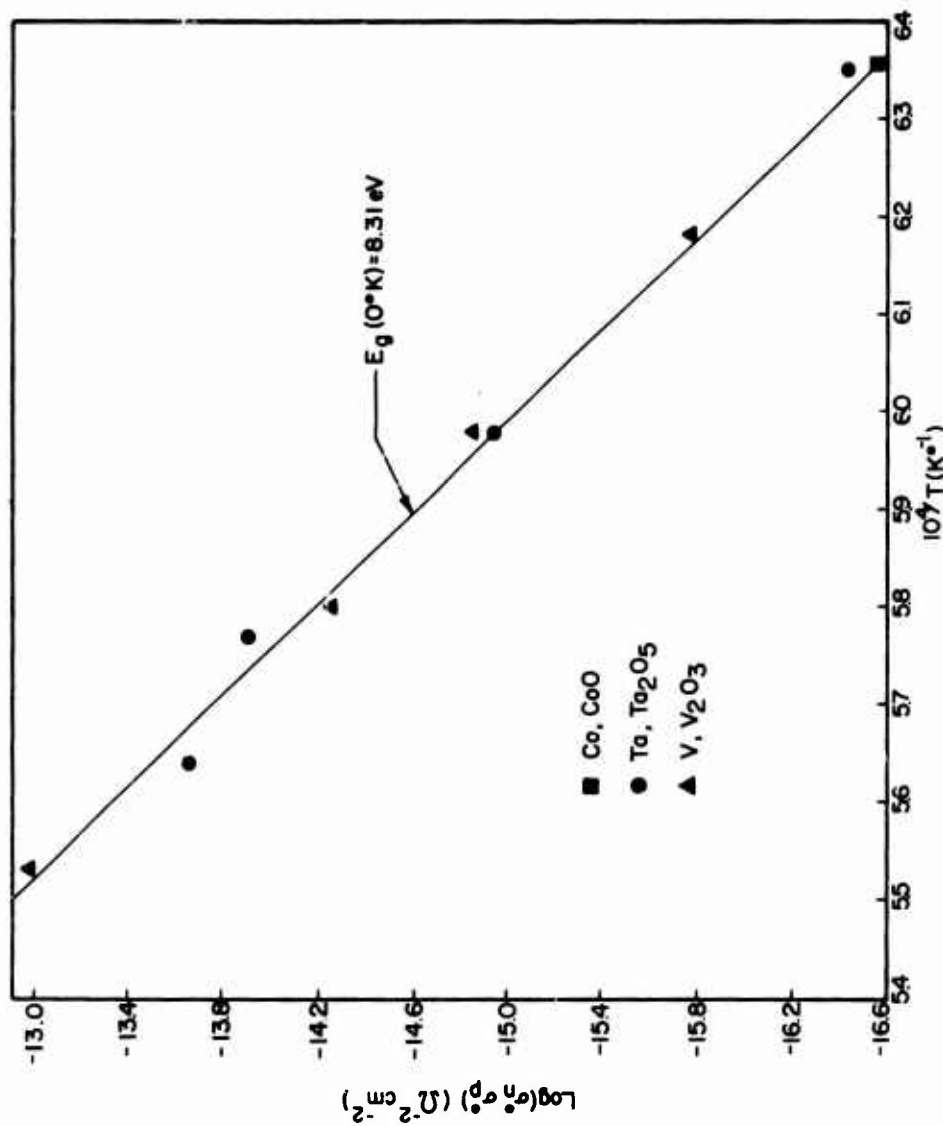


Figure 106. Plot of  $\text{Log } \sigma_n \sigma_p$  as a Function of  $1/T$ , Giving the  $0^\circ\text{K}$  Band Gap Energy.

Bates,<sup>(67)</sup> using a Mo shield around the sample and bias voltages between -10 and +20 V, measured the current between electrodes and chamber walls. The current was measured with and without a sample. Differences in magnitude and temperature dependence of the current were noted when the bias voltage was varied between positive and negative. Current-voltage curves were made but not reported, and some "effective system work functions" were determined. The most interesting conclusion was that for a ThO<sub>2</sub> sample the shunting current due to thermionic emission and gas phase conduction was as great as--if not greater than--the current through the sample; hence, the bulk conductivity was unmeasurable. Some experimental problems were responsible for severe bends or breaks in the curves, but the specific problem could not be identified. The possibility of changes in conduction mechanism (electronic to ionic) was suggested.

The most recent paper by the French group<sup>(69)</sup> provides much useful information. They conducted a thorough study of many of the problems associated with high-temperature research. One of their experiments involved the direct measurement of the leakage currents between hot and cold regions of the furnace and between the electrodes and hot or cold regions of the furnace. The increase in current with increasing temperature was striking, especially between the electrodes and hot regions of the furnace tube, which indicated high emission from the furnace walls. Also, the leakage current was strongly influenced by the bias voltage applied between the electrodes or between the electrodes and the wall. The emission from the furnace walls was shown to contribute heavily to the leakage between measuring probes and could be significantly reduced by application of suitable voltages. The effects of temperature and sample shape were also studied. The increased leakage current at high temperature is strongly dependent upon sample geometry. (In this case the critical factors are the number and location of leakage paths and total area exposed to the furnace wall.) From a series of calculations and from measurements using a number of different gas atmospheres, it was concluded that thermal ionization of the gas phase is not responsible for the leakage currents. By means of a special experimental setup, ZrO<sub>2</sub> was resistance heated in air, and the emission was captured by a cold Faraday cup. Measurements were made of both electron and ion emission by varying the bias voltage and sign.

in 600 torr  $O_2$  is fortuitous. Although the electrical properties of high purity bulk  $SiO_2$  have been adequately described, these properties do not explain the oxidation behavior of silicon or silicon-base materials. It appears that either the electrical properties of bulk  $SiO_2$  differ from those of grown  $SiO_2$  films or the rate of growth of the  $SiO_2$  films is controlled not by an ionic or electronic mechanism but by an electrically neutral transport mechanism--or both.

## DEFECT STRUCTURE OF $\text{Ta}_2\text{O}_5$

The defect structure of  $\text{Ta}_2\text{O}_5$  has been investigated by Kofstad,<sup>(53)</sup> who measured the electrical behavior of samples prepared from oxidized Ta metal powder. On the basis of his results, Kofstad suggested that the predominant defects were oxygen vacancies and electrons at low  $\text{O}_2$  pressures and oxygen interstitials and electron holes at high  $\text{O}_2$  pressures. Kudrak and Sienko,<sup>(54)</sup> who studied the properties of very highly reduced  $\text{Ta}_2\text{O}_5$  ( $\text{Ta}_2\text{O}_{4.73}$ ), observed that this material exhibited metallic conduction behavior at room temperature and below. They suggested that the observed properties arose from a high concentration of Ta interstitials resulting in significant d-level overlap and degenerate electron gas behavior.

Kofstad,<sup>(55)</sup> on the basis of his previous electrical measurements<sup>(53)</sup> and subsequent data on the oxidation behavior of Ta metal, proposed a defect-structure model for  $\text{Ta}_2\text{O}_5$  in which oxygen vacancies were the predominant ionic defect over most of the temperature and  $\text{O}_2$  pressure range of the earlier measurements; however, at  $\text{O}_2$  pressures near 1 atm, the concentration of this species was effectively fixed by the presence of lower valence cation impurities. He further suggested that this situation might result in a significant ionic contribution to the total conductivity in the impurity controlled region.

The present study was initiated to check this hypothesis and to assess quantitatively the departure from stoichiometry occurring in  $\text{Ta}_2\text{O}_5$

### Experimental Procedure

Polycrystalline  $\text{Ta}_2\text{O}_5$  samples were prepared by cold-pressing 99.999% powder (Electronic Space Products, Inc., Los Angeles, California) into discs in a nylon die and sintering them at  $1450^\circ\text{C}$  for 72 hr in air. The resulting pellets were cut into the form necessary for measurement.

Electrical conductivity was measured by a three terminal, guarded electrode technique using a conductance bridge (Wayne Kerr Corp., Montclair, New Jersey) and an external oscillator operating at 10 kHz. Connections to the disc-shaped sample were through several coatings of Pt paste (No. 6082, Engelhard Industries, Murray Hill, New Jersey).

Seebeck coefficients were determined on sample bars  $\approx 3 \times 4 \times 12$  mm with a Pt6Rh-Pt30Rh thermocouple attached at each end. The emf developed across the sample was measured between the 6% Rh leads with a high impedance digital voltmeter, and the Seebeck coefficient was determined from the slope of a plot of  $\Delta E$  (the potential difference) vs  $\Delta T$  (the measured temperature difference between the ends of the sample). The temperature gradients imposed did not exceed  $10^\circ\text{C}$ .

Weight change was measured with a recording microbalance (Model 14-F, Wm Aiksworth & Sons, Inc., Denver, Colorado). This system and the procedures followed are described in detail elsewhere.<sup>(56)</sup>

Ionic transference numbers were obtained by measuring the emf developed across a disc-shaped sample with differing  $\text{O}_2$  pressures at the electrodes. Details of the technique are given in Reference 57.

### Results and Discussion

The conductivity behavior (Figure 107a) is characterized by a broad, relatively pressure independent region at high  $\text{P}_{\text{O}_2}$ 's, with dependences at low pressure varying from about  $-1/4$  to  $-1/6$ . Also, at the highest  $\text{P}_{\text{O}_2}$ 's, there is evidence of p-type behavior, although the data are insufficient for assignment of a pressure dependence. These results are virtually identical to those of Kofstad,<sup>(53)</sup> except that the present measurements show no "anomalies" at  $1380^\circ\text{C}$ ,  $\approx 60^\circ\text{C}$  above the temperature at which transformation of  $\beta$ - to  $\alpha$ - $\text{Ta}_2\text{O}_5$  occurs.

In the results of transference number determinations (Figure 107b), at the high pressures where the conductivity shows a minimum,  $t_i$  is nearly unity. A possible model for explaining the results of Figure 107 is



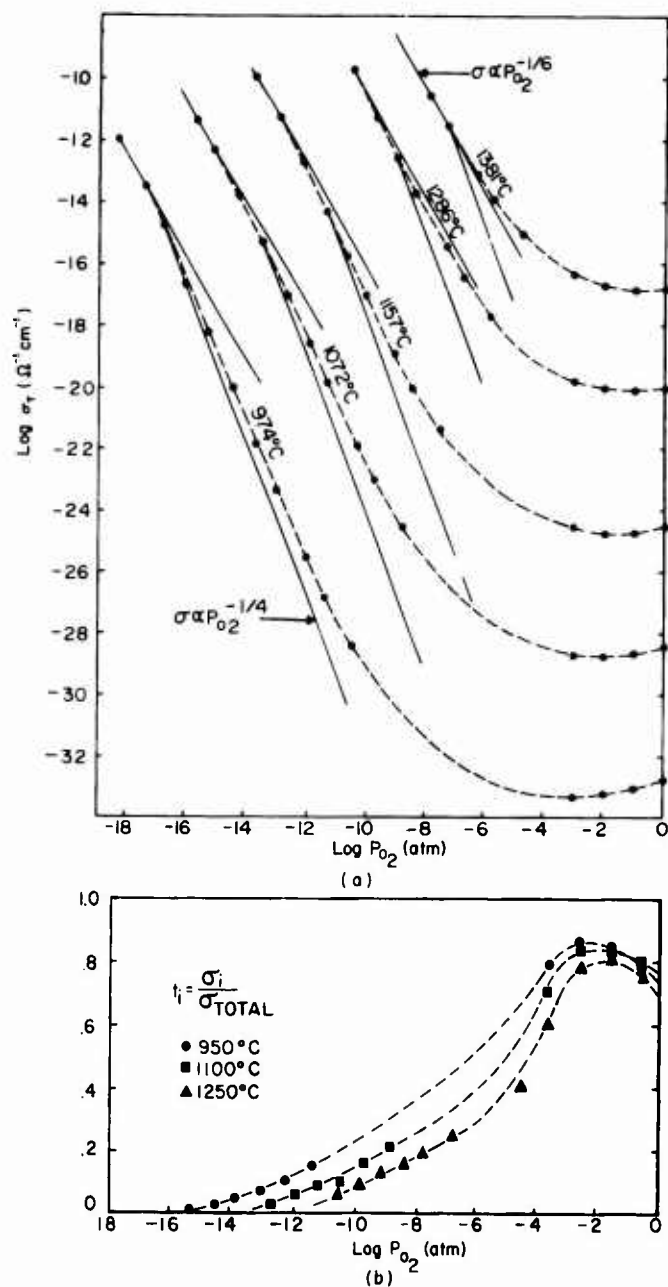
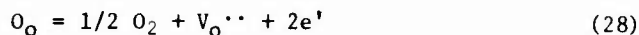


Figure 107. (a) Electrical Conductivity and (b) Ionic Transference Number of Ta<sub>2</sub>O<sub>5</sub> as Functions of P<sub>O<sub>2</sub></sub>.

$$2[V_O^{\bullet\bullet}] = n + l \quad (27)$$

where, in the usual Kröger-Vink notation, twice the concentration of doubly ionized oxygen vacancies ( $V_O^{\bullet\bullet}$ ) is assumed to be equal to the sum of the electron concentration ( $n$ ) and the total effective concentration of charges arising from the presence of lower valence impurity ions (without making assumptions about the impurity species responsible), i.e.,  $l = [F_M^I] + 2[F_M^{II}] + \dots + j[F_M^j]$ .

If it is assumed that oxygen vacancies are created according to the quasichemical reaction



where  $O_O$  is a lattice oxygen and  $e'$  is a "free" electron, the corresponding mass action expression may be written as

$$K = P_{O_2}^{1/2} [V_O^{\bullet\bullet}] n^2 \quad (29)$$

and Eqs. (27) and (29) can be combined for obtaining an equation for  $n$ ,

$$2KP_{O_2}^{-1/2} = n^3 + n^2 \quad (30)$$

This expression has two extreme cases. For  $n \gg 1$ ,  $n \propto P_{O_2}^{-1/6}$ ; this situation corresponds to the electroneutrality condition  $2[V_O^{\bullet\bullet}] = n$ . On the other hand, if it is assumed that  $n$  is  $\ll 1$ ,  $n \propto P_{O_2}^{-1/4}$ , then the corresponding neutrality condition is  $2[V_O^{\bullet\bullet}] = l$ . In the latter case, the concentration of oxygen vacancies is essentially fixed by the effective cation-impurity content.

If Eq. (27) holds and the electronic and ionic mobilities are not too disparate, the total conductivity may be expected to exhibit a  $P_{O_2}^{-1/6}$  dependence at very low  $O_2$  pressures and an ionic pressure-independent region at high pressures. This behavior is exactly that observed in Figure 107, excluding the very limited p-type region for which too few data are available

to permit speculation. It remains to be shown that this model can account for the other feature of Figure 107a, i.e., the varying slope on the low-pressure side of the curve.

It may be wise at this point, however, to justify the assumption of oxygen vacancies as the predominant ionic defect, as opposed to the other most likely choice--that of Ta interstitials. Although the conductivity data are not sufficiently accurate to permit discrimination between the  $P_{O_2}^{-1/6}$  dependence expected for doubly ionized oxygen vacancies and electrons and the  $P_{O_2}^{-5/24}$  dependence for fully ionized Ta interstitials and electrons, oxygen vacancies are believed to be the more plausible defect on the basis of the observations that 1) oxidation of Ta metal seems to proceed by oxygen diffusion through a  $Ta_2O_5$  scale<sup>(55)</sup> and 2) the accepted predominant ionic defects in the present experimental range in  $Nb_2O_5$  (a very similar material) are doubly ionized oxygen vacancies.<sup>(55)</sup>

However, Kudrak and Sienko,<sup>(54)</sup> on the basis of density measurements, postulated that Ta interstitials were predominant in the very highly reduced condition. As noted by Kofstad,<sup>(55)</sup> this situation is quite plausible since it can be shown easily that  $[Ta_i^{\bullet\bullet}]$ --the concentration of doubly charged Ta interstitials--must be proportional to  $P_{O_2}^{-3/2}$ , whereas  $[V_o^{\bullet\bullet}] \propto P_{O_2}^{-1/6}$  (if  $[V_o^{\bullet\bullet}] \gg [Ta_i^{\bullet\bullet}]$ ). Because of the relatively large pressure dependence for Ta interstitials, they are expected to become the predominant species at some low  $P_{O_2}$ .

The expression for the total conductivity is  $\sigma_{total} = \sigma_n + \sigma_i = ne\mu_n + 2[V_o^{\bullet\bullet}]e\mu_i$ , where  $\mu_n$  and  $\mu_i$  are the electron and vacancy mobilities, respectively. Then  $\sigma_{total}/e\mu_n = n + 2[V_o^{\bullet\bullet}]\beta$ , with  $\beta = \mu_i/\mu_n$ . From Eq. (27),  $\sigma_{total}/e\mu_n = \beta(n+I) + n$ , or

$$\log \sigma_{total} = \log [\beta(n+I) + n] + \log(e\mu_n) \quad (31)$$

Since  $n$  is determined by Eq. (30), Eq. (31) can be used to plot  $\log \sigma_{total}$  as a function of  $\log P_{O_2}$  for various  $\beta$ 's and  $I$ 's, if it is assumed that  $\mu_n$  is  $P_{O_2}$ -independent. Several such plots are shown in Figure 108; all the

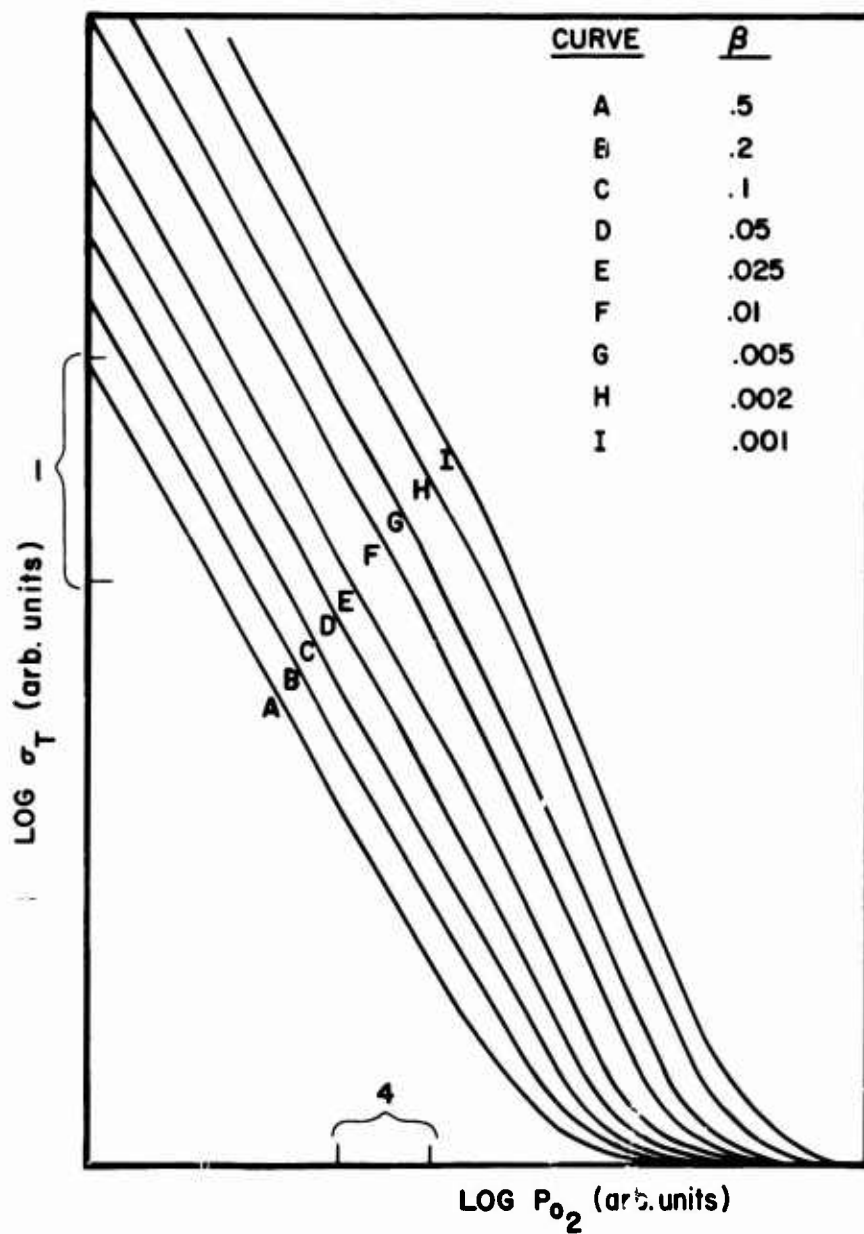


Figure 108. Plot of  $\text{Log } \sigma_T$  as a function of  $\text{Log } P_{O_2}$  Derived from Eq (31).

curves have a pressure-independent region at high  $P_{O_2}$ 's and a pressure-dependent region of varying slope at low  $P_{O_2}$ 's. The low-pressure slopes show a transition from a region of  $P_{O_2}^{-1/4}$  dependence to one of  $P_{O_2}^{-1/6}$  dependence. The extent of the former region is determined by the parameter  $\beta$ ; an increase in  $\beta$  results in a smaller region of  $P_{O_2}^{-1/4}$  dependence between the  $P_{O_2}^{-1/6}$ -dependent and pressure-independent extremes. For sufficiently precise conductivity data, this model can be fit to the data and  $\beta$  can be determined. The data available in the present study, however, were sufficient for application of this analysis only at the 974°, 1072°, and 1157°C isotherms. The  $\beta$ 's determined and the resulting fits to the data are shown in Figure 109. When a thermally activated form is assumed for  $\beta$  ( $\beta \propto \exp(-\Delta H_m/kT)$ ), an observed activation energy ( $\Delta H_m$ ) of  $\approx 2.0$  eV (or 46 kcal/mole) results. If the electronic mobility is temperature-independent or weakly dependent,  $\Delta H_m$  will be the activation energy for the vacancy mobility.

The ionic conductivity,  $\sigma_i$ , in the high-pressure region can be obtained from the data of Figure 107. When the temperature dependence of this quantity is calculated, the value obtained is 1.79 eV (or 41 kcal/mole), very near the 2.0 eV value found for  $\beta$ . This agreement indicates that the effective cation-impurity concentration is essentially independent of temperature from 950° to 1250°C, necessitating, of course, the same constancy for the oxygen-vacancy concentration in this range.

In addition, from parabolic oxidation data for Ta metal, Kofstad<sup>(58)</sup> has estimated the activation energy for the diffusion coefficient of oxygen ions to be 40 to 45 kcal/mole or 1.8 to 2.0 eV. If the Einstein relation is applied, an activation energy of 1.6 to 1.8 eV for the vacancy mobility for constant oxygen-vacancy concentration can be calculated, in agreement with the computation of  $\Delta H_m$  and in support of the assumption that the electron mobility is not strongly temperature dependent.

Since  $\beta$  has been determined from the curve fitting procedure, it is clear that an estimate of either the electronic or ionic mobility will allow determination of the other. In principle, the electronic mobility can be obtained from a combination of conductivity and either Seebeck coefficient

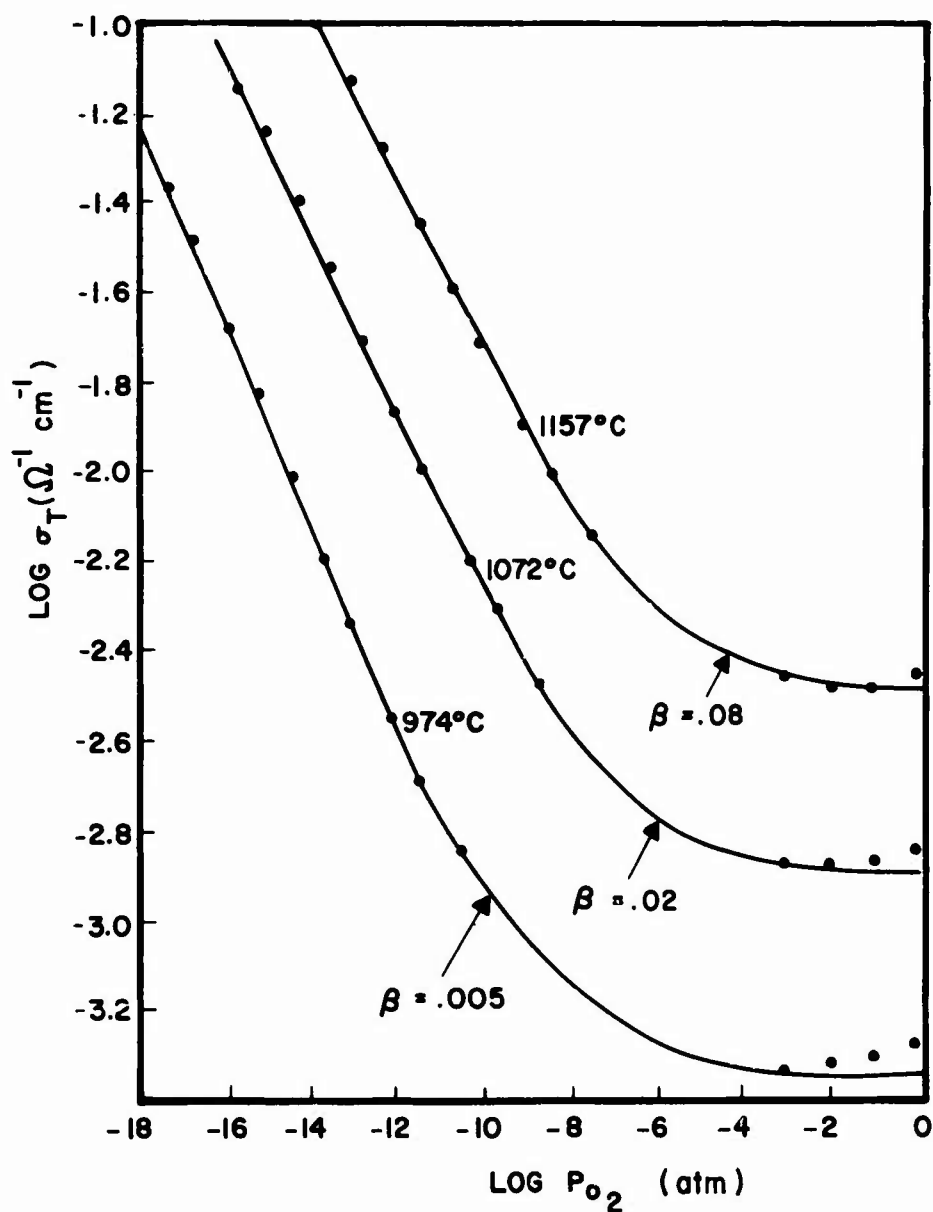


Figure 109. Determination of  $\beta$  as a Function of Temperature Obtained from Eq (31) and from Conductivity Data of Fig. 107(a).

or weight change data; the latter give the electron concentration at very low  $O_2$  pressures, where the neutrality condition  $n = 2[V_O^{\bullet\bullet}]$  holds.

The weight change data are summarized in Figure 110 as the calculated oxygen vacancy concentration at  $P_{O_2} = 10^{-16}$  atm as a function of  $1000/T$  ( $^{\circ}K$ ). Vacancy concentrations at other pressures are calculated from these values and the relation  $[V_O^{\bullet\bullet}] \propto P_{O_2}^{-1/6}$ . This dependence was assumed primarily to agree with the conductivity data, since the weight change data were not precise enough for unambiguous confirmation. These values, however, should allow a fair approximation of the electron mobility, which is calculated at  $P_{O_2} = 10^{-16}$  atm and  $1100^{\circ}C$  to be  $\approx 0.05$   $cm^2/V\text{-s}$ .

The apparent activation energy for the weight change data, 1.5 eV, is somewhat lower than the 1.9-eV value calculated from the temperature dependence of the conductivity data extrapolated to  $P_{O_2} = 10^{-16}$  atm. Whether this difference is real and can be attributed to an activated electronic mobility or is an artifact arising from the inherent limitations of the weight change measurement is not clear.

Because of the large ionic transference numbers at high  $O_2$  pressures, Seebeck coefficient measurements in that region cannot be used for estimation of electronic defect concentrations. At  $P_{O_2} = 10^{-16}$  atm, however electronic transference number is essentially one--the Seebeck coefficient data can be approximated by the simplified expression for a single electronic carrier (electrons),

$$Q = (k/e) [A_n + \ln (N_c/n)] \quad (32)$$

where  $Q$  is the Seebeck coefficient in  $V/^{\circ}K$ ,  $A_n$  is a constant related to the average kinetic energy of motion of the electron,  $N_c$  is the conduction band density of states,  $k$  is Boltzmann's constant, and  $e$  is the electronic charge.

Figure 111 shows measured Seebeck coefficients. Although, according to Eq. (32),  $n$  cannot be determined uniquely from  $Q$ , these data agree with electron concentrations determined from the weight change data, if

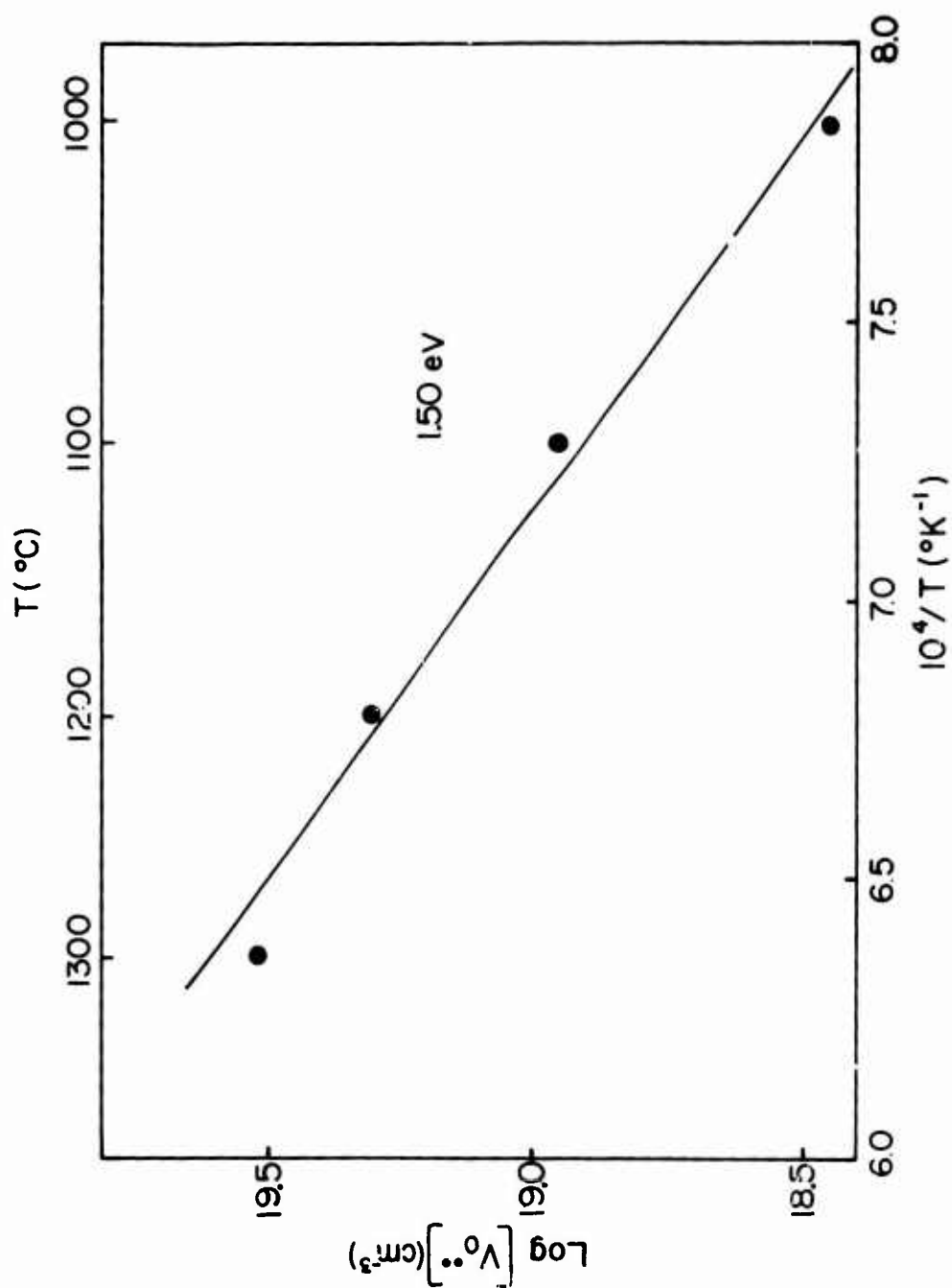


Figure 110. Oxygen Vacancy Concentration in  $\text{Ta}_2\text{O}_5$  at  $P_{\text{O}_2} = 10^{-16}$  (atm) Determined from Weight Change Measurements.<sup>2</sup>



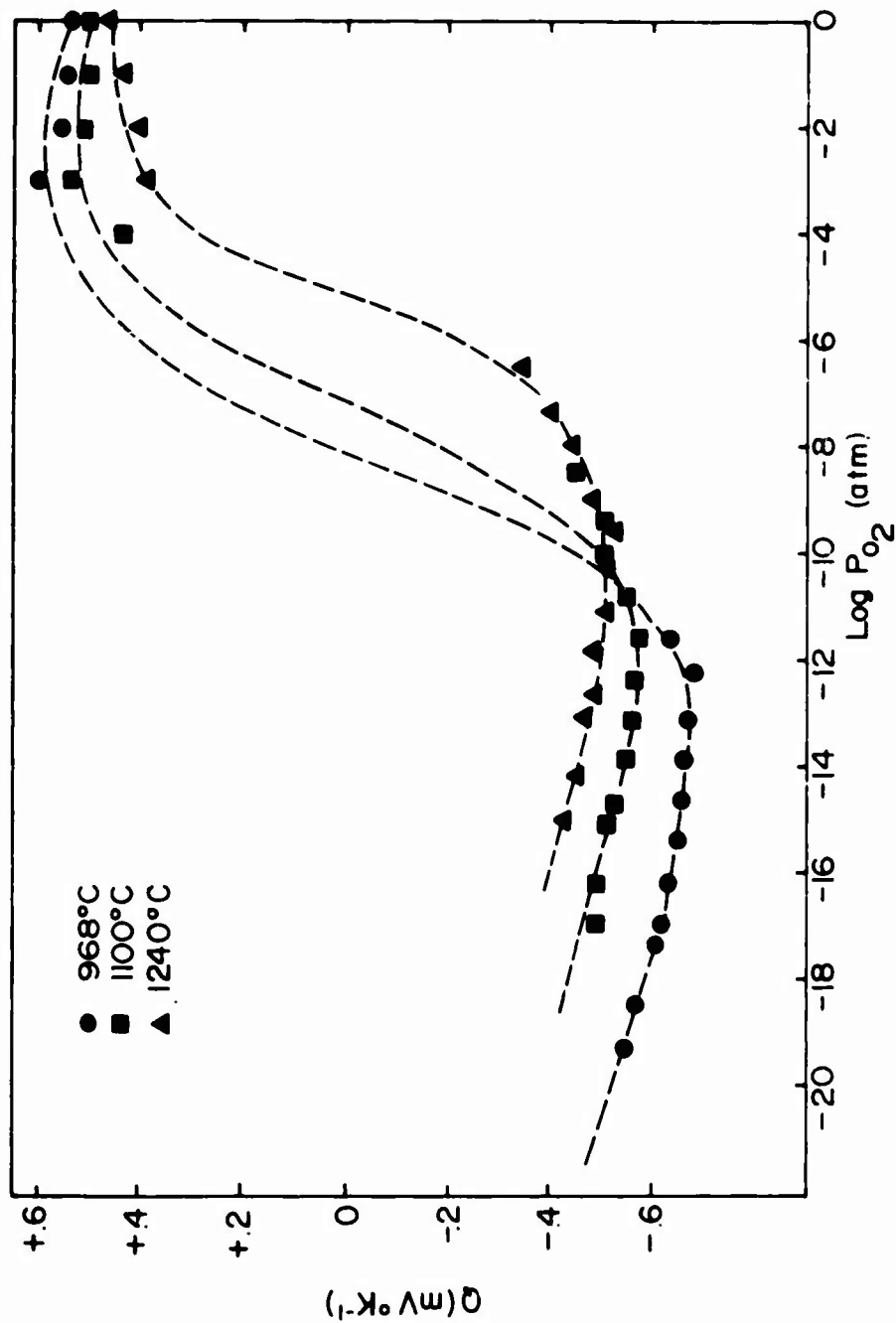


Figure 111. Seebeck Coefficient of  $\text{Ta}_2\text{O}_5$  as a Function of  $P_{\text{O}_2}$ .

$A_n \approx 0$  and  $N_c = 3 \times 10^{17}/\text{cm}^3$ . These values are consistent with a very narrow band conduction model, <sup>(59, 60)</sup> as might be expected from the rather low electronic mobility calculated.

With a reasonable estimate of the electron mobility and  $\mu$  for 1100°C, the oxygen vacancy mobility can be estimated as  $2 \times 10^{-3} \text{ cm}^2/\text{V-s}$  at this temperature and, as noted, is proportional to  $\exp(-1.8 \text{ eV}/kT)$ .

With the combination of conductivity and transference number data at this temperature, the oxygen vacancy concentration--and, consequently, the effective impurity concentration in the high pressure region--can be estimated also. From the 1100°C data, a doubly ionized oxygen vacancy concentration of  $[V_{O''}] \approx 3 \times 10^{18}/\text{cm}^3$  can be calculated. Since, in this pressure range, the approximation  $2[V_{O''}] = 1$  holds, an effective negative charge concentration of  $6 \times 10^{18}/\text{cm}^3$  is found. If the cation impurities responsible for these charges are considered to have an effective triple charge (e.g.,  $\text{Mn}^{3+}$ ,  $\text{Mg}^{2+}$ ,  $\text{Ni}^{2+}$ ), then  $[F_M''']$ , the concentration of this species, will be  $\approx 2 \times 10^{18}/\text{cm}^3$ , or  $[F_M'''] \approx 70 \text{ ppm}$ . Although no corroboration of this value is available, it may be compared with the results of the mass-spectrographic analysis of the sample after measurement (Table IV). If the concentration of the light elements Li and Na (which, it is suspected, were present only on the surface of the sample as a result of furnace tube and handling contamination) is neglected, the major impurities are Ni, Cu, Ca, K, and Mg. It appears that the concentration of these species (particularly the Ni and Cu, which most probably were bulk contaminants introduced during sample preparation) agrees--at least to order of magnitude--with the calculated effective impurity concentration.

As mentioned, the apparent activation energy for conduction at  $P_{O_2} = 10^{-16} \text{ atm}$  was found to be 1.9 eV. Since in this region  $n = 2[V_{O''}]$ , from Eq. (29)  $2K = P_{O_2}^{1/2} \cdot n^3$ , or since  $K$  depends exponentially on  $\Delta H_{V_{O''}}$  [the heat of incorporation of a doubly charged oxygen vacancy according to Eq. (28)],  $\Delta H_{V_{O''}} = 5.7 \text{ eV} = 131 \text{ kcal/mole}$ . This value compares to that of 103 kcal/mole for  $\text{Nb}_2\text{O}_5$  (Ref. 55) and is perhaps to be expected if the smaller deviation from stoichiometry of  $\text{Ta}_2\text{O}_5$  is considered.

Since  $t_e$  is essentially independent of temperature at high  $P_{O_2}$ 's,  $\tau_e$  has nearly the same activation energy as  $\tau_{total}$  ( $\approx 1.8$  eV), indicating from a Becker-Frederikse<sup>(61)</sup> type analysis that the intrinsic band gap in this material at 0°K is  $\approx 3.6$  eV.

In summary, measurements of electrical conductivity, weight change, ionic transference number, and Seebeck coefficient in  $Ta_2O_5$  strongly support the defect model proposed by Kofstad<sup>(55)</sup> and have allowed quantitative determination of several important mass transport and electrical parameters of this material.

TABLE IV  
MASS SPECTROGRAPHIC ANALYSIS OF  $Ta_2O_5$   
(ppmw)

Element	As-Received Powder	Sample After Measurement	Element	As-Received Powder	Sample After Measurement
Li	0.05	150	Co	0.03	<1
Be	<0.002	0.6	Ni	0.5	50
B	0.007	0.1	Cu	0.1	70
F	1	0.4	Zn	0.3	3
Na	2	150	Ga	<0.3	1
Mg	1	30	Zr	0.1	0.4
Al	6	10	Nb	6	6
Si	2	10	Mo	0.1	0.2
P	<0.1	1	Rh	<0.03	5
S	1	7	Cd	0.03	0.2
Cl	150	2	Sn	0.1	3
K	0.5	50	I	0.02	0.1
Ca	5	50	Ba	0.1	0.2
Sc	<0.03	<0.2	Ce	0.01	0.3
Ti	$\leq 0.2$	$\leq 0.4$	W	1	0.4
V	$\leq 0.1$	$\leq 0.2$	Pt	$\leq 0.2$	$\leq 1$
Cr	<0.2	$\leq 2$	Pb	<0.1	$\leq 0.3$
Mn	<0.2	$\leq 0.6$	Bi	<0.02	1
Fe	2	10			

## ELECTRICAL PROPERTY MEASUREMENTS ON REFRACTORY OXIDES ABOVE 1600°C

The general purpose of this area of research was to explore the experimental problems associated with electrical conductivity measurements above 1600°C and to develop the capability for making these measurements up to 2000°C. The topics to be discussed here include the problem of noise in the electrical measuring circuits, the evaporation of shields and electrodes, and the effect of thermionic emission on electrical measurements.

A specific problem investigated was the determination of the role, importance, and magnitude of thermionic emission (electrons emitted either from the walls of the furnace or from the sample) and ion emission (mainly from the furnace walls, although also from the sample). Thermionic emission depends mainly on the temperature of the apparatus and has the same effect as short circuiting the measurement. In this investigation emphasis was placed upon understanding the effect of thermionic emission on conductivity measurements and minimizing the "leakage" flow between the top and bottom electrodes used for electrical measurements and also between the walls and these electrodes.

The problems associated with thermionic emission are of particular interest because in several investigations on ceramic materials the conductivity data plots show breaks or changes in slope at about the same temperatures as data from thermionic and photoelectric measurements.

Bondarenko and Tsarev<sup>(62)</sup> studied the thermionic emission of  $\text{Sc}_2\text{O}_3$ ,  $\text{Y}_2\text{O}_3$ ,  $\text{La}_2\text{O}_3$ ,  $\text{TiO}_2$ ,  $\text{ZrO}_2$ ,  $\text{HfO}_2$ , and  $\text{ThO}_2$ . Temperatures of over 2300°C were attained by bonding the oxides to W heaters. Although their experimental conditions were not discussed in detail, thermionic constants were evaluated and Richardson plots were made; for all of the oxides, a break or change in slope occurred at some high "transition" temperature. Conductivity data from the present investigation on  $\text{HfO}_2$  show a break at about 1300°C, which is the same temperature at which a change in thermionic properties occurs.<sup>(62)</sup>

The electrical and thermionic properties of ceramic materials at high temperature are of immediate interest to MHD programs where the demand exists for electrode materials capable of functioning at extremely high temperatures in adverse environments. Although ceramic materials are presently being used, new requirements demand that their electrical properties be improved and their emission contribution to the plasma be utilized.

#### Summary of Applicable Literature

Thermionic emission has been the subject of intense research for many years, particularly during the 1930's and 40's. Much of the research was of a fundamental nature aimed at determining and understanding the work function, surface barriers, and quantum reflection coefficients of various metals. The practical interest in thermionic emission was caused by the demand for efficient high power vacuum tubes for radar and other electronic systems. Hence, the emphasis was placed on maximizing the emission and lowering the work function. A result of this work was the development of the thoriated tungsten cathodes which became very important in high power vacuum tubes. Barium-strontium oxide was also developed as an efficient low temperature, high emission density emitter. An extensive review of the role of  $\text{ThO}_2$  in electronics from both fundamental and practical considerations has been given by Danforth.<sup>(63)</sup>

The fundamental equation of thermionic emission is the Richardson-Dushman equation,

$$j = AT^2 \exp(-\phi/kT) \quad (33)$$

where  $j$  is the emission current density,  $T$  is the temperature,  $\phi$  is the work function (in eV), and  $A$  is a constant equal to  $4\pi mek^2h^{-3} = 120 \text{ A/cm}^2\text{-deg}^2$ . Simplified derivations yield this equation quite readily. However, experimental data yield widely varying results for values of  $A$ . For example, the values for  $A$  given in the literature are: 75 for W and 160 for Cs, but only 3.2 for Cs on W. One reason for these discrepancies is that the constant  $A$  must be multiplied by  $1 - r$ , where  $r$  is a quantum reflection coefficient;

i.e., electrons are internally reflected at the surface even though energetically they are candidates for emission. Other complicating factors in the accurate measurement of the true  $A$  and  $\epsilon$  are (1) space charge in the vicinity of the surface, (2) presence of an external field, (3) thermal expansion ( $\epsilon$  and  $r$  are temperature dependent), (4) dependence of  $\epsilon$  on crystallographic plane, (5) presence of adsorbed gases on the surface, and (6) the macroscopic area of the emitter's not necessarily being the actual surface area. Hence, for a complete, fundamental determination of the thermionic properties of a material, precise measurements must be made on high purity, oriented single crystals whose surfaces are atomically clean under ultrahigh vacuum with precise temperature control.

Much of the fundamental research on thermionic emission has been done on W single crystals. The standard reference on this work is the very extensive review paper by Herring and Nichols;<sup>(64)</sup> other papers by Nichols<sup>(65)</sup> and Smith<sup>(66)</sup> are also useful from a fundamental point of view. These studies are not of direct interest to the present program because emphasis was placed on extreme precision; very fine, single crystal wires of ultrapure material, grown along exact crystal planes, were used in high vacuum tubes surrounded by numerous shields, screens, viewing and emission apertures, grids, and collectors. The surface of the wires was atomically clean, and parameter measurements were precise. With ceramic materials, measurements of this type are nearly impossible. Furthermore, the intent of this program was not to determine the precise thermionic constants of materials in general but rather to determine the function of both thermionic emission and ionic emission in a furnace or similar high-temperature environment and the effect of these emissions on measurements of other properties such as conductivity. The main area of interest was determining "effective thermionic properties" of ceramic materials to be used in high-temperature applications.

Research that is directly applicable to the present project has been performed by Bates,<sup>(67)</sup> investigators at the National Bureau of Standards,<sup>(68)</sup> and a research team in France.<sup>(69-71)</sup>

It was concluded, with supporting calculations, that the principal leakage currents encountered at high temperatures are due to thermionic emission from the walls in the form of a complex mixture of electrons, ions, and charged molecules of adsorbed gas. It was shown that the use of a guard ring, extending over the entire hot zone of the furnace, was quite essential for measurements at 1700°C. The apparatus used by the French group was first described by Mitoff.<sup>(72)</sup>

### Experimental Procedures

Initial emphasis on this project was placed on extending conductivity measurements to 1750°C by utilizing the three terminal, guard ring technique in the normal manner in the Harraeus Rh-wound furnace. The electrical conductivity of  $\text{HfO}_2$  and  $\text{Al}_2\text{O}_3$  to 1750°C was measured. Some discrepancies in the data were noted when comparing the values obtained from thick and thin crystals of  $\text{Al}_2\text{O}_3$ . The "bulk" conductivities determined from thick and thin samples--after a correction for sample geometry--differed by 10.2%, and the activation energies differed by 7%. The differences observed were consistent over the temperature range studied. Therefore, they do not appear to be due to thermionic effects; i.e., no high-temperature effect could be attributed to increased emission or leakage. The crystals--especially the thin one--had a few obvious imperfections, such as cracks and regions of different optical density.

The literature on the electrical and defect properties of sapphire single crystals is extensive. The papers consulted include W. J. Lackey,<sup>(73)</sup> T. Matsumura,<sup>(74)</sup> and Brook, Yee, and Kroger.<sup>(75)</sup> These papers have extensive bibliographies citing various measurement techniques and results. Also, each addresses the problem of very high temperature measurements to a different degree. Principal interest in these data was comparison of the results of our measurements on sapphire crystals with those in the literature. It has been pointed out by Bates<sup>(67)</sup> that conductivity data on sapphire which varies by seven orders of magnitude can be found in the literature. Figure 112 is taken from the paper by Brook, Yee, and Kroger<sup>(75)</sup> (Figure 2). Two data points from the present study have been superimposed; these data for the thin (1.74mm)

The above electrical measurements suggest that  $\text{SiO}_2$  is a mixed conductor with its defect concentration established by impurities within the  $\text{SiO}_2$  network. The nature of the oxygen defect--oxygen ion interstitial or vacancy--could not be determined from the measurements.

Knowledge of the nature of the oxygen ion defect is not required for prediction of the magnitude of the scaling rate constant of silicon from the conductivity values. The scaling rate constant is given by

$$k = - \int_{\mu_{\text{O}_2}'}^{\mu_{\text{O}_2}''} \frac{\sigma_{\text{el}} \sigma_{\text{ion}}}{[\sigma_{\text{el}} + \sigma_{\text{ion}}]} \frac{d\mu_{\text{O}_2}}{2Z_2 F^2} \quad (23)$$

where  $\sigma_{\text{el}} = \sigma_p + \sigma_n$  is the electronic conductivity,  $\sigma_{\text{ion}}$  is the ionic conductivity,  $Z_2$  is the valence of the ionic defect (assumed equal to -2 for  $\text{SiO}_2$ ), and  $\mu_{\text{O}_2}''$  and  $\mu_{\text{O}_2}'$  are, respectively, the oxygen chemical potential at the ambient-scale and scale-silicon interface. A computer program in which  $k$  was calculated from the experimental conductivity values was written with the assumption that

$$\sigma_{\text{ion}} = \text{const} \quad (24)$$

$$\sigma_p \propto P_{\text{O}_2}^{1/4} \quad (25)$$

$$\sigma_n \propto P_{\text{O}_2}^{-1/4} \quad (26)$$

The oxidation data of Tripp<sup>(38)</sup> were used for comparison. At 1350°C in 600 torr oxygen, the experimental scaling rate constant is  $10^{-8.32} \text{ g}^2 \text{ cm}^{-4} \text{ hr}^{-1}$ . The value obtained from Eq. (23) is within one order of magnitude of this experimental value. The complex logarithmic pressure dependence of the scaling rate constant predicted from Eq. (23), however, does not agree with the 3/4-power  $P_{\text{O}_2}$  dependence obtained experimentally.<sup>(38)</sup> It is concluded, therefore, that the agreement in scaling rate constants



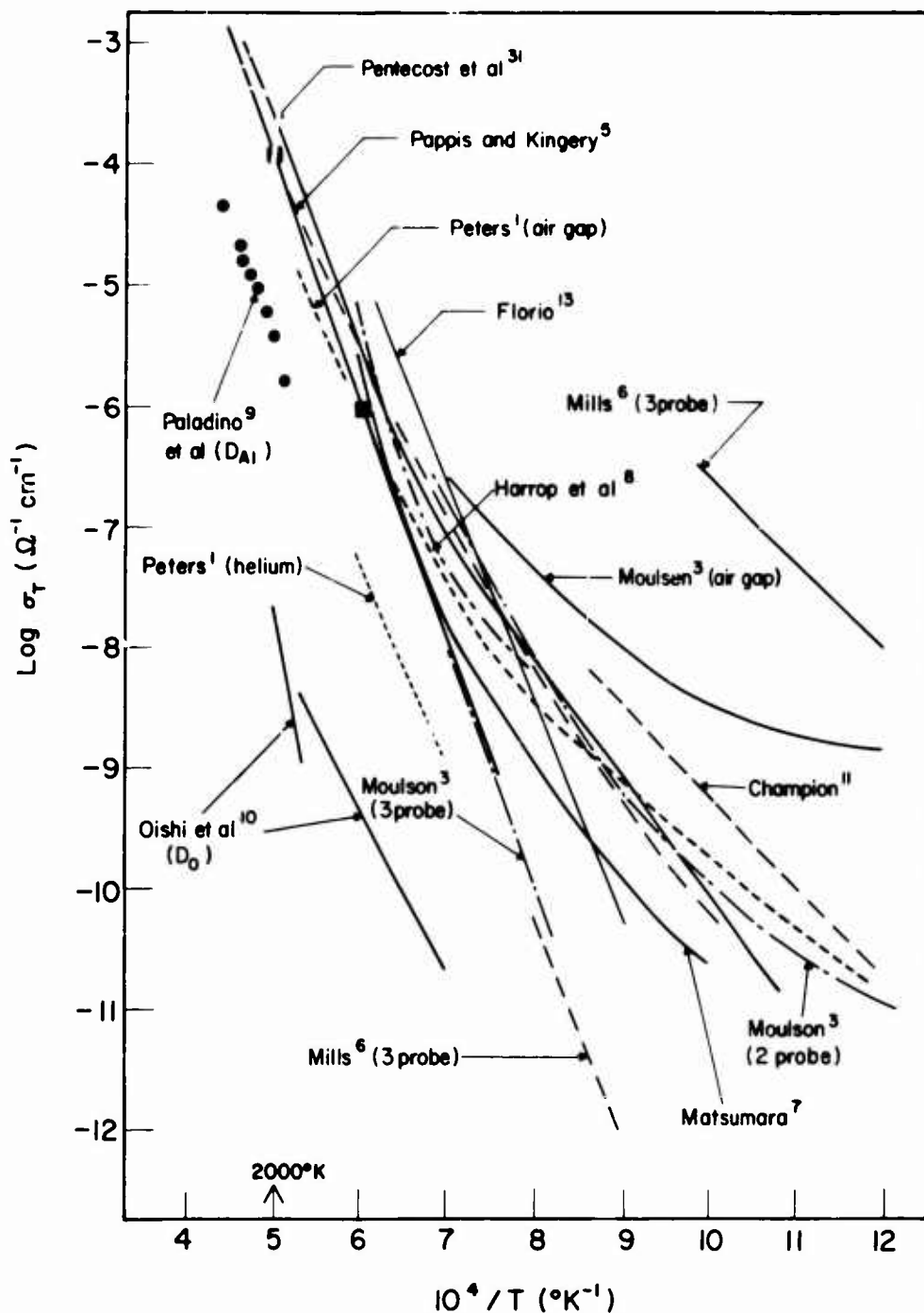


Figure 112. Comparison of Electrical Conductivity Data for  $\text{Al}_2\text{O}_3$  Single Crystals (Two Data Points from Present Study). Figure and References taken from Brook et al.<sup>(75)</sup>

sapphire crystal (activation of 3.57 eV) appear to fit the corresponding conductivity curves in the other papers nearly as well. There were no indications of an avalanche of current or breakdown of the gas surrounding the sample; that is, the conductivity plots were straight lines from 1200°C to 1750°C.

All measurements discussed here were made in air by using an Harraeus furnace and a Wayne-Kerr bridge driven at 10 kHz. The thermocouples were Pt - 30% Rh, Pt - 6% Rh. The samples were 1/2 inch in diameter and less than 1/4 inch thick. A standard three probe measurement technique in which the bottom of the sample was coated with Pt was used. On the top of the sample a dot of Pt at the center and a grounded ring of Pt around the edge were placed. Figure 113 is a drawing of the sample region of the hot zone in the furnace. The support rods, thermocouple rods, and alumina cup were coated with Pt paint or foil.

Much of the effort on this project involved the measurement of the conductivity of the air gap between Pt electrodes in the usual measurement configurations except that the sample was removed. This yields an essentially direct measurement of leakage currents, including those from thermionic emission, ion emission, and gas phase conduction. Numerous problems were encountered during these measurements. Pt coatings on the rods and sample evaporated quite rapidly at temperatures above 1600°C. The evaporation was very noticeable because of a sharp increase in electrical noise in the measuring circuits. It is absolutely essential that the rods carrying the electrode be well coated with Pt and the sample area be completely shielded with a Pt can. The sample holder rods also bent and warped, which made it very difficult to open the sample cup. Hence, the sample holder was rebuilt several times. Initial data indicated that conductivity of the air gap was several orders of magnitude lower than those of the sapphire. Arrhenius plots of conductivity were essentially linear.

During the initial conductance vs air gap measurements, an air gap could not be set at room temperature and be expected to remain constant as a function of temperature because of thermal expansion effects on the parts

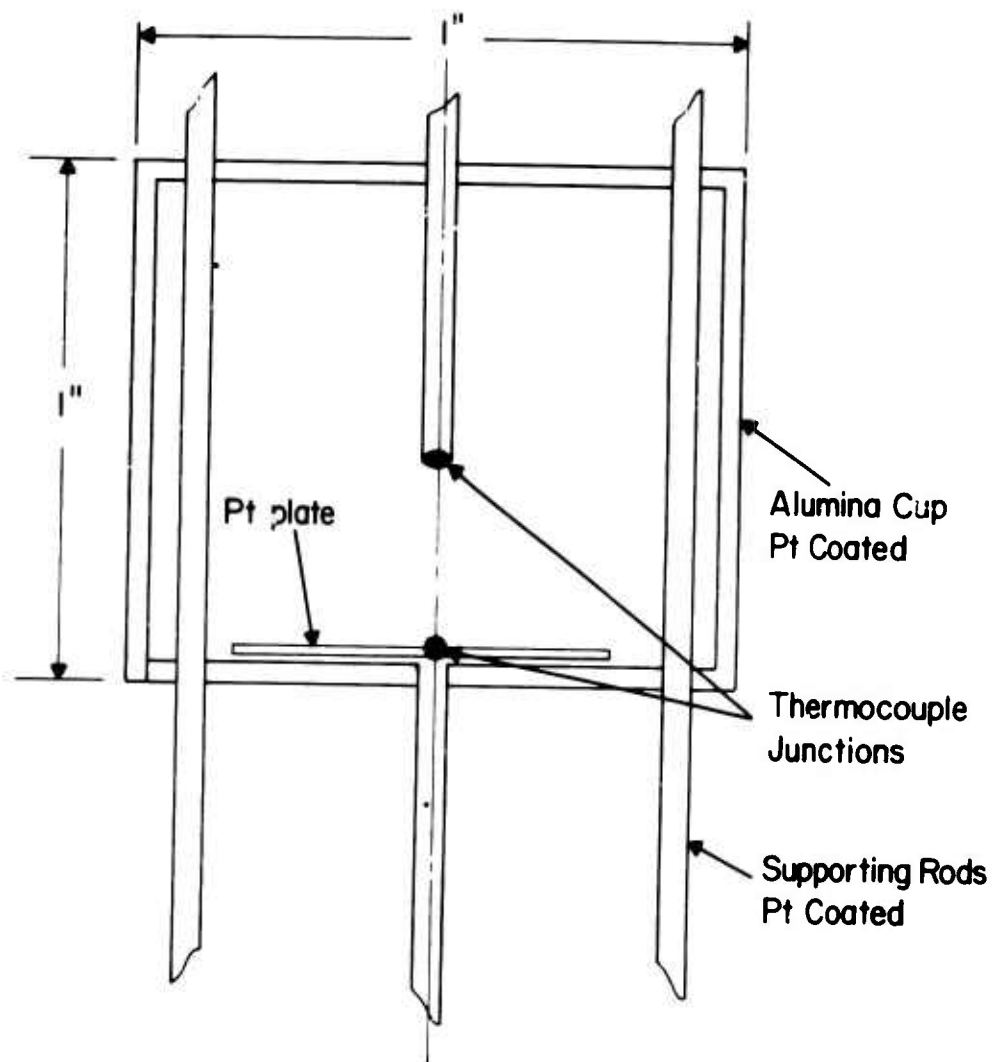


Figure 113. Schematic Diagram of Sample Region of Conductivity Measurement Apparatus.

in the sample holder. Hence, the holder was rebuilt with a screw arrangement at the top in order that the air gap could be set or changed in a controlled manner at any temperature by counting the number of turns on the screw from zero gap length (electrodes shorted).

The top section of the holder was further modified by making the center rod which carries the instrumentation wires from 3/16-in. diam alumina rather than 1/16 in. The top section extended down to the "sample region" and supported the Pt-coated alumina cup that surrounded the sample. The bottom section of the holder was supported from the bottom of the furnace by a similar large diameter rod but was independent of the top section. The two sections were adjusted in such a way that the Pt shields in the furnace hot zone made electrical contact. The wires for the bottom thermocouple were brought out through the bottom of the furnace.

The use of large diameter center rods and the mechanical uncoupling of the two sections eliminated many of the strains in the system, and this arrangement proved to be sufficiently durable to withstand the remaining strains. The warping, bending, and cracking of the rods were reduced significantly, and data were taken smoothly and continuously with few interruptions.

### Results

The measurements of the conductance of the air gap are summarized in Figure 114. The two curves on the left represent measurements of the conductance between the two thermocouple beads made with the original apparatus. The vertical displacement between the two curves is consistent with the difference in air gap length. The upper complete curve represents the conductance between the top thermocouple bead and a Pt plate (having the same diameter as a typical sample) welded to the bottom thermocouple. The increased conductance shown by this curve is consistent with the increased metal area exposed to the hot zone. The shorter curves represent some of the variation observed in the data. These variations are by no means the largest observed; the large variations of slope, continuity, and magnitude of conductance could--in nearly all cases--be traced to degradation of the Pt shield or

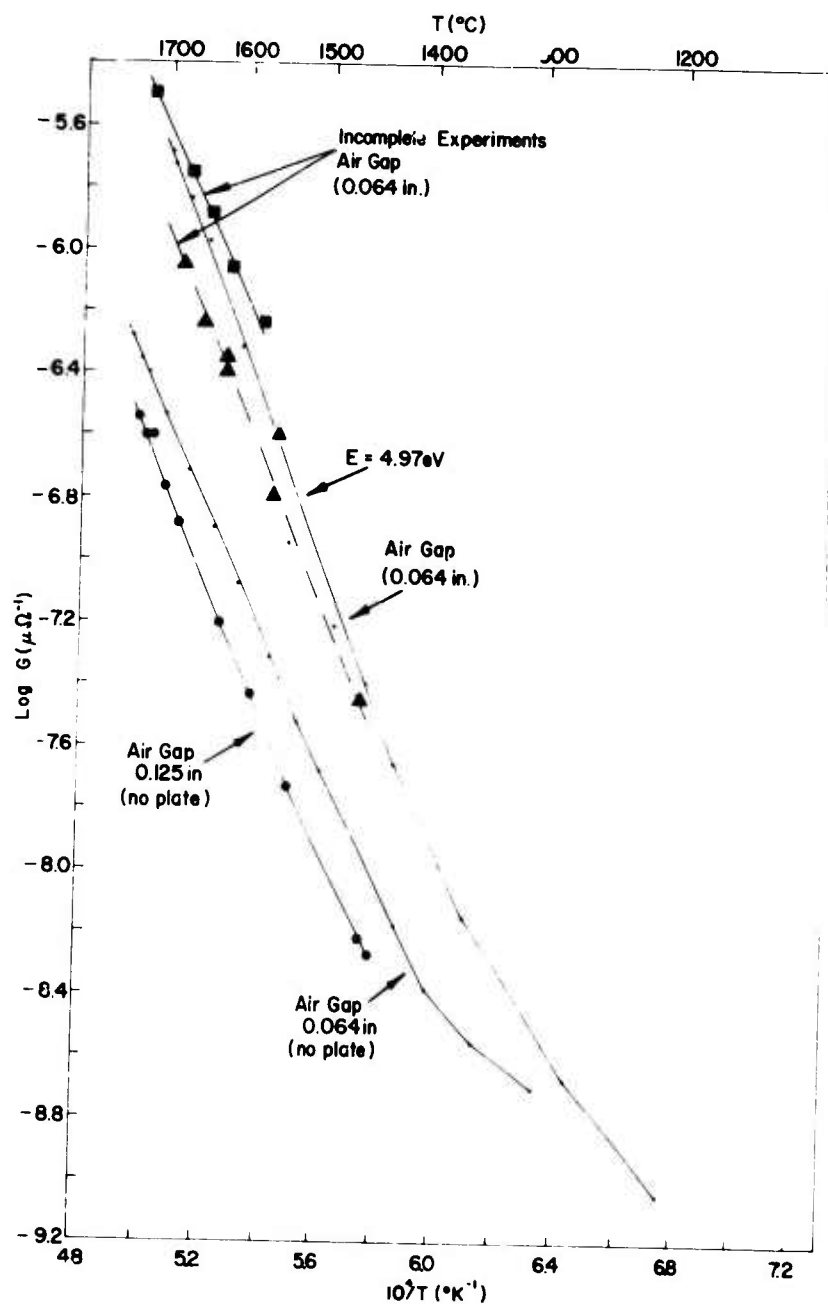


Figure 114. Conductance Between Electrodes without a Sample, Measured in Air.

rod coatings or to bending, warping, and expansion of the rods. The data represented in Figure 114 were taken under optimum experimental conditions. The lines are quite straight and parallel in the high-temperature region; there is no evidence of an avalanche or breakdown of conduction at the highest temperature, nor is it apparent that the  $T^2$  dependence of thermionic emission dominates the conductance.

The conductance of the air gap as a function of air gap distance is shown in Figure 115. The data, taken at four temperatures, are shown to fall on reasonably straight lines. The scatter of the 1715°C data probably is due to the degradation of the Pt coatings which occurred prior to the experiment. The linear dependence of the conductance on the distance is significant because it eliminates the likelihood that gas conduction with an associated space charge and saturation region plays an important role in the observed phenomena. The slopes of these lines decrease with increasing temperature; i.e., the 1715°C data are less dependent on distance than the 1405°C data. A possible explanation is that the emission from the alumina cup surrounding the air gap (which is totally independent of air gap distance) becomes more significant at the higher temperatures. If these data are plotted on a log-log scale, as in Figure 116, it can be seen that the slopes are  $\sim -2$  at the large distances and nearly zero for small distances. A slope of  $-2$  implies  $I \propto 1/d^2$ , which is the usual field dependence for two point charges. This reassures us that the bulk of the conduction is directly between the electrodes and that space charge and wall emission effects are small, except where the electrode separation is extremely small. The number of data points is insufficient to permit definite conclusions on this matter.

The current between the bottom thermocouple and the alumina cup surrounding the sample region was measured directly. A Keithley electrometer with the positive terminal connected to the thermocouple was used, and a positive current was indicated. The data, plotted in the usual manner for a Richardson-Dushman plot, i.e.,  $\log(I/T^2)$  vs  $1/T$ , are shown in Figure 117. The data fall on a surprisingly straight line having a slope which yields a thermionic emission energy ( $\phi$ ) of 3.97 eV. Extrapolation yields an  $A$  value of  $0.1 \text{ A/cm}^2/\text{deg}^2$ . These values of  $\phi$  and  $A$  are probably much more reasonable than

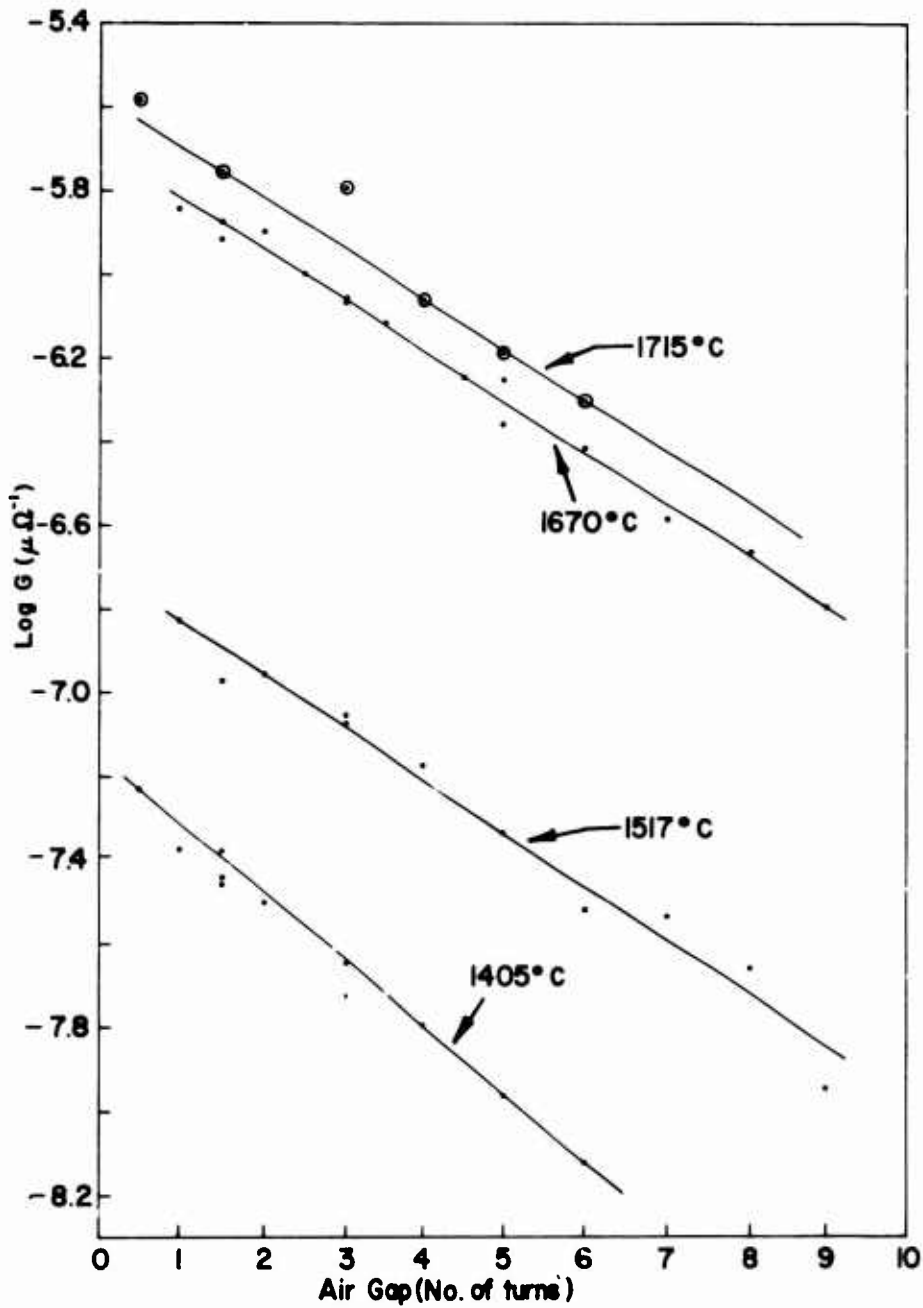


Figure 115. Conductance of Air Gap as a Function of Air Gap Distance (1 1/2 Turns = 1/16 in.).

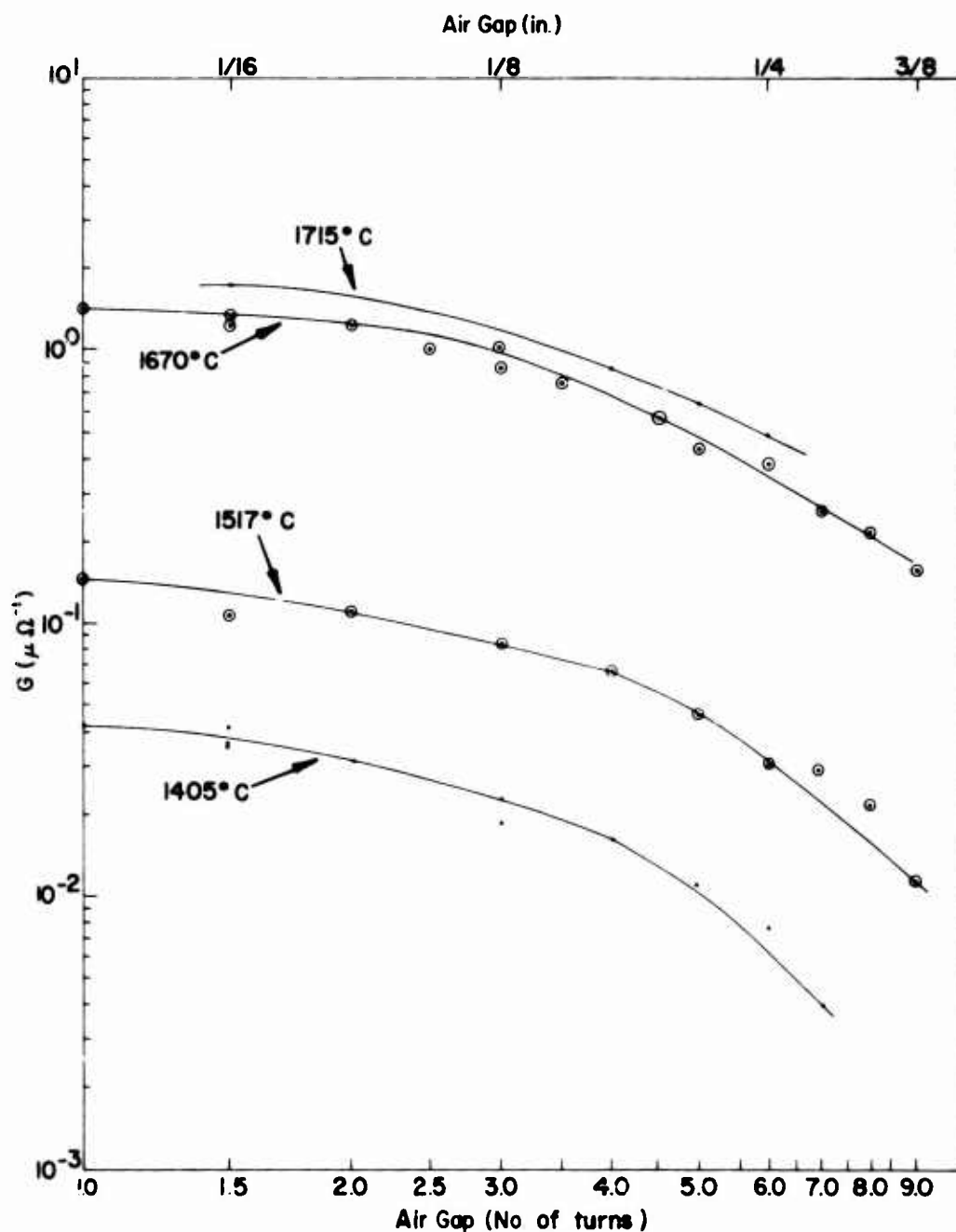


Figure 116. Log Log Plot of Air Gap Conductance as a Function of Air Gap Distance (1 1/2 Turns = 1/16 in.).



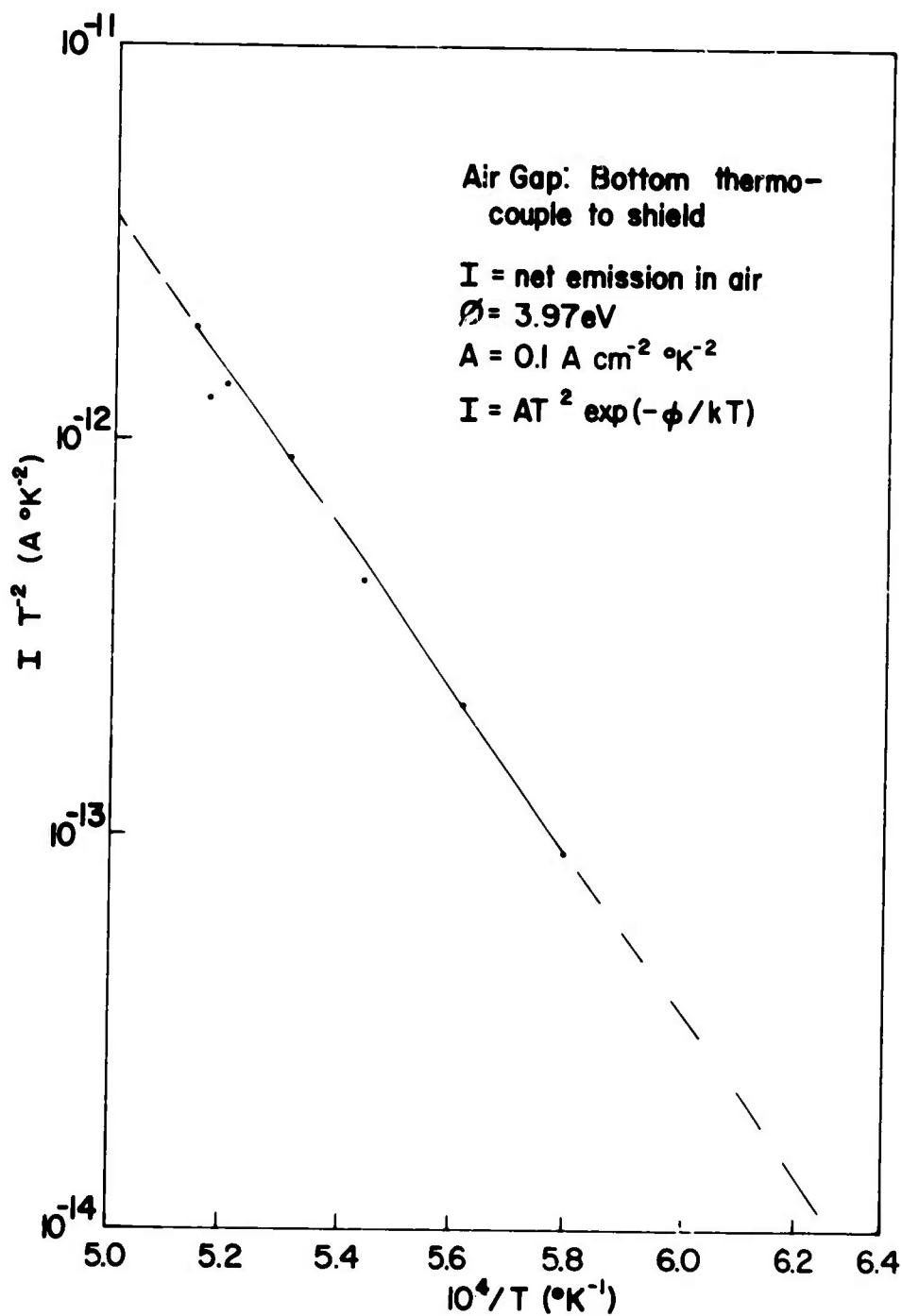


Figure 117. Richardson-Dushman Plot of Air Gap Data.

should be expected. The value of  $\phi$  for Pt is 5.32 eV and for  $\text{Al}_2\text{O}_3$  is 4.7 eV. <sup>(76)</sup> The value for A is within the range given in the literature. Thermionic constants are usually determined by using a cold Cu electrode as an emission collector. In this case, both the Pt and the  $\text{Al}_2\text{O}_3$  are hot (the  $\text{Al}_2\text{O}_3$  is probably hotter than the Pt); therefore, a net emission current from both parts is being measured. Also, since the geometry of the contributing elements is quite awkward, emission is coming from many directions. However, it is concluded that the observed current involves negative species ( $e^-$ ) emitted by the Pt and/or positive ions emitted by the  $\text{Al}_2\text{O}_3$ . This conclusion is in agreement with that of the French work reported earlier. <sup>(69)</sup>

The conductance of an air gap was measured with a dc bias voltage applied to the  $\text{Al}_2\text{O}_3$  shield surrounding the sample region. The results are shown in Figure 118. The application of a positive voltage resulted in a very large reduction of the conductance between the thermocouples. The reduction was several orders of magnitude for only a few applied volts. Application of a negative voltage increased the conductance to saturation.

These changes of conductance with bias voltage are in agreement with the hypothesis of positive and negative charge species from Figure 117. Electrons traveling between the two measurement electrodes (or electrons coming from the Pt thermocouples by thermionic emission) are swept to the positively biased alumina wall, thus reducing the transport of charge between the electrodes and in turn the observed conductance. A negative voltage on the shield increases the positive ion emission from the walls and repels the electrons coming from the electrodes, which causes an increased conductance. The saturation may be a gas phase conduction effect and a function of temperature (as indicated in Figure 117) and gas pressure (not varied in this study).

When a sample was placed between the electrodes, bias voltage dependence was not observed. Bias voltages of  $\pm 200$  V were applied to the shield with negligible effect on the conductance. The thermionic emission of the Pt and alumina is a small effect compared with the conductance of alumina. Also, a sample in place will cover the electrodes, shielding them from the walls.

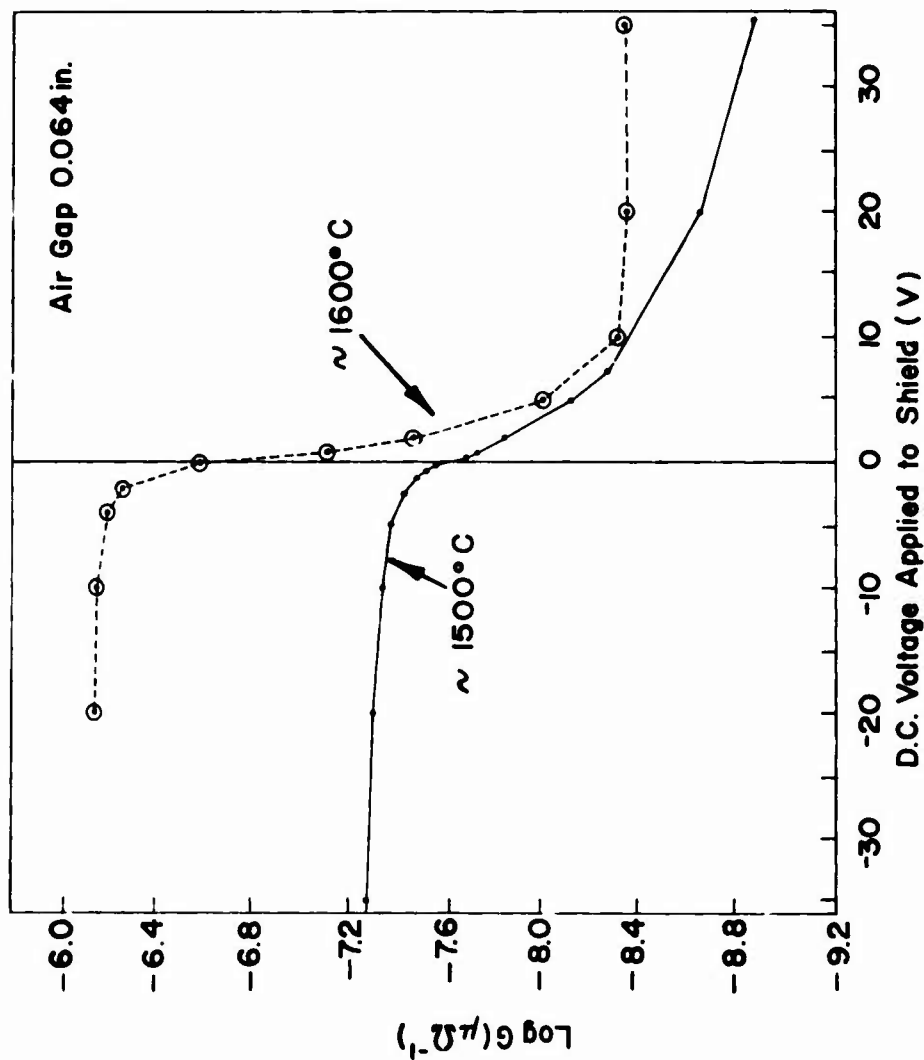


Figure 118. Effect of Bias Voltage on Air Gap Conductance.

The data shown in Figure 119 summarize the conductance measurements on sapphire single crystals of two thicknesses. The data for the air gap measurements are also shown for comparison purposes. Note that the conductances associated with the air gaps are about two orders of magnitude less than those for the equivalent sapphire crystals. Note also that the conductance plots for the sapphire crystals are straight, nearly parallel lines extending to the highest temperature. As shown previously, these values for the conductance of sapphire agree with values in the literature.

### Conclusions

High-temperature conductivity measurements have shown that it is possible and practical to extend the measurement of electrical properties of materials to 1750°C if suitable experimental precautions are exercised. Thermionic emission does not appear to be a serious problem affecting the electrical conductance to these temperatures.

Precautions that must be taken in order to ensure accurate, reproducible results are as follows:

- 1) The sample region and the wires used for measurement must be well shielded with Pt. The thickness and continuity of the shielding can be monitored easily by observing the amount of electrical noise in the measuring circuit. The reproducibility and general sensitivity of the data are dependent on the integrity of the shielding. The shields should be connected to a common ground for best results.
- 2) Suitable separation of the various elements in the circuit is essential. The Pt coatings on the rods carrying electrical wires must stop 1/8 in. from the ends of the rods, or leakage may occur, causing an apparent short circuit. When the bias voltage is applied to the cup surrounding the sample region, care must be taken to prohibit the coated rods from touching the Pt shielding of the cup.
- 3) For these high-temperature measurements, thermal expansion of the rods and the increased brittleness of coated rods must be taken into account.

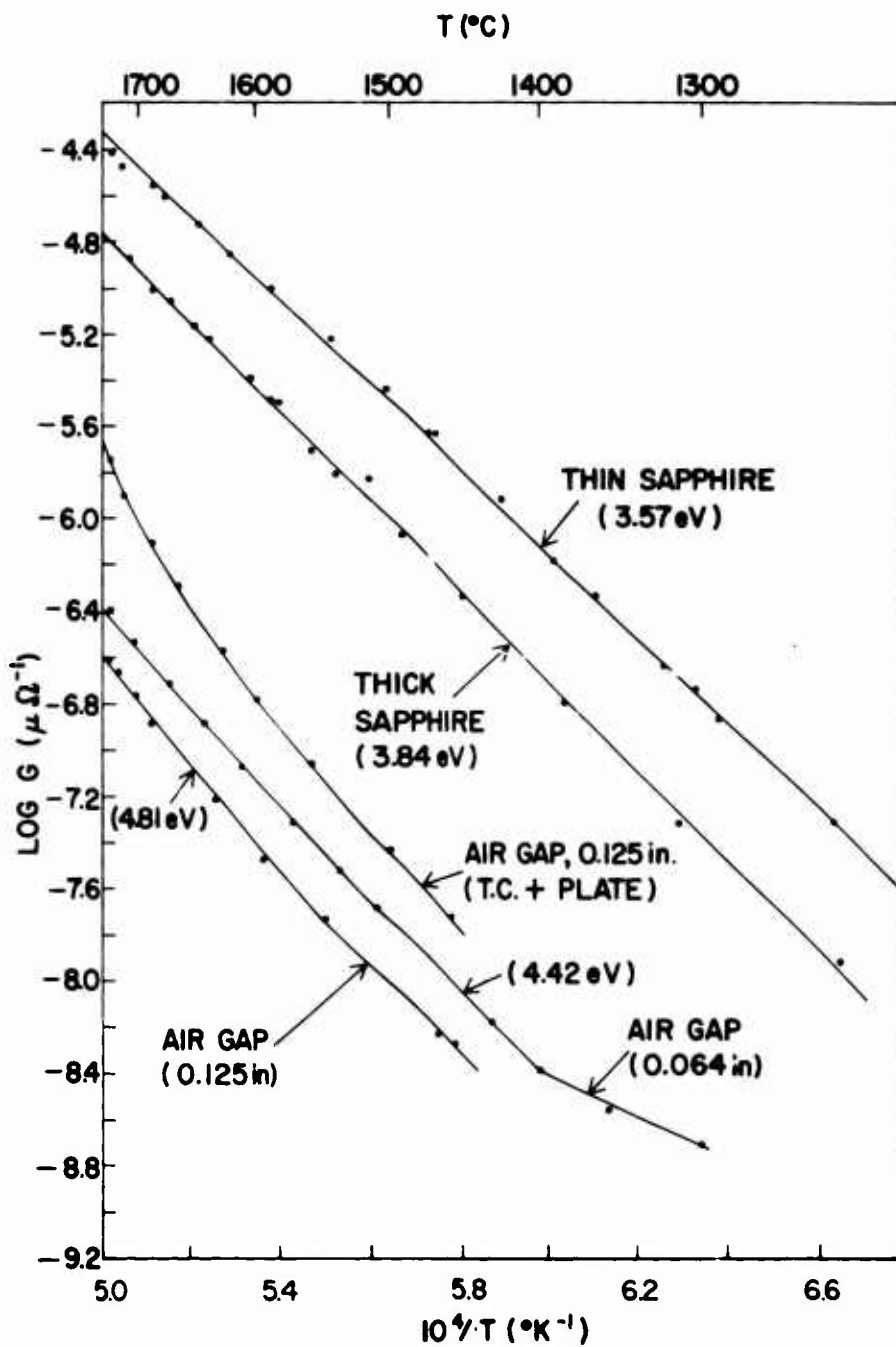


Figure 119. Comparison of Air Gap Conductance with Conductivity of Sapphire.

## INTERDIFFUSION STUDIES ON THE CoO-MgO SYSTEM

High-temperature solid state reactions have received considerable attention in recent years because of their importance during the oxidation of metals and refractory materials where more than one reaction product is formed. Because of the complexity of multicomponent solid state reactions, where second (or more) phase products are formed, it is often desirable to gain a mechanistic understanding of these reactions in simpler or prototype systems. This knowledge can then be applied to the more complex system.

Cobalt oxide and magnesium oxide form one such prototype system in which no second-phase product is formed during the high-temperature solid state reaction. Therefore, the reaction rate is characterized by one parameter the interdiffusion coefficient  $\bar{D}$ . The purpose of this study was to 1) develop analysis techniques for obtaining  $\bar{D}$  for the CoO-MgO system, 2) determine  $\bar{D}$  as a function of composition, temperature, and oxygen partial pressure, and 3) compare these results with those of other workers, both in the present system and in other similar transition metal monoxide-MgO systems.

### Experimental

Single crystals of both CoO and MgO were used for this investigation. MgO crystals (impurity analysis given in Table V) were provided by M. M. Abraham, C. T. Butler, and Y. Chen at the Oak Ridge National Laboratory. The CoO crystals (impurity analysis given in Table VI) were cut from a single crystal boule obtained from Dr. A. Linz at M.I.T. Specimens ( $\sim 3 \times 4 \times 5$  mm) of both materials were prepared with the (100) crystallographic plane parallel to the surface and were polished with 1  $\mu$ m diamond paste. The crystals were preannealed separately, for 12 hr at the same temperature and environment that would exist during the interdiffusion experiments. The couples were held together with Pt/10% Rh wire. Interdiffusion experiments were conducted at 100°C increments from 1100–1500°C at 1 atm oxygen pressure and in  $8 \times 10^{-6}$  atm oxygen pressure. Electron-beam microprobe determination of concentration profiles was obtained by

TABLE V  
MASS SPECTROGRAPHIC ANALYSIS OF MgO (in ppma)

Element	ORNL MgO	Element	ORNL MgO
Ag	< 1	Mo	< 1
Al	10	N	41
As	< 1	Na	< 1
B	< 1	Nb	<30
Ba	< 3	Ni	< 3
Be	< 1	P	10
Bi	< 3	Pb	< 3
Ca	50	Rb	< 5
Cd	<10	S	< 2
Co	< 3	Sb	<10
Cr	1	Si	15
Cs		Sn	< 3
Cu	< 0.1	Sr	3
Fe	7	Ta	<30
Ge	<10	Ti	1
Hg	<10	V	< 3
K	< 3	W	<10
Li	< 1	Zn	<50
Mg	Main	Zr	< 5
Mn	< 1		

TABLE VI  
MASS SPECTROGRAPHIC ANALYSIS OF CoO (in ppma)

Element	Single Crystal	Element	Single Crystal
Li	1	Ca	20
C	625	Cr	10
N	55	Mn	80
Na	490	Fe	70
Mg	10	Ni	250
Al	40	Cu	25
Si	55	Zn	55
K	20	Mo	<1

slicing the couples perpendicular to the interface plane and mounting in a standard plastic holder with CoO and MgO standards.

### Analysis Techniques

Since the difference in molar volumes between pure CoO and pure MgO is <4%, the well known Matano-Boltzmann analysis rather than the more general Wagner analysis was used.<sup>(77)</sup> The Boltzmann transformation of Fick's Second Law for variable  $\tilde{D}$  was first used by Matano<sup>(78)</sup> to analyze diffusion phenomena. Fick's Second Law is written as

$$\frac{\partial c}{\partial t} = \frac{\partial}{\partial x} \left( \tilde{D} \frac{\partial c}{\partial x} \right) \quad (34)$$

For cation interdiffusion in an essentially rigid anion sublattice, Eq. (34) may be written as

$$\frac{\partial c_{\text{Co}^{2+}}}{\partial t} = \frac{\partial}{\partial x} \left( \tilde{D} \frac{\partial c_{\text{Co}^{2+}}}{\partial x} \right) \quad (35a)$$

and

$$\frac{\partial c_{\text{Mg}^{2+}}}{\partial t} = \frac{\partial}{\partial x} \left( \tilde{D} \frac{\partial c_{\text{Mg}^{2+}}}{\partial x} \right) \quad (35b)$$

where the cobalt and magnesium ion concentrations have been included. The assumption that the interdiffusion phenomenon is a result of cation interdiffusion in a rigid oxygen sublattice is supported both by experimental observation of similar systems and by values for diffusion coefficients obtained by Blank and Pask,<sup>(79)</sup> Chen et al.,<sup>(80,81)</sup> and Harding et al.<sup>(82,83)</sup>

Application of the Boltzmann transformation to Eq. (34) for a semi-infinite diffusion-couple geometry results in the relations

$$-1/2 \int_0^{c_0} x dc = 0 \quad (36)$$



and

$$\tilde{D}(c') = - \frac{1}{2t} \left( \frac{dx}{dc} \right)_{c'} \int_0^{c'} x dc \quad (37)$$

where 0 and  $C_0$  are the cation concentrations at + and - infinity,  $t$  is the time of the diffusion anneal, and  $(dx/dc)_{c'}$  represents the reciprocal of the slope of the concentration-vs-distance profile evaluated at the concentration  $c'$ . The  $x$ 's are distances measured from the so-called "Matano Interface" defined by Eq. (36), where the  $x=0$  plane is the "mass-balance" plane of the diffusion couple. According to Eq. (37) the interdiffusion coefficient may be calculated at every point on the experimentally determined concentration-vs-distance profile, provided sufficiently precise data can be obtained to allow reliable calculation of the integrals and slopes involved. Since Eq. (34) is equivalent, in our case, to the two expressions (35a) and (35b), then Eqs. (36) and (37) must have similar counterparts. It is thus possible to calculate two independent, corroborative  $\tilde{D}$ 's at each point in the couple--one from the cobalt ion profile and one from the magnesium ion profile.

A computer aided correction of the microprobe data was used to obtain interdiffusion coefficients. The Matano program was based on one used by J. J. Stiglich<sup>(84)</sup> in a study of the NiO-CoO system with some modifications. His program provided for a slight "smoothing" of the input concentration-vs-penetration distance data by least squares fitting of five points at a time on the profile to a third-degree polynomial until all points had been fitted and recalculated. This procedure was found to be ineffective in the present study, probably because as many as 400 points were used to determine a profile--as opposed to the 100 maximum used by Stiglich.

Suppose one desires to calculate  $\tilde{D}$  at the concentration  $C_i$  on the profile, where the concentration distance input data pairs are  $(C_i, X_i)$ , where  $(C_1, X_1)$  is the first data point on the profile and  $(C_N, X_N)$  is the last. According to Eq. (37), in order to calculate  $\tilde{D}(C_i)$  one must calculate the area under the profile up to  $C_i$  and the reciprocal of the slope at  $C_i$ . The area calculation is relatively insensitive to irregularities in the profile, but the slope calculation is strongly affected since the slope is given by

$$\left(\frac{dx}{dc}\right)_{C_1} = \frac{X_{i+1} - X_{i-1}}{C_{i+1} - C_{i-1}}$$

One solution to the problem, of course, would be to expand the range over which the slope is calculated, such as

$$\left(\frac{dx}{dc}\right)_{C_1} = \frac{X_{i+20} - X_{i-20}}{C_{i+20} - C_{i-20}}$$

This change would drastically reduce the sensitivity of the calculated slope to irregularities in the profile; however, it would also cause the slope to be averaged over the concentration range chosen and would not reflect accurately the change of slope with concentration along the profile.

A better method seemed to be the fitting of the monotonic section of the profile to a sixth-degree polynomial. Not only would the data be smoothed by the fit, but the instantaneous slope at any point would be readily calculable from the easily differentiated polynomial. This procedure has been used quite successfully, and the results presented here were obtained by this method.

### Results and Discussion

Figure 120 shows a pair of unsmoothed profiles resulting from the microprobe analysis of a couple which had been annealed under the conditions indicated. The profiles display a marked asymmetry, with the penetration of magnesium ions further into the CoO than that of cobalt ions into the MgO. Also shown in Figure 120 is the Matano interface, drawn at 1523  $\mu\text{m}$ .

As noted earlier, interdiffusion in this system is believed to be the result of cation migration in an immobile oxygen ion lattice. Some confirmation of this was found in the absence (within the experimental precision of the experiment) of any discrepancy between the position of the calculated Matano interface and the original CoO-MgO crystal interface; that is, no

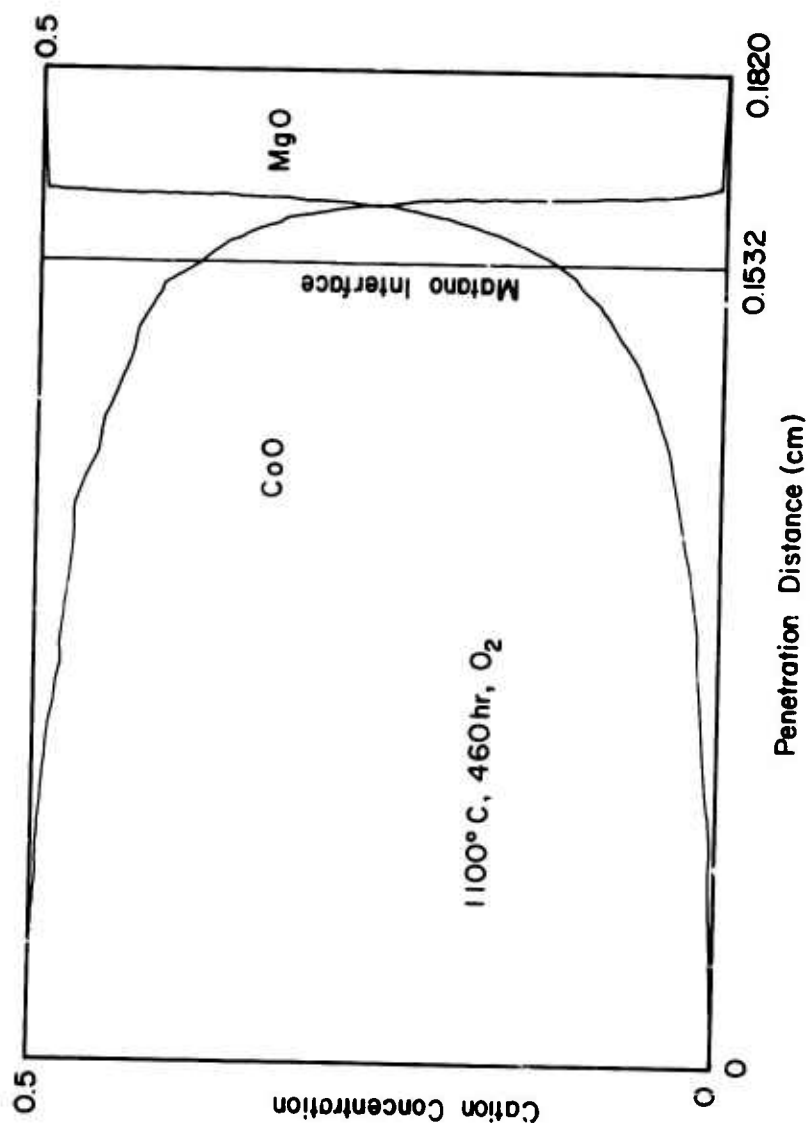


Figure 120. Plot of Cation Concentration as a Function of Distance for CoO-MgO Interdiffusion Couple No. 8.

classical Kirkendall marker shift was observed for any of the couples of this system.

Figure 120 is also illustrative of one other feature found to be generally true, that the magnesium-ion profile was always more well-behaved than the cobalt ion profile; that is, the magnesium trace showed fewer "bumps," "dips," and irregularities. Whether this is due to some effect of impurities or imperfections in the CoO or is a statistical artifact due to the different microprobe counting rates on the traces is not clear at this time. Because of these fluctuations in the Co trace, the data obtained from the Mg trace are believed to be more reliable, and--except where indicated--the following results are calculated from the Mg trace only.

A plot of the calculated interdiffusion coefficient for the same couple shown in Figure 120 (couple No. 8) is shown in Figure 121, where the ordinate is  $\log \bar{D}$  and the abscissa is the atomic concentration of the cation. The data from the Co profile are referred to the lower scale and those from the Mg are referred to the upper. Note that the upper and lower abscissae are complementary to allow direct comparison of the  $\bar{D}$ 's obtained from the two profiles. The agreement is quite good. Over the range from about 10 to 40% cation concentration,  $\log \bar{D}$  shows a linear dependence on composition. At the high and low concentration ends of the plot, the data are less reliable because the integrated areas under the profile become quite small. A correction due to Hall<sup>(85)</sup> can be applied to the data in these regions; this consists of a fit of the data to an error function solution. Here, however, those results considered to be most reliable will be emphasized, that is, those data in the range 10 to 40 at% cation concentration.

Table VII is a summary of the composition dependences of  $\bar{D}$  observed for all couples investigated. If  $\bar{D} = \exp(-\beta \cdot X_{\text{MgO}})$ , where  $X_{\text{MgO}}$  is the mole fraction of MgO, then the  $\beta$ 's determined from the linear portion of plots similar to that of Figure 121 may be tabulated. As the table shows,  $\beta$  for the couples annealed in oxygen at one atmosphere total pressure was found to range from a low of 3.46 to a high of 3.98, with no discernible temperature trend. Similarly, the couples annealed in the 8 ppm O<sub>2</sub>/Ar mixture ( $P_{\text{O}_2} = 8 \times 10^{-6}$  atm) at the same total pressure produced  $\beta$ 's from 3.48 to 3.98, again with no evident trend. The average  $\beta$ 's calculated in the two cases

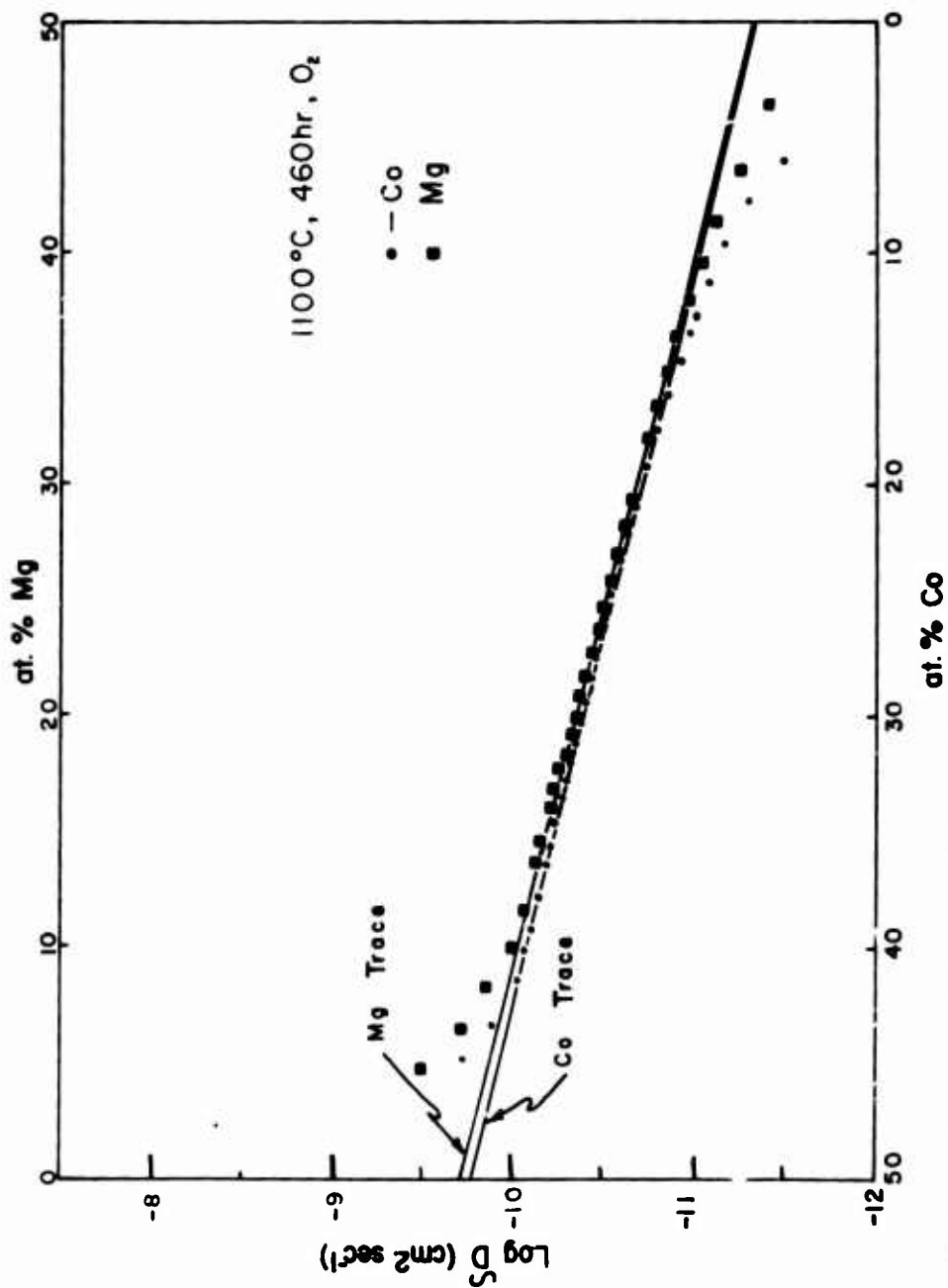


Figure 121. Plot of Calculated Diffusion Coefficient as a Function of Composition for CoO-MgO Couple No. 8.

TABLE VII

COMPOSITION DEPENDENCE OF  $\tilde{D}$  AS A FUNCTION OF  
TEMPERATURE AND OXYGEN PARTIAL PRESSURE

$$\tilde{D} \propto \exp(-\beta \cdot X_{\text{MgO}}) \text{ (where } X_{\text{MgO}} = \text{mole fraction MgO)}$$

$P_{\text{O}_2} = 1 \text{ atm}$			$P_{\text{O}_2} = 8 \times 10^{-6} \text{ atm}$		
Temp ( $^{\circ}\text{C}$ )	Couple No.	$\beta$	Temp ( $^{\circ}\text{C}$ )	Couple No.	$\beta$
1100	8	3.46	1200	6	3.86
1200	3a	3.91			
1200	3b	3.89			
1300	1	3.80	1300	11	3.75
1300	2	3.75			
1400	5	3.98	1400	12	3.98
1400	7	3.75			
1500	9	3.49	1500	10	3.48
	Avg. =	3.75		Avg. =	3.77
RESULT					
$\tilde{D} \propto \exp(-3.76 \cdot X_{\text{MgO}})$					

were nearly identical (3.75 and 3.77), which implies that over this temperature and  $P_{\text{O}_2}$  range the compositional dependence of  $\tilde{D}$  is constant and may be written as  $\tilde{D} \propto \exp(-3.76 \cdot X_{\text{MgO}})$ .

An exponential dependence of the interdiffusion coefficient upon composition has been found by other workers, notably Blank and Pask,<sup>(79)</sup> Zintyl,<sup>(86)</sup> and We',<sup>(87)</sup> for systems analogous to the CoO-MgO system. Schmalzried<sup>(88)</sup> related data obtained by Zintyl on defect concentrations in the NiO-MgO system to the interdiffusion results of Blank. Zintyl's results in the CoO-MgO system may be correlated with the present results in a similar manner. Zintyl concluded that the cation vacancy concentration in CoO-MgO solid solutions is of the form  $[V_M''] \propto \exp(-\beta \cdot X_{\text{MgO}})$ , where  $[V_M'']$  is the concentration of cation vacancies (assumed, for convenience, to be doubly ionized).

If local thermodynamic equilibrium is presumed to prevail everywhere in the couple and if the hole mobility is much greater than either cation mobility, then  $\tilde{D}$  is related to the cation self-diffusion coefficients by the Darken relation, Eq. (38), for an ideal solid solution:

$$\tilde{D} = X_{\text{MgO}} D_{\text{Co}^{2+}} + X_{\text{CoO}} D_{\text{Mg}^{2+}} \quad (38)$$

Since the self-diffusion coefficients are directly proportional to the vacancy concentration, the following equations may be written:

$$D_{\text{Mg}^{2+}} = D_{\text{Mg}^{2+}}^0 [V_M''] = D_{\text{Mg}^{2+}}^0 X_0 \exp(-\beta \cdot X_{\text{MgO}}) \quad (39)$$

$$D_{\text{Co}^{2+}} = D_{\text{Co}^{2+}}^0 [V_M''] = D_{\text{Co}^{2+}}^0 X_0 \exp(-\beta \cdot X_{\text{MgO}}) \quad (40)$$

where the  $D^0$ 's are primarily the cation jump frequencies, and Zintyl's observation of an exponentially dependent cation vacancy concentration is assumed.

When Eqs. (38), (39), and (40) are combined, the result is

$$\tilde{D} = [D_{\text{Mg}^{2+}}^0 - X_{\text{MgO}}(D_{\text{Mg}^{2+}}^0 - D_{\text{Co}^{2+}}^0)] \cdot X_0 \exp(-\beta \cdot X_{\text{MgO}}) \quad (41)$$

Now, if it is assumed that  $D_{\text{Mg}^{2+}}^0 \approx D_{\text{Co}^{2+}}^0$  (which is probably not unreasonable, in view of the similar ionic radii and electronic polarizabilities of Mg and Co), then the second term in the brackets vanishes and Eq. (41) becomes

$$\tilde{D} = D_{\text{Mg}^{2+}}^0 \cdot X_0 \exp(-\beta \cdot X_{\text{MgO}}) \quad (42)$$

Therefore, the interdiffusion coefficient varies exponentially with the same dependence as that found for the cation vacancy concentration.

If the derivation of Eq. (42) is valid, then the  $\beta$  determined from our interdiffusion experiments should agree with that determined by Zintyl. As noted earlier, it was found in the present investigation that  $\beta = 3.76$  over

the experimental range studied. Zintyl found  $\beta$  for CoO-MgO solid solutions to decrease with increasing temperature, from 4.44 at 1100°C to 3.42 at 1500°C. Although no significant trend of  $\beta$  with temperature was observed in the present study, the two results are considered to be in agreement.

It is clear from Eq. (38) that the interdiffusion coefficients measured at the composition extremes (that is, at  $X_{\text{MgO}} = 0$  and  $X_{\text{MgO}} = 1$ ) must correspond to  $D_{\text{CoO}}^{\text{Mg}^{2+}}$  and  $D_{\text{MgO}}^{\text{Co}^{2+}}$ , respectively. The latter quantity has been determined by Wuensch and Vasilos<sup>(89)</sup> to be described by  $D_{\text{MgO}}^{\text{Co}^{2+}} = 5.78 \times 10^{-5} \exp(-2.06 \text{ eV}/kT)$ . The former quantity may be estimated in the following manner:

Extrapolating the results of Blank and Pask on the NiO-MgO system to the composition  $X_{\text{NiO}} = 1$  leads to the expression

$$D_{\text{NiO}}^{\text{Mg}^{2+}} = 6.32 \times 10^{-5} \exp(-1.86 \text{ eV}/kT)$$

If it is assumed that

$$D_{\text{CoO}}^{\text{Mg}^{2+}} = D_{\text{NiO}}^{\text{Mg}^{2+}} \frac{[V_M'']_{\text{CoO}}}{[V_M'']_{\text{NiO}}}$$

then the results of Zintyl (confirmed by the work of Stiglich<sup>(84)</sup> and Chen<sup>(81)</sup>) indicate that the ratio  $[V_M'']_{\text{CoO}}/[V_M'']_{\text{NiO}}$  is about 30 and independent of temperature over the experimental range of the present study. Therefore,

$$D_{\text{CoO}}^{\text{Mg}^{2+}} \sim 1.9 \times 10^{-4} \exp(-1.86 \text{ eV}/kT)$$

is estimated.

Figure 122 is a plot of the interdiffusion coefficients determined in this study as a function of  $1000/T(^{\circ}\text{K})$  for the four compositions indicated. The solid lines through these data are shown with a slope corresponding to an activation energy of 46.8 kcal/mole or 2.03 eV. The solid squares and the



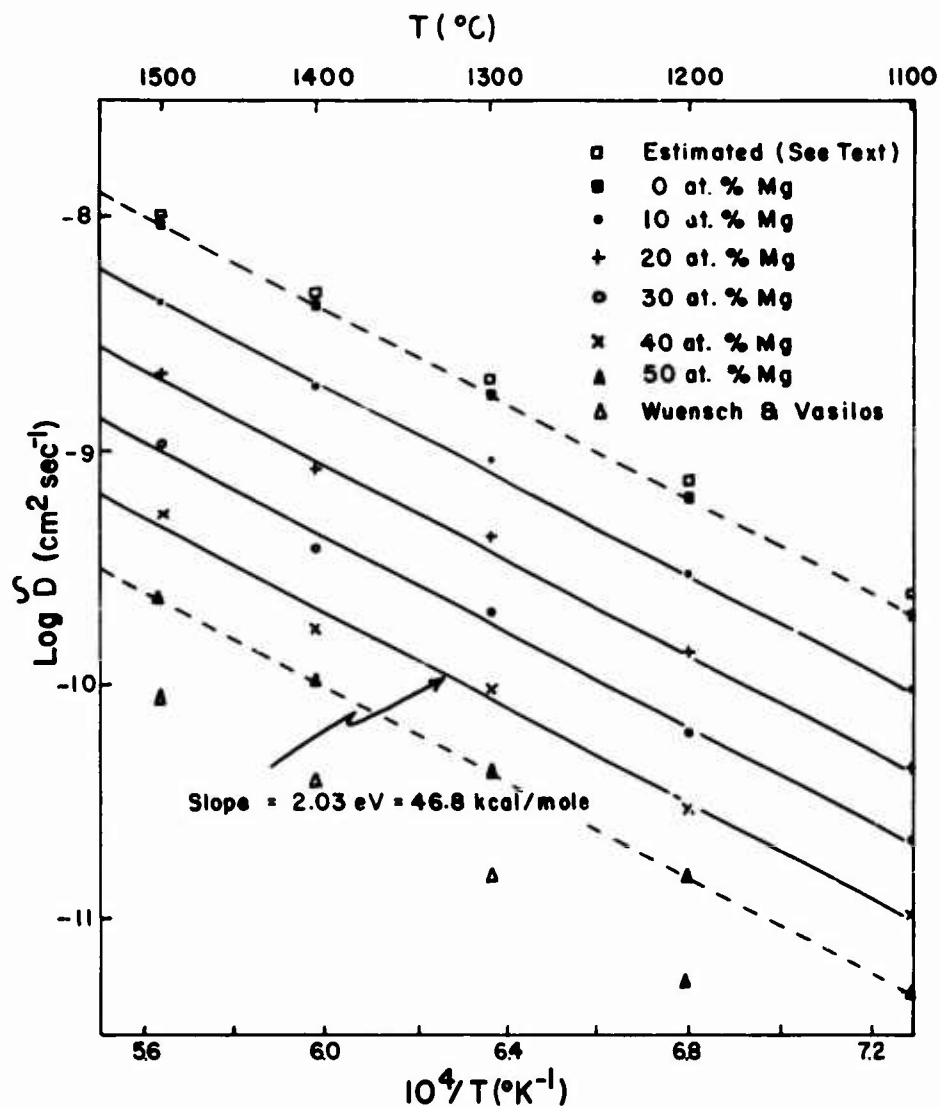


Figure 122. Plot of Calculated Interdiffusion Coefficient as a Function of  $1000/T$  ( $^\circ\text{K}$ ) for Couples Annealed in  $P_{O_2} = 1 \text{ atm}$ .

dashed line through them represent the interdiffusion coefficients obtained by extrapolating the data of this study to the composition extreme  $X_{\text{MgO}} = 0$  and, as such, should correspond to  $D_{\text{CoO}}^{\text{Mg}^{2+}}$ . Calculated values of  $D_{\text{CoO}}^{\text{Mg}^{2+}}$ , from the estimation described above, are shown for comparison as open squares; the agreement is good.

Similarly, values of  $D_{\text{MgO}}^{\text{Co}^{2+}}$ , obtained by extrapolation of data from the present study to the composition  $X_{\text{MgO}} = 1$ , are displayed as solid triangles; values of  $D_{\text{MgO}}^{\text{Co}^{2+}}$ , as measured by Wuensch and Vasilos, are shown as open triangles. The agreement must be considered only fair, since a factor of two discrepancy is present.

The data obtained for the couples annealed at  $P_{\text{O}_2} = 8 \times 10^{-6}$  atm are shown in Figure 123. The same activation energy (2.03 eV) as that found for the couples annealed in oxygen seems to fit the data well. However, the oxygen pressure dependence of the interdiffusion coefficient implied by Figures 122 and 123 is about  $P_{\text{O}_2}^{1/9}$ , somewhat less than the  $P_{\text{O}_2}^{1/6}$  dependence expected on the basis of the cation vacancy dependence in CoO. This discrepancy could arise from several factors:

- 1) The cation vacancy concentration in the CoO crystals was impurity influenced rather than uniquely defined by the temperature and oxygen partial pressure. However, this argument seems unlikely since impurity control might be postulated at the lower temperatures of this study, but the cation vacancy concentration at the higher temperatures should be far greater than any impurity concentration consistent with Table VI. One would, therefore, expect to see a larger pressure dependence at higher temperatures. This behavior was not observed.
- 2) The data are not sufficiently precise to permit reliable determination of the oxygen pressure dependence. Although it is difficult to estimate confidence levels and error limits for the data fairly, it seems that the data could not reasonably be forced to fit a  $1/6$  or larger dependence.

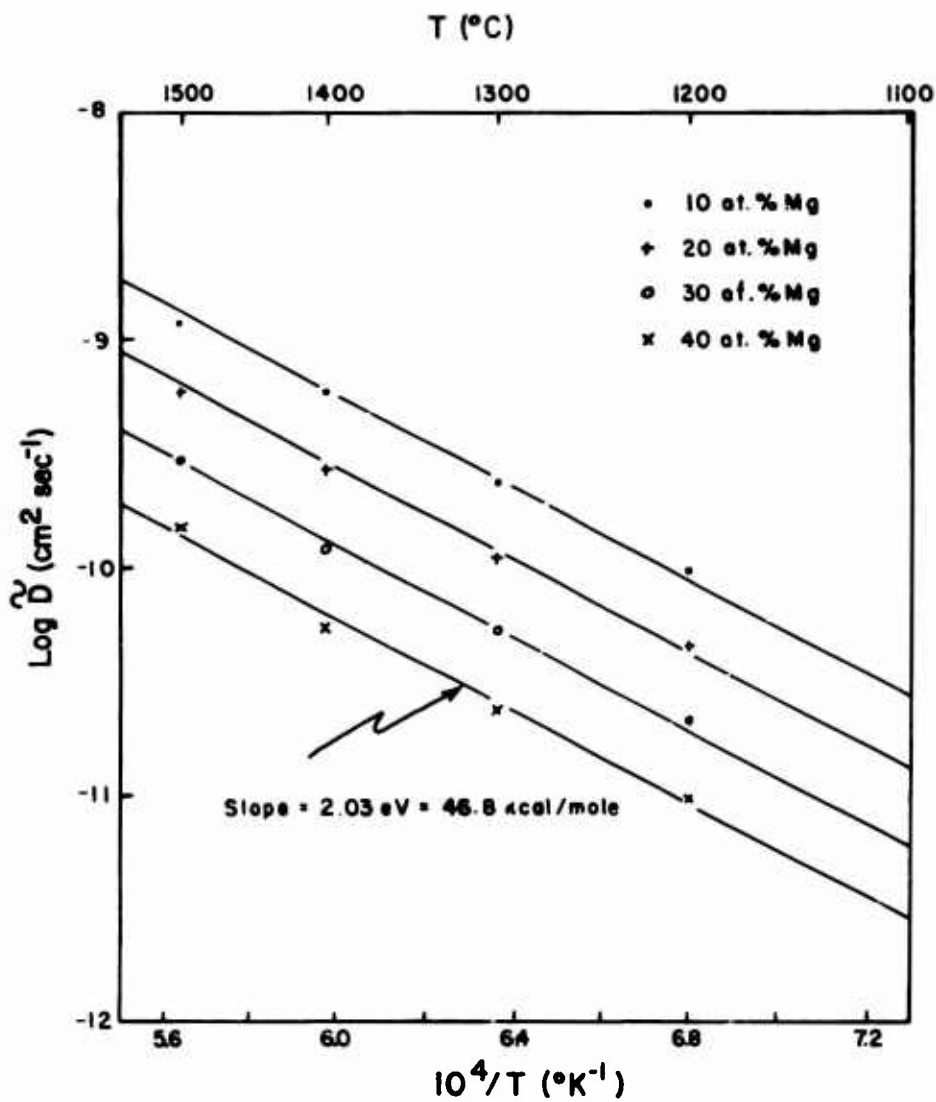


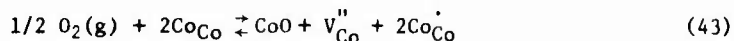
Figure 123. Plot of Calculated Interdiffusion Coefficient as a Function of  $1000/T(^\circ\text{K})$  for Couples Annealed in  $P_{\text{C}_2} = 8 \times 10^{-6} \text{ atm}$ .

- 3) The oxygen partial pressure established in the low  $P_{O_2}$  diffusion anneals was actually higher than that calculated. This possibility seems to merit the most consideration. Although clean furnace tubes were used and care was taken to prevent leaks in the system, it seems reasonable to assume that unforeseen problems influenced the oxygen activity in situ of one anneal. However, three separate annealing furnaces were used for high, medium, and low temperature anneals, and it does not appear likely that the same factor could influence the results in all three systems. A leak in one system, for example, would obviously not affect anneals made in the other two. In addition, the self-consistency of the results casts considerable doubt on this explanation.

Therefore, no convincing explanation can be given for the oxygen pressure dependence discrepancy at this time.

As stated above, the interdiffusion coefficients determined in this study were found to vary exponentially with the mole fraction of magnesium oxide. This result has been related to Zintyl's observation of a similar dependence of the cation vacancy concentration. A fundamental problem is the origin of this exponential dependence.

The incorporation of oxygen into CoO occurs as



and

$$\Delta G_{44}^0 = -RT \ln \left( \frac{[V_{Co}''] [Co_{Co}^{\bullet}]^2}{P_{O_2}^{1/2} [Co_{Co}]^2} \right) \quad (44)$$

For small deviations from stoichiometry,  $[Co_{Co}] = x_{CoO} = 1 - x_{MgO}$ . Also, electrical neutrality of the crystal requires that  $2[V_{Co}''] = [Co_{Co}^{\bullet}]$ .

Hence,

$$\Delta G_{44}^0 = -RT \ln \left( \frac{[\text{Co}_{\text{Co}}^{\cdot}]^3}{2P_{\text{O}_2}^{1/2} (1 - X_{\text{MgO}})^2} \right) \quad (45)$$

and

$$\Delta G_{44}^0 (X_{\text{CoO}}=1) = -RT \ln \left( \frac{[\text{Co}_{\text{Co}}^{\cdot}]^3 X_{\text{CoO}}=1}{2P_{\text{O}_2}^{1/2}} \right) \quad (46)$$

therefore

$$\Delta G_{44}^0 - \Delta G_{44}^0 (X_{\text{CoO}}=1) = -RT \ln \left( \frac{[\text{Co}_{\text{Co}}^{\cdot}]^3}{[\text{Co}_{\text{Co}}^{\cdot}]^3 X_{\text{CoO}}=1 (1 - X_{\text{MgO}})^2} \right) \quad (47)$$

By titration of the trivalent cations in quenched MgO - CoO solid solutions, Zintyl found that  $\Delta G_{44}^0 - \Delta G_{44}^0 (X_{\text{CoO}}=1) = 36.3 X_{\text{MgO}}$  (kcal). If it is assumed that  $\Delta G_{44}^0 (X_{\text{CoO}}=1) = 1.75 \text{ eV} = 40.3 \text{ kcal}$ , in accordance with Bransky and Wimmer,<sup>(90)</sup> then  $\Delta G_{44}^0$  for  $X_{\text{MgO}} = 1$  is  $40.3 + 36.3 = 76.6 \text{ kcal} = 3.32 \text{ eV}$ . This value is in agreement with the 3.4 eV found by Harding et al.<sup>(82)</sup> for the enthalpy of formation of a Schottky defect in MgO. In the absence of any impurity effects, this activation energy is expected for the interdiffusion coefficients determined in this study extrapolated to the composition extreme  $X_{\text{MgO}} = 1$ . However, this is not the case since the temperature range of this study is still well within the extrinsic range of diffusion in MgO. This point has been noted by Blank and Pask,<sup>(79)</sup> and Wuensch and Vasilos,<sup>(80)</sup> among others.

Zintyl attributes the linear variation in  $(\Delta G_{44}^0 - \Delta G_{44}^0 (X_{\text{CoO}}=1))$  with  $X_{\text{MgO}}$  to an increase in energy of the system with increasing magnesium oxide concentration due to the loss of quantum mechanical resonance of the  $\text{Co}^{2+} - \text{Co}^{3+}$  ions; that is, in the pure CoO crystal, each  $\text{Co}^{3+}$  ion is surrounded by twelve  $\text{Co}^{2+}$  nearest neighbors. If the energy barriers represented by the intervening oxygen ions are not too large, then a significant reduction in

energy of the system will occur by the quantum mechanical "spreading" of the deficit electron's charge over all the cations, with the resonance stabilizing the trivalent state. If one of the nearest-neighbor Co cations is now replaced by a magnesium ion, the symmetry of the system is lost, and the resonance is disturbed because of the inability of the magnesium ion to achieve the trivalent state. (With magnesium, the trivalent state would require removal of an electron in the inert gas shell, a prohibitively energetic process.)

Determinations of the mole fraction of trivalent metal ions as a function of mixed oxide composition have also been attempted for the system FeO-MgO<sup>(91,92,93)</sup> and FeO-MnO.<sup>(94)</sup> Brynstad and Flood<sup>(91)</sup> attempted to explain their results in FeO-MgO by an assumption that complexes of one vacancy and two Fe<sup>3+</sup> ions were created with no change in the enthalpy of the system with increasing MgO content. Such an assumption applied to the CoO-MgO system results in Eq. (44), where  $\Delta G^0$  is constant for all  $X_{MgO}$ . Therefore, it follows that  $[Co_{Co}]^3 \propto (1 - X_{MgO})^2$  at constant  $P_{O_2}$ . This dependence fails to agree with Zintyl's experimental results.

Werner<sup>(95)</sup> has also invoked the disturbance of the quantum mechanical resonance between Cu<sup>+</sup> and Cu<sup>2+</sup> ions to explain results obtained on the deviation from stoichiometry as a function of composition in the system Cu<sub>2</sub>S - Ag<sub>2</sub>S. A decrease in cation vacancy concentration with increasing concentration of Ag<sub>2</sub>S was found at constant sulphur activity; specifically, an increase in the free reaction enthalpy of 14 kcal at  $X_{Ag_2S} = 0.5$  over that of pure Cu<sub>2</sub>S was observed. By comparison, Zintyl found an increase of  $36.3/2 = 18$  kcal in  $\Delta G^0$  at  $X_{MgO} = 0.5$  over  $\Delta G^0$  of pure CoO.

In conclusion, the interdiffusion phenomenon in this system was found to exhibit many of the features observed in other transition metal monoxide-magnesium oxide systems--for example, the exponential dependence of  $\bar{D}$  on composition, the absence of any detectable Kirkendall shift, and an activation energy corresponding to the enthalpy of motion of the transition metal cation in MgO.

SECTION V  
MECHANICAL PROPERTIES AND MICROSTRUCTURES OF  
HIGH-TEMPERATURE Ti-BASE ALLOYS

The two most widely used titanium alloys in jet engine compressor blades and vanes have the following compositions: Ti-6wt%Al-2wt%Sn-4wt%Zr-2wt%Mo (Ti-6242) and Ti-6wt%Al-2wt%Sn-4wt%Zr-6wt%Mo (Ti-6246). Both of these alloys consist mainly of h.c.p.  $\alpha$  phase and b.c.c.  $\beta$  phase; Al and Sn stabilize the  $\alpha$  phase, while Mo stabilizes the  $\beta$  phase. These alloys are amenable to a variety of thermomechanical treatments which produce a wide range of mechanical properties and microstructures in the alloys. The aim of the present investigations was to study specific aspects of the mechanical properties of the alloys at room and elevated temperatures and to correlate the mechanical properties with microstructures.

TENSILE PROPERTIES TO 550°C AND MICROSTRUCTURES IN  
QUENCHED AND AGED Ti-6Al-2Sn-4Zr-6Mo ALLOY

Ti-6wt%Al-2wt%Sn-4wt%Zr-6wt%Mo (Ti-6246) is a high yield strength, alpha ( $\alpha$ ) + beta ( $\beta$ ) alloy developed for jet engine applications. A recent study<sup>(96)</sup> has shown that quenching of this alloy from high temperatures near the  $\beta$  transus produces a martensitic phase,  $\alpha''$ , having an orthorhombic lattice. This type of transformation is viewed as lattice distortion of the more normally observed hexagonal martensite phase,  $\alpha'$ , and occurs in many binary titanium alloys which contain higher  $\beta$ -stabilizer solutes.<sup>(97-99)</sup>

The tempering of the orthorhombic martensite in the temperature range 500-600°C hardens and severely embrittles the Ti-6246 alloy.<sup>(96)</sup> In preliminary experiments of the present investigation, the alloy containing tempered martensite developed a very high yield strength at a testing temperature of 550°C. An attempt was made in this study to obtain a range of tensile properties at room temperature and at 550°C in quenched and tempered Ti-6246 alloy.

Standard tensile specimens were machined from the alloy bar stock that had been extruded to 95% reduction in area at 940°C. Two types of heat treatments were employed to vary the microstructures. In one type, specimens

were annealed at different temperatures ranging from 800–950°C, water quenched (w.q.), and then subjected to a fixed aging treatment at 550°C for 48 hr; the purpose was to obtain higher volume fractions of primary  $\alpha$  with decreasing annealing temperatures in the ( $\alpha+\beta$ ) phase field. The second type of heat treatment consisted of a fixed annealing treatment at 950°C for 1 hr, w.q., and then aging for 48 hr at 550°, 575°, and 600°C, the purpose was to change the microstructure of the tempered martensite. The tensile specimens were tested at room temperature and at 550°C in the Instron machine at a cross-head speed of 0.05 cm/min. Thin foils for transmission electron microscopy (TEM) were prepared by a standard technique.<sup>(100)</sup>

#### Tensile Properties at Room Temperature and at 550°C

For all heat treatments except 800°C anneal, the alloy was totally brittle at room temperature. The fracture strength in the gauge section of brittle specimens was in the neighborhood of 1035 MN/m<sup>2</sup>. Specimens that were annealed at 800°C, w.q., and then aged at 550°C for 48 hr exhibited a limited ductility of 2% elongation to fracture. The yield strength for this aging treatment was found to be 2000 MN/m<sup>2</sup>.

Figure 124 shows the tensile properties at 550°C as a function of different annealing treatments but a fixed aging treatment of 48 hr at 550°C. For an annealing temperature of 800°C, a yield strength of 725 MN/m<sup>2</sup> was obtained. With increasing annealing temperatures up to 950°C, the strength increased, and for this annealing temperature a very high yield strength of 1140 MN/m<sup>2</sup> was obtained. It should be noted that the heat treatments that produced high yield strengths at 550°C were also responsible for complete loss of ductility at room temperature. All specimens were reasonably ductile at 550°C. Figure 125 shows the tensile properties at 550°C as a function of different aging temperatures but a fixed annealing treatment at 950°C. With increasing aging temperatures, the yield strength drops considerably.



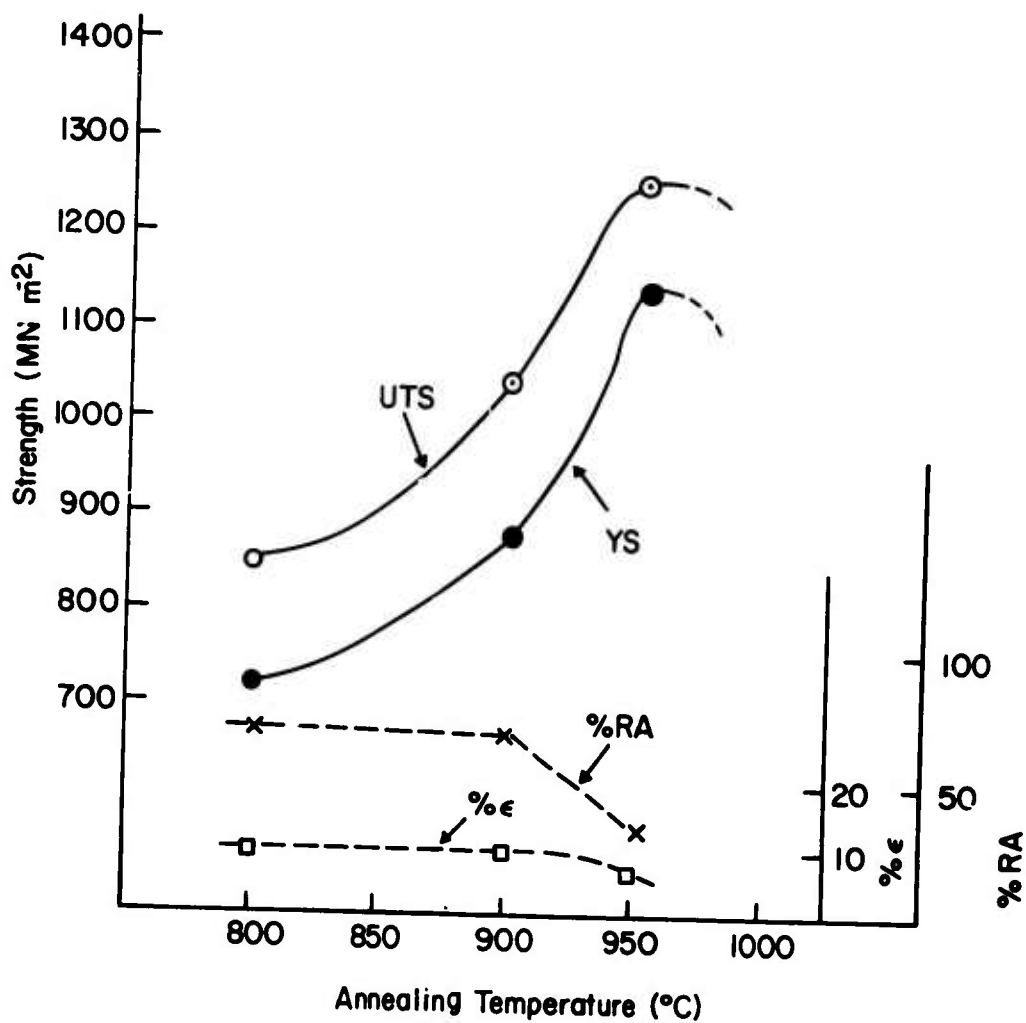


Figure 124. Tensile Properties of Ti-6246 at 550°C as Function of Annealing Temperature. Specimens Water Quenched from Annealing Temperatures and Then Aged at 550°C for 48 hr.

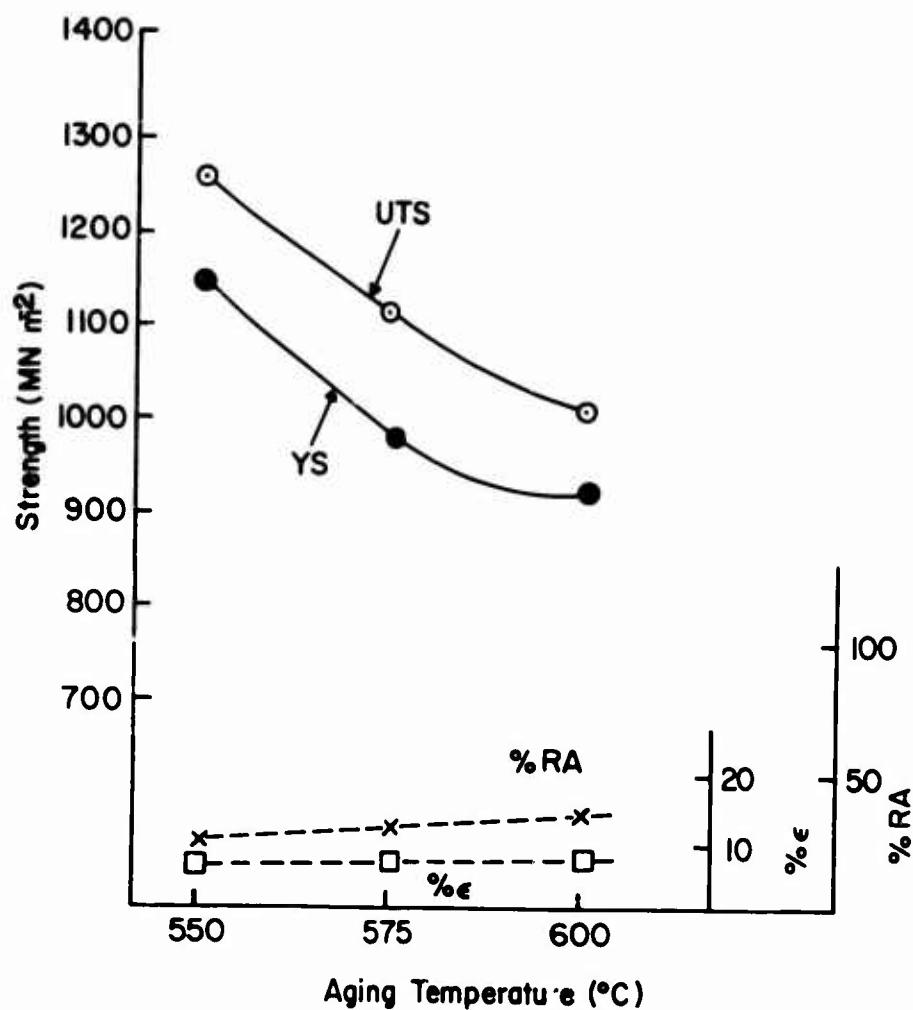


Figure 125. Tensile Properties of Ti-6246 at 550°C as Function of Aging Temperature. Specimens Annealed at 950°C and Water Quenched Prior to 48 hr Aging Treatments.

### Microstructure Correlations

Figure 126 is the bright-field electron micrograph of a specimen annealed at 800°C for 1 hr, w.q., and aged for 48 hr at 550°C. A high volume fraction of large primary- $\alpha$  plates can be observed. This heat treatment had imparted to the alloy limited room temperature ductility (2% elongation to fracture) and also a low yield strength (725 MN/m<sup>2</sup>) at 550°C. Since the large primary- $\alpha$  plates are able to undergo plastic deformation, the limited room temperature ductility as well as the low yield strength at 550°C for this heat treatment might be attributed to the presence of a high volume fraction of the primary- $\alpha$  phase. For the specimens quenched from 800°C, x-ray diffraction revealed the presence of  $\alpha$  and retained  $\beta$  phases, no peaks corresponding to the orthorhombic martensite were observed.

The 950°C/1 hr  $\rightarrow$  w.q.  $\rightarrow$  550°C/48 hr heat treatment rendered the alloy totally brittle at room temperature but at 550°C imparted a high yield strength of 1140/MN/m<sup>2</sup>. Figure 127 is a light micrograph showing the general microstructure which corresponds to this heat treatment. A very low volume fraction of primary- $\alpha$ -phase particles (shown by the arrow) confirms that the annealing treatment at 950°C was carried out just below  $\beta$  transus. The dark-etching matrix reveals the structure of the aged martensite. In the quenched condition from 950°C, the x-ray diffraction pattern at  $2\theta$  values between 30 and 42° showed five peaks characteristic of orthorhombic martensite. (96,101)

The tempering behavior of the orthorhombic martensite was followed in greater detail by aging the specimens that had been quenched from 950°C for different periods at 550°C. The diamond-pyramid hardness data are presented in Figure 128 as a function of aging time. In the quenched condition the alloy is not very hard (DPH = 283), but even a short aging period of 15 min increases the hardness considerably (DPH = 462). TEM observation of the specimen in the quenched state revealed, in most of the thin foil, streaked  $\beta$ -phase diffraction patterns; the corresponding bright-field images revealed a highly defected matrix containing few martensite plates. The absence of  $\beta$ -phase peaks in the x-ray diffraction of the quenched bulk specimens indicates that during the TEM thin foil preparation, apparently

Reproduced from  
best available copy.

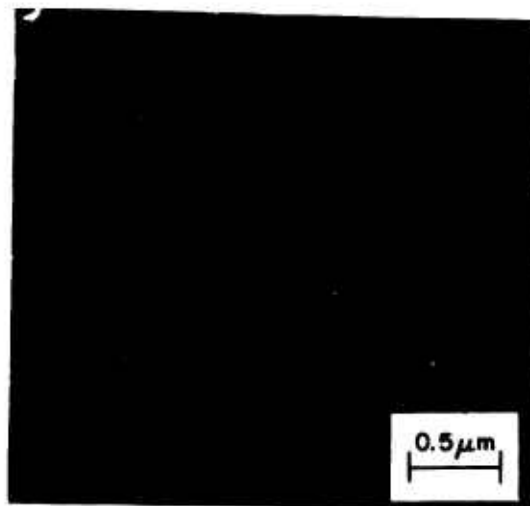


Figure 126. Bright-Field Electron Micrograph Showing High Volume Fraction of Primary- $\alpha$  Plates. Heat Treatment: 800°C/1 hr  $\rightarrow$  w.q.; 550°C/48 hr  $\rightarrow$  air cool (a.c.).

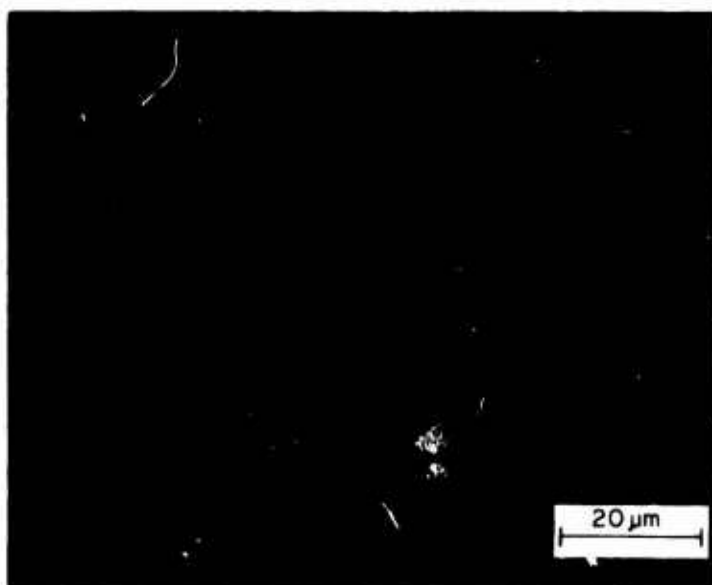


Figure 127. Light Micrograph Showing General Microstructure of Tempered Martensite. Light Particles, as Shown by Arrow, Belong to Primary- $\alpha$  Phase. Heat Treatment: 950°C/1 hr w.q.; 550°C/48 hr a.c.

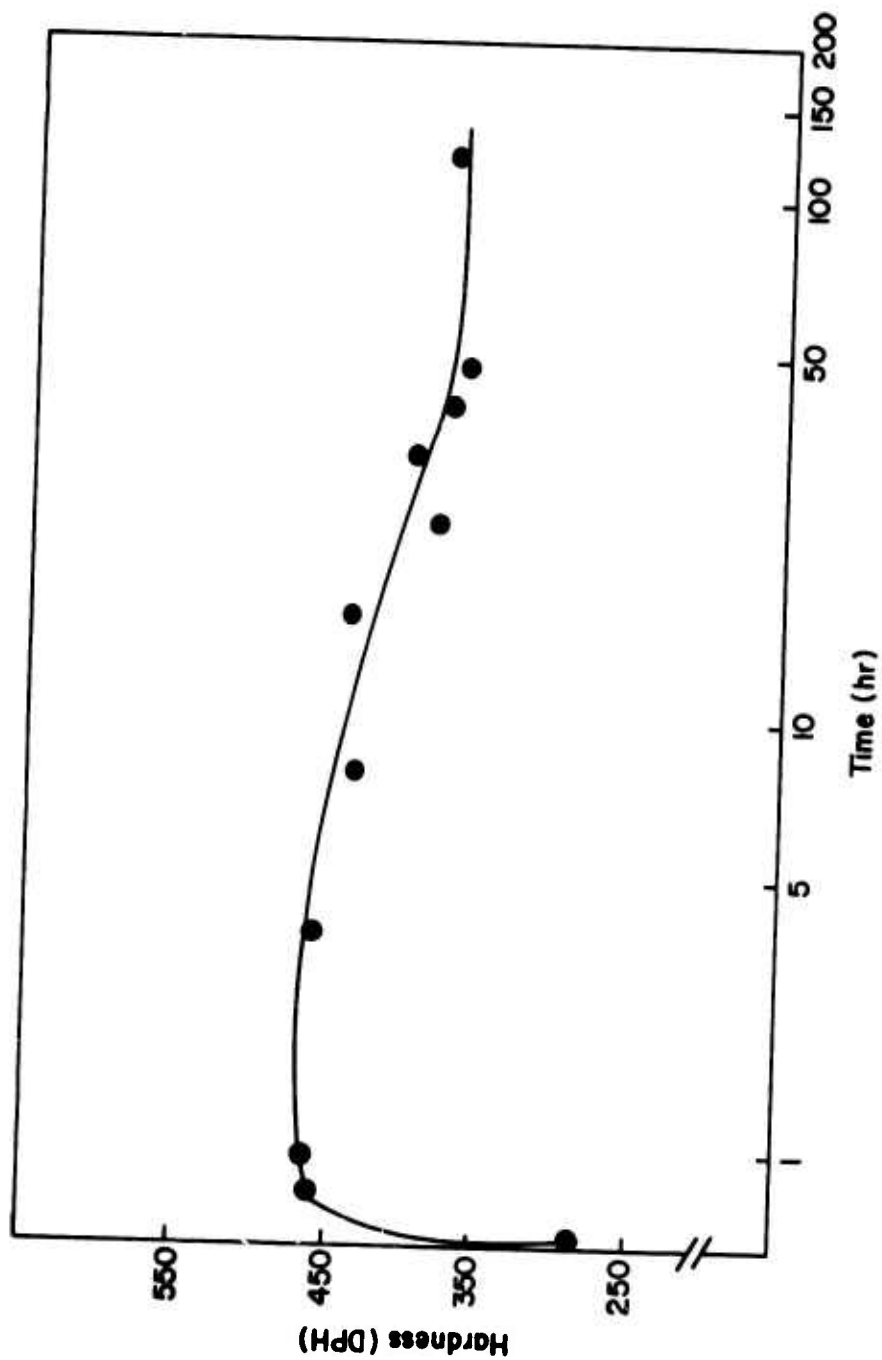


Figure 128. Diamond-Pyramid Hardness Values of Ti-6246 as Function of Aging Time at 550°C. Specimens Annealed at 950°C/1 hr + w.q. Prior to Aging Treatments.

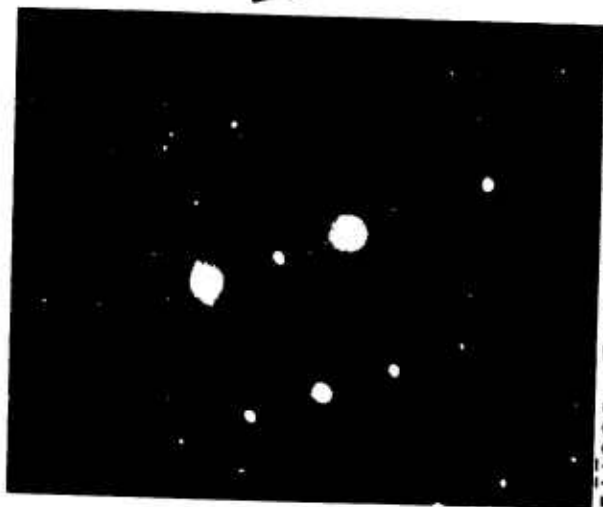
the bulk martensite reverts partially to  $\beta$  phase, in agreement with the conclusions of Margolin et al.<sup>(96)</sup>

TEM observations of the specimens aged for 8 hr at 550°C (DPH  $\sim$  392) revealed, in most of the thin foil, the tempered martensite; however, scattered areas belonging to the  $\beta$  phase were also observed in the thin foil. Since the specimens possessed a high degree of hardness for this aging treatment, it seemed unlikely that some of the martensite had reverted to the  $\beta$  phase during electrolytic thinning; it was concluded, therefore, that small amounts of the  $\beta$  phase had been retained during the quenching process. The amount of retained  $\beta$  was so small that it could not be detected by x-ray diffraction. Figures 129(a) and (b) are, respectively, the bright-field electron micrograph and the corresponding selected area diffraction pattern showing the tempered martensite microstructure. The diffraction pattern was indexed as  $[\bar{1}\bar{1}20]_{\alpha}$  zone coinciding with  $[100]_{\beta}$  zone; the dark-field electron micrograph taken from the  $(110)_{\beta}$  reflection illuminated internal  $\beta$  precipitates in the hexagonal martensite plates. The x-ray diffraction also revealed the presence of low intensity, broad  $\beta$  peaks in addition to hexagonal  $\alpha$  peaks. Figure 130(a) is a diffraction pattern taken from regions containing retained  $\beta$ ; this pattern was indexed as  $[111]_{\beta}$  zone, coinciding with all the Burger's variants of the  $\alpha$  phase. Figure 130(b) is the dark-field electron micrograph taken from the  $(10\bar{1}1)_{\alpha}$  reflection showing the  $\alpha$ -phase particles in the retained- $\beta$  matrix.

In summary, the present study on the tempering behavior of orthorhombic martensite in Ti-6246 alloy corroborates an extensive investigation by Margolin et al.<sup>(101)</sup> Quenching of this alloy from 950°C to room temperature produces a microstructure containing mostly orthorhombic martensite and small amounts of retained  $\beta$ . Aging at 550°C then precipitates very small  $\beta$  particles in the martensite plates; the orthorhombicity of the martensite lattice is lost, and the crystallography of  $\beta$  precipitation follows the well-known  $\alpha \rightarrow \beta$  Burger's relationship. The precipitation of  $\beta$  particles makes the alloy very hard and inductile and also very strong at 550°C. In addition, the aging process precipitates  $\alpha$  particles in the retained  $\beta$ .



(a)



$[\bar{1}120]_{\alpha}$  Zone Axis  $\parallel [001]_{\beta}$  Zone Axis

(b)

Figure 129. (a) Bright Field Electron Micrograph Showing Precipitate Contrast in the Tempered Martensite. Heat Treatment:  $950^{\circ}\text{C}/1 \text{ hr} \rightarrow \text{w.q.}; 550^{\circ}\text{C}/8 \text{ hr} \rightarrow \text{a.c.}$   
 (b) Corresponding Electron Diffraction Pattern Showing  $[\bar{1}120]_{\alpha}$  Hexagonal Zone Axis Coinciding with  $[001]_{\beta}$  Zone Axis.



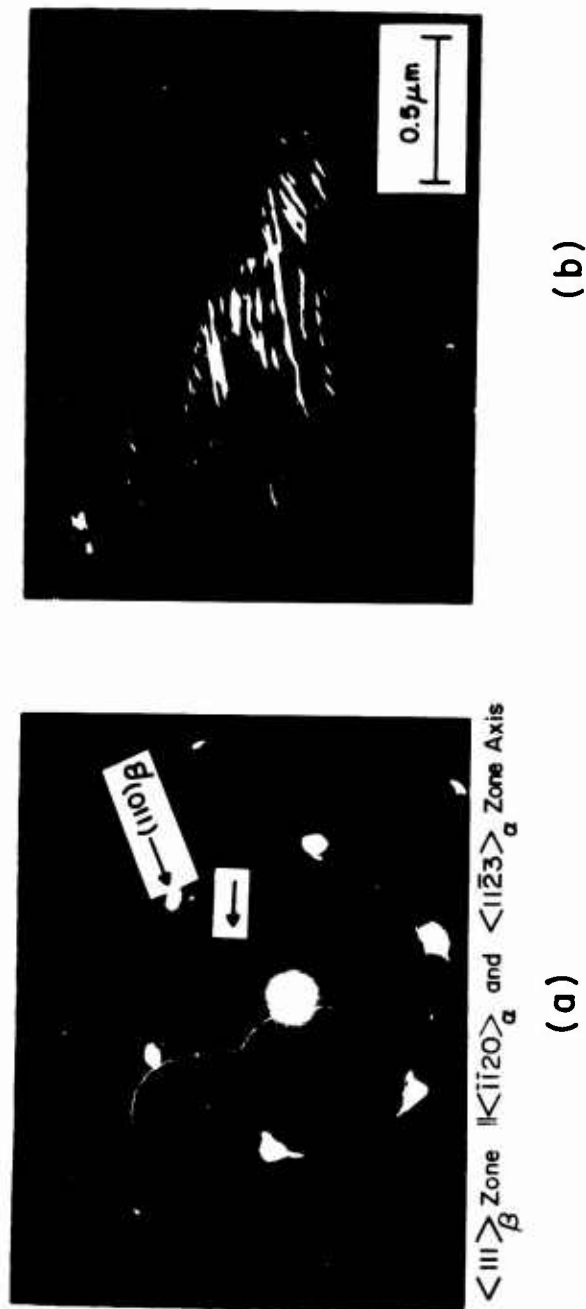


Figure 130. Different Area of the Thin Foil of Figure 129 Showing Region of Retained  $\beta$  in which  $\beta$  Particles Have Precipitated. (a) Dark-Field Micrograph. (b) Electron Diffraction Pattern.

## EMBRITTLEMENT OF Ti-6Al-2Sn-4Zr-2Mo ALLOY BY $\alpha_2$ -PHASE PRECIPITATION

Ti-6Al-2Sn-4Zr-2Mo (Ti-6242) is a commercially available titanium alloy for jet engine applications in the use temperature range 370° to 540°C. Standard thermomechanical treatments impart to the alloy high elevated temperature strength and creep resistance by producing high volume fractions of the  $\alpha$  phase in equilibrium with small amounts of the  $\beta$  phase. However, this alloy is known to exhibit a room temperature embrittlement after prolonged exposure at the use temperature.

In a recent investigation,<sup>(102)</sup> loss of room temperature fracture toughness of Ti-6242 alloy was obtained experimentally as a function of exposure times at temperatures ranging from 425° to 600°C. The activation energy for the embrittlement process was shown to be nearly equal to that for diffusion of aluminum and tin in titanium; this observation was taken as evidence for the formation of  $\alpha_2$ -phase [based upon  $Ti_3(Al,Sn)$ ] domains. It was concluded, therefore, that the room temperature embrittlement was caused by the diffusion controlled formation and growth of ordered  $\alpha$ -phase domains in the  $\alpha$  matrix. However, no microstructural observation of the presence of the  $\alpha_2$  phase was made. The purpose of the present investigation was to correlate the room temperature tensile properties and fracture toughness of the Ti-6242 alloy with the presence of the  $\alpha_2$ -phase precipitates observed directly by thin foil transmission electron microscopy (TEM).

Standard tensile and standard V-notched specimens were prepared from the alloy bar stock which had been processed and swaged in the ( $\alpha+\beta$ )-phase field at 900°C. One set of specimens was subjected to a stress-relieve anneal at 600°C for 8 hr; a second set was subjected to the same stress-relieve heat treatment but, in addition, was subsequently aged at 540°C for 1000 hr. The tensile specimens were tested at room temperature at a cross-head speed of  $5 \times 10^{-2}$  cm/min. The gauge length of the specimens was 2.85 cm. The V-notched bars were precracked in fatigue and then subjected to three point bend tests in order to determine the approximate fracture-toughness value,  $K_{Ic}$ .<sup>(103)</sup> Thin foils for TEM observation were prepared by electrolytic thinning and polishing at -50°C, following the procedure of Blackburn and Williams.<sup>(100)</sup>

The room temperature mechanical properties of the alloy resulting from two types of heat treatments are presented in Table VIII. The data show that the 0.2% offset yield strength of the alloy in the aged condition is higher than that in the stress-relieve anneal condition. However, the percent elongation at failure, the percent reduction in area, and the approximate  $K_{IC}$  value are lower in the aged condition. The room temperature loss of ductility, as reflected in the reduced values of both  $K_{IC}$  and percent RA, is quite considerable.

TABLE VIII  
ROOM TEMPERATURE MECHANICAL PROPERTIES OF Ti-6Al-2Sn-4Zr-2Mo  
ALLOY IN THE STRESS-RELIEVED AND AGED CONDITIONS

Processing History	Heat Treatment	0.2% Offset Yield Stress MN/m <sup>2</sup>	Percent Elongation at Failure	Percent Reduction in Area	Approximate $K_{IC}$ Values MN/m <sup>2</sup> m <sup>1/2</sup>
900°C Processed	600°C for 8 hr, air cooled	1090.00	15.20	38.70	55.5
900°C Processed	600°C for 8 hr, 540°C for 1000 hr, air cooled	1125.00	12.15	25.66	40.3

Figure 131 is a bright-field electron micrograph showing general  $\alpha$ - $\beta$  microstructure in the 900°C processed and 600°C/8 hr annealed condition. The microstructure consists of large, equiaxed primary- $\alpha$  grains that formed during the 900°C processing and subsequent air cooling and prior- $\beta$  grains containing large secondary- $\alpha$  needles that precipitated in the  $\beta$  grains during the 600°C/8 hr annealing treatment. For the annealed condition, Figure 132 represents a  $[2\bar{1}\bar{1}0]_{\alpha}$ -zone-axis diffraction pattern taken from a primary- $\alpha$  grain. The arrow in the micrograph indicates the position at which extremely weak  $\{01\bar{1}1\}_{\alpha_2}$  super-lattice reflections could be observed in the microscope; however, they are not readily apparent in the printed micrograph. The observation of the  $\alpha_2$  reflection indicated that ordered  $\alpha_2$ -phase domains had already formed in the  $\alpha$  phase even for the short annealing time of 8 hr at 600°C. Attempts to illuminate these domains in the dark field were unsuccessful because of the very weak intensity of the super-lattice spots;

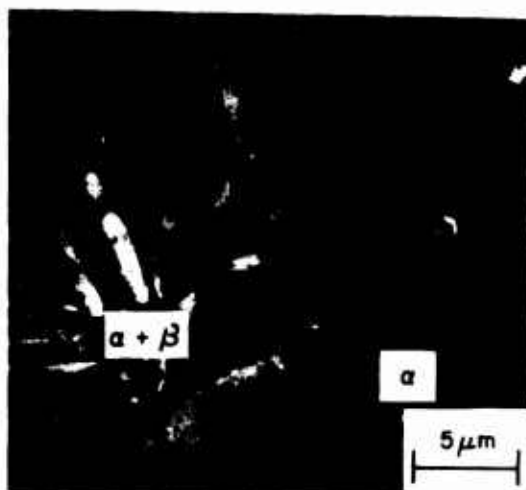


Figure 131. Bright-Field Electron Micrograph Showing  $\alpha + \beta$  Structure in Ti-6242 Alloy. 1650°F Processed Air Cooled; 1100°F/8 hr Stress Relieved.

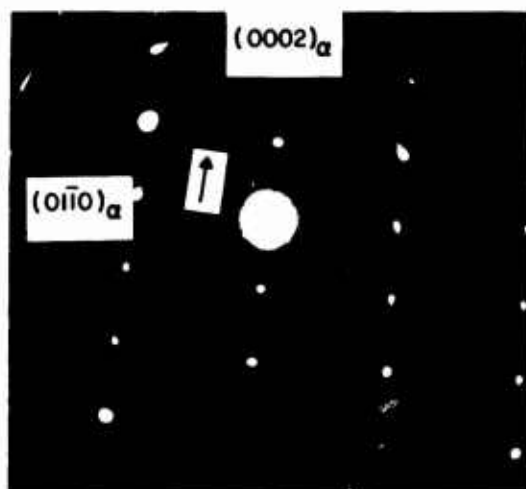


Figure 132. Selected Area Diffraction Pattern Taken from a Primary Grain of Figure 131.  $[2\bar{1}10]_\alpha$  Zone Axis. Arrow Shows Position of Faint  $(0111)_\alpha$  Reflection.

therefore, it appears that the  $\alpha_2$ -phase domains are extremely small in the annealed conditions.

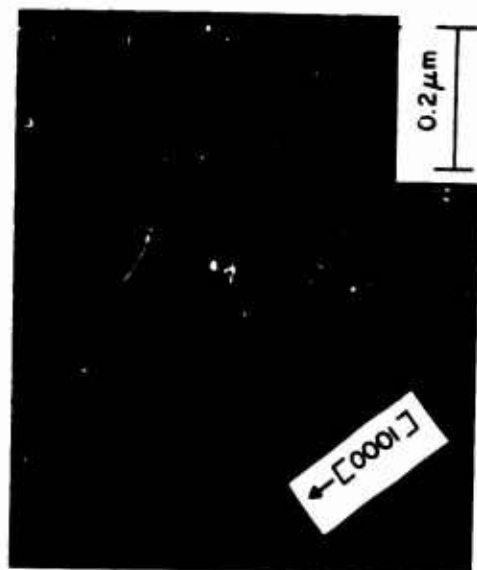
TEM observations of the second set of specimens (aged at 540°C for 1000 hr) revealed more intense super-lattice reflections, and therefore it was possible to illuminate the  $\alpha_2$  phase in dark field. Figures 132(a) and (b) are, respectively, the  $[2\bar{1}\bar{1}0]_{\alpha}$ -zone-axis diffraction pattern and the dark field taken from the  $(01\bar{1}1)_{\alpha_2}$  reflection. The dark-field micrograph shows a uniform distribution of the  $\alpha_2$ -phase precipitate needles  $\sim 550$  Å long and  $\sim 50$  Å in diam. TEM observation of the dark-field image generated from operative  $\alpha_2$  reflections in the  $[0001]_{\alpha}$ -zone-axis diffraction pattern revealed circular cross sections of the  $\alpha_2$ -phase needles. It can be seen from Figure 133 that the longitudinal direction of the  $\alpha_2$  needles is parallel to the c-axis of the  $\alpha$  lattice; the shape and orientation of the  $\alpha_2$  phase are similar to those reported for binary Ti-Al alloys.<sup>(104,105)</sup> In the bright field the distribution of the  $\alpha_2$  needles was revealed by elastic strain-field contrast in the  $\alpha$  matrix, indicating that the  $\alpha_2$  particles are coherent with the  $\alpha$  matrix.

The present investigation, together with a recent study by Shambler,<sup>(102)</sup> shows that in the Ti-6242 alloy, the  $\alpha$ -stabilizer (6wt%Al and 2wt%Sn) content is not sufficiently low to suppress  $\alpha_2$ -phase precipitation. Although the binary Ti-Al phase diagram proposed by Blackburn<sup>(104)</sup> indicates that the Ti-6wt%Al alloy is in the single  $\alpha$ -phase field up to 935°C, a ternary addition of 2wt%Sn appears to promote formation of the  $\alpha_2$  phase upon low-temperature aging. It is possible that, since the Ti contents of the Ti-6242 alloy partition into  $\alpha$  and  $\beta$  phases in the 600°C F/8 hr annealed condition and since the Al and Sn are  $\alpha$ -stabilizers, the effective proportions of Al and Sn in the  $\alpha$  phase may be more than their initial nominal composition.

The increase in yield strength in the aged condition (see Table 7) can be attributed to the resistance which the coherent, ordered  $\alpha_2$  particles offer to the glide dislocations. The  $\alpha_2$  particles are extremely small (see Figure 133) and, therefore, are likely to be sheared by the dislocations. It has been shown in Ti-Al base alloys<sup>(105)</sup> that the shearing of the  $\alpha_2$  particles results in the formation of highly planar, heterogeneous slip which is responsible for embrittlement of the alloys.



(a)



(b)

Figure 133. (a)  $[2\bar{1}0]_1$  -Zone-Axis Diffraction Pattern Showing Intense  $(01\bar{1})_2$  Super-Lattice Reflections. (b) Dark Field Taken from the  $\alpha_2$  Reflection Showing Uniform Distribution of  $\alpha_2$  Needles.  $1450^\circ\text{F}$  Processed. Air Cooled;  $110^\circ\text{F}/8\text{ hr}$  Stress Relieved, Followed by  $1000^\circ\text{F}/1000\text{ hr}$  Aging Treatment.

## SECTION VI

### ELECTRON-MICROPROBE ANALYSIS OF HIGH-TEMPERATURE MATERIALS

A material irradiated under proper conditions emits x-rays having characteristic energies for each element present. These x-rays arise from electronic transitions from high-energy levels to inner shell vacancies created when an inner electron is ejected by the primary radiation. Upon dropping into these vacancies, the electrons emit their excess energy in the form of x-rays. When electrons from higher energy levels return to the K-shell, the resulting x-rays form a K spectrum. When electrons return to the L-shell, an L spectrum results; likewise, an M spectrum appears when the electrons fall into the M-shell. Thus, one element may have several characteristic spectra.

The primary radiation source for the creation of inner shell vacancies within a specimen in the electron microprobe is a beam of electrons. An electron microprobe consists basically of an electron gun which is a source of electrons, magnetic lenses which focus the electrons into a beam and onto the sample, a vacuum chamber which encloses the gun and sample chamber, spectrometers which detect the emitted x-rays, and associated electronics which control the electron optics, counting, and readout equipment.

The spectra produced from a sample in the electron microprobe are characteristic of the elements present and thus yield qualitative information. Since the intensity of the x-ray signal is directly related to the amount of the element present, this relationship can be used for quantitative analyses. Chemical analysis using the electron microprobe is an appealing concept since volumes of  $\sim 1 \mu\text{m}^3$  can be examined, and thus local volumes of heterogeneous materials can be analyzed.

#### QUANTITATIVE ANALYSIS

##### Procedures

For this study raw data from an electron microprobe consisted of a measured intensity (counting rate) of the characteristic x-radiation from an element in a

specimen and from that same element in its pure state (i.e., from the sample and from the added standards) together with their respective background counting rates. Of course, some elements are not obtainable in the pure state, and in these cases well characterized compounds containing the element of interest were used. Several procedures are available for transforming these raw data--after background and instrumental errors have been corrected for--into quantitative values. (106)

Instrumental errors arise from instabilities of the electronic equipment, finite recovery time of the x-ray detectors (detector dead time), and mechanical drift of the spectrometers and specimen stage. These errors can be corrected for if one is sufficiently familiar with the particular instrument from which the data are obtained. For example, detector dead time can be measured and mechanical drift accounted for by assuming that the drift is linear with time. Familiarity with the equipment enables the operator to determine the cases in which such an assumption may not be valid. Electronic instabilities have been minimized by proper design of the electronics by instrument manufacturers.

Background counting rate is measured (with a crystal spectrometer) by detuning the spectrometer to both sides of the peak position and averaging the two values obtained. This quantity is then subtracted from the peak counting rate. The ratio of the peak intensity of the element under analysis in the specimen to that of the pure element ( $I/I_0$ )--after instrumental and background corrections--is then proportional to the weight fraction of that element in the specimen.

Finally, a correction procedure must be applied to the intensity ratio since errors result from the interaction of radiation and sample. Correction procedures which have been used are (1) comparison with standards, (2) calibration curves, (3) analytical approach using correction factors, and (4) combinations of these procedures. Quantitative results in this report involve the use of correction factors (with or without a computer program) and the construction of calibration curves using these factors. The correction factor defines the proportionality constant which transforms intensity ratios to weight fractions. The necessary corrections can be conveniently divided



into three parts, although the parts overlap somewhat. These three parts are called atomic number correction (Z), absorption correction (A), and fluorescence correction (F). The fluorescence correction is necessary because both white and characteristic x-radiation are emitted from the sample. This fluorescence effect is usually small, being greatest when an element having an emitted wavelength just smaller than the absorption edge of the element under analysis is present. The atomic number correction is due to the back-scattering of some of the exiting electrons by the specimen and the stopping power of the specimen for electrons. Absorption corrections are necessary because the sample material itself absorbs produced x-rays. Since the correction factor is dependent on the concentration of each element present, iterative calculations must be performed until some predetermined tolerance is reached. Hand calculations on ternary and higher systems are extremely tedious; therefore, a computer program encompassing these corrections written by Colby<sup>(107)</sup> was adapted to the CDC 6600 computer to obtain weight percents of the elements under analysis.

### Standards

Since methods for obtaining quantitative data involve a comparison of the intensity of the unknown to that of a standard--preferably a pure element--well characterized standards are essential.

### Light Metals and Their Oxides

Light element analysis is a problem not only because of the lack of suitable pure elements for use as standards but also because the x-ray energies emitted from these elements are very low, resulting in significant scatter and, in turn, inefficient detection and collection. Also, the spectra for the very light elements are wide bands, which make determination of the peak positions difficult. Because of these problems several light-metal/metal-oxide systems were studied to determine whether there is close correspondence between the experimental intensity ratios and the calculated values when the correction factor approach is used. The  $\text{TiO}_2/\text{Ti}$ ,  $\text{MgO}/\text{Mg}$ ,  $\text{Al}_2\text{O}_3/\text{Al}$ , and  $\text{SiO}_2/\text{Si}$  systems were studied. These particular systems were chosen because of the interest in light metals in  $\text{SiO}_2$  oxidation scales and also because characterizations of these oxides would aid in the choice of an oxygen standard.

The metals used and their forms and/or purities are listed below:

Ti	99.999
TiO <sub>2</sub>	single crystal
Si	99.99
SiO <sub>2</sub>	polycrystal 99.99
Al	99.99
Al <sub>2</sub> O <sub>3</sub>	single crystal
Mg	ribbon (later found to contain ~ 1.5% Mn)
MgO	single crystal 99.99

Material of four-nines purity is adequate for electron-microprobe standards, and most of the above materials are at least this pure. For two of the single crystal oxides, no purity is specified; however, it is felt that they are probably at least four-nines pure. The Mg ribbon was found to contain a significant amount of impurity. This impurity was discovered after data had been collected; in subsequent investigations purer Mg was used.

The calculated curves in Figure 134 were drawn by applying the aforementioned mathematical corrections at various accelerating potentials to the theoretical weight fractions of the metals in their respective oxides. These are the curves that one would expect the experimental uncorrected intensity ratios to follow. Theoretical values of  $I/I_0$  (corresponding to weight fractions) for Ti in TiO<sub>2</sub>, Mg in MgO, Al in Al<sub>2</sub>O<sub>3</sub>, and Si in SiO<sub>2</sub> are listed on the ordinate; these curves would, of course, be parallel to the abscissa. Only one point was determined for Ti in titania since the critical excitation voltage of the Ti K<sub>α</sub> radiation is 4.964 kV and thus 15 kV is about the optimum operating voltage for this element (2-1/2 to 3 times the critical voltage). All calculations were made and experimental data collected using the K<sub>α</sub> radiation since these are the most intense x-ray peaks for these metals.

From the calculated curves, not including the Ti point, the following observations may be made:

- 1) For this range of accelerating potentials, the curves are nearly linear.
- 2) As the atomic number of the metal increases, less total deviation from the theoretical value is evident at any given accelerating voltage.

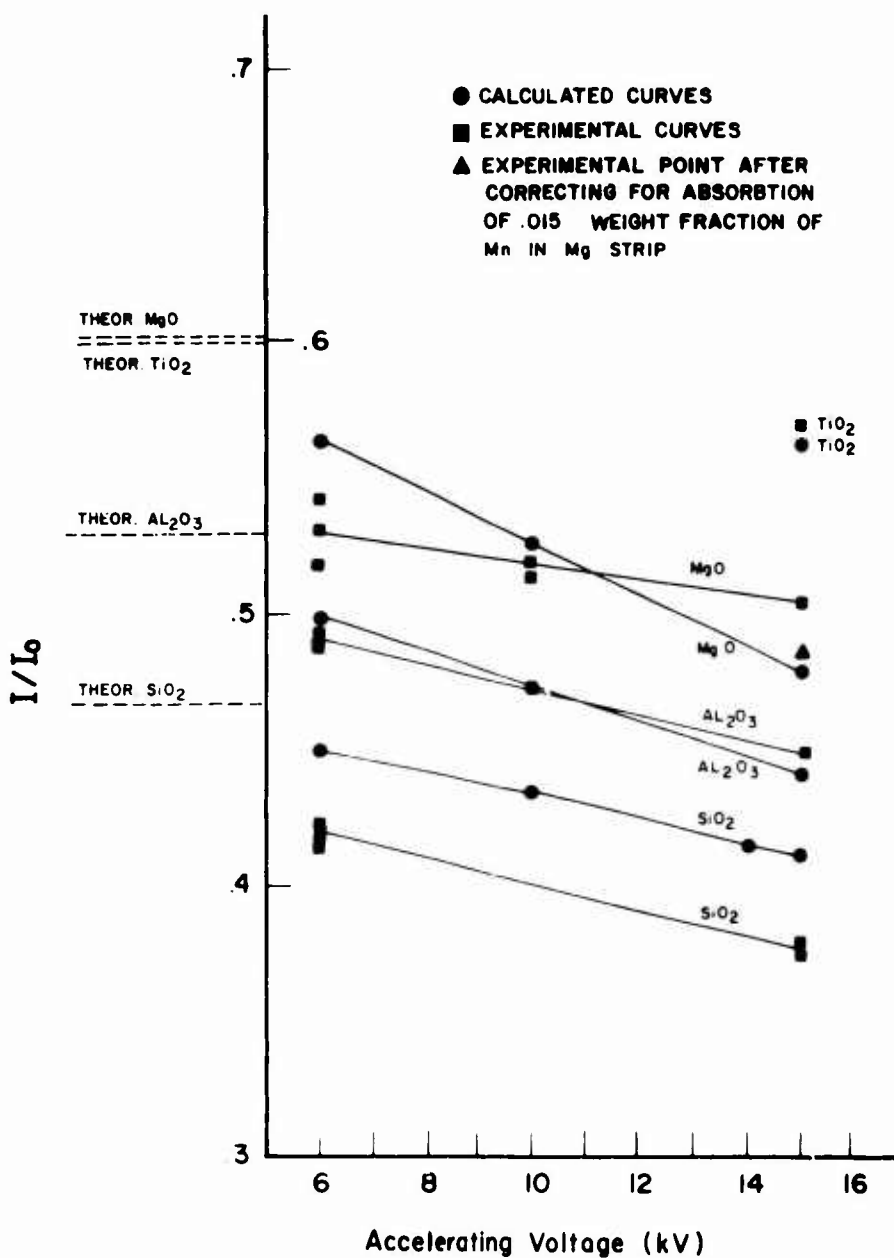


Figure 134. Calculated and Experimental Curves of the Intensity Ratios of the Metal Radiation in the Metal/Metal Oxide System as a Function of Accelerating Voltage.

- 3) As the accelerating voltage increases, the calculated values for each metal deviate further from the theoretical value; i.e., the slopes of the curves are negative.
- 4) As the atomic number of the metal increases, less deviation from the theoretical value is apparent; i.e., the slopes become less negative with increasing Z.

These observations illustrate one principle of microprobe analysis, that the magnitude of the corrections necessary can be minimized if the lowest possible operating voltage is used. However, this minimum voltage should be about 2-1/2 to 3 times the critical excitation potential of the radiation being detected in order to obtain an optimum yield of x-rays. The critical excitation voltages for Mg, Al, and Si are 1.3, 1.6, and 1.8 keV, respectively; therefore, the voltages used in this study are well above optimum values.

The experimental curves in Figure 134 were drawn by using the uncorrected intensity ratios of the characteristic  $K_{\alpha}$  radiation of the metal in the oxide and of the pure metal. Ideally, these experimental curves fall on the calculated curves; but, as can be seen in the figure, they do not. Each system and its deviation from the ideal will be discussed.

The Ti intensity ratio deviates from the calculated value by about 0.8. Since Ti is fairly reactive, an oxide layer on the surface of the "pure" metal would tend to decrease the  $I_o$ , which would result in a higher intensity ratio,  $I/I_o$ , where I is the Ti  $K_{\alpha}$  signal from  $TiO_2$  and  $I_o$  is the Ti  $K_{\alpha}$  signal from the Ti metal.

Subsequent to obtaining of data on the MgO/Mg system, it was found that the Mg ribbon contained about 1.5% Mn. A correction, taking into account the presence of this element, showed that the intensity ratio for the Mg  $K_{\alpha}$  signal from MgO and pure Mg gave an experimental point at 15 kV, indicated by the triangle in Figure 134. This data point deviates from that obtained previously by 0.7 units and is much closer to the calculated value than was the original experimental point. The experimental points at other accelerating voltages on the curve would also be lowered upon correction; however, the effect would tend to decrease with increasing accelerating voltage, resulting

in a curve retaining its negative slope. The presence of a significant amount of Mn--if unevenly distributed in the Mg ribbon--could also account for the large scatter in experimental points for the MgO/Mg system. In addition, the specimen geometry of the metal (ribbon) introduces the possibility that certain areas of the metal are extremely thin and thus at higher accelerating voltages the volume sampled is not entirely that of the sample but includes some underlying mounting material. An oxide film on the Mg metal would also tend to decrease the Mg  $K_{\alpha}$  signal and result in a higher than expected intensity ratio, as in the case of the Ti. However, the fact that this effect should decrease with accelerating voltage does not explain the higher than calculated intensity ratio of 15 kV and the lower than calculated intensity ratio at lower accelerating voltages.

The Al  $K_{\alpha}$  radiation intensity ratios are near the calculated ones, with the curve behavior similar to that of the Mg curve, i.e., higher than calculated values at high kV and lower than calculated values at low kV. The foregoing data, which result in nonparallel experimental and calculated curves, indicate that the mathematical corrections are not adequate for dealing with the low atomic number elements. The most probable reason for this unreliable behavior is that parameters such as mass attenuation coefficients, mean ionization potentials, and other constants are not well defined for the lighter elements. Consequently, estimates must be made, and, therefore, the calculations do not reflect the true behavior of the lighter elements.

The experimental curve for the Si/SiO<sub>2</sub> system is approximately parallel to the calculated curve, which indicates that, when  $Z \geq 14$ , the mathematical corrections are more accurate in describing real systems than when  $Z < 14$ . SiO<sub>2</sub> was the only polycrystalline oxide studied, and its density may not be close to the theoretical density, which would result in a low intensity ratio. If one assumes the SiO<sub>2</sub> to be 93% dense, then the experimental curve falls very near the calculated curve (a deviation of  $\pm 0.2$ ).

#### Hf/HfO<sub>2</sub> Standards

Because of the interest in the oxidation of HfB<sub>2</sub>, an investigation of a HfO<sub>2</sub> standard was undertaken. Two spectra from Hf are available for

examination--L and M--with the choice of spectrum primarily dependent upon the other elements present in the system under study (i.e., no interfering spectra should be present).

Figure 135 gives the experimental intensity ratios for the  $L_{\alpha}$  and  $M_{\alpha}$  spectra, as functions of accelerating potential of the exiting radiation. The calculated values--although somewhat lower than the experimental ones--follow this trend, i.e., increasing intensity ratio with increasing accelerating potential. This trend is opposite that for the light metal oxide systems for the following reason. In both cases the atomic number (Z) effect tends to yield a lower intensity ratio than the theoretical value and this (Z) correction factor approaches unity as the energy of the exiting radiation increases; however, the absorption correction factor (A) behaves differently in each case. For the light metal/metal oxide systems, the (A) factor tends to yield a lower intensity ratio than the theoretical value and decreases with increasing kV; for the Hf/HfO<sub>2</sub> system, the (A) factor tends to yield a higher intensity ratio than the theoretical value (thus offsetting the Z correction somewhat) and increases with increasing kV. The result is that the total correction factor for the Hf/HfO<sub>2</sub> system approaches unity as the kV is increased, at least up to 25 kV. Similar behavior is exhibited by the Y/Y<sub>2</sub>O<sub>3</sub> system. These cases illustrate exceptions to the principle of operation at the lowest accelerating voltage in order to minimize corrections.

#### Sr-Doped LaCrO<sub>3</sub>

Sr-doped LaCrO<sub>3</sub> is of interest as an MHD electrode material. Accurate determination of small amounts of Sr in LaCrO<sub>3</sub> is difficult with the electron microprobe because the third order Cr  $K_{\alpha}$  peak occurs at the Sr  $L_{\alpha}$  position, which is the peak generally used for analysis. Three obvious methods may be used in circumventing this problem: (1) use of the Sr  $K_{\alpha}$  radiation for analysis, (2) lowering of the electron accelerating potential until the higher orders of Cr  $K_{\alpha}$  are suppressed, and (3) use of the Sr  $L_{\beta}$  peak for analysis.

The first method has the disadvantage that one must go to high accelerating voltages (> 35 kV)--out of range for most electron microprobes--to obtain an adequate  $K_{\alpha}$  signal. Use of the second method decreases the possibility of making a Cr analysis and a Sr analysis simultaneously because at these low accelerating potentials the Cr  $K_{\alpha}$  yields are small. The third method

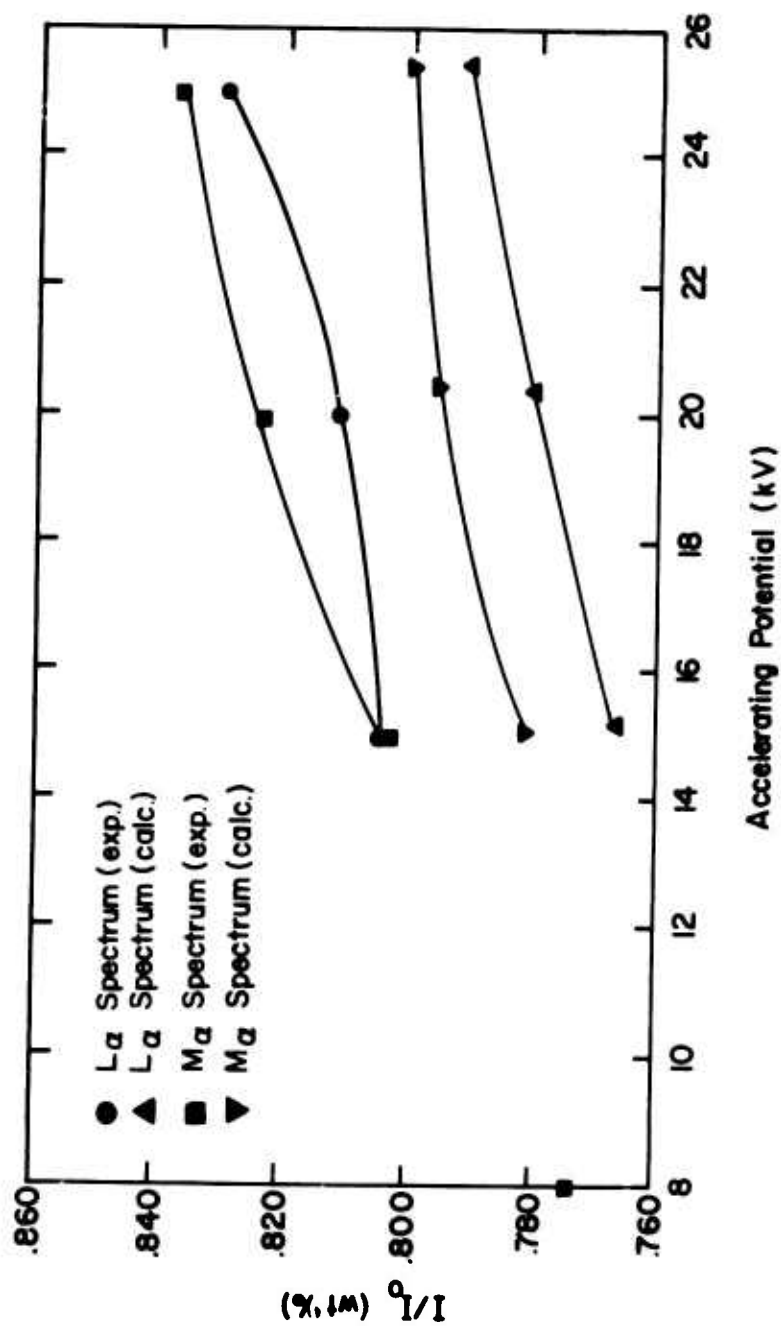


Figure 135. Intensity Ratios for Hafnium in Hafnium Dioxide as Function of Accelerating Potential.

has the disadvantage that long counting periods must be used to achieve statistical accuracy since the  $L_{\beta}$  peak has less than one-half the intensity of the  $L_{\alpha}$  peak.

In order to examine the intensities of the  $L_{\alpha}$  and  $L_{\beta}$  peaks as functions of accelerating voltage, four standards of Sr-doped  $\text{LaCrO}_3$  were prepared. X-ray fluorescence analysis of three of these yielded the following weight percentages of Sr in  $\text{LaCrO}_3$ : 3.5, 5.5, and 7.2. The fourth standard had a nominal value of 9.7 wt%. The results are shown in Figure 136, where counts/sec for the  $L_{\alpha}$  and  $L_{\beta}$  spectra (8.5 and 15 kV accelerating potential, respectively) are plotted as a function of weight fraction of Sr. The  $L_{\beta}$  peak was used at the higher accelerating voltage because of the interference of its Cr  $K_{\alpha}$  peak at these energies.

An alternative to the above three methods is the use of an energy dispersive spectrometer. This instrument collects and separates all x-ray energies simultaneously, and an analysis can be performed without interference of higher orders. One disadvantage of these spectrometers is their poor resolution ( $\approx 170$  eV as compared to  $\approx 1$  eV for wavelength dispersive spectrometers). Also quantitative analysis using energy dispersive spectrometers has not been placed on so firm a footing as that using crystal spectrometers. Another disadvantage of these spectrometers is that the necessary window between the signal and the detector prevents detection of the long wavelengths associated with the low atomic number elements. In an effort to obtain a comparison between the two types of spectrometers (wavelength and energy dispersive), a preliminary study was undertaken to examine these Sr-doped  $\text{LaCrO}_3$  samples. The samples were examined in the electron microprobe by using a crystal spectrometer and in a scanning electron microscope by using an energy dispersive spectrometer. Both instruments utilized a 15-kV beam of electrons.

The data are shown in Figure 137. With the exception of the point obtained with the energy dispersive detector corresponding to 0.097 weight fraction, the sample points lie in straight lines for both types of detectors. The deviation of points from the straight line is less for the energy dispersive detector which may reflect that the counts have been integrated and that more total counts were obtained than with the wavelength dispersive



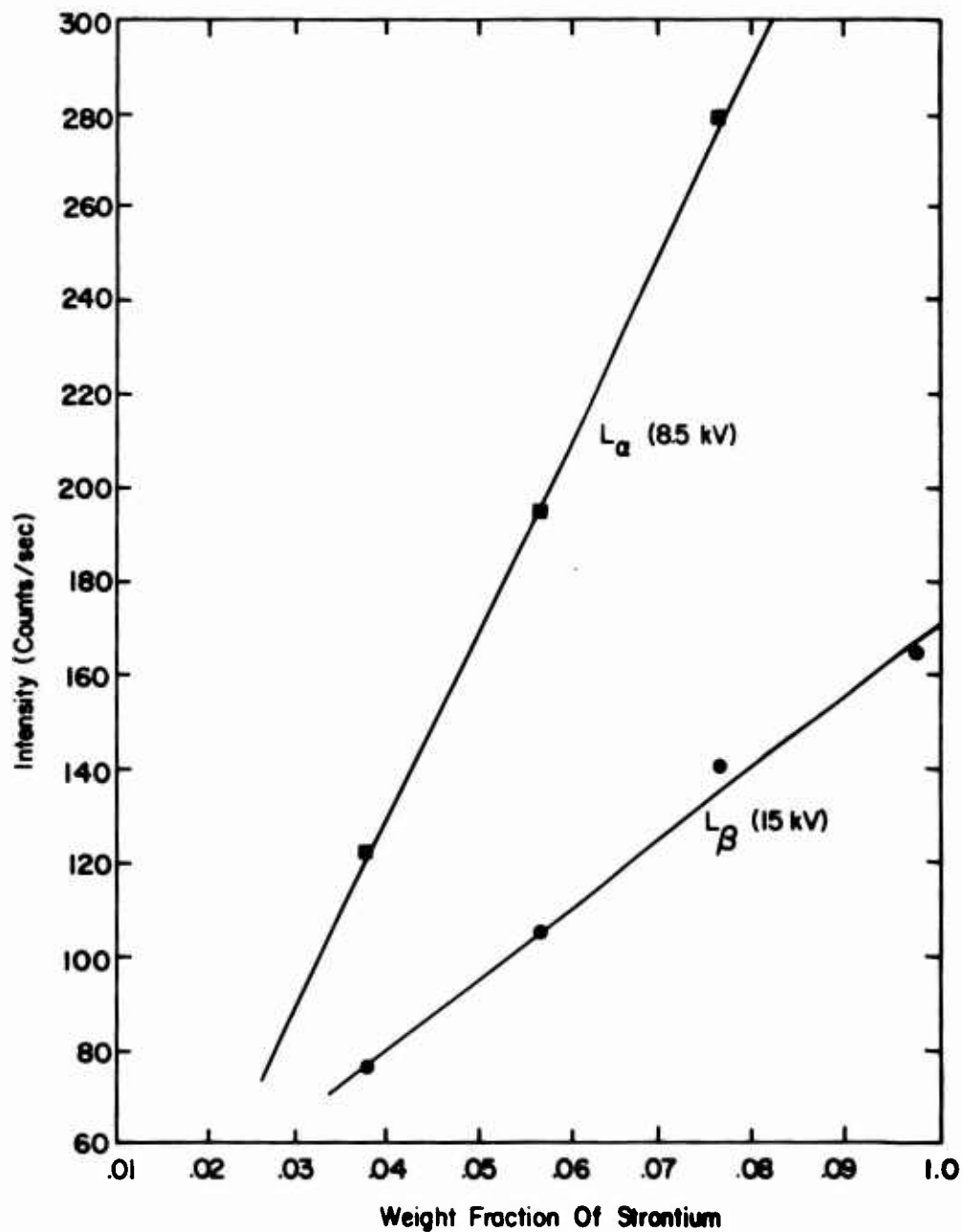


Figure 136. Intensity of Strontium X-Radiation as Function of Weight Fraction of Strontium in Lanthanum Chromite.

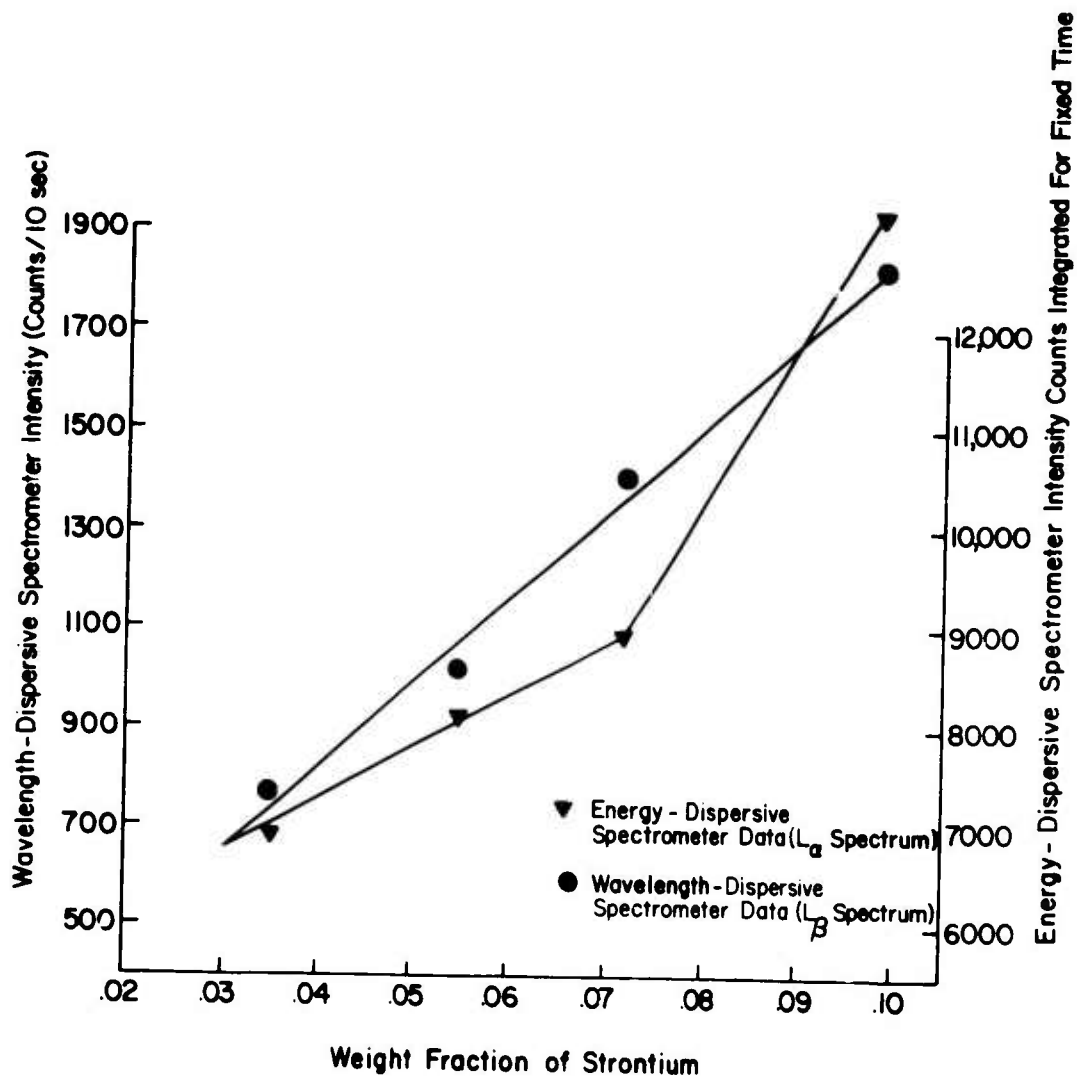


Figure 137. Strontium X-Ray Intensities from Strontium in Lanthanum Chromite.

spectrometer, resulting in better statistics. The reason for the one point being distant is unknown.

The results from these standard samples show that the use of an energy dispersive system for quantitative analysis is feasible for Sr-doped systems at low concentrations up to ~ 7.5 w/o.

#### CHEMICAL-COMBINATION ANALYSIS BY X-RAY EMISSION ENERGY SHIFTS

The shift in the peak energy of the emitted x-ray spectrum of an element upon chemical combination is well known. This energy change occurs because for each compound the electrons which give rise to the spectrum have different energies. The values of these energies will depend upon the environment of the element, i.e., the identity of the neighboring elements, type and multiplicity of bonds formed, etc. These energy shifts are a few eV in value, with the largest shifts occurring when the spectra arise from valence electron transitions since these electrons are those most affected upon chemical combination. Emission x-ray spectra can be used, therefore, not only to identify type and amount of elements present but also to extract certain information about the chemical bonds present.

The  $K_{\alpha}$  spectra of the third period metals (Mg, Al, Si), which originate from M to K electron transitions, involve valence electrons and thus show the greatest effect upon chemical combination of all the emitted x-ray spectra from this series of metals. Although these metals and several of their compounds have been studied extensively, <sup>(108-119)</sup> no simple correlation between the energy shift and the parameters of the compound has been reported. Baun and Fischer, <sup>(109,110)</sup> for example, show that structurally similar compounds yield similar spectra, but they could not show correlation between the spectra and the coordination number of the metal. Dodd and Glen <sup>(113)</sup> studied the shift of the emission x-ray peak from the third period metal oxides, with the metal atoms in different coordination positions, and found that the  $K_{\alpha}$ -spectra peak position shifted to the lower energies when the metal went from six- to four-fold coordination. These data indicate that the chemical bonding effect is reflected more in x-ray band shape than in peak energy shift. They discussed their results in terms of the molecular orbital (MO) theory.

A less rigorous but equally extensive approach to predict the behavior of the emission x-ray spectra and to elucidate the nature of the bonds formed is needed. To this purpose the  $K_{\beta}$  spectra from the third period metals in the elemental state and in the combined state were investigated.

### Experimental

The successful use of commercially available x-ray microprobes as x-ray spectrometers for studying the peak shifts of emitted x-rays has been reported previously. (112,113,120) The instrument used in the present investigation was an Applied Research Laboratory EMX-SM operated at 10 kV. No special modifications were made to the instrument, and no special techniques were used in collecting the data. An ammonium-dihydrogen-phosphate crystal was used as the dispersing medium, and a sealed proportional counter served as the detector. All  $K_{\beta}$  spectra were recorded on a strip chart driven at the rate of 1 in./min, and the spectrometer scanned the desired wavelength range at the rate of 0.02 Å/min. The value of the beam current was chosen in such a way that the number of counts at the peak of the spectrum would be approximately the same for the element metal and for its compounds. Consequently, typical beam currents varied from 0.2 to 0.6  $\mu$ A.

Several spectra for each element and compound were taken (some on different days) to determine reproducibility. The spread in the data for the peak energy was different for each metal studied, being 0.3, 0.5, and 0.6 eV for Mg, Al, and Si, respectively. The use of a step-scan motor on the spectrometer and longer counting times would improve the counting statistics and should decrease the spread in data; however, the method used was of sufficient precision for detecting differences in peak energies of the  $K_{\beta}$  spectra and was less time consuming.

All elements and their compounds studied were at least 99.99% pure (spectroscopic grade), were single crystals which are reasonably pure, or as in the case of polycrystalline SiC, Si<sub>3</sub>N<sub>4</sub>, and AlN, were crystallographically pure as determined by x-ray diffraction techniques. The samples were metallographically mounted and polished, and a thin layer of carbon was vacuum deposited on the surface to prevent charge buildup.

The peak of the  $K_{\alpha}$  spectrum from the pure metal was used as a standard. The position of this peak was assigned the literature value in energy units for the  $K_{\alpha}$  x-ray emitted from the metal.<sup>(121)</sup>  $K_{\alpha}$  peaks from the metal in its compounds were then calculated from this standard position by assuming a linear relationship between energy and spectrometer setting. This assumption is a reasonable one for the small energy ranges involved. Thus each series of compounds for a single metal had its own standard (the  $K_{\alpha}$  spectrum of the pure element) from which the energies of the emitted x-ray peaks were determined.

### Results

The  $K_{\alpha}$  spectra for magnesium, aluminum, and silicon from the elements and from certain compounds were obtained as described above. A typical set of spectra is shown in Figure 138. The curves have been smoothed and the intensities adjusted in such a way that the relative intensities have no significance; only the peak positions are important. As reported by several authors,<sup>(108-119)</sup> the  $K_{\alpha}$  peak emitted from the metal atoms shifts to the lower energies upon chemical combination, and satellite peaks appear in the spectra from the compounds.

Table IX gives the peak energies (in eV) of the  $K_{\alpha}$  spectra from the third period metals and some of their compounds. For a given metal in combination with second period nonmetals (carbides, nitrides, oxides, and fluorides), the peak shifts progressively toward the lower energies as the atomic number of the nonmetal increases. Some literature values (in parentheses) and the experimental values for this investigation are in reasonable agreement. The differences can be attributed to experimental error in this study and the differences in experimental procedures. Since only the relative displacement of the energy peak--and not the absolute value of the energies--is important, differences between literature values and values from the present investigation were not considered to be critical.

### Discussion

Correlations of the peak energy shift of emitted x-ray spectra upon chemical combination and atomic parameters such as coordination number, electronegativity, valence, and crystal structure have been only partially

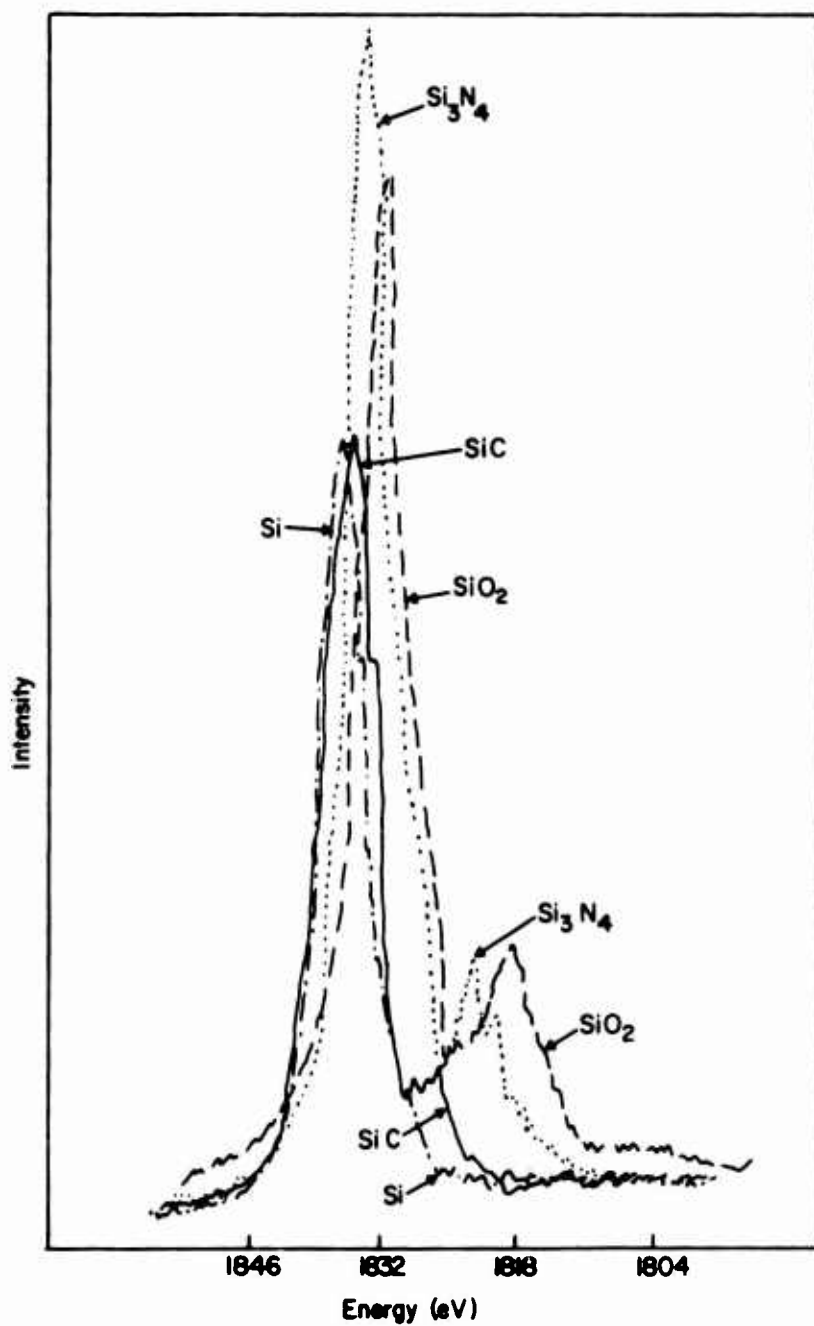


Figure 138. Silicon K<sub>p</sub> X-Ray Emission Spectra for the Element, Carbide, Nitride, and Oxide.

TABLE IX  
PEAK ENERGIES (IN eV) OF  $K_{\beta}$  X-RAY EMISSION FROM THIRD-PERIOD METALS<sup>†</sup>

Element	State				
	Metal	Carbide	Nitride	Oxide	Fluoride Chloride
Mg	1302.0 [1301.7] (110)			1297.7 [1295.3] (110)	1295.5 1298.0
Al	1557.3 [1557.5] (110)		1555.1 [1555.5] (110)	1553.6 [1553.0] (110)	1553.6
Si	1835.6 [1836.1] (110)	1835.0 [1835.9] (118)	1833.6	1832.1 [1831.8] (110)	

<sup>†</sup> Selected literature values in brackets.

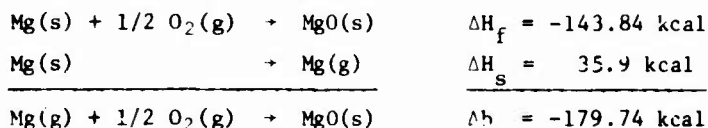
successful. Malissa and Grasserbauer<sup>(122)</sup> have shown a relationship between the peak energy shift of emitted x-rays from oxygen, carbon, nitrogen, fluorine, and chlorine in combination with some metals and standard heats of formation of the compounds. Thus a relationship exists between the peak energy shift and the amount of ionic character of the bonds formed. Therefore, it seems reasonable that a dependence of this shift, for the third period metals in combination with nonmetals, upon chemical thermodynamic properties can be found.

The  $K_{\beta}$  spectra from the third period metals arise from transitions of M-shell electrons to K-shell vacancies, with the excess energy emitted as x-ray photons. The energy of the emitted photons will thus be dependent upon the difference between the initial energy of an electron in an M shell (valence electron) and the final energy of the electron in the K shell. When the environment of the emitting element changes (e.g., upon chemical combination), this energy difference between the two electronic states will change and be observed as a shift in the energy spectrum of the emitted x-rays. This shift will reflect the change in energy between a metal-metal bond and a metal-nonmetal bond. According to Pauling<sup>(123)</sup> the energy of a metal-metal bond is approximately the same as that of a single covalent bond; therefore, the energy difference involved in the  $K_{\beta}$  spectra shift for these metals is the difference in energy between a pure covalent bond and a partial ionic bond. This ionic energy results from the valence electrons being in a lower energy state, which decreases the energy gap between the M and K shells and causes a lower energy x-ray to be emitted when the metal is combined with a nonmetal.

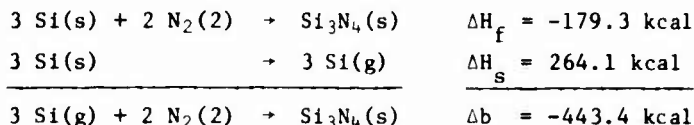
These two bond energies can be calculated from chemical thermodynamic quantities, viz., heats of sublimation and formation. The metal-metal bond energy is roughly equal to the standard heat of sublimation of the metal, while the energy of the metal-nonmetal bonds is equal to the standard heat of formation of the compound. The difference in bond energy is, therefore, the difference in these two standard heats, with consideration of the number of bonds formed by the metal in the compound, i.e., the valence of the metal.



Two sample calculations will be given to illustrate this analysis. Literature values for these standard heats, in some cases, compare poorly. For the sake of consistency, all thermodynamic values used in these calculations were taken from a single reference,<sup>(124)</sup> although other literature values would have yielded closer correspondence between calculated and experimental data for some compounds. The calculations are as follows:



where Δb is the difference in bond energies. Since each magnesium atom forms two bonds (valence + 2), the energy difference per bond is -89.87 kcal = -3.89 eV. Similarly,



In this compound, silicon forms four bonds per atom (valence + 4); therefore, Δb is divided by twelve. The energy per bond is -36.8 kcal = -1.59 eV.

The above calculations predict that the K<sub>β</sub> spectrum peak of Mg will shift toward the lower energies by 3.89 eV upon combining with oxygen, and the K<sub>β</sub> spectrum peak for silicon will shift toward the lower energies by 1.59 eV when silicon combines with nitrogen to form Si<sub>3</sub>N<sub>4</sub>.

Table X gives the results of such calculations for a number of compounds together with the experimentally obtained values of the change in peak energy of the K<sub>β</sub> spectrum from the third period metals in combination with several nonmetals. The change in peak energy (ΔeV) times 100 divided by the peak energy of the K<sub>β</sub> spectrum from the pure metal gives the percent change (% ΔeV). With few exceptions the comparison is good, upon consideration of the previously mentioned disagreement in literature values of the thermodynamic

TABLE X  
CALCULATED AND EXPERIMENTAL VALUES FOR CHANGE IN PEAK  
ENERGIES OF THE K<sub>β</sub> EMISSION SPECTRA FOR SOME THIRD-  
PERIOD METAL COMPOUNDS

Compound	ΔeV		Percent ΔeV		Percent Ionic Character <sup>a</sup>
	Calc.	Exp.	Calc.	Exp.	
MgF <sub>2</sub>	-6.5	-6.5	0.50	0.50	86
MgO	-3.9	-4.3	0.30	0.33	73
MgCl <sub>2</sub>	-4.1	-4.0	0.32	0.31	55
Al <sub>2</sub> O <sub>3</sub>	-4.0	-3.7	0.26	0.24	63
AlCl <sub>3</sub>	-3.5	-3.7	0.22	0.24	43
AlN	-2.4	-2.2	0.15	0.14	43
SiO <sub>2</sub>	-3.2	-3.5	0.17	0.19	50
Si <sub>3</sub> N <sub>4</sub>	-1.6	-2.0	0.09	0.11	30
SiC	-1.2	-0.6	0.07	0.03	12

<sup>a</sup>After Pauling<sup>(121)</sup>

quantities; the experimental error in this investigation adds somewhat to the discrepancies. The possible exception to near agreement is the data for SiC. The value for the peak energy of the  $K_{\beta}$  spectrum of silicon in SiC is very close to that of the pure silicon. Indeed, the difference between these peaks is just at the edge of the spread in data. Yet each time the spectra were taken, the SiC peak fell consistently lower on the energy scale than those from the elemental silicon. Therefore, the large discrepancy shown in Table X between calculated and experimental value is thought to be due not to experimental error but to a poor value for the heat of formation of SiC. Different  $\Delta H_f$  values for SiC in the literature add credence to this argument. For example one source gives a value of  $\Delta H_f$  of 1.43. Using this value for calculations, the  $\Delta eV$  would be -1.0 which would be well within the experimental spread for silicon.

Since the peak energy shifts of the emitted x-rays are related to thermodynamic values, they are also related to the amount of ionic character of the bonds formed in the compounds. The compounds in Table X are listed in decreasing order of %  $\Delta eV$ . For compounds containing second period nonmetals, the order is in fact in decreasing amount of ionic character of the chemical bonds formed. Values for the percent ionic character of the bonds, obtained from Pauling's<sup>(121)</sup> electronegativity values and formula, are listed in the last column.

A plot of percent ionic character of the compound versus the percent change in energy peak of the  $K_{\beta}$  spectra is given in Figure 139. Both calculated and experimental values of %  $\Delta eV$  are shown. All compounds containing the second period nonmetals fall on a smooth curve having progressively decreasing slope. For the carbides, nitrides, and oxides studied, the curve is nearly linear. The points for the chlorides do not fall on the curve although the same trend as noted for the compounds containing the second period nonmetals is present; i.e., for a given nonmetal the %  $\Delta eV$  increases as the atomic number of the metal decreases.

The explanation for the chlorides not conforming to the curve followed by the binary compounds containing the second period nonmetal lies in the method by which the value for the amount of ionic character was obtained.

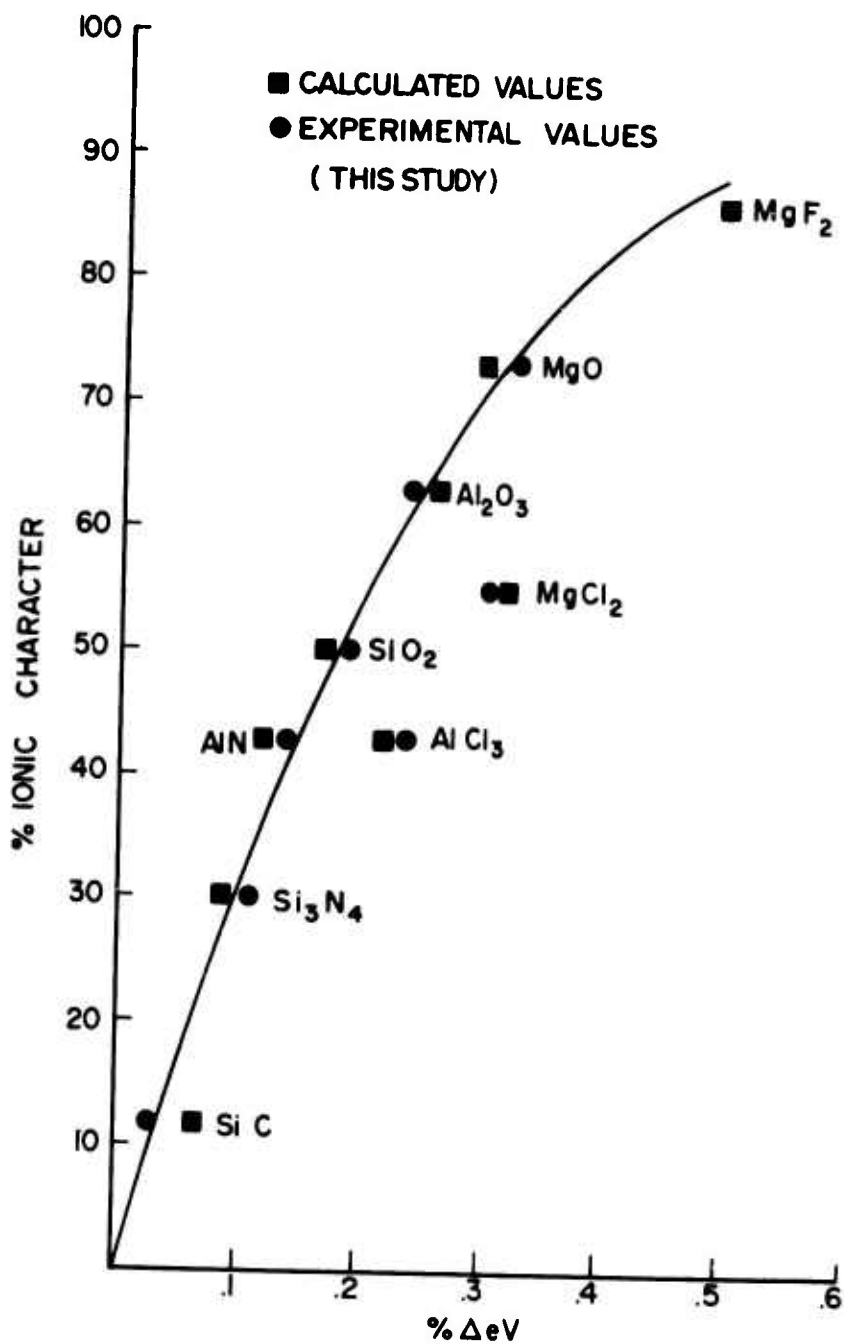


Figure 139. Percent Ionic Character Calculated from Pauling's Electronegativities and Formula vs percent Change in Energy of  $K_{\beta}$  X-Ray Emission Spectra of the Metals from a Number of Compounds.

The formula for calculating these values is only approximate; therefore, in some cases the calculated amount of ionic character is not a reflection of the actual amount present in the compounds. When the single bond enthalpies (standard heats of formation divided by the number of bonds per molecule)--roughly equal to the amount of ionic character--are examined, the values 77 and 55, for  $\text{MgCl}_2$  and  $\text{AlCl}_3$ , respectively, result. With these values for the amount of ionic character instead of those calculated from Pauling's electronegativities and formula, the points representing the chlorides should fall very nearly on the curve.

### Conclusion

The shift of the peak energy of the emission x-ray spectra involving valence electron transitions of the third period metal due to chemical combination can be predicted as to magnitude and direction from calculations using standard heats of sublimation of the metals and standard heats of formation of the compounds. These calculations should be generally applicable for all binary compounds and some higher multiple-element compounds. For example, results from the ternary compound  $\text{NaAlO}_2$  show that the shift of the  $K_\beta$  spectrum peak for aluminum is -5.0 and -4.8 eV for the calculated and experimental values, respectively. Probably the necessary condition for applying these calculations to any compound is that the metal atom must have all single bonds to the same type of nonmetal.

The percent shift of the peak energy of the third period metals spectra is shown to be related to the amount of ionic character of the chemical bonds formed. A simple relationship exists between the percent ionic character of the compound and the percent shift of the emission spectra. This shift can be used to determine the amount of ionic character of the bonds formed in a compound and also to determine chemical species, although this latter application must be tempered with some knowledge of the elements present. A shift of -3.7 eV for the aluminum  $K_\beta$  spectrum could, for example, indicate the presence of either  $\text{Al}_2\text{O}_3$  or  $\text{AlCl}_3$ . It is also possible for this value to be characteristic of some other aluminum compound. On occasion it is desirable to distinguish between  $\text{SiO}_2$  and  $\text{Si}_3\text{N}_4$ , for example, when the

nonmetal cannot be detected due to a lack of a suitable diffracting crystal for the spectrometer. In such cases, the oxide can be distinguished easily from the nitride by the amount of shift of the emitted x-ray spectrum.

## REFERENCES

1. B. E. Deal and A. S. Grove, J. Appl. Phys. 36, 3770 (1965).
2. A. G. Revesz and R. J. Evans, J. Phys. Chem. Solids 30, 551 (1969).
3. K. Motzfeldt, Acta Chem. Scand. 18, 1596 (1964).
4. P. J. Jorgensen, M. E. Wadsworth, and I. B. Cutler, J. Am. Ceram. Soc. 42, 613 (1959).
5. R. F. Adamsky, J. Phys. Chem. 63, 305 (1959).
6. T. Nakatogawa, J. Chem. Soc. Japan, Ind. Chem. Sect. 57, 348 (1954).
7. W. W. Pultz, J. Phys. Chem. 71, 4456 (1967).
8. G. Ervin, Jr., J. Am. Ceram. Soc. 41, 347 (1958).
9. I. A. Ygvorskii, V. I. Elchin, G. G. Gnesin, and G. S. Oleinik, Poroshkovaya Metallurgiya 1, 77 (1968).
10. D. D. Khrycheva and R. I. Bresker, Ogneupory 34, 57 (1969).
11. H. C. Graham, W. C. Tripp, and H. H. Davis, in Progress in Vacuum Microbalance Techniques (T. Gast and E. Robens, ed.) Vol. 1, (Heyden and Son, Ltd., New York, 1972), pp. 125-143.
12. F. J. Norton, Nature 191, 701 (1961).
13. E. W. Sucov, J. Am. Ceram. Soc. 46, 14 (1963).
14. P. Kofstad, High Temperature Oxidation of Metals, (John Wiley and Sons, Inc., New York, 1966), p. 125.
15. R. H. Doremus, in Modern Aspects of the Vitreous State (J. D. MacKenzie, ed.) Vol. 2, (Butterworths, Washington, 1962), pp. 1-71.
16. L. Kaufman and E. V. Clougherty, Air Force Materials Laboratory Report RTD-TDR-63-4096, Part 1 (Air Force Materials Laboratory, Wright-Patterson Air Force Base, Ohio, December 1963).
17. L. Kaufman, E. V. Clougherty, and J. B. Berkowitz-Mattuck, Trans. Met. Soc. AIME 239, 458 (1967).
18. J. B. Berkowitz-Mattuck, J. Electrochem. Soc. 113, 908 (1966).
19. E. V. Clougherty, D. Kalish, and E. T. Peters, Air Force Materials Laboratory Report AFML-TR-68-190 (Air Force Materials Laboratory, Wright-Patterson Air Force Base, Ohio, July 1968).

20. W. C. Tripp and H. C. Graham, J. Electrochem. Soc. 118, 1195 (1971).
21. H. C. Graham, H. H. Davis, I. A. Kvernes, and W. C. Tripp, in Ceramics in Severe Environments (W. W. Kriegel and H. Palmour III, eds.) (Plenum Publishing Co., New York, 1971), p. 35.
22. W. C. Tripp, H. C. Graham, and H. H. Davis, Am. Ceramic Soc. Bull. 52, 612 (1973).
23. W. W. Smeltzer and M. T. Simnad, Acta. Met. 5, 328 (1957).
24. S. C. Singhal and F. F. Lange, Paper No. 38-BC-73F presented at the Fall 1973 Meeting of the American Ceramic Society, Pittsburgh, September 23-26, 1973.
25. J. W. Hinze, W. C. Tripp, and H. C. Graham, Paper No. 28-S2-74 presented at the 76th Annual Meeting of the American Ceramic Society, Chicago, April 28-May 2, 1974.
26. J. W. Hinze, W. C. Tripp, and H. C. Graham, in Mass Transport in Ceramics (A. H. Heuer and A. R. Cooper, eds.) (Plenum Publishing Co., New York, in press).
27. W. W. Smeltzer, R. R. Haering, and J. S. Kirkaldy, Acta. Met. 9, 880 (1961).
28. P. Kofstad and S. Espevik, J. Less Common Metals 12, 382 (1967).
29. C. Wagner, J. Appl. Phys. 29, 1295 (1958).
30. E. A. Gulbransen and S. A. Jansson, Oxid. of Metals 4, 181 (1972).
31. J. W. Colley, MAGIC IV, A Computer Program for Quantitative Electron Microprobe Analysis, (Bell Telephone Laboratories, Inc., Allentown, Pa., 1971).
32. J. N. Fleck, "Fiber and Composite Materials - Bibliography," MCIC Report-72-09 (Battelle Columbus Laboratories, Columbus, Ohio, July 1972).
33. F. Lange, J. Am. Cer. Soc. 56, 445 (1973).
34. S. Sarian, J. Mat. Sci. 8, 251 (1973).
35. J. D. MacKenzie, Modern Aspects of the Vitreous State (Butterworths, London, 1960).
36. G. W. Morey, Properties of Glass (Reinhold Publishers, New York, 1964).
37. W. A. Weyl and E. L. Marboe, Constitution of Glasses, Vols. I and II (John Wiley and Sons, New York, 1964).



38. C. F. Smith and W. B. Crandall, U.S. Patent No. 3,378,431, dated April 16, 1968.
39. J. R. Ligenza and W. C. Spitzer, J. Phys. Chem. Solids 14, 131 (1960).
40. F. Trusell and H. Diehl, Anal. Chem. 35, 674 (1963).
41. W. C. Tripp, H. H. Davis, and H. C. Graham, "Microbalance Techniques Associated with Oxidation Studies," in Vacuum Microbalance Techniques, Vol. 9 (Plenum Press, 1970).
42. J. Stringer, MCIC Report 72-08 (Battelle Columbus Laboratories, Columbus, Ohio, June 1972).
43. R. W. Hardt, J. A. Gambino and P. A. Bergman, "Hot Corrosion Problems Associated with Gas Turbines," ASTM Spec. Tech. Publ. No. 421, June 1966, p. 64.
44. J. A. Goebel, F. S. Pettit and G. W. Goward, Met. Trans. 4, 261 (1973).
45. J. A. Goebel and F. S. Pettit, Met. Trans. 1, 1943 (1970).
46. A. U. Seybolt, Trans. TMS-AIME 242, 1955 (1968).
47. A. U. Seybolt, "Na<sub>2</sub>SO<sub>4</sub> - Superalloy Corrosion Mechanism Studies," G. E. Report 70-C-189 (General Electric Research and Development Center, Schenectady, New York, June 1970).
48. C. S. Giggins, B. H. Kear, F. S. Pettit, and J. K. Tien, Met. Trans. 5, 1685 (1974).
49. C. S. Giggins and F. S. Pettit, J. Electrochem. Soc. 118, 1782 (1971).
50. C. Wagner, Proc. Int. Comm. Electrochem. Thermo. Kinetics (CITCE) 7, 361 (1957).
51. J. W. Patterson, E. C. Bogren, and R. A. Rapp, J. Electrochem. Soc. 114, 752 (1967).
52. Y. Ishikawa, Y. Sasaki, Y. Seki, and S. Inowaki. J. Appl. Phys. 34, 867 (1963).
53. Per Kofstad, J. Electrochem. Soc. 109, 776 (1962).
54. D. Kudrak and M. Sienko, Inorg. Chem. 6, 880 (1967).
55. Per Kofstad, Corrosion 24, 379 (1968).
56. W. C. Tripp, R. W. Vest, and H. C. Graham, pp. 107-27 in Vacuum Microbalance Techniques, Vol. 6 (A. W. Czanderna, ed.) (Plenum Press, New York, 1967).

57. L. Heyne, in Mass Transport in Oxides (J. B. Wachtman, Jr., and A. D. Franklin, eds.) [Nat. Bur. Stand. (U.S.) Spec. Publ., No. 296, 1968], pp. 149-164.
58. Per Kofstad, private communication.
59. I. Bransky and N. M. Tallan, J. Chem. Phys. 49, 1243 (1968).
60. A. J. Bosman and C. Crevecoeur, Phys. Rev. 144, 763 (1966).
61. J. H. Becker and H. P. Frederikse, J. Appl. Phys. 33 (1, Suppl.), 447-53 (1962).
62. B. V. Bondarenka and B. M. Tsarev, Radio Eng. and Electronics 4, 22 (1959).
63. W. E. Danforth, "Thorium Oxide in Electronics," in Advances in Electronics, Vol. 5 (Academic Press, New York, 1953).
64. C. Herring and M. H. Nichols, Rev. Mod. Phys. 21, 185 (1949).
65. M. H. Nichols, Phys. Rev. 57, 297 (1940).
66. G. F. Smith, Phys. Rev. 94, 295 (1954).
67. R. R. Schemmel, R. L. Gordon, and J. L. Bates, "Insulation Resistivity Measurements at High Temperatures," submitted to Nuclear Applications and Technology.
68. H. P. R. Frederikse and W. R. Hosler, Final Report on Contract FY8994-71-00052 (NBS, Washington, D. C., Oct. 1972).
69. J. P. Loup, N. Jonkier, A. M. Anthony, High Temperature-High Pressure 2, 75 (1970).
70. J. P. Loup, A. M. Anthony, Phys. Stat. Sol. 38, 499 (1970).
71. N. Jonkier, and A. M. Anthony, C. R. Acad. Sc. Paris 268, 1459 (1969).
72. S. P. Mitoff, J. Chem. Phys. 41, 2561 (1964).
73. W. J. Lackey, "Effect of Temperature on Electrical Conductivity and Transport Mechanisms in Sapphire," (preprint).
74. T. Matsumura, Can. J. Phys. 44, 1685 (1966).
75. R. J. Brook, J. Yee, and F. A. Kroger, J. Amer. Ceram. Soc. 54, 444 (1971).
76. U. S. Fomenko, Handbook of Thermionic Properties, (Plenum Press, New York, 1966).
77. C. Wagner, Act. Met. 17, 99 (1969).

78. C. Matano, Jap. J. Phys. 8, 109 (1933).
79. S. L. Blank and J. A. Pask, J. Amer. Ceram. Soc. 52, 669 (1969).
80. W. K. Chen and R. A. Jackson, J. Phys. Chem. Solids 30, 1309 (1969).
81. W. K. Chen, N. L. Peterson, and W. T. Reeves, Phys. Rev. 186, 887 (1969).
82. B. C. Harding, D. M. Price, and A. J. Mortlock, Phil. Mag. 23, 399 (1971).
83. B. C. Harding and D. M. Price, Phil. Mag. 24, 253 (1973).
84. T. J. Stiglich, Jr., J. B. Cohen, and D. W. Whitmore, J. Am. Ceram. Soc. 56, 119 (1973).
85. L. D. Hall, J. Chem. Phys. 21, 87 (1953).
86. G. Zintyl, Z. Phys. Chem. 48, 340 (1966).
87. G. C. T. Wei and B. J. Wuensch, Bull. Amer. Ceram. Soc. 52, 350 (1973).
88. H. Schmalzried and J. B. Holt, Z. Phys. Chem. N.F. 60, 220 (1968).
89. B. J. Wuensch and T. Vasilos, J. Chem. Phys. 36, 2917 (1962).
90. I. Bransky and J. M. Wimmer, J. Phys. Chem. Solids 33, 301 (1972).
91. J. Brynestad and H. Flood, Z. Electrochem., Ber. Bunsenges Physik. Chem. 62, 953 (1958).
92. H. J. Engell, Z. Physik. Chem. Neue Folge 35, 192 (1962).
93. M. H. Tikhanen and R. Makkenen, Proc. 5th Int. Sympos. Reactivity Solids, Munich 1964, (1965), p. 313.
94. H. J. Engell and H. K. Kohl, Z. Electrochem., Ber. Bunsenges Physik. Chem. 66, 684 (1962).
95. A. Werner, Z. Physik. Chem. Neue Folge 47, 267 (1965).
96. H. Margolin, E. Levine, M. Young, and I. Greenhut, AFML-TR-73-172 (Air Force Materials Laboratory, Wright-Patterson Air Force Base, Ohio, 1973).
97. J. C. Williams and B. S. Hickman, Met. Trans. 1, 2648 (1970).
98. L. A. Bagariatskii, G. I. Nosova, and T. V. Tagunova, Probl. Metalloved. Metal. 5, 210 (1958); Soviet Phys. Doklady, English Transl., p. 1014 (1959).
99. A. R. G. Brown, D. Clark, J. Eastbrook, and K. S. Jepsen, Nature 201, 914 (1964).

100. M. J. Blackburn and J. C. Williams, *Trans. TMS-AIME* 239, 287 (1967).
101. J. C. Williams, *Titanium Science and Technology*, Vol. 3, (Plenum Press, New York-London, 1973), p. 1433.
102. C. E. Shamblen, *Met. Trans.* 2, 277 (1971).
103. ASTM Standards E399, *Am. Soc. Testing Mater.*, 1972.
104. M. J. Blackburn, *Trans. TMS-AIME* 239, 1200 (1967).
105. G. Lutjering and S. Weissmann, *J. Nucl. Med.* 18, 785 (1970).
106. L. S. Birks, *Electron Microprobe*, 2nd Ed., (John Wiley and Sons, New York, New York, 1971).
107. J. W. Colley, *MAGIC IV, A Computer Program for Quantitative Electron Microprobe Analysis*, (Bell Telephone Laboratories, Inc., Allentown, Pa., 1971).
108. W. L. Baun and D. W. Fischer, AFML-TR-64-350 (Air Force Materials Laboratory, Wright-Patterson Air Force Base, Ohio, 1964).
109. W. L. Baun and D. W. Fischer, *Nature* 204, 642 (1964).
110. W. L. Baun and D. W. Fischer, *Advances in X-ray Analysis*, Vol. 8, (W. M. Mueller, G. R. Mallett and Marie Fay, eds.) (Plenum Press, New York, 1965), p. 371.
111. D. W. Fischer and W. L. Baun, *J. Appl. Phys.* 36, 534 (1965).
112. D. M. Koffman and S. H. Moll, *Advances in X-ray Analysis*, Vol. 9, (G. R. Mallett, Marie Fay, and W. M. Mueller, eds.) (Plenum Press, New York, 1966), p. 329.
113. C. G. Dodd and G. L. Glen, *J. Appl. Phys.* 39, 5377 (1968).
114. C. Senemaud and C. Hague, *J. de Phys., Coll. Sup.* 32, C4-193 (1971).
115. G. Wiech and E. Zöpf, *J. de Phys., Coll. Sup.* 32, C4-200 (1971).
116. Von F. Freund and M. Hamich, *Z. Anorg. Allg. Chem.* 385, 209 (1971).
117. K. Läger, *J. Phys. Chem. Solids* 33, 1343 (1972).
118. B. Kern, *Z. Physik* 159, 178 (1960).
119. D. E. Day, *Nature* 200, 649 (1963).
120. E. W. White and G. V. Gibbs, *Am. Mineralogist* 52, 985 (1967).

121. E. W. White and G. G. Johnson, Jr., Earth and Mineral Sciences Experiment Station Special Publication No. 1-70 (Pennsylvania State University, University Park, Pennsylvania, July 1970).
122. H. Malissa and M. Grasserbauer, *Monat. für Chem.* 102, 1545 (1971).
123. L. Pauling, The Nature of the Chemical Bond, 3rd Ed. (Cornell University Press, Ithaca, New York, 1960).
124. F. D. Rossini, D. D. Wagman, W. H. Evans, S. Levine, and I. Jaffe, Selected Values of Chemical Thermodynamic Properties, NBS Cir. 500 (U. S. Dept. of Comm., Washington, D. C., February 1, 1952).